NUMERICAL STUDY ON EMBANKMENTS RESTING ON LIQUEFIABLE SOIL WITH MITIGATION MEASURES

A THESIS

Submitted in partial fulfilment of the requirements for the award of the degree

of

DOCTOR OF PHILOSOPHY

in

CIVIL ENGINEERING

by

ABHIJIT CHAKRABORTY

DEPARTMENT OF CIVIL ENGINEERING
INDIAN INSTITUTE OF TECHNOLOGY ROORKEE
ROORKEE - 247 667 (INDIA)
SEPTEMBER, 2023

INDIAN INSTITUTE OF TECHNOLOGY ROORKEE

STUDENT'S DECLARATION

I hereby certify that the work presented in the thesis entitled **"NUMERICAL STUDY ON EMBANKMENTS RESTING ON LIQUEFIABLE SOIL WITH MITIGATION MEASURES"** is my own work carried out during a period from July, 2018 to July, 2023 under the supervision of Dr. Vishwas A. Sawant, Professor, Department of Civil Engineering, Indian Institute of Technology Roorkee, Roorkee.

The matter presented in this thesis has not been submitted for the award of any other degree of this or any other Institute.

Dated: **(ABHIJIT CHAKRABORTY)**

SUPERVISOR'S DECLARATION

This is to certify that the above mentioned work is carried out under my supervision.

Dated: **(VISHWAS A. SAWANT)**
Supervisor

ABSTRACT

Interaction of pore fluid with soil solids during ground excitation results in reduction of load sharing capability of soil. This phenomenon causes increase in excess pore pressure and further causes reduction in shear strength of the soil. A stage may come when there will be complete loss in the strength. This stage is termed as 'Liquefaction' of soil. Seed and Lee (1966), Seed and Idriss (1971), Seed (1979), and Seed et al. (1985) provided significant experimental framework related to the liquefaction phenomena and cyclic mobility. Physical understanding is well established, whereas analytical and numerical approaches are still an area of challenge.

Highway infrastructures (embankments, slopes, retaining wall etc.) when built on liquefiable soil layer can be a cause of disruption when underlying foundation soil liquefies during earthquake event. Based on detailed literature study on embankment-liquefiable foundation soil systems, a numerical study has been planned to examine the effect of liquefaction on the embankment. Based on the preliminary study, different mitigation methods are considered further.

Numerical models have been developed in PLAXIS 2D and PLAXIS 3D. The constitutive behavior of foundations soils has been represented by UBC3D-PLM model. The same has been defined by Mohr-Coulomb model for embankment soil. Due to the increase in sideways shear stresses below the embankment toe, embankment undergoes excessive settlement. The soil beneath the embankment never attains liquefaction condition, however the region near the toe and free-field liquefies.

In order to mitigate the liquefaction of foundation soil below the toe regions, stone column mitigation has been adopted in the numerical model. In case of plane strain idealization, the equivalent plane strip approach has been considered to derive the equivalent parameters (bulk modulus, permeability). Based on a detailed parametric study considering the number, diameter and spacing of stone columns, optimum spacing to diameter ratio for effective mitigation of liquefaction has been found out. Further, a seismic study is carried out considering 10 different ground motions with a wide range of Arias Intensity. With increasing Arias intensity of ground motions, the embankment settlement is observed to be increasing almost linearly. Stone column mitigation is less effective in case of higher ground accelerations.

Due to the higher dissipation of pore pressure, stone columns are less effective in reducing settlement during the dissipation stage (post-liquefaction). To deal with this problem, based on the

understanding from past literature, a hybrid pile-stone column mitigation model is adopted. The effectiveness of hybrid model is evaluated against the stone column mitigation and the densification of foundation soil below the toe region. For understanding the effect of nature of earthquake motion, 25 real ground motions are considered. The embankments are found to be showing higher settlement in case of ground motions with lower frequency. The hybrid pile-stone column mitigation is very much effective in controlling the shear-induced settlement of embankment as well as volumetric strain caused by dissipation.

Based on the recent experience of sequential earthquakes in Turkey (2023), it has been observed that most of the building and structures failed during the after-shock events. However, the effect of sequential ground motion on earth structures resting on liquefiable ground condition is an important aspect. In the present study, effect of mainshock-aftershock earthquake events is considered using 3D FEM modeling. Two different mitigation approaches as stone column mitigation and gravel berm along the slope of embankment, are considered in this case. It is observed that, there is a high chance of re-liquefaction of foundation soil below embankment without any mitigation. Re-liquefaction occurred for aftershock events with very less intensity in comparison to the corresponding mainshock event. Among the gravel berm and stone column mitigations, later is found to be more satisfactory in reducing liquefaction and re-liquefaction- induced embankment settlement. However, gravel berm mitigation is found to be effective in reducing differential embankment settlement at the top surface.

Vulnerability of a structure depends on many factors and in order to evaluate the vulnerability of earth embankment, fragility study has been carried out. A wide range of parameters are considered in this study. Parametric study considering relative density of foundation soil, embankment geometry, depth of liquefiable layer, and effect of densification are carried out. Based on the analysis it has been observed that the relative density and thickness of liquefiable layer are primary parameters and embankment geometry are secondary parameters, for the vulnerability of embankment.

ACKNOWLEDGEMENTS

First of all, I would like to thank God Almighty for giving me the opportunity and guidance to achieving my goal and to be successful in this part. To the most important, it gives me great pleasure to expresses my extreme gratitude and deep regards to my supervisor Dr. Vishwas A Sawant, Professor, Department of Civil Engineering, IIT Roorkee for his continuous support, excellent guidance, moral support, motivation, and timely supervision throughout this 5 years journey.

I also wish to express my sincere thanks to Head, Civil Engineering Department, IIT Roorkee for extending me the facilities and cooperation for the successful completion of this work.

My sincere thanks to Prof. Mahendra Singh, Dr. Kaustav Chatterjee, and Dr. Avinash Swain for their kind support and timely suggestions throughout the work. I am also thankful to Prof. N. K. Samadhiya for his suggestions and motivations. Thanks to other faculty members of the department who have directly or indirectly extended their helps. Thankful to the office staffs of Department of Civil Engineering for their help throughout the process.

I am thankful to family of Prof. Vishwas A. Sawant for helping me during all good and odd times at Roorkee. It is also my great pleasure to acknowledge the support provided by my seniors, friends, and co-research scholars Dr. Vinay Kumar Chandaluri, Dr. Siddharth Mehndiratta, Dr. Anant Kiran Kokane, Dr. Arpit Jain, Sai Kumar, Mr. Hansraj, Utkarsh, Aman, Aradhana, Yamini, and all others of the research group.

I am thankful to my friends Dr. Saikat Das, Sourajit, Debraj, Sudipta, Satyabrata and other during my stay at Vigyan Bhawan Hostel in IIT Roorkee for sharing all the good and bad times together. Sincere gratitude towards Suman Banerjee for his kind guidance during this period.

I am grateful to Ms. Sayanti Banerjee for continuous motivation, support and all the help during this period. I sincerely and gratefully acknowledge the blessings of my parents for their support and inspiration for pursuing higher studies. Grateful to my mother for always standing beside me during all my low times. Thankful to my sister, brother-in-law, and nephew for all the love and support.

Last but not the least; I want to express my sincere thanks to all those who directly or indirectly helped me at various stages of this journey.

September, 2023 (Abhijit Chakraborty)

TABLE OF CONTENTS

LIST OF FIGURES

LIST OF TABLES

NOTATIONS

Notation	Description
σ_v'	Effective overburden stress
V_s	Shear wave velocity
M_w	Moment magnitude
τ_{max}	Maximum shear stress
a_{max}	Maximum ground acceleration
γ	Unit weight
g	Acceleration due to gravity
τ_{av}	Average shear stress
r_d	Stress reduction factor
R_D	Relative density
σ_d	Deviatoric stress
N_{CYL}	Number of cycles
N_1^{60}	Field SPT value normalized to 100 kPa
p_a	Atmospheric pressure
C_N	Overburden correction factor
C_E	Energy ratio correction factor other than 60%
C_R	Rod length rigidity correction factor
C_B	Correction factor for bore hole diameter greater than 115 mm
C_S	Correction factor for type of sampler
q_{c1N}^{cs}	Clean-sand cone penetration resistance normalized to 100 kPa
C_Q	Cone penetration resistance normalizing factor for overburden
M	Mass matrix
C	Damping matrix
K	Stiffness matrix
F	Load vector
$(\boldsymbol{u}, \dot{\boldsymbol{u}}, \ddot{\boldsymbol{u}})$	Displacement, velocity, and acceleration vectors
α_R and β_R	Rayleigh coefficients
α and β	Time integration coefficients

σ	Stress tensor
p	Pore pressure
ε	Strain tensor
$\dot{\varepsilon}$	Strain rate
D	Constitutive matrix
f	Yield function
ε^e and ε^p	Elastic and plastic components of strain
λ	Plastic multiplier
ϕ	Friction angle
c	Cohesion
g	Plastic potential function
ψ	Dilatancy angle
φ_{mob}	Mobilized friction angle
K	Elastic bulk modulus
G	Elastic shear modulus
K_B^{*e} and K_G^{*e}	Bulk and shear moduli numbers
m_e and n_e	Factors define the dependence of soil stiffness on stress
K_G^{*p} and n	Plastic shear modulus number and plastic shear modulus exponent
$hard$	Correction factor for densification law
n_{rev}	Shear stress reversal number during the loading–unloading event
$f_{ac,hard}$	Curve fit parameter from corrected densification law
ϕ_p	Peak friction angle
ε_{dil}	Deviatoric strain during dilation phase
$f_{ac,post}$	Post-liquefaction factor
R_f	Failure ratio
K_w	Bulk modulus of water
K_u and K_d	Undrained and drained bulk modulus
ν_u	Posson's ratio during the undrained condition
ν'	Posson's ratio during the drained condition
γ_{dry}	Dry unit weight
k	Permeability

e_{max} and e_{min}	Maximum and minimum void ratio
r_u	Excess pore pressure ratio
E	Modulus of elasticity
Q	Discharge
$p_{stonecolumn}$	Perimeter of actual stone column
D	Diameter of stone column
S	Spacing
i	Hydraulic gradient
A	Cross-sectional area
$k_{equivalent}$	Equivalent permeability
$K^{e}_{B,equivalent}$	Equivalent bulk modulus
$p_{planestrip}$	Perimeter of equivalent plane strip
$r_{u,max}$	Maximum excess pore pressure ratio
Δu	Change in pore pressure
$r^{Eff-zone}_{u,max}$	Maximum excess pore pressure ration in effective zone
$U_{x,max}$	Maximum outflow horizontal deformation
S/D	Spacing to diameter ratio
f_p	Predominant frequency
T_p	Time period
I_a	Arias Intensity
$E_{equivalent}$	Equivalent modulus of elasticity
τ	Equivalent dynamic shear stress
$\Delta_{e,dif}$	Relative embankment settlement parameter
$S^{main/after}_{r,i}$	Settlement ratio for main shock to aftershock events
$U^{GBM/SCM}_{z,i}$	Settlement of mitigated embankment model
$U^{BM}_{z,i}$	Settlement of benchmark embankment model
$Ratio_{ru}$	Ratio of maximum excess pore pressure ratio of aftershock to main shock
$Ratio_S$	Ratio of settlement of aftershock to main shock
dl	Damage level
P_f	Likelihood of a damage level for a specific intensity level

β_{tot}	Lognormal standard deviation
β_{RTR}	Record-to-record collapse uncertainty
β_{DR}	Design requirement-based collapse uncertainty
β_{TD}	Material test data-related uncertainty
β_{MDL}	Modeling-related uncertainty
G_s	Specific gravity
D_{50}	Mean particle size
W	Width of embankment
h	Height of embankment
H_{liq}	Thickness of liquefiable layer
μ	Median seismic demand in 'g'
θ_{is}	Intensity-settlement slope
A_r	Area replacement ratio
L_e	Effective densification distance
B	Embankment base width
R_{rate}	Embankment damage ratio

CHAPTER 1
INTRODUCTION

1.1 GENERAL

When there is a significant ground shaking, water-logged sediments that are loosely packed close to the ground surface begin to liquefy. During earthquakes, liquefaction that occurs under constructed structures and other facilities can seriously harm those structures. As an illustration, the 1964 Niigata earthquake in Japan triggered liquefaction at many places, which led to the extensive destruction of numerous buildings. Similarly, the Loma Prieta earthquake in 1989 in California produced significant subsidence, fracture, and lateral spreading of the ground top in the Marina neighbourhood of San Francisco due to the liquefaction of soils and debris that were placed in a lagoon.

One of the main causes of damage to earth structures constructed over loose saturated granular soils is liquefaction-induced ground displacements driven on by earthquake shaking. There have been several reports of liquefaction-induced failure or near-failures of buildings during various earthquakes, including river dykes, highway embankments, and earth dams (Inagaki et al. 1996; Adalier 1996). Highway elements including bridges, tunnels, embankments, cuts, slopes and retaining walls are highly vulnerable to earthquake shaking, which can substantially impact the transportation services in both the short-term and long-term activities. During an earthquake event, the ability of various lifeline facilities (tunnels, trenches, embankments, retaining walls, levees, and others) to move individuals and goods is essential. Road embankments are part of the transportation infrastructure and are constructed for split-level junction purposes or to cross varied terrain. When such geotechnical structures are situated in seismically active regions and are supported by loose saturated sandy deposits, an earthquake shaking and soil liquefaction might result in serious damage. It is very crucial to investigate the vulnerability of such geotechnical structures while assessing the seismic risk of the transportation network. Moreover, it becomes important to design an effective foundation mitigation for important geotechnical structures situated in an expected liquefaction zone.

1.2 MECHANISM OF LIQUEFACTION

The reaction of a saturated sandy layer to an earthquake is a very important and complex topic of soil dynamics. There is now no fully good generalized solution considering heterogeneity of various aspects. The consequences of the gradual excess pore pressure (EPP) development that occurs during an earthquake determine the dynamic response of loose to medium sands. The acceleration of the

earthquake produces dynamic shear strains and stresses that cause slip at the interface of granular materials. At the generated shear strain values during earthquakes, this inter-granular slip causes volumetric compaction (Silver and Seed, 1971). Volumetric compaction happens slowly because saturated sand particles cannot drain water quickly. The outcome is an increase in pore pressure as some of the inter-granular stresses from the loosening sand skeleton are transferred to the pore-water. The variation in volume between the compaction caused by granular slip and a decrease in pore-water volume caused by increasing pressure within pores and drainage is absorbed by the structural rebound caused by the decrease in effective stress in the sand skeleton. When an earthquake is strong, the pore pressures that are produced may rise to the point where the effective stresses are zeroed out. Sand as a result has very little shear strength and briefly deforms like a liquid, which is known as a zero effective stress condition in soil and denotes the occurrence of liquefaction (Seed and Idriss, 1967). In contrast, the zero effective stress state could never form in denser sand, leading instead to cycles of alternate contraction and dilatation. 'Cyclic mobility' is what is meant by this. Pore pressure will be generated and dissipated simultaneously during earthquake motion if a saturated sandy layer can drain. As a result, pore pressure will build at a slower pace than it would for undrained sand. The pore pressures produced by an earthquake at different points within undrained layers of sand are not going to be in immediate equilibrium with one another, and a continual redistribution occurs under the existing gradients created by the seismic movements. The net consequences of simultaneous creation and redistribution are shown by the pore pressure that has been established at any given time.

1.3 EMBANKMENT ON LIQUEFIABLE SOIL

Large-slide failure of lower Van Norman Dam (NRC 1985) due to 1971 San Fernando earthquake is an eye-opening catastrophe caused by foundation soil liquefaction. Failure of 140 ft high embankment caused flooding of entire nearby region and slipped beneath water (Fig. 1.1.a). Another typical example is road embankment failure due to Au Sable Forks earthquake in New York (Fig. 1.1 b). The slide-failure of road embankment caused by liquefaction of fill material at the toe of embankment.

(a) (b)

Fig. 1.1 (a) Lower Van Norman dam failure, California (Seed et al. 1973); (b) Road embankment failure during the Au Sable Forks earthquake in New York (Gingery 2003).

Earth embankment failures may endanger the safety of property and negatively impact thousands of lives. It is of paramount importance to thoroughly evaluate the safety of these constructions. One of the main factors in the collapse of embankments is an earthquake (examples of earthquakes include the 2011 Tohoku earthquake and the 1995 Hyogoken Nambu earthquake that struck the Pacific Coast). A wide variation of earthen constructions, including coastal dykes, levees, earth dams, and embankments, can be severely destroyed by earthquakes, mostly due to earthquake-induced liquefaction.

From the previous studies it can be observed that the soil beneath the embankment does not reach zero effective stress state, whereas soil in the free field approaches zero effective stress condition. The reason behind this difference in the behavior of stress states at two different locations was the spatial variation in stress conditions. For such situations conventional liquefaction assessment becomes very much tedious. It is highly challenging to predict the seismic behaviour of intricate soil constructions like earth dams using theoretical approaches. In such case, the laboratory scaled model testing (shake table testing, dynamic centrifuge testing) has become a crucial alternative approach to assess the response of such complex geotechnical structures resting on such problematic soil (liquefiable soil). Problems with earth embankments built above deposits of liquefiable soil in earthquake prone regions are particularly challenging. It is very much essential to build proper remedial strategies, which can be quite difficult both fiscally and technically. Because of the high expenditures required, it is not practical to remediate every one of these structures, even if it were theoretically possible. Many embankment structures may not need to be remedied if it could be determined the amount of damage these structures could withstand while continuing to be able to carry out their primary purpose. Identifying the deformations and dynamic reaction mechanisms that occur in these dam/foundation systems will improve our capacity to develop remedial procedures in

a more efficient and cost-effective manner in situations requiring rehabilitation. According to technical literature, earth dams and other earth structure-soil systems may be significantly comprehended through the use of the centrifuge dynamic model testing approach (Arulanandan 1993; Kimura 1995; Adalier et al. 1998). However, many times it becomes challenging to conduct research program using centrifuge testing facility without proper knowledge. Conducting such detailed physical model testing is a challenging task and expensive as well. Moreover, the numerical modeling in recent times became a very efficient economic alternative method to such complex modeling problems.

Numerical modeling has become an effective alternative in simulating such complex problem with better accuracy. Simulation of liquefaction phenomena generally deals with large strain level problem. Selection of proper constitutive model with proper calibration of material model parameters are very important aspect to be considered. Accuracy of the constitutive model must also be verified against physical model testing or field testing. The last few decades have seen a major advancement in the field of soil constitutive models for sands in undrained condition (Yang et al., 2003; Taiebat and Dafalias, 2008; Andrianopoulos et al., 2010; Boulanger and Ziotopoulou, 2013; Ye et al., 2012; Galavi, 2021). For liquefaction assessment, till age SPT values are the most preferred parameter in the field. Many recent constitutive models are also based on the SPT value for model parameters in hypothesizing a soil layer. In the present study a well-calibrated effective stress based elasto-plastic UBC3D-PLM material model (Galavi et al., 2013) has been used. The UBC3D-PLM model is incorporated in PLAXIS 2D and 3D finite element program-based software as a user-defined soil model (UDSM).

1.4 APPROACHES OF ANALYSIS

Significant progress has been made over the past five decades in characterizing the liquefaction phenomenon. Three major strategies are used: (1) field measurements before, during, and/or after earthquakes; (2) lab experiments; and (3) numerical models. Three alternative approaches as total stress approaches, quasi-effective stress approaches, and effective stress-based techniques (fully coupled methods) have been established in the theoretical investigations.

Though many geotechnical engineering issues may be idealized as quasi-static analysis or dynamic analysis within one-phase media, it is challenging to anticipate the dynamic soil behaviour using total stress techniques because of the coupled effects between the solid and the fluid. Saturated soil really functions as a two-phase media. The fluid-soil interaction should be considered in a practical

strategy. The framework for the consideration of liquid-saturated porous materials that is most consistently developed is the mixture theory, which is distinguished by the idea of volume fractions. Through experimental and numerical research, the behaviour of porous media that have been saturated with fluid has been examined. But because of the important role that soils play in the construction of roads, foundations, hydraulic structures, and earth retaining structures, soils in particular have garnered a lot of attention. The literature makes it abundantly evident that liquefaction phenomena involve the interplay of EPP and soil skeleton. As a result of this interaction, the soil-fluid composite weakens during periodic motions like earthquakes leading to serious damages. The intermediary EPP appears to build-up during the motion, decreasing the inter-particle interaction in the solid state of the soil, and leading to a loss of strength.

Drained static behaviour for the two phases, soil skeleton (the deformable porous material) and fluid (incompressible) phase, can be postulated for extremely slow processes with proper drainage. Even for nonlinear issues, these two phases may be separated, and solutions for the structure of soil and pore fluid can be discovered individually, using standard kinematics and effective stress concepts. On the other hand, if drainage is avoided and the loading is delivered quickly, it is possible to assume that the area is undrained and compute the EPP using the bulk modulus of fluid. In this case, only one set of field equations has to be solved. Such dissociation does not take place, nevertheless, under temporary consolidation and dynamic situations.

To ensure the safe behaviour of engineered structures during transient consolidation and dynamic situations, a qualitative and quantitative forecast of the events leading to permanent deformation or an unacceptable high build-up of EPP is crucial. The behaviour of a two-phase porous media may be modelled using a variety of techniques. They are often divided into coupled and uncoupled techniques. The reaction of saturated soil is modelled in the uncoupled analysis without taking into consideration the interaction among soil and fluid, and the EPP is then independently accounted for using a EPP generation model. A mathematical framework is created in the coupled analysis to compute the displacements and pore pressures simultaneously during each time step. Compared to an uncoupled method, it is quite similar to the liquefaction phenomenon.

Contrary to the majority of engineering materials, soil constitutive relationships are very nonlinear even during the early stages of loading. The soil-structure, loading-rate, stress-history, strain-level, and present stress-state are only a few of the variables that have a substantial influence on the deformation and strength properties of soils. To create appropriate constitutive models in practice, the behaviour of the soil must be idealized. Complex soil behaviour occurs when there is seismic

stress. Even if liquefaction does not take place, the formation of high EPP may cause excessive soil softening, weakening, or partial loss of stability, as well as deficiencies in bearing capacity. An important explanation of the soil constitutive behaviour is required for the rational analysis of the prediction of earthquake-generated EPP. Additionally, during seismic analysis, the constitutive model must be able to forecast irreversible changes in volume.

The necessity for the creation of an accurate numerical instrument to successfully anticipate liquefaction becomes increasingly essential. Numerical approaches are often well adapted for modeling the key mechanism and boundary conditions for issues involving the deformation of a soil mass. An effective and flexible numerical approach for simulating geotechnical engineering issues is the finite element method (FEM). Every FE model, however, has to have its domain constrained at a certain finite boundary. For investigations involving wave propagation, a typical constrained boundary of the domain may result in the seismic waves reflecting back and superimposing with the outgoing waves. As a result, one of the biggest challenges in FEM is dealing with the boundary conditions necessary to simulate the dynamic behaviour of semi-infinite soil media. In order to deal with this issue, PLAXIS has different boundary conditions as viscous boundary, free-field boundary, compliant base, tied-degrees of freedom.

In order to simulate earthquake excitation, softening behaviour of soil, significant deformations, the buildup of EPP with consequent loss of shear strength, distribution of EPP, and potential progressive collapse, an advance constitutive relation is needed. The model should also be able to forecast deformations that persist long after seismic loading has stopped and consolidation has occurred with the release of EPP. Since inertial loads would also need to be taken into account, the resultant mathematical formulation would be highly nonlinear.

The present research is based on calibration of an advanced non-linear effective stress-based elasto-plastic constitutive model UBC3D-PLM for modeling underlying liquefiable soil. The study is comprising of: (i) calibration of material model parameters; (ii) comparison of generated cyclic loading response using calibrated parameters with laboratory cyclic tests available in literature; (iii) implementation of verified model parameters to achieve the objectives of the study.

1.5 OBJECTIVES OF THE STUDY

Objectives of this study is to evaluate the response of an earthen embankment resting above liquefiable soil. Based on 2D and 3D FEM numerical modeling of embankment-liquefiable soil system is carried out. Then different mitigation measures are considered as liquefaction-induced embankment settlement countermeasure. Mitigation considering stone columns, hybrid pile-stone

column mitigation, densification, and gravel berms are considered. The effect of sequential ground motion is also considered in the present research. Study also considered fragility assessment of embankments considering a wide range of parameters influential for embankment response under seismic loading event.

1.6 SCOPE OF STUDY

The current study has been focused on modeling liquefaction behaviour and countermeasure in a saturated soil system under cyclic and seismic excitation based on a thorough evaluation of the literature relevant to the aforementioned issues. The suggested research objectives have been separated into the following sections:

i. To investigate the stone columns as mitigation measures for earthen embankment resting on liquefiable soil. Effect of stone column diameter (D), spacing to diameter ratio (S/D), for cyclic loading and seismic ground motions are considered.
ii. To evaluate the efficacy of a hybrid pile-stone column method for embankment structures along with densification and stone column mitigation models. Effectiveness of the models are evaluated for a wide range of seismic ground motions in comparison to the model without any mitigation.
iii. To examine the effect of sequential ground motions in the embankment response considering three-dimensional model with the occurrence of re-liquefaction of the foundation liquefiable soil.
iv. To assess the fragility behaviour of highway embankment resting on liquefiable foundation soil. Effect of mitigation on the fragility response has also been considered in this particular study.

Despite the fact that few of the aforementioned factors have been studied independently in few past studies, no effort has been made to combine them all into one thorough study approach. Because of this, the current work is unique and original.

1.7 ORGANISATION OF THESIS

The entire thesis has been divided into eight chapters as provided below with **Chapter 1** being introduction. The contents of other chapters have been outlined below.

Chapter 2 highlights large volume of literature pertaining to various aspects of liquefaction-induced responses of earthen embankment. The entire literature has been divided into 5 categories; namely, empirical relations for quantification of liquefaction, numerical studies on liquefaction modeling,

field and laboratory based physical observations of embankment-liquefiable foundation soil system, different mitigation measures adopted as countermeasure for liquefaction-induced embankment settlement, and numerical study on embankment resting on liquefiable soil.

Chapter 3 presents the finite element formulations used in the program PLAXIS (2D and 3D). It further reports salient features of MC model and effective stress-based elastoplastic UBC3D-PLM constitutive model for simulating liquefaction triggering mechanism under dynamic loading considering the undrained behaviour.

Chapter 4 has been dedicated towards two-dimensional numerical modeling of earthen embankment resting on liquefiable soil along with proposed stone column mitigation beneath the toe regions of embankment. Study highlights the efficacy of stone column mitigation considering a parametric variation of diameter of stone columns, spacing of stone columns and effect of loading amplitude.

Chapter 5 includes comparative study on three different mitigation approaches namely, densification, stone column mitigation, and hybrid pile-stone column mitigation. Study considered 25 different real ground motions for a wide range of variation of earthquake loading scenario. Performance evaluation of different mitigation techniques are carried out.

Chapter 6 presents three-dimensional modeling of earthen embankment along with two different mitigation models namely, stone column mitigation and gravel berm along the slopes of embankment. Response of embankment models under ten sequential ground motions are evaluated. Study highlights importance of re-liquefaction consideration during after-shock event.

Chapter 7 highlights fragility assessment of highway embankment considering the embankment geometrical properties and foundation liquefiable soil properties. Incremental dynamic analysis (IDA) has been carried out for nine different ground motions for a large number of parametric variations.

Chapter 8 summarizes the conclusions drawn from each chapter and highlights the scope for the future research.

CHAPTER 2
LITERATURE REVIEW

2.1 GENERAL

Seismic liquefaction of foundation sandy soil is a critical aspect in geotechnical investigation, and past studies have highlighted several damage incidents of earth embankment under seismic events like 1940 El Centro earthquake (Seed, 1968), 1964 Alaska earthquake (McCulloch and Bonilla, 1967), 1995 Hyogoken-Nambu earthquake (Matsuo, 1996), 2011 Tohoku earthquake (Sasaki et al., 2012); 2012 Emilia earthquake (Di Ludovico et al., 2020).

Embankments are situated in seismically active regions. Many of these are supported by loose saturated sandy deposits, an earthquake shaking and soil liquefaction might result in serious damage. Therefore, it is crucial to investigate the vulnerability of such geotechnical structures while assessing the seismic risk of the transportation network. Liquefaction-induced large slide of the Lower Van Norman Dam (NRC 1985) occurred during the 1971 San Fernando earthquake led to the flooding of a nearby heavily populated area. Similar destruction of embankment structures was also reported after the 1995 Osaka-Kobe earthquake. Past studies (Yamada, 1966; McCulloch and Bonilla 1967; Matsuo 1996; Adalier et al. 1998) have given deeper insights into such catastrophic damage to earthen embankments when the underlying foundation soil liquefies.

It is very much essential to design an effective mitigation measure for important geotechnical structures situated in probable liquefaction zone. For liquefaction prediction, till now SPT values are the most widely adopted parameter. Some of the constitutive models derive model parameters from the SPT value in the field.

Earlier studies were directed in the assessment of liquefaction potential based on the soil strength parameters. With advancement in computing facilities, attempts were directed in numerical prediction of liquefaction behaviour. According available literatures is discussed in separate groups. Though pioneering studies and stages in the liquefaction assessment have been outlined, more emphasis is given on studies related to embankments on liquefiable soils. Relevant studies on mitigation measures are also included. Aspects like sequential loading and fragility assessment are also discussed with respect to embankments on liquefiable soils.

2.2 SOIL LIQUEFACTION

Following devastating earthquakes in Niigata, Japan, and Alaska in 1964, Seed and Idriss (1971) created the fundamentally straightforward method to calculate liquefaction potential. The process

entails computing the maximum cyclic shear stress that soil can resist normalised to the effective overburden stress $\sigma_v^{'}$ (CRR) and the cyclic stress ratio (CSR), stress that can be generated in an earthquake of a specific ground acceleration normalised to $\sigma_v^{'}$.

Cyclic resistance ratio can be evaluated from either laboratory or field test results. Four approaches are widely used.

1. Cyclic triaxial test-based CRR
2. SPT N value based CRR
3. CPT resistance based CRR
4. Shear wave velocity based CRR

The two most used indices for assessing the liquefaction properties of soils are the Cone Penetration Test (CPT) and Standard Penetration Test (SPT). CPT offers a variety of benefits that elevate it as principal site characterization tool in some geologic contexts, despite the fact that the SPT was initially employed to build liquefaction correlations. Large penetrometer tests (LPT), Becker Penetration Tests (BPT), and Shear Wave Velocity (V_s) tests are more frequently utilized in exceptional circumstances and less frequently the SPT and CPT in liquefaction studies. These various site characterization technologies typically play complementary roles and work best when utilised in combinations.

2.3 REVIEW OF LITERATURE

2.3.1 Empirical Relations

After noticeable devastation observed during Alaska and Niigata earthquakes in 1964, researchers had given serious attention to problem of liquefaction. Studies had been focused to evaluate liquefaction potential of sandy strata which can withstand a design earthquake.

Several researchers conducted liquefaction tests on various types of sand, and the findings were collected by Seed and Idriss in 1971. For a specific number of load cycles, average standard curves for first liquefaction had been produced. The field evaluated potential for liquefaction can then be assessed using these curves.

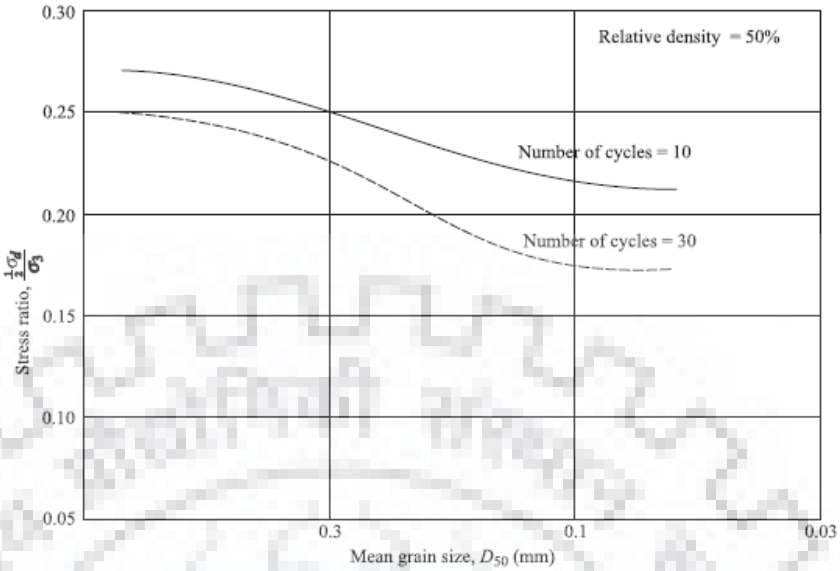

Fig. 2.1 Stress ratio generating liquefaction of sand in 10 and 30 cycles (after Seed and Idriss, 1971).

Through the efforts of numerous researchers, the development of SPT and CPT based liquefaction assessment procedures have advanced over time. Japanese engineers were the first to develop SPT-based correlations, which eventually led to the fundamental work of Seed et al. (1983, 1985), which established the benchmark for more than two decades. Idriss and Boulanger (2008) made recent revisions to SPT-based techniques.

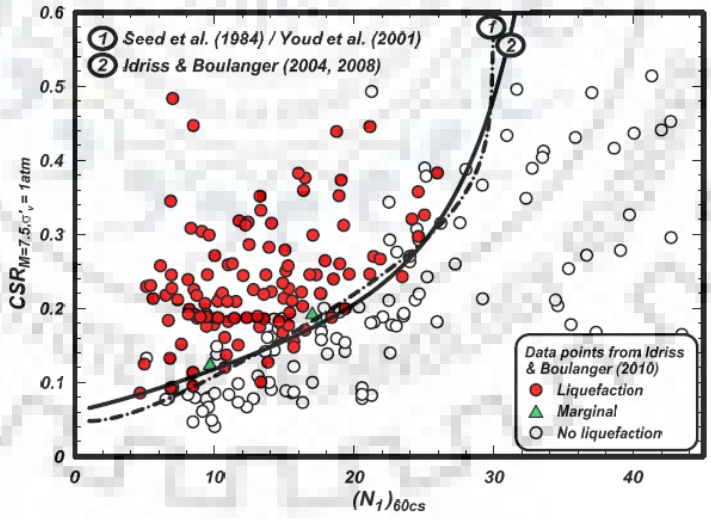

Fig. 2.2 SPT-based liquefaction initiation database from case histories incorporating Idriss-Boulanger (2008) approach.

In Fig. 2.2, the case history information (from Idriss and Boulanger 2018) converted *CSR* corresponding to M_w = 7.5 are compared to the SPT-based techniques from Youd et al. (2001), and Idriss and Boulanger (2008).

Seed and Idriss (1981) then suggested using correlations among SPT and CPT values to adapt the liquefaction initiation charts that were subsequently accessible for use with the CPT. The establishment of CPT-based methods initiated with work by Zhou (1980) utilizing findings. Robertson and Wride (1998) developed CPT-based liquefaction triggering procedures which were further modified to account for fines content (Idriss and Boulanger 2008). The set of case histories of clean sand from modified to an equivalent vertical stress of 1 atm and M_w = 7.5 are compared in Fig. 2.3 with five recent correlations.

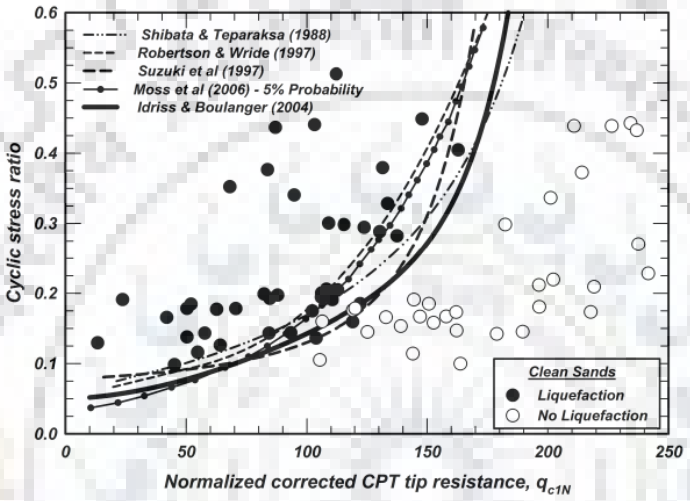

Fig. 2.3 Comparison of liquefaction status with CPT database of case histories for clean sand condition (after, Idriss and Boulanger 2008).

The quality and quantity of SPT and CPT case histories are continuously improving as a result of recent seismic events, such as information from the 2010–2011 Canterbury sequential earthquakes in New Zealand (van Ballegooy et al. 2014) and the 2011 M_w = 9.0 Tohoku earthquake in Japan (Tokimatsu et al. 2012, Cox et al. 2013). For instance, 50 superior case histories of liquefaction and non-liquefaction during the Canterbury sequential earthquakes of 2010–2011 were collected by Green et al. (2014). These case histories included underlying profiles for which the crucial layer could be determined with an acceptable level of confidence. The option to review liquefaction triggering methods and update them as necessary arises from the incorporation of these as well as additional information in liquefaction triggering databases.

Through significant research conducted by Seed (1979), Seed and Idriss (1982), and Seed et al. (1985), the assessment of liquefaction potential process has been consistently refined and improved over time. Twenty experts attended a workshop that T. L. Youd and I. M. Idriss organised in January

1996 to update the streamlined approach and take into account the findings of research from the previous ten years. The following chapter goes into more detail about the four strategies listed above.

Cyclic Stress Ratio (CSR)

Maximum shear stress τ_{max} is mainly dependent on maximum ground acceleration $a_{\max}$ during earthquake. Horizontal inertial force is product of mass and $a_{\max}$. Consequently, horizontal shear stress is ratio of inertial force with area given by $\tau_{max} = \gamma h\, a_{\max} / g$. This relation is applicable for rigid column. For the deformable nature of the soil, τ_{max} at depth h is reduced using reduction factor r_d. Further τ_{max} can be converted into average shear stress τ_{av} for equivalent number of significant stress cycles.

$$\tau_{av} = 0.65\,\tau_{max} = 0.65\,\gamma h \frac{a_{\max}}{g} r_d$$

Cyclic stress ratio CSR is ratio of τ_{av} to effective overburden stress.

$$CSR = \frac{\tau_{av}}{\sigma'_{v0}} = 0.65 \frac{a_{\max}}{g} \frac{\sigma_{v0}}{\sigma'_{v0}} r_d$$

Reduction factor r_d can be approximated as linear function of depth z over three depth zones as $r_d = a_z - b_z\, z$ (Liao and Whitman 1986, Grasso et al. 2021). Constants a_z and b_z have been defined in Table 2.1. Value of 0.504 can be adopted for depth greater than 30 m.

Table 2.1 Constants a_z and b_z for reduction factor.

a_z	b_z	Range for z
1.0	0.00765	$z \le 9.15\,m$
1.174	0.0267	$9.15\,m < z \le 23\,m$
0.744	0.008	$23\,m < z \le 30\,m$

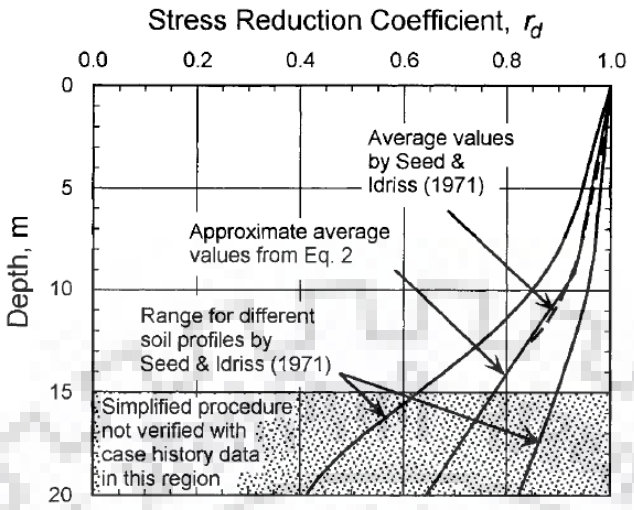

Fig. 2.4 Stress reduction Coefficient

Liquefaction resistance (CRR) assessment

Four methods are frequently employed for *CRR* prediction.

1. Cyclic triaxial test-based
2. SPT-*N* value based
3. CPT resistance based
4. Shear wave velocity based

Cyclic triaxial test-based CRR

Several researchers conducted liquefaction tests on various types of sand, and the findings were collected by Seed and Idriss in 1971. For a particular number of load cycles, average typical curves for first liquefaction were produced. The liquefaction potential in the field can then be evaluated using these curves.

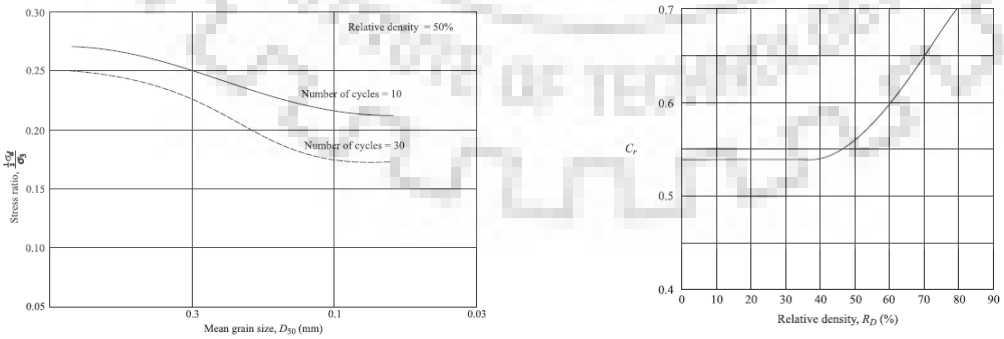

Fig. 2.5 (a) In cycles of 10 and 30, CRR causing liquefaction of sand (after Seed and Idriss, 1971) (b)Variation of C_r with relative density.

Normalized shear stress $CRR = \tau_h / \sigma'_{v0}$ required to trigger liquefaction can be computed from following relation.

$$CRR = \left(\frac{\tau_h}{\sigma'_{v0}} \right)_{R_{D2}} = C_r \left(\frac{\sigma_d}{2\sigma_3} \right)_{R_{D1}} \frac{R_{D2}}{R_{D1}}$$

The relative density R_{D1} (shown in the figure as 50%) is used for laboratory cyclic triaxial tests, and R_{D2} represents the relative density of sand under field conditions. With respect to density, C_r factor varies.

Table 2.2 Substantial number of cycles

M_w	7	7.5	8
Number of cycles (N_{CYL})	10	20	30

SPT N value based CRR

Over time, very rigorous criteria for evaluating resistance to liquefaction depending on the SPT has been developed. Those criteria are integrated in $CSR_{7.5}$ - N_1^{60} (clean sand condition) plot. N_1^{60} is the field SPT value normalized to $\sigma'_v \approx 100\ kPa$ under 60% hammer energy ratio (ER). It is further modified to account for different test conditions other than overburden pressure correction (C_N). IS 1893:2016 drafted following relationship to account all factors. Fines content and bore-hole conditions have some effect on SPT results.

$$N_1^{60} = N_m C_N C_E C_B C_R C_S$$

N_m is measured standard penetration resistance. $C_N = \sqrt{p_a / \sigma'_{v0}} \leq 1.7$ is overburden correction factor. C_E is correction for ER other than 60%. C_R is correction factor to accommodate rigidity of rod length less than 10 m. C_B is correction factor for borehole diameter greater than 115 mm. C_S accounts for samplers with or without liners

A graph of the computed CSR and associated data from locations where liquefaction impacts were or were not noticed after earlier quakes of magnitudes of about 7.5 may be found in Figure 3.4. On this graph, CRR curves were placed cautiously to distinguish between areas where data suggested liquefaction and areas where data suggested non-liquefaction. Curves had been produced for cohesionless soils with three fines contents boundaries (5%, 15%, 35%). The CRR curves in Fig.

2.6 are applicable directly for M_w = 7.5. Magnitude scaling factor MSF needs to be applied for earthquakes of different magnitudes.

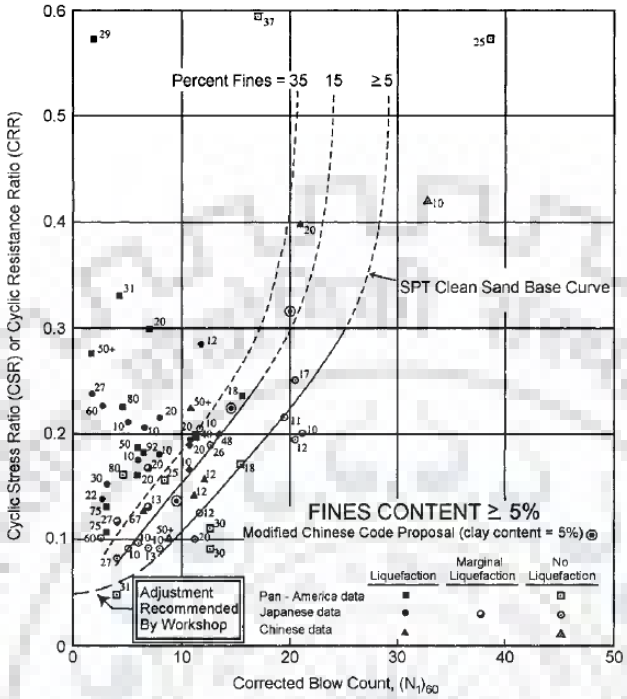

Fig. 2.6 Based on the data from Liquefaction Case Histories, SPT based Clean-Sand curves for M_w = 7.5 earthquakes (Modified from Seed et al. 1985).

Youd et al. (2001) had approximated following relationship for SPT-relationship with CRR.

$$CRR_{7.5} = \frac{1}{34 - N_1^{60cs}} + \frac{N_1^{60cs}}{135} + \frac{50}{\left(10N_1^{60cs} + 45\right)^2} - \frac{1}{200}$$

Influence of Fine Content

Seed et al. (1985) noted a visible rise in CRR with fines content (FC). It is unclear whether this increase is brought on by a rise in resistance to liquefaction or a fall in penetration resistance. Using the available database, CRR curves for different fines had been identified.. For improved compatibility with to the empirical database as to better assist spreadsheet calculations, a revised adjustment for fines content was created.

Plasticity present in some fine grained soils can absorb seismic energy during plastic deformation. This can alter liquefaction resistance (increase). Few guidelines have been drafted based on consistency limits and present moisture content. However, they are not widely accepted yet. The corrections for fines content (*FC*) should be applied with care for plastic fines. Idriss and Seed

suggested following correction to N_1^{60} for converting to equivalent clean sand value N_1^{60cs} (after Youd et al. 2001).

$$N_1^{60cs} = \alpha + \beta\, N_1^{60}$$

where, $\alpha = 0$ $\beta = 1.0$ $FC \le 5\%$

$$\alpha = Exp\left(1.76 - \frac{190}{FC^2}\right) \quad \beta = 0.99 + \frac{FC^{1.5}}{1000} \quad 5\% < FC < 35\%$$

$\alpha = 5.0$ $\beta = 1.2$ $FC \ge 35\%$

Idriss and Boulanger (2008) approximated clean sand base SPT curve with following relationship:

$$CRR_{M=7.5,\sigma_v=1} = Exp\left(\frac{N_{1,60}^{cs}}{14.1} + \left(\frac{N_{1,60}^{cs}}{126}\right)^2 - \left(\frac{N_{1,60}^{cs}}{23.6}\right)^3 + \left(\frac{N_{1,60}^{cs}}{25.4}\right)^4 - 2.80\right)$$

Correction ΔN_1 to N_1^{60} to an equivalent clean sand value, N_1^{60cs}:

$$\Delta N_1 = Exp\left(1.63 + \frac{970}{100\,FC + 1} - \left(\frac{1570}{100\,FC + 1}\right)^2\right)$$

CPT base assessment

The development of a practically continuous penetration resistance profile for stratigraphic interpretation is one of the CPT's main advantages. Compared to results obtained from different penetration tests, the CPT data are typically more reliable and reproducible. Additionally, the continuous profile enables a more precise description of the soil layers. The following equation can be used to approximate the clean-sand base curve shown in Figure 2.7 (Robertson and Wride, 1998):

$$CRR_{7.5} = 0.833\frac{q_{c1N}^{cs}}{1000} + 0.05 \qquad for \quad q_{c1N}^{cs} < 50$$

$$CRR_{7.5} = 93\left(\frac{q_{c1N}^{cs}}{1000}\right)^3 + 0.08 \qquad for \quad 50 \le q_{c1N}^{cs} < 160$$

q_{c1N}^{cs} is clean-sand cone penetration resistance normalized to atmospheric pressure p_a = 100 kPa.

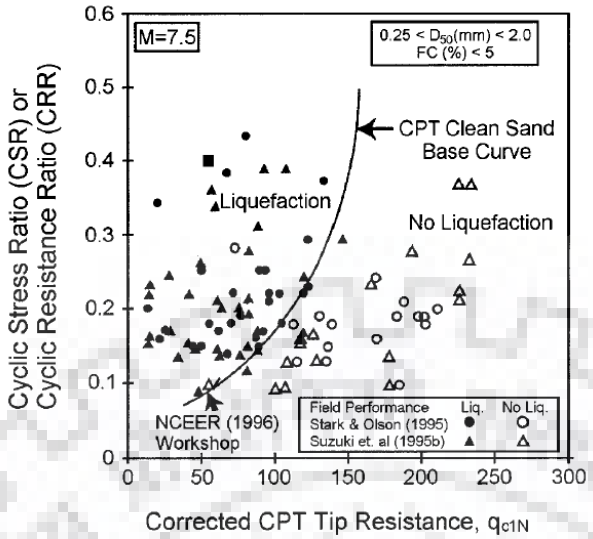

Fig. 2.7 The recommended curve for calculating the CRR from CPT data and empirical data of liquefaction from different case histories (taken from Robertson and Wride, 1998).

Normalization of Resistance of Cone Penetration

Tip resistance must be normalised for the CPT technique. Normalised, dimensionless resistance to cone penetration is the result of this transformation $q_{c1N} = C_Q \, q_c / p_a$. C_Q is cone penetration resistance normalizing factor for overburden $C_Q = \left(p_a / \sigma'_{v0} \right)^n \leq 1.7$. n is varying exponent depending on the soil type between 0.5 to 1 (Olsen 1997). q_c is tip resistance in CPT. to field cone penetration measured at the tip.

CPT resistance ratio (sleeve friction f_s divided by the cone tip resistance q_c) often rises with soil plasticity and *FC*, it is possible to establish the type of soil and amount of fines from CPT.

Robertson and Wride (1998) devised Index I_c. based on normalized cone resistance Q and normalized friction ratio F.

$$I_c = \sqrt{\left(3.47 - \log Q\right)^2 + \left(1.22 + \log F\right)^2}$$

$$\textit{where} \quad Q = \left(\frac{q_c - \sigma_{v0}}{p_a} \right) \left(\frac{p_a}{\sigma'_{v0}} \right)^n \quad \textit{and} \quad F = \frac{f_s}{q_c - \sigma_{v0}} \times 100\,\%$$

If I_c > 2.6, then soil is too clayey to liquefy. To verify the type of soil and resistance to liquefaction, samples of soil should be gathered and examined.

To verify that the soil is not liquefiable, criteria like the Chinese criterion may be used. According to the known Chinese criteria, which were established by Seed and Idriss in 1982, liquefaction can only take place if all three of the subsequent circumstances are true:

1. The weight percentage of clay (particles that smaller than 5 μ) is about 15%.
2. 35% liquid restriction is allowed.
3. The natural water content exceeds the liquid limit by 0.9 times.

The soil is likely to be granular if the computed I_c is less than 2.6, in which case CQ and Q ought to be recalculated with an exponent of n = 0.5.

The classification of the soil is non-plastic and granular if the revised I_c is 2.6.

As mentioned in the following section, this I_c is utilised to calculate liquefaction resistance. However, the soil tends to be extremely silty as well as plastic if the revised I_c is more than 2.6. It is necessary to recalculate q_{c1N} with an intermediate exponent of n = 0.7. The value for q_{c1N} is then recalculated and used to recalculate I_c.

To confirm the kind of soil and to verify the liquefiability based on additional criteria, samples of all soils having an I_c of 2.4 or higher should be taken and examined.

Calculation of the Normalised Equivalent Cone Penetration Resistance for Clean-Sand

$$q_{c1N}^{cs} = K_{cs} q_{c1N}$$

Factor K_{cs} depends on I_c. It is unity for value of I_c less than or equal to 1.64. Else it is computed from following relation.

$$K_{cs} = -0.403\, I_c^4 + 5.581\, I_c^3 - 21.63\, I_c^2 + 33.75\, I_c - 17.88$$

Criteria for measuring liquefaction resistance using V_s

By applying the following equation, the standard methods for adjusting penetration resistance to take into account overburden stress are followed (Sykora 1987; Kayen et al. 1992; Robertson et al. 1992):

$$V_{s1} = V_s \left(p_a / \sigma'_{v0} \right)^{0.25}$$

V_{s1} = shear wave velocity normalized for overburden.

The suggested correlation among CRR and V_{s1} by Andrus and Stokoe (1997):

$$CRR = 0.022 \left(\frac{V_{s1}}{100} \right)^2 + 2.8 \left(\frac{1}{V_{s1}^* - V_{s1}} - \frac{1}{V_{s1}} \right)$$

V_{s1}^* is lower bound of V_{s1} beyond which liquefaction will not trigger for a given fines content FC.

$$V_{s1}^* = 217.5 - 0.5\, FC \quad m/s; \qquad 5 \le FC \le 35 .$$

$V_{s1}^{*} = 215\ \ m/s;$ $\quad FC < 5 \quad$ and $\quad V_{s1}^{*} = 200\ \ m/s;$ $\quad FC > 35.$

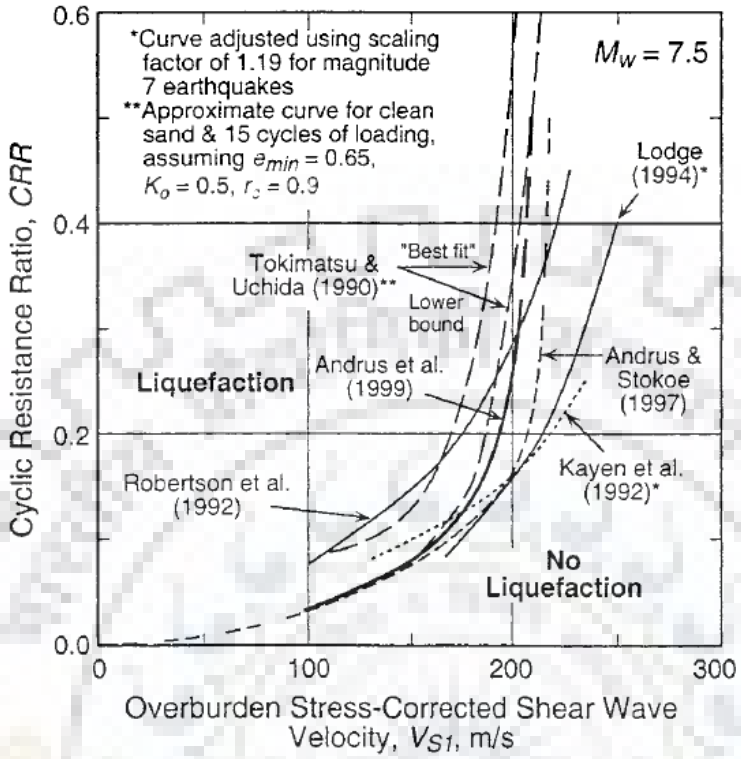

Fig. 2.8 Data on empirical liquefaction combined with suggested CRR verses V_{s1} data (following Andrus and Stokoe, 2000).

Factor of safety (FOS) equation against the liquefaction is expressed in terms of CRR, CSR, and MSF in order to demonstrate how magnitude scaling factors affect estimated hazards:

$$FOS = \frac{CRR_{7.5}}{CSR} \times MSF \times K_{\sigma} \qquad where, \quad MSF = \frac{10^{2.24}}{M_w^{2.56}}$$

$CRR_{7.5}$ is the CRR during earthquakes with a magnitude of 7.5.

Idriss and Boulanger (2008) suggested following relations for magnitude scaling factor *MSF* to CRR and correction factor to CRR for overburden pressure K_{σ}.

$$MSF = 6.9\ Exp\left(\frac{-M}{4}\right) - 0.058 \quad \le 1.8$$

$$K_{\sigma} = 1 - C_{\sigma}\ Ln\left(\frac{\sigma_v^{'}}{p_a}\right) \quad \le 1.1$$

$$C_{\sigma} = \frac{1}{18.9 - 2.55\sqrt{N_{1,60}^{cs}}} \quad \le 0.3 \qquad N_{1,60}^{cs} \le 37$$

2.3.2 Numerical Studies

It requires considerable time and effort to anticipate liquefaction using physical modelling and centrifuge modelling. In an effort to predict and simulate soil liquefaction, many numerical algorithms have been developed using the modern, high-speed computing facility. These computational models are efficient in simulating precise nonlinear behaviour, such as saturated soil under seismic loads. They are generically categorized as coupled, partially-coupled, and uncoupled approaches on the basis of handling interaction between solid and fluid phases.

These numerical models require to be calibrated and verified first for physical experiments in order to determine the responses more precisely. The VELACS study, funded by the NSF during 1991 to 1993, was one of the biggest ones to determine the efficacy of these numerical models. Dynaflow, DIANA-SWAN, SWANDYNE, DYSAC2, LINOS, SUMDES, LIQCA, and QUAD4 were a few of the numerical models utilised in the VELACS study (Arulanandan and Scott, 1993).

Uncoupled Analysis

Uncoupled approach deals with solid and fluid phases separately. Numerical simulation using an uncoupled analysis predicts displacements and volumetric strains. Then these results are utilized further to calculate excess pore pressure (EPP). This method of analysis relies on the substantial dependency among phenomena so that they have a significant impact on one another during dynamic loading. If there is no significant connection between them, an uncoupled approach may offer reasonable predictions of how the soil mass will behave under cyclic loading. Newmark's method is most frequently adopted method for time history analysis. SHAKE (1-D) or QUAD4 (2-D) are two main programs used widely for simulating liquefaction phenomenon in uncoupled approach. The yield criterion depends on degraded soil properties.

The part of the average acceleration records greater than the yield value is double integrated in time domain to evaluate lateral displacement of the surface with minimum yield acceleration (Cooke, 2000). Martin et al. (1975) proposed a densification model for liquefaction. In saturated sand, if drainage is not allowed to occur during the loading stage, the tendency for contraction during cycles of loading leads to a progressive increase in EPP. This approach is predicated on the notion that the complete volumetric strain during a drained simple shear test is identical with the permanent volumetric strain during an undrained simple shear test.

Finn et al. (1977) emphasized to consider the different parameters while computing the behaviour of saturated sand layers subjected to a seismic loading. These key parameters were initial in-situ

shear modulus, the variation of shear modulus with shear strain, simultaneous build-up and dissipation of EPP, changes in effective mean normal stress, hardening and damping.

From the cyclic triaxial results, Chern and Chang (1995) created a mathematical framework for obtaining the liquefaction property of soil under earthquake-induced cyclic loads. This model was able to predict cyclic shear strength, number of cycles require for causing liquefaction and generation of EPP. A porous media model for fluid accumulation and flow within a domain was developed by White and Zaman (1998).

Liyanapathirana and Poulos (2002) proposed numerical model based on effective stress. This model can be used to predict EPP and loss in shear strength due to seismic loading. EPP was evaluated using the equivalent cycle pore pressure model proposed by Seed et al. (1976). One of the main advantages of the proposed model is that it requires few model parameters in comparison with other ground response analyses. The earthquake response analysis of a deeply buried ventilation stack that took into account the impacts of SSI (soil-structure interaction) was presented by Jaya et al. (2008, 2012). Site-specific design ground motion was applied to the finite element domain. Specific charts were developed from laboratory tests for site-specific modulus reduction and damping ratio. These charts were employed to simulate nonlinear behaviour. Results highlighted strong correlation of site relative stiffness and the depth of soil layer. Similar study was extended to study the effects of SSI on seismic response of a deeply embedded Nuclear Island Building.

Partially Coupled Analysis

The partially-coupled analysis considers the partial interactions between the solid and fluid media in a simplified way. Unknown displacements are accounted for while solving the equations for stress equilibrium. Shear strains are then used to determine plastic volumetric strains which are linked with EPP. These steps are performed at every time step. These analyses tend to use less complex soil models and easily obtainable soil properties. But sometime these assumptions may result in inaccuracies in expected behaviour (Cooke, 2000). The literature reported variable success ratio using the partially coupled approach for evaluating the behaviour of liquefiable soil. Puebla et al. (1997) successfully implemented the UBCSAND constitutive model in FLAC to predict EPP and deformations in liquefiable sand below an embankment. Finn (1988, 1991) also successfully validated the results obtained by TARA-3 with centrifuge studies results.

Lo'Pez-Querol and Bla´zquez (2007) presented a unified liquefaction constitutive model considering endochronic theory. The constitutive model considers contractive and dilative behaviors along with soil collapse. A 2-D coupled finite element code CMLIQ (Cyclic Mobility and Liquefaction) was

developed. The predictions from the numerical model were checked with centrifuge tests experimental results for successful validation.

Oka et al. (2012) presented numerical study on assessment of liquefaction potential of granular soils below embankment using QUAKE/W program. Based on the computed normal and shear stresses, a methodology had been suggested to account for the additional stresses (generated due to presence of embankment) in the application of cyclic stress method. Dashti and Bray (2013) incorporated UBCSAND model in FLAC-2D to validate the response obtained from centrifuge studies of shallow foundations resting on liquefiable sand. The soil model was able to capture the impact of deviatoric displacements and volumetric strains under partially drained condition. One limitation was noticed for the case of slower rates of earthquake energy application. The extent of soil softening and accumulated displacement was over-predicted four times.

Coupled Analysis

In coupled numerical analysis, coupled total stress equilibrium equation and fluid continuity equation are used to represent the liquefiable soil domain. Inertial coupling is a benefit when solving these equations that incorporate the coupling between the solid and fluid phases under dynamic loads. Pore pressures have been treated as unknowns in addition to displacements. The resulting simultaneous equations of dynamic equilibrium and fluid continuity are solved for deformations and EPP. The ability of various fully-coupled finite element programs to forecast the response of soil that is saturated under the dynamic loading has been investigated by numerous researchers.

FEM is a classical numerical tool. It is feasible to transform the mixture theory in the regime of elastoplastic nonlinear constitutive models for evaluating the consistent solutions of displacements and pore pressure.

First off, to examine flow across saturated porous media, Sandhu and Wilson (1969) developed a finite element approach. The dynamic stress equilibrium equation and equation of continuity for a completely saturated soil now uses a variational principles method. The consequent coupled equations are numerically solved using approximations from finite elements.

In the realm of finite element framework, Ghaboussi and Wilson (1973) established a variational method for solving Biot's equations for saturated porous media. This formulation accounts for the compressibility of solids and fluid phases. In order to replicate the dynamic interaction, wave propagation experiments had been conducted in saturated soils.

Numerous methods of analysis on the numerical modelling of the Biot-type formulations were compiled by Zienkiewicz et al. (1984). Subsequently, the numerical solution was used to examine the dynamic behaviour of saturated porous materials in undrained and drained states.

Using the findings of centrifuge system soil testing (VELACS), Popescu and Prevost (1993) offered the verification of a mathematical model that utilised multi-yield plasticity theory. The model parameters were calculated using numerical correlation formulas based on the outcomes of conventional laboratory experiments. It was advised to employ an individual set of constitutive parameters in the numerical simulation.

Using the *u-p* formulation (*u*- deformation of the solid state and *p*- pore pressure), Oka et al. (1994) developed a simple and accurate numerical FEM based method for liquefaction response prediction. EPP is treaded as unknown variable for each element. Then fluid continuity equation had been spatially discretized in time domain using the finite difference approach. To demonstrate the shear stress – shear strain behaviour of loosely packed sandy particles subjected to sinusoidal loading, a non-linear kinematic hardening criterion was incorporated into a nonlinear elasto-plastic constitutive model.

To analyse the soil-structure-foundation region of the Middle Channel Bridge, Zhang (2003) suggested a novel nonlinear mathematical model implemented in the OpenSees software. The earthquake excitation along the boundary of the soil domain was explained more clearly and simply by the model. The computational procedure was applied to simulate the seismic response to examine the effects of soil nonlinearity with lateral spreading.

A computational model that is based on the effective-stress technique was presented by Byrne et al. (2004). The findings of the centrifuge test had been validated using this model. The visible restriction on liquefaction at that specific depth was primarily caused by a lack of complete saturation and densification throughout the depth as a result of the implementation of the high-acceleration measure during the centrifuge investigation.

Taiebat et al. (2007) suggested a fully linked dynamic algorithm built on the u-P formulation for assessing the liquefaction potential in saturated sandy soil deposits. In the time domain, coupled equations have been incorporated using the generalised Newmark approach. A critical-state two-surface plasticity model with a densification model was adopted for modeling soil. EPP predictions were in agreement with centrifuge test observations in case of the critical state two-surface plasticity model.

Shahir and Pak (2010) discussed the dynamic behaviour of shallow foundations on liquefiable soils using a three-dimensional coupled analysis. The results of experimental centrifuge measurements are used to test and verify simulations of the suggested numerical model. A reasonable relationship was put forth to evaluate the displacement caused by liquefaction of a stiff foundation above uniformly loose to medium-fine sand. Additionally, a thorough parametric analysis was done for a few significant parameters.

Based on Biot's porous media theory, Shan et al. (2012) established accurate solutions to the 1-D transient analysis of an incompressible one layer saturated soil under four different boundary conditions. In addition to proposing satisfactory initial conditions along with boundary conditions, a relationship was derived among the displacement of solid (u) and the relative displacement (w).

Based on Biot's porous media theory, Kumari and Sawant (2021) simulated saturated soil medium as two-phase material. Infinite elements had been employed to simulate unbounded saturated sandy layer infinite boundaries. To ascertain the responses of pore-fluid and soil-skeleton, a computer algorithm is created through a fully coupled dynamic analysis. To represent the inelastic behaviour of soils under seismic stress, a generalised non-associative and plasticity-bounding surface model called Pastor-Zienkiewicz Mark III had been taken into consideration. While considering unbounded domain, a considerable decrease in deformation and EPP had been noticed. Additionally, it was shown that important factors including permeability, earthquake severity, and shear modulus significantly influenced the response to liquefaction.

The observed behaviour of liquefiable ground has been successfully predicted by finite element computer algorithms, whether they are partially or fully coupled, according to the existing literature. In some specific circumstances, the success rate appears to be influenced by the type of challenge analysed. As a result, a numerical code must be carefully chosen after being evaluated for its capacity to forecast the liquefaction behaviour given the variety of applicable conditions.

2.4 PHYSICAL OBSERVATIONS ON EMBANKMENTS

Safety of embankment dams is seriously jeopardized by earthquake-induced liquefaction of foundation soil. Around the world, during different earthquakes, there have been numerous reports of embankment failures due to liquefaction. When the soil below embankment is susceptible to liquefaction, different distress states in embankments can develop leading to severe damages of embankment. The devastating collapse of the Sheffield dam during the 1925 Santa Barbara EQ was a recognized illustration of an embankment failure in this category (Seed 1968; Seed et al. 1969). The embankment had a maximum of 7.6 m of height and 210 m long. An earthquake caused a 2 m

deep foundation layer of silty sand to sandy silt below the dam to liquefy, with ground accelerations of up to 0.15 g. The whole water in the reservoir was lost when a portion of the dam measuring 100 m long dropped around 30 m downstream (d/s).

However, seismic liquefaction of foundation sandy soil is a critical aspect in geotechnical investigation, and past studies have highlighted several damage incidents of earth embankment under seismic events like 1940 El Centro earthquake (Seed, 1968), 1964 Alaska earthquake (McCulloch and Bonilla, 1967), 1995 Hyogoken-Nambu earthquake (Matsuo, 1996), 2004 M 6.6 Niigata-ken Chuetsu and 2007 M 6.6 Niigata-ken Chuetsu-oki earthquakes (Kwak et al., 2016), 2011 Tohoku earthquake (Sasaki et al., 2012); 2012 Emilia earthquake (Chiaradonna et al., 2019).

Past studies (Yamada, 1966; McCulloch and Bonilla 1967; Matsuo 1996; Adalier et al. 1998; Aydingun and Adalier 2003; Adalier and Sharp 2004; Lee et al. 2014) have given deeper insights into such catastrophic damage to earthen embankments when the underlying foundation soil liquefies. Studies employing centrifuge and shake table equipment have provided more in-depth understandings of the behaviour of earthen embankments lying on liquefiable soil (Koseki et al. 1994; Inagaki et al. 1996).

Any sub-structure situated in earthquake prone area and supported on loose saturated sands, an earthquake shaking and soil liquefaction might result in serious damage (Ledezma et al., 2012; Cubrinovski et al., 2012; Yamaguchi et al., 2012; Lombardi and Bhattacharya, 2014). Therefore, it is crucial to investigate the vulnerability of such geotechnical structures while assessing the seismic risk of the transportation network.

Yamada (1966) carried out field investigation to evaluate damage occurred due to Niigata 1964 earthquake in Japan. The majority of the soil in this area was formed by newly placed artificial fill and recent alluvial deposits, both of which were made of rather homogenous, loose, and saturated sand. The railway fill that crossed the affected area settled exclusively and, in some cases, fully failed or slumped, causing the bridge pier to move and rotate while still having a well foundation. The fill in Uetsu-Line was raised in a small, valley between sand hills, between Dedo Street and Nishime Street. A 150 m long and 7 m high fill collapsed in one direction. It followed by sliding of sand and water mixture over the ground up to 110 m from the middle of the track.

Yokomura (1966) provided deeper insights to clarify the relationship between the foundation soils of river dykes and the damage caused by the earthquake and to provide some reference information for the reconstruction effort. The earthquake caused serious damage near the Awashima Island northwest of Niigata Prefecture, especially in Niigata City along the rivers of Shinano and Agano.

The devastated area covered a 27 km stretch upstream (u/s) from the mouth of the Agano River. Between 1957 and 1963, for instance, there was a 40 cm subsidence of the foundation in the area between the river mouth and Taihei Bridge. Due to the earthquake, particularly in Niigata City, alluvial loose sandy foundations along these two major rivers were subjected to the liquidization phenomena, and many cracks or depressions of the dykes were brought on by the slide of silty soils. The following categories relate to damage of river embankment and associated infrastructure.

1. The top of the embankment are cracking, depressed, and subsiding
2. The river embankment slopes cracking, expanding, and failing
3. The toe of the embankment slopes cracking and failing
4. Berm cracking and depression along the embankment
5. The boiling phenomenon above the riverside
6. Leakage through the foundation of embankment
7. The scouring and erosion of the backside slope of embankment brought on by shock waves and overflow water, as well as the subsequent floods.

Kawakami and Asada (1966) reported the damage of ground and sub-structures during the Niigata earthquake (June 16, 1964). The grounds of the Shonai Plains, surrounding Sakata City, and the Niigata Plains, around Niigata City, are alluvial and hard tertiary deposits, respectively, and many of the structures experienced significant damage as a result of the breakdown of sandy ground. The Niigata Plains have an 80-160 m thick alluvial deposit. The marine clay deposit, which is 20 meters thick, and the sandy deposit, also known as the sand dune, cover the lowest portion of the alluvial deposit, which is a marine deposit made up of numerous layers of clay, silt, and sand. The Niigata Earthquake caused two different types of damage to earthen structures: damage resulting from the vibration of the structures themselves and damage resulting from the liquefaction of sand. The Niigata and Shonai Plains of alluvial deposit were discovered to have significant damage to earth structures as a result of ground liquefaction, such as slides, settlements, and subsidence, as well as sandblows on toes and berms of embankments. Along with the embankments built on soft foundations, such as the dykes along the Mogami and Oyama rivers, and others, the embankments built on hard tertiary deposit foundations that were situated close to the epicenter also sustained significant damage. The major causes of the subsidence of earthen buildings were collapse at the toe of slopes or sinking into the soft ground.

McCulloch and Bonilla (1967) discussed about the widespread damage caused by the physiographic conditions in which wet unconsolidated water laid sediments mobilised during the rail road damage

caused by Alaska 1964 earthquake. In gently sloping and almost flat terrain, the mobilised sediments went almost horizontally towards topographic depressions. The disturbed sediments were composed of silt, extremely fine sand, and gravel, according to surface observation and data from available bore holes. A reduction of bearing strength and transient horizontal displacements appear to have occurred along with the mobilization, according to some evidence. During the first two months survey after the earthquake event, major damages had been seen all over the region. In case of embankments, differential settlement had been observed.

Lee and Schofield (1988) studied the behaviour of embankments during earthquakes through centrifuge modeling. The findings from the study demonstrate that positive pore pressures are produced during an earthquake, especially at the crest, of an embankment or island that is loose or medium dense. In the worst situation, liquefaction, and the decoupling of surcharge motions from crest motions occur as a result of the embankment softening and lowering of resonance frequency caused by this pore pressure development. Spiky acceleration recordings are found at the shoulders of an island or an embankment when a strong earthquake occurs there. The transmission of dilation fronts through the cyclic mobility of sand, which may be responsible for these records.

Koga and Matsuo (1990) performed shake table tests on earth embankment resting on saturated sandy ground. Study considered six small scale models exposed to different input accelerations. Study shows the liquefaction of free ground within few cycles, whereas the soil below the embankment did not liquefy. The liquefied soil found to exhibit sharp acceleration response. Since underlying soil being softer due to the development of EPP, embankments slump and crack. For earthquake with a large duration and low frequency, the amount of such damage is more extensive. Study concluded that the spiky acceleration of the liquefied ground was caused by the cyclic mobility effect.

Steedman and Madabhushi (1993) performed four centrifuge tests on embankments with confined liquefiable soil layers. Embankments were built with a steeper slope on one side in order to provide a safety factor comparable to the downstream slope of an equivalent embankment with outward seepage. On the side of the model embankment with the greater slope, these liquefiable zones were kept inclined. The upstream slope was mostly unaffected throughout all of the centrifuge experiments. The top of the loose confined zone was almost invariably moved where the slip started. Strong suction pressures were detected in the pore pressures near the crest and base of the embankment, indicating that these zones have dilated.

Pillai and Stewart (1994) carried out a thorough field, laboratory, and analytical investigations to evaluate the liquefaction potential of the foundation soil of Duncan dam in southeastern British Columbia. A series of sands, silts, and gravels serve as the foundation for the 39 m high embankment. Liquefaction potential of the foundation soil was calculated using total stress approach. In this study, liquefaction potential was evaluated using soil parameters based on CPT (Seed's approach) and laboratory testing of undisturbed soil samples collected in situ following ground freezing (Lab method). Both the Lab technique and Seed's method predicted a considerable degree of liquefaction of the foundation soils under d/s slope in the right side of the dam for M_w = 6.5, *PGA* = 0.12g.

More than 40,000 people died as a result of the 1988 M_s 6.8 earthquake in Armenia, which also left the northwest region of the nation in utter ruin. Yegian et al. (1994) reported that the liquefied sands contained a high gravel percentage (nearly 50%). According to the analysis, loose to medium-dense gravelly soil layers that are unrestricted by drainage can endure substantial peak ground accelerations (0.5*g* to l.0*g*) without liquefaction. However, even a little layer of impermeable top soil of 30 cm thickness can obstruct drainage, liquefy such soils, and cause considerable lateral spreading and deformations.

A1-Homoud et al. (1995, 2000) reviewed the geological characteristics related to a number of specified dam locations in Jordan, as well as the tectonic influences on the dam foundations and reservoir edges. It is suggested that dynamic loads and associated risks, such as embankment acceleration zoning, foundation liquefaction risk, and rockhead rupture must be considered while designing embankment dams along such site.

Adalier (1996) carried out dynamic centrifuge test to evaluate the response of earthen embankment resting on liquefiable ground. Study pointed out that the liquefiable soil beneath the embankment did not reach initial liquefaction condition due to the increase in vertical effective stress due to embankment weight. r_u was observed to be increasing with the depth below the embankment, which is usually found to be opposite to the free field condition. However, the ground in the free field found to be liquefied easily. Study shows that the principal cause for embankment failure was due to bearing capacity failure as a result of increased EPP in the foundation soil.

About 1,200 relatively small-scale irrigation earth dykes were harmed in some way during the 1995 Hyogoken-Nambu earthquake. Within a 90 km circle around the epicenter, damage to earth dams was seen, with the majority of it happening within a 30 km circle. Liquefaction may have caused to damage in some of the earth dams that were the focus of soil surveys done by Tani (1996).

Information from both this and earlier earthquakes demonstrated that there is a constant correlation between magnitude, and the projected maximum damage rate of earth dams.

In a seismic rehabilitation study of 30 important earth dams by Marcuson et al. (1996) it could be observed that 21 embankments had deficient foundation materials. Among them most of the foundation soil deposit were encountered to be liquefiable in nature. Since the Lower San Fernando Dam disaster on February 9, 1971, the majority of seismic remediations for earth dams have been carried out, according to the information and data gathered during the current research. The majority of the issues have been related to liquefaction. The case studies show an increasing trend towards using post-quake deformed shape assessments to assess the effectiveness of suggested engineered remediations.

Matsuo (1996) reported damage of river embankments at different locations after the Hyogoken-nambu 1995 earthquake. Six rivers with 32 sites with a total length of 9,290 m were found to have damage. Two embankments namely Torishima and Nishijima dykes of the largest river Yodo-gawa in the Kansai region flows through Osaka were seriously damaged. However, the Yodo-gawa is not the river that is closest to the epicenter. Sand boils were seen on the ground surface close to the dykes at the majority of the damaged sites. The settlement of Torishima dyke crossed 2 m on the Kilopost 0.5-1.9 km, with a maximum of 3 m. In case of Nishijima dyke crack formed at the top measured between 20 and 150 cm in width, with 1.2 m subsidence. The toe was moved laterally about 1 m. These facts suggested that the main cause for damage was liquefaction of the foundation soil.

Olson et al. (2000) presented findings of stability analyses for upstream slope failure of the North Dyke of Wachusett Dam near Clinton, Massachusetts. Purpose was to calculate the mobilized shear strength in the liquefied soils during failure. Other liquefaction flow failure case histories that have been documented in the literature are consistent with the back-calculated shear strength taking the kinetics of failure into account. It is advised that, in order to ascertain the shear strength mobilized during flow failure, the kinetics of failure be taken into account.

Park et al. (2000) executed 12 different cases of embankment model shaking table tests to investigate the behaviour of embankment resting on liquefiable ground. Initial liquefaction in a free field is followed by embankment failure brought on by lateral ground flow. Liquefaction becomes easier as liquefiable layer thickness increases. There was Holocene sandy soil in the upper part of the subsurface profile with an SPT *N* value of 10 or less. These facts suggest that the main reason for the damage to the embankment was soil liquefaction.

Krinitzsky and Hynes (2002) examined 15 earth dams following the Bhuj 2001 earthquake in India. All the dams were found to be built on sandy, unconsolidated alluvial soil which are prone to liquefaction during earthquake. Dams were found to fall apart due to liquefaction in the foundation, which also results in unequal settlements. Additional soil block displacements resulted from lateral spreading driven by more shaking.

In Japan, the remedial measures for river dykes resting on liquefiable soil deposit have often been incorporated after the Hyogoken-nambu earthquake. In order to create conventional approaches to evaluate crest settlement Okamura and Matsuo (2002) performed a number of centrifuge tests to assess the seismic embankment response. Grouting by deep mixing, densification by sand compaction piles, and sheet pile confinement were mitigation measures considered in this study. It was found that embankment models with countermeasures tend to sustain higher EPP under the toes than embankment without mitigation. The implementation of the lateral confinement as part of the remedy is believed to be the cause, leading to an increased contractive volume change in the sands beneath the embankment. Consequently, this phenomenon contributes to the unavoidable settlement of the embankment crest.

Olson and Stark (2003) suggested a method to use the yield strength ratio to analyze the onset of liquefaction in sloped ground subject to a static shear stress. To assess the shear strengths and strength ratios mobilised at the triggering of liquefaction, 30 flow failures cases were simulated. Strength ratios during the flow failures were between 0.24 and 0.30. They were found to be in order with corrected CPT and SPT values.

Ng et al. (2004) executed centrifuge tests on loose decomposed granite model embankments to examine the seismic stability and liquefaction potential of loose fill slopes. The measured maximum r_u varied from 0.70 to 0.85 during the 0.3*g* of strong uniaxial shaking. A relatively smaller crest settlement of 5.8 mm was observed without complete liquefaction and flow slides. The maximum r_u in case of the bi-axial test ranged from 0.75 to 0.87. These were slightly higher than the uni-axial test results. The crest settlement was 27% higher compared to uni-axial shaking. According to test results, loose CDG fill slopes in Hong Kong can withstand suggested design PGA range of 0.08 to 0.11*g*.

Koseki et al. (2006) reported damage to earth structures on the national highways of Japan during the 2004 Niigata-ken Chuetsu earthquake. National highways and prefectural roads were shut down at 101 locations right after the main-shock. There were 17 locations where the key national highway routes were shut down. However, they were reopened after ten days. On the other hand, Two

locations across mountainous terrain had significant damage, necessitating the construction of detours. The route no. 8 had embankment failures, potentially as a consequence of the liquefaction of a subsurface layer of loose sand as well as concentration of transverse ground water flow.

Okamura et al. (2006) performed centrifuge study to examine the pressure on the rigid vertical walls used as lateral barrier for embankments. The dynamic earth pressure increment of liquefied sand was observed proportional to the wall acceleration and increases with increasing average embankment load. For practical usage, a useful formula for the earth pressures was established.

Sengara et al. (2006) carried out survey of infrastructure damages after the 2004 Sumatra earthquake and five weeks later the 2005 Nias–Simeulue earthquake. These assessments showed numerous incidents of damages that were likely brought on by intense ground shaking and subsequent liquefaction driven foundation or embankment failures. Survey suggested a seismic micro-zonation establishment to pinpoint the spatial variability of intense ground motions in order to reconstruct the infrastructure in the area.

Namdar and Pelko (2011) carried out shaking table tests to evaluate the embankment response subjected to foundation soil liquefaction. Experimental and analytical techniques have been used to assess the forces generated in the model. In the shaking table experiment, EPP was detected using pore pressure sensors, and embankment stability had been evaluated using analytical techniques. The indirect simulation technique demonstrated unequivocally that stability and deformation could be accurately calculated, and earthen structures could be planned or redesigned based on that for maximizing safety factors, obtaining maximum stability, and achieving the lowest project cost.

Koseki et al. (2012) compiled statistics on the damage reported for railway embankments for bridges due to the 2011 Tohoku earthquake in Japan. In lowland places, embankments built on liquefiable or soft subsurface layers experienced significant settlement. Sliding collapse occurred on an embankment built in a valley in a mountainous region. Between Izumizaki and Yabuki Stations, along the JR Tohoku Line, 200k400m away, excessive settlement of an embankment was observed. Another embankment settlement was observed along the JR Narita Line, located at 25.5 km between Kobayashi and Aziki stations. Another embankment between Sakunami and Yatsumori Stations at a distance of 30.3 km was collapsed. In all these cases presence of loose sandy subsoil was observed, which indicates the saturated sandy subsoil may have liquefied and induced a large deformation of embankments.

Okamura et al. (2013) caried out a thorough examination through centrifuge testing of the damaged levees that had been dissected. It was discovered that foundation consolidation had been responsible

for the levee base bowl-shaped subsidence. An underlying mechanism is speculated to have been the levee deformation brought on by the foundation consolidation. The deformation of the embankment during shaking can be attributed to the saturated zone in embankments and the drainage boundary conditions.

In order to study how earthen embankments with different liquefiable foundation conditions deformed as a result of liquefaction following mainshock-aftershock sequential ground motions, Maharjan and Takahashi (2014) conducted a series of centrifuge tests. According to the test results, an embankment resting on non-homogeneous soil deposits sustains greater damage than one built on a foundation of uniform sand of similar relative density. Study revealed a major impact of sequential ground motions on the accumulated embankment deformation.

Mohri et al. (2014) reported the damages to the agricultural facilities in Tohoku district, Japan, due to the 2011 Tohoku earthquake which includes damage to coastal dykes, farmland behind embankments, and disruption of life support systems including irrigation systems in areas far from the coast. Numerous small earth dams, other dams, and pipe systems suffered damage in Fukushima Prefecture. 745 small earth dams in Fukushima Prefecture out of 3730 dams suffered damage from sliding failure or embankment settlement. Small earth dams were breached at three different locations, severely harming the areas downstream.

Villavicencio et al. (2014) in a recent study discussed failure of a total 38 sand tailing dams in Chile. Significant seismic activity in the country has been the main cause of failures. Almost 50% of the failures were caused by liquefaction, 32% by slope instability and seismically generated deformations, and 18% by over-toppling with flow failure. These mechanical instability events primarily occurred in upstream-built sand tailings dams with retaining dykes less than 40 m height that were in use (53%) or abandoned (47%) and connected to medium-scale mining sector of Chile.

In order to assess certain aspects influencing the seismic behaviour of hill side embankments made of sand or silt and resting on a stiff base slope, a series of centrifuge model tests were executed by Enomoto and Sasaki (2015). The test results revealed that one of the key causes of earthquake-induced embankment failure was seepage water. Installing the toe drain significantly enhanced the seismic performance of embankments. When compared to poorly graded sands, well-compacted embankments made of silty soils with high fines concentration performed better.

Kartha et al. (2016) conducted model tests on embankments on liquefiable soil using 1D shake table. The experimental findings indicate that the existence of embankments will cause a greater buildup of EPP. The embankment will prevent dissipation any EPP that develops through the top surface.

Huang and Zhu (2016) conducted dynamic centrifuge tests to predict performance of embankments under seismic loading. An experiment-based safety assessment of the liquefaction resistance of a embankment has been carried out. This reservoir, an important undertaking constructed in the center of a coastal estuary in 2007, provides approximately fifty percent of the untreated waters for Shanghai, China.

Yang et al. (2018) performed number of model tests on high embankments to determine high embankment failure types and the effectiveness of seismic protection against buried strike-slip fault movement. High embankment failure was mostly due to tensile failure due to buried strike-slip fault movement. The energy dissipation impact of various aseismic measures plays a significant role in seismic effect.

A controlled in situ milliseconds delay blasting (MDB) experiment was executed by Zhang et al. (2019) to examine the behaviour of a sandy area during liquefaction in addition to the liquefaction-induced deformation as well as casualties to an embankment and a slightly buried reinforced concrete structure. Numerous strain gauges reported out unrecoverable strains as the concrete structure experienced significant (uneven) settling and tilt. The field experiment described in this work shows that the created scheme and the aforementioned MDB technique are efficient in producing a liquefied site, which may be utilised to analyze the behaviour of neighboring structures after liquefaction.

Zhou et al. (2019) carried out shaking table tests to study the failure modes of high slopes and response under dynamic loading. According to test results, PGA amplification coefficients increased with height. It was marginally greater in concave slope than the convex slope. According to the results, integral sliding above the slope surface, shoulder collapse, and the development of the sliding surface are the characteristics of the failure modes of the concave slope. Slips in the soil layer and collapse of the slope close to the sloping surface make up the majority of the failure modes of convex slope.

Pramaditya and Fathani (2021) conducted centrifuge model tests on embankment resting on a liquefiable foundation ground subjected to 2011 Tohoku earthquake motion. The manifestation of EPP revealed the liquefaction to have taken place at 3 m and 6 m depth in the free field as well as 6 m in the foundation earth beneath the embankment. Additionally, sand boils were seen on the ground surface. The lateral spreading of the foundation ground was identified as one of the causes of the embankment settlement.

Carey et al. (2022) executed detailed centrifuge study to evaluate the influence of sand gradation on the system-level performance under strong shaking. Two 10-degree submerged embankments were used in the experiment. One was made of poorly graded sand and the other of well graded sand. They were placed side by side in a rigid model container. According to the results, embankments built at equal relative densities would both liquefy (r_u approach 1.0). However, embankments built with well-graded sand experiences less severe deformations. The stability of the embankment was strengthened by greater dilatancy of the well-graded sand, increased resistance to the development of EPP, and reduced liquefaction-induced deformations.

Harada et al. (2022) performed centrifuge tests to examine the dynamic behaviour of embankments on liquefied ground. After earthquakes, longitudinal tensile cracks have frequently been seen at the crest and slopes. The major body of the embankment appears to be deformed to stretch equally horizontally as a result of the liquefaction and lateral spreading of the foundation ground, according to video image analysis, which is the initial finding of this study. Although there is essentially no difference in the horizontal strain between the top and bottom of the embankment, tension cracks only appear at top. According to the conventional Rankine theory, this is easily explained by the fact that, in situations when the vertical load is modest, tensile failure occurs before shear failure. It is particularly significant to be able to describe the onset of stress-induced cracks using simple classical theory since it indicates how easily it may be used in practice.

The liquefaction-induced river-levee failure caused by the 2011 Tohoku earthquake was investigated by Tsukamoto et al. (2022) at three different areas. In the field experiments, penetration tests were performed. An empirical approach was developed to assess *CRR* of soils incorporating effect of fines. It was discovered that the main causes of failures were the presence of shallower water table, the vulnerability to soil liquefaction of the loose granular soil below the river levee, and presence of less permeable clay layer below liquefiable soil.

Ha et al. (2023) performed 1-*g* shake table tests on railway embankment model by varying embankment height and non-liquefiable layer thickness below the embankment under seismic loading. The findings demonstrate that both parameter control liquefaction and lateral flow of the foundation soil. Based on a number of findings, it has been proposed that the foundation ground should be strengthened up to 1.5 times the embankment height, or more than 6 m, in order to provide safety against settlement resulting from liquefaction.

Kim et al. (2023) developed a straightforward spring type shaking table equipment to examine the seismic response of a geotextile tube-reinforced embankment installed on liquefiable soil. The

variations in the response acceleration and shear stress-strain relationship were examined, as well as the impact of soil improvement and reinforcement. The findings indicated that seepage-induced liquefaction was the prime cause of the embankment damage. Study demonstrated the necessity of analyzing the liquefaction potential of soils also next to embankments. It was linked with excessive surface accelerations recorded in the embankment soil as a result of lateral spreading.

Saade et al. (2023) recently conducted centrifuge model testing of homogeneous embankment on liquefiable soil. Responses on embankment model are described in terms of EPP, acceleration response, settlement, and the embankment model deformation pattern. There was only a small amount of EPP measured for the places under the embankment with high confining pressure where liquefaction did not occur. After two cycles, there was a considerable increase in EPP for the location where the soil liquefied at a depth of less than 6 m below the surface of the ground, along with a noticeable decrease in vertical effective stress. Due to soil liquefaction, the soil below the embankment became soft, allowing the embankment to move like a rigid block.

Based on a shaking table test, Yoo and Kwon (2023) conducted a study to simulate the liquefaction phenomena, paying particular attention to the soil behaviour mechanism as a result of the reliquefication effect. The behaviour of liquefaction and re-liquefaction in the area where an embankment was built on the coastal land was studied. The embankment model was built above the model ground. The first excitations did not cause liquefaction when the higher ground layer was made up of a non-liquefiable layer; instead, the third excitation caused liquefaction. It was determined that even if the major earthquake did not induce liquefaction, liquefaction might still happen as a result of aftershocks brought on by a rise in groundwater owing to a sequence of earthquakes. However, unanticipated liquefaction damage could happen if there are several earthquakes in a row.

2.5 DIFFERENT MITIGATION MEASURES

A centrifuge testing program was carried out by Adalier et al. (1998) to evaluate the effectiveness of retrofit earthquake mitigation measures for liquefiable foundations under existing embankments. Under conditions of dynamic base excitation, the behaviour of a cohesive highway embankment supported on a loose saturated sand layer was examined. This embankment foundation system was examined in a set of five distinct model tests, first without, then with the four liquefaction countermeasure methods of densification, cement deep-soil mixing, gravel berms, and sheet-pile enclosure. Analysis and comparison have been done on how each countermeasure affects both foundation EPP and embankment deformations. It is found that the countermeasures put in place

only effectively minimize embankment vertical deformations by a maximum of roughly 50%. However, in other circumstances, cracking and lateral spreading of the embankment were essentially eliminated. Moderate embankment cracking occurred by the reduction of lateral spreading due to densification. Embedment of solidified zones into foundation liquefiable zone resulted in a highly satisfactory result. By providing direct lateral support or confinement to the embankment body, the berm minimized lateral deformations. The sheet pile enclosure prevented the liquefied foundation from expanding laterally. Additionally, liquefaction inside the enclosed foundation was observed to diminish dynamic shear excitation within the embankment body and to produce a base isolation mechanism.

Dynamic centrifuge tests were performed by Okamura and Matsuo (2002) to assess the dynamic performance of embankments with and without countermeasures in order to provide a foundation for a traditional approach to assess crest settlement. Three different forms of countermeasures implemented in Japan, the deep mixing method for solidification, the sand compaction piles for densification, and the sheet pile enclosure have been tested. It has been observed that the EPP under the toes of embankment produces higher values with countermeasures than the model without countermeasures. It was seen that countermeasures control the lateral displacement of the foundation soil and shear deformation of the embankment. The inevitable crest settlement was caused by a higher EPP beneath the embankment as a result of the remedial actions, which increased the contractive volume change of sand under the embankment. The volumetric strain of the liquefied sand beneath the embankment and displacement predictions of the remediation zone have shown to be significant variables in assessing crest settlements.

Adalier and Sharp (2004) evaluated the seismic behaviour of a zoned embankment dam with saturated sandy soil foundation under moderate earthquake conditions by conducting four precisely instrumented geotechnical centrifuge model tests. Investigations were conducted to determine the advantages of densification technique. According to test results, there may be an ideal depth for treating for densification, below which the reduction in earthquake-induced deformations is moderate. Small, isolated regions of loose material within a densified volume of soil might not affect the effectiveness of treatment in general and are not always associated with detrimental displacements.

Okamura and Tamura (2004) proposed a viable prediction method for liquefaction-related settlement for embankment treated with the deep mixing approach. An empirical relationship between crest settlement and displacement of the remediated zone is developed based on a number of centrifuge

tests of embankments. Based on the test results a calculation methodology for the displacement of the mitigated zone was developed. According to the method, the subgrade reaction forces at the base of the repaired zone are assessed using a macroscopic failure envelope and a plastic displacement potential in the general load space. This technique may be helpful for designing countermeasures based on a predetermined limit settlement.

Okamura et al. (2006) conducted a program of centrifuge tests to evaluate the effects of embankment above liquefiable ground on the pressure on the rigid vertical walls. Earth pressure was measured using built-in earth pressure cells. Regardless of the amplitude and frequency of the input motion, the dynamic increment of the earth pressure of liquefied sand is proportional to the acceleration of the rigid wall and increases with increasing average embankment load. The residual component of the earth pressure, on the other hand, is discovered to be accurately predicted using FEM under the assumption that the liquefied soil acts as an incompressible elastic body. For the sake of practical application, a useful formula for earth pressures is established. As a corrective step against liquefaction-caused embankment failure, further centrifuge tests were conducted on models with densification zones beneath embankment toes. It was discovered that as long as the liquefied soil behaves as a heavy fluid and the countermeasure fails to soften noticeably, the presented equations hold true regardless of the movement of walls.

Stamatopoulos et al. (2013) conducted a thorough field preloading investigation using a 9 m high embankment on a liquefaction-prone site. Geophysical studies, cone penetration tests, and SPT were carried out both before and after preloading. During preloading, a portion of the embankment collapsed. Methods for predicting stresses and displacements, failure risk during preload embankment construction, and improvements in shear wave velocity and cyclic liquefaction strength brought on by the preloading are provided and demonstrated.

To explore the seismic response of embankment slopes with various reinforcing techniques, Lin et al. (2015) performed shaking table tests on three embankment slope models (unreinforced, 2-layer reinforcement, and 4-layer reinforcement). The seismic response of embankment slopes with different types of reinforcement was compared. The findings indicate that the reinforced embankment slope has a higher natural frequency than the unreinforced embankment slope. It is less responsive to seismic excitation.

A study was conducted by Vijayasri et al. (2016) to evaluate the cyclic behaviour and dynamic characteristics of Renusagar pond ash samples. With and without geotextiles, reconstituted pond ash samples were tested in strain-controlled cyclic triaxial experiments at various confining pressures,

loading frequencies, and cyclic shear-strain amplitudes. The results reveal that the geotextile-reinforced pond ash samples had improved friction angle, drainage characteristics, and liquefaction resistance. The pond ash reinforced with geotextiles can be a useful material for embankments.

In a study by Boulanger et al. (2018), soil-cement walls were used to treat a 9 m thick saturated loose sand layer beneath a 28m high embankment. A 30 m long section near the toe of the embankment had soil-cement walls built through the loose sand layer. It was topped with a 7.5m tall berm. With peak horizontal base accelerations of 0.05 g, 0.26 g, and 0.54 g for the first, second, and third occurrences, respectively, the model was shaken by a scaled earthquake motion. Employing methods used in engineering practice, the outcomes of the centrifuge model test and 2-D nonlinear dynamic simulations are compared for the two stronger shaking episodes. The consequences of changing the shear strength of soil cement, the processes for simulating the soil-cement tensile yielding, the cyclic strength of the loose sand layer, and the dynamic loading history were all demonstrated using parametric studies.

Wang et al. (2018) presented a study to assess the efficiency of laponite for liquefaction mitigation using centrifuge testing. The laponite-treated model was run with a centrifugal acceleration of 45g using a constructed reservoir embankment foundation as the prototype. In contrast to the untreated model, the laponite-treated model demonstrated lesser formation of EPP and decreased deformations. The study presents experimental evidence that extends beyond the elemental scale to demonstrate the positive impacts of laponite as anti-liquefaction measure.

Four centrifuge experiments were carried out by Tizando et al. (2020) to design, carry out, and evaluate the efficacy of dense granular column (DGC) under controlled testing conditions. It was determined that the main factor limiting the seismic deformations of the embankment was densification in conjunction with shear reinforcement. Area ratio and the shear modulus ratio of DGC and surrounding soil are crucial factors in determining the stress distribution between two materials. They also govern the degree of softening and strain accumulation in different layers. The experimental findings highlight the significance of considering factors such as soil stiffness and density before and after DGC installation, confining pressure distributions, kinematic constraints, and activity of various mitigation mechanisms when assessing the effectivenes of DGCs as mitigation measure.

In order to investigate the application of sheet pile as mitigation measure under varying sequential ground vibrations, Saha et al. (2020) conducted a series of centrifuge experiments. Sheet piles efficiently reduced the lateral spreading of both thin and thick liquefiable foundations. The

experimental results also demonstrated that the effectiveness of the sheet pile is strongly impacted by the liquefaction-induced softening of the dense bearing stratum immediately underneath the loose foundation.

Sand compaction piles (SCP) were taken into consideration by Li et al. (2021) as a preventive measure against liquefaction to densify loose strata by constructing dense sand piles. A series of dynamic centrifuge tests are conducted to examine the effect on the liquefaction-induced embankment crest settlement. The existence of the improvement zone established in the foundation ground helped to reduce the lateral displacement below the embankment toes and crest settlement.

Pourakbar et al. (2022) performed a series of centrifuge experiments on soil-cement (SC) column treated ground to examine the combined effects of surcharge loading and liquefaction-induced lateral spreading. It was aimed to determine the various internal failure modes of a group of SC columns. The findings were also used to look into how SC columns capacity prevent settlements or deformations with increasing flexural strength. It was discovered that the main mechanism of failure both during and after the cracking of SC columns was shear and tilting failure. The test findings demonstrated that increasing the SC columns flexural capacity may reduce the risk of earthquake-induced liquefaction and related damage. Reinforced soil-cement (RSC) columns perform better than conventional SC columns.

2.6 NUMERICAL STUDY ON EMBANKMENT-LIQUEFIABLE SOIL SYSTEM

Significant development in the field of numerical modeling can be seen in past few decades. Numerical modeling under the framework of finite element method (FEM), finite difference method (FDM), discrete element method (DEM) gained popularity in simulating complex nonlinear dynamics problem. For simulating liquefaction related large deformation problem, selection of constitutive model is very much important aspect. A significant development in the area of soil constitutive models for sands can be observed in the last few decades (Yang et al. 2003; Taiebat and Dafalias 2008; Andrianopoulos et al. 2010; Boulanger and Ziotopoulou 2013; Ye et al., 2012; Galavi, 2021). It is worth to be mentioned that constitutive models such as UBC3D-PLM (Petalas and Galavi, 2013), CycLiq (Wang et al., 2014; Wang et al., 2021), PM4Sand (Boulanger and Ziotopoulou, 2015), Ta-Ger (Tasiopoulou and Gerolymos, 2016), and Sanisand-Msf (Yang et al., 2022) have shown significant development in the field of simulation of liquefaction and post-liquefaction behaviour.

A risk analysis was conducted by Groot et al. (1995) to produce a workable method for calculating the probability of a flow slide. The liquefaction potential of the sand, which depends on its density

and stress state, as well as the slope geometry, define the danger of a flow slide. The method that is being described allows for the analysis of the impacts of sand characteristics and geometry together. By identifying the parameters that contribute the most to the uncertainty and, thus, require further study to lower the estimated flow slide probability, analysis also helps to optimize design processes. An elastic-plastic stress-strain model for sand was provided by Puebla et al. (1997). The model parameters were selected based on triaxial and simple shear experiments. The effectiveness of model was further confirmed by a centrifuge test and prediction of the CANLEX field event response. Analysis reveals that a static liquefaction failure would have occurred if the embankment had been 16 m high rather than 8 m.

Finn (1998) used substantial displacement to mimic the flood protection dykes failing in Hokkaido, Japan, after the Kushiro-oki earthquake in 1993. Then, by combining displacements to geometric features of the dykes, such as height, slopes, and liquefiable layer thickness, the technique was utilised to predict displacements in dykes with potential for liquefaction. Data on dyke displacement from the 1994 Nansei-oki earthquake was used to confirm the predictions. The effects of liquefaction mostly depend on the residual strength of liquefied soils. However, the residual strength may depend on accumulated strains.

Through a numerical analysis considering two different approaches - one dealing with fully coupled plasticity model and the other a model based on a collapse-surface approach - Byrne et al. (2000) conducted stress-strain modelling of a centrifuge test performed on a model of a sand embankment resting on liquefiable soil. While the impacts of drainage were considered and the direction of loading was taken into consideration, it was discovered that the results from both approaches were in fair agreement with the measurements.

Elgamal et al. (2002) presented set of computational simulations for a number of centrifuge tests on embankments on a liquefiable foundation soil. Three different embankment models (benchmark model without any measure, densification below embankment toe, sheet-pile enclosure below embankment) are used in the centrifuge test. In order to reproduce the aforementioned centrifuge tests statistically, a two phase (solid-fluid) fully coupled FEM formulation includes a newly calibrated soil stress-strain constitutive model. The importance of post-liquefaction dilative behaviour of foundation soil is highlighted through comparison of the numerical results with the experimental findings.

Based on examples from the 1993 Hokkaido-Nansei-oki and 1995 Hyogoken-Nambu earthquakes in Japan, Ozutsumi et al. (2002) conducted a series of effective stress analyses on the

dynamic performance of river dykes. Seven case histories that were chosen for the studies feature crest settlements in dykes (3 to 6 m high) that range from none to 2.7 m and show signs of liquefaction at the foundation soil. The parameters of the effective stress model, which is based on a multiple shear mechanism, were derived after site inspection and laboratory tests. Depending on the geotechnical characteristics of the foundation soils beneath the dykes, the effective stress model has a respectable ability to reproduce the varied degrees of settlements. The benefits of mixing clay layers with liquefiable soil layers for decreasing liquefaction-induced dyke settling are highlighted by analyses.

Adalier and Adigyun (2003) carried out fully coupled numerical analysis using effective stress based FEM code DIANA-SWANDYNE II for clayey embankment resting on liquefiable soil. Results of numerical analyses are compared with data obtained from the centrifuge tests. The dynamic response (including acceleration, EPP and deformations) compared favourably with their numerically predicted counterparts. The impact of each countermeasure with respect to the benchmark model is also explored. However certain discrepancy could be observed between in the computed and observed EPP and vertical deformations beneath the embankment because of the inability of the code to deal with large strain problem.

A numerical technique for liquefaction analysis of saturated soils involving significant deformation was presented by Di and Sato (2003). The revised Lagrangian approach and Biot's two-phase mixture theory serves as the foundation for the formulation. A mass conservation equation and an equilibrium equation make up governing equations. The FE-FD coupled approach discretizes governing equations in space and time domain. The behaviour of saturated soils under dynamic stress is described by a cyclic elasto-plastic constitutive model. With significant deformation, the coefficient of porosity is thought to change. It is presumable that the void ratio acts as a function of the coefficient of permeability. According to the large deformation analysis, liquefaction occurs deeper than it does in the soil surrounding an embankment that has been subjected to substantial seismic motion.

A series of fully coupled FEM assessments of the behaviour of the renowned lower San Fernando Dam to the earthquake of 1971 were given by Ming and Li (2003). To represent soil behaviour across the complete spectrum of loading circumstances observed, a critical state model was used incorporating the concept of state-dependent dilatancy. The findings demonstrate unequivocally that a flow slide occurred on the upstream side and suggest that, had the downstream berm not been built

prior to the occurrence, a downstream flow slide might take place. The analyses also demonstrate that an upstream berm might be added to effectively stop the upstream flow slide.

In order to quantify the long-term deformations caused by the 2001 Bhuj earthquake within six earth dams, Singh et al. (2005) provided a simple method of analysis. The method is based on the Hynes-Griffin and Franklin (1984) upper bound relationship between the ratio a_{yield}/a_{max} and permanent deformation. Only one of the three dams, which were all located within 150 lm of the earthquake's epicenter, actually collapsed as a result of the event. According to analysis, this straightforward method may be used to quickly evaluate the seismic safety of earth dams that are similar to those that were built without taking earthquake loading into account.

A new constitutive model was applied by López-Querol and Blázquez (2006) to predict the mechanism of failure of a road embankment on liquefiable ground. In order to reflect the dilative soil behaviour, a new flow rule incorporating a soil degradation state parameter has been included into the constitutive law. The authors linked 2-D FEM code, which uses the constitutive law, enables the detection of the failure processes of road embankments under seismic loadings. The mechanical collapse of the soil was not resolved by the corrective measure of densifying the lower strata of the embankment. However, the installation of two drainage berms on either side of the embankment prevents the mechanism of soil collapse while having no impact on the rise in EPP. Failure caused by either of the two causes was avoided by installing a drainage layer immediately beneath the pavement.

Using an effective stress-based, fully coupled FEM, Huang et al. (2008) assessed the seismic behaviour of an earth embankment built on liquefiable soil. Based on a cyclic elastoplastic constitutive model that was created within the framework of the Armstrong-Frederick type non-linear kinematic hardening concept, a material constitutive model for sandy soil is taken into consideration. The numerical model has been found to reasonably reflect the basic liquefaction elements of the embankment foundation system.

A case study of the seismic response of an earth embankment founded on liquefiable soils in the Kansai area of western Japan was presented by Huang et al. (2009). The study considered a calibrated cyclic elasto-plastic constitutive model for modeling liquefiable sand and Biot dynamic coupled theory. Under the plane strain condition, analyses were conducted using the dynamic effective stress based FEM program (LIQCA). The findings demonstrate that the earthquake shaking causes the foundation soil to fully liquefy and reach high r_u close to 1.0. At the end of the earthquake,

the severe liquefaction results in 60 cm of the crest settlement and 1.0 m of lateral spreading at the embankment toe.

Using a unified state-dependent dilatancy sand model and a fully coupled FEM technique, Ming et al. (2011) evaluated seismic response of the upper San Fernando dam. Study examined the influence of the unit weight of soil and earthquake intensity on the flow deformation. According to analysis, once flow liquefaction is caused by a sufficiently powerful earthquake, the difference between the shear stress necessary for equilibrium and the shear strength of the liquefied soil dominantly controls the earthquake-induced flow deformation.

Oka et al. (2012) carried out dynamic liquefaction analysis for river embankments on a foundation ground with various soil profiles and ground water tables. Soil profiles include liquefiable sandy layer and a clayey soil. A cyclic elasto-plastic model was incorporated for sandy soil which is capable of indicating both the strain-induced degradation. Clayey soils were modeled by an elasto-visco-plastic model. Analyses highlights the effects of the soil profiles and the time duration of the earthquake motion on the deformation behavior of the river embankments. Results are found to be consistent with the deformation and the failure of the embankments due to the 2011 off the Pacific Coast of Tohoku Earthquake.

Athanasopoulos-Zekkos and Seed (2013) developed a simplified method for the liquefaction triggering evaluation of earthen levees. Study is based on systematic equivalent linear 2D dynamic response analyses on levee sites representative of three distinct California Central Valley regions. The site and topographic effects on the peak ground acceleration, as well as the shear stresses and cyclic stress ratios for a series of profiles throughout the levee sites, are discussed in further depth along with two other aspects of the dynamic response and performance of earthen levees. A simplified methodology has been suggested for determining the factor of safety against the triggering of soil liquefaction.

To study flow in liquefied soils, Huang et al. (2013) developed a soil-water-coupled smoothed particle hydrodynamics (SPH) modelling approach. While permeability, porosity, and interaction forces can be coupled to describe water-saturated porous media, water and soil were modelled as separate layers. An embankment failure in north Sweden was taken into consideration as an application of the method. The coupled SPH method performed adequately in simulating the embankment failure with the site investigation. SPH approach can accurately predict the horizontal displacement and velocity of soils following liquefaction. Response resemble the flow processes of liquefied soils.

A numerical method for a 2-D seismic study of an embankment dam which considers the spatial variability of soil parameters was presented by Lizarraga and Lai (2014). The method incorporates random field theory and sophisticated numerical modelling into a probabilistic framework. Anisotropic random fields with varying auto correlation distances in the vertical and horizontal axes are used to model geotechnical characteristics. Fully nonlinear time-history studies are run for various ground motions using this stochastic representation of the soil domain. The fragility functions of the embankment-liquefiable foundation soil system are derived using the analysis results, taking into consideration the spatial variability of the foundation soil properties.

Using 3-D FEM in the PLAXIS 3D program, Bhatnagar et al. (2016) provided a numerical investigation on an embankment resting on liquefiable soil loose liquefiable deposit. The El Centro earthquake acceleration base-input excitation has been applied to the model, which is keeping track of displacements, liquefaction potential, and EPP. Utilising an effective stress-based UBC3D-PLM constitutive model, liquefiable soil is modelled. Densification of the sand layer and sheet pile enclosure beneath the embankment toes are two separate liquefaction countermeasure strategies that are being studied. It has been noted that the sheet pile solution is successful in reducing displacements but has little impact on EPP. The soil-column mitigation was the most successful in preventing the growth of EPPs and displacement beneath the embankment.

Considering saturated and natural water table conditions, Mohanty and Patra (2016 a,b) studied seismic response study of the Panipat pond ash embankment. Using the OpenSees platform, nonlinear FE analysis has been performed. For both saturated and natural water table circumstances, predicted r_u found to be greater than or equal to 1.0 below upstream and downstream sites of the pond ash embankment. Near the toe and first rise slope of the pond ash embankment, the horizontal and vertical displacements were observed to be maximum. The pond ash embankment was not found to be safe against liquefaction and lateral spreading under full saturation condition.

Boulanger et al. (2018) numerically simulated the centrifuge model test of an embankment on a liquefiable foundation layer treated with soil-cement walls. Three alternative peak acceleration amplitudes were considered while shaking the model with a scaled earthquake motion. Using methods used in engineering practice, the outcomes of the centrifuge model test and 2-D nonlinear dynamic simulations were compared for the two stronger shaking incidents. Findings from the comparison justify the application of these numerical modelling techniques for investigation of embankment dams with soil-cement treatment of liquefiable soils in their foundations, including the representation of a treatment zone with area-weighted composite properties.

Nearly 1195 river embankments in the Tohoku region were damaged after the 2011 Tohoku earthquake, typically as a result of the embankment fill soil liquefaction. Utilising the three-phase coupled FEM program OMVI2DDY, which was specifically created to deal with the enormous strain behaviour of partially saturated soil, Chen and Kimoto (2018) modelled the deterioration of an embankment close to the Naruse River. A cyclic elasto-plastic constitutive model based on the nonlinear kinematical hardening rule was improved by taking into account stiffness recovery during reconsolidation in order to replicate the reconsolidation behaviour. The embankment is severely damaged and deformed primarily towards the land side. The settlement at the top of the embankment was 2.5 m. Study highlighted the capability of the numerical technique in reproducing the major aspects of the actual damaged pattern.

Rapti et al. (2018) conducted a study to demonstrate the global dynamic reaction and interaction of an earth structure-foundation system in order to quantify the process of collapse caused by the liquefaction of the foundation soil. Levee damage has been found to be closely related to both the development of liquefaction and the dissipation of EPP. Within the liquefied area, a circular collapse surface develops and continues towards the crest on both sides of the levee.

Using a simplified total-stress approach, Lee et al. (2019) performed a seismic deformation analysis of embankment dams. A FDM computer program (FLAC 2D) has been used in simulating experimental on embankment dam prototypes in dynamic centrifuges. Uncoupled modelling with a primitive constitutive model was used as a simpler approach. The laboratory stress-strain curves for the dilative soils were used to calculate quasi-steady-state strengths. There is a substantial confidence in the predicting ability of FLAC 2D from comparison of numerical and experimental results. The v_{max}/a_{max} ratio of the seismic input motions and the estimated settlements showed a strong correlation.

Lopez-Caballero et al. (2016) performed numerical simulations using FEM to evaluate the preloading approach as a way to improve it and lessen the liquefaction potential and induced settlements in a sandy soil profile. The behaviour of the soil is represented by the elastoplastic multi-mechanism model, or ECP model. Numerical findings and laboratory test results justified effectiveness of Preloading strategy for preventing liquefaction for the road embankment.

Vijayasri et al. (2016) used a fully coupled nonlinear FEM analysis with the PressureDependMultiYield material model in OpenSees to present the dynamic response analysis of a 52 m high pond ash embankment located in Renusagar, northern India. Data from cyclic triaxial experiments on samples of pond ash were used to calibrate constitutive material models of the pond

ash material. Between the embankment base and crest, there was a noticeable acceleration response amplification that ranged from 1.43 to 4.2. A significant amplification in the displacement has been noticed with values up to 17.3 cm in the horizontal direction and 45 cm in the vertical direction, respectively.

By adding the soil-water coupled finite deformation analysis program GEOASIA with the inertial term, Nonaka et al. (2017) extended a macro-element method to dynamic situations. The results of a 2D approximate model using the new macro-element method were compared with those of a 3D exact model, where vertical drains were precisely represented by finely dividing the FEM mesh in the case of a sand ground improved by the EPP dissipation method under the embankment. This comparison served to verify the new macro-element method in a dynamic problem. It was discovered that the novel microelement method could quantitatively analyze the impact of drain spacing on a liquefaction countermeasure. The use of the macro-element approach increases computation efficiency since mesh dividing greatly reduces computational efforts.

In order to analyze the multi-hazard fragility of river earthen dykes in earthquake and flood-prone locations due to liquefaction, Tyagunov et al. (2018) introduced a methodology. Between the gauges at Andernach and Düsseldorf, the approach has been applied to the region along the Rhine River reach and associated floodplains. Liquefaction Potential is used to analyze the fragility of earthen dykes. In a Monte Carlo simulation (MCS), uncertainties in the geometrical and geotechnical dyke parameters were considered. Due to the high moisture content in the dyke core, quantitative fragility analysis demonstrates that a rise in floodwater level lowers the PGA threshold that causes liquefaction.

Using the Prevost multi-yield surface plasticity model in the OpenSees platform, Tabatabaei et al. (2019) carried out a number of 2-D plane strain fully coupled FE simulations. Parametric study examined the impacts of the embankment height, the permeability of the foundation soil, and the input motion PGA. Crest settlement was significantly influenced by embankment height. Analysis reveals that the 2.5 m embankment failed due to flexural beam failure, and the 5 m and 10 m embankments failed due to slumping.

On stochastic and uniform alluvial layers subjected to a variety of input motions, Paull et al. (2020) presented simulations for embankments ranging in height from 5 to 45 m. Sensitivity scenarios included the effects of different parameters defining the alluvium and embankments. As the magnitude of alluvium horizontal variation relative to embankment base width rises, the variety in deformation patterns derived with stochastic models also increases. In the nonlinear dynamic

analysis of embankments, recommendations are made regarding the variables to consider while choosing representative features for spatially varying alluvial foundations and associated variability in the response.

For the nonlinear large deformation and failure study of river embankments subjected to strong earthquakes, Shahbodagh et al. (2020) suggested a numerical model based on mixture theory. In the large deformation regime with the revised Lagrangian adoption, the governing equations are discretized using FEM. Clayey soil is considered to be modelled by a cyclic elasto-viscoplastic model. Sand is modelled by a cyclic elasto-plastic model. The failure types and damage patterns of river embankments seen during the 2011 Tohoku earthquake have been considered for simulations. The ground motion amplitude and duration can significantly change the river embankments failure mode.

The effectiveness of woven geotextile in enhancing the seismic performance of a pond ash embankment situated at Renusagar, in seismic zone III of India, was examined by Vijayasri et al. (2020). Woven geotextiles, employed as reinforcing materials, are positioned at the first and third strata of the pond ash embankment. The geotextile-reinforced pond ash embankment has been modelled using FEM. The solid phase of the embankment material is generated using the PressureDependMultiYield model in OpenSees, while the fluid phase is modelled using Fluid Solid Porous Material. Using data collected from seismic zones III and IV, a general expression was developed for the shear modulus and damping ratio of pond ashes reinforced with and without woven geotextiles. The three layers of geotextile reduced lateral displacement up to 17% and EPP up to 45%. The study focused on the advantages of using woven geotextile as a reinforcing material in construction fills, earth dams, and highway embankments.

A numerical model was created by Tabatabaei et al. (2020) to examine the efficacy of sand columns in enhancing the stability and strength of embankments. The Prevost multiyield constitutive model was used to model the saturated foundation soil in OpenSees using FEM. In parametric analyses, the behaviour of embankments during earthquakes was examined for a range of heights, sand column area replacement ratios (A_r), soil permeability, and earthquake peak ground accelerations (PGA). When placed on a group of sand columns, it has been found that short height embankments performed better in terms of embankment stability and settlement. With a constant area replacement ratio, the soil permeability is the primary factor involved in the optimum sand column diameter.

Through the use of a multi-fidelity coding technique, Lopez-Caballero (2021) performed probabilistic seismic analysis for liquefiable embankments. Numerous non-linear dynamic FEM

simulations were carried out with this objective in mind. The output of the pricey FE model is represented for a large number of earthquake records by a surrogate model based on a multi-fidelity method. This method combines computational low-fidelity data with sparse high-fidelity data to create the training database. The accuracy of the forecast made by the suggested surrogate model is compared to those from direct numerical FE analysis, according to a comparison with the FE reference results.

Cascone et al. (2021) investigated the combined effect of the vertical component of the input motion and weakening effect of EPP build-up on a zoned earth dam. The hysteretic model Sigmoidal 3 from FLAC library was used to characterize the non-linear and dissipative soil behaviour. Advanced plane-strain non-linear dynamic assessments were conducted on two effects using a FD numerical model calibrated on a precise geotechnical characterization. A set of horizontal and vertical input motions that have been carefully chosen to consider potential frequency coupling with the dam are used to test for the presence of ultimate limit states in the dam embankment.

A suitable in-situ countermeasure was suggested by Gu et al. (2021, 2022). The seismic performance of the grouting liquefaction mitigation method was numerically assessed. Elasto-plastic constitutive model Cyclic Mobility (CM) was taken into consideration in order to capture the cyclic shearing and liquefaction features of cohesive clay and cohesionless soil in embankments. This model also considers soil structure interaction, stress-induced anisotropy, and over-consolidation. The dynamic behaviour of embankments in fully saturated sandy deposits, during an earthquake, and long-term post-consolidation are investigated numerically using the coupled water-soil phases with FEM and FDM. A comparison analysis shows that the countermeasure in place is successful in minimizing co- and post-seismic liquefaction-induced deformation. However, when grouting the saturated sandy layer was implemented together with suitable preventive measures to preserve the slope, there is limited failure on the embankment slope as opposed to deep-seated failure in the embankment-soil system.

To simulate co-seismic slope stability and liquefaction-induced embankment failure under earthquake loading, Feng et al. (2021) introduced the Material Point Method (MPM). The influences of slope geometry, soil characteristics, and excitation frequencies are taken into consideration when analyzing topographic amplification and various slope failure types. In order to explore the liquefaction mechanism and accompanying dam failure utilising two case histories (Success dam failure located at Porterville, California, and Lower San Fernando dam failure), a completely nonlinear bounding surface soil model is constructed in the two-phase soil-water coupled MPM

framework. The MPM has a lot of potential for assessing risk and consequences related to seismic slope failure and soil liquefaction quantitatively.

Khalil and Lopez-Caballero (2021) used probabilistic seismic hazard analysis (PSHA) to estimate the embankment damage that would sustain from liquefaction as a result of successive earthquakes over a specified working life. Based on effective stress formulations, the Ecole Centrale Paris (ECP) elastoplastic multi-mechanism model (also known as Hujeux model), was selected for this study. The results show that, upon successive loading, the cumulative damage is either gradual with or without significant damages or abrupt with significant damages. This study demonstrated the significance of loading history since it has an impact on the embankment overall performance.

Wu et al. (2021) investigated the impact of ground vibrations that are analogous to near-fault pulses on the seismic performance of earth dams that are vulnerable to liquefaction-induced damage. In order to simulate the nonlinear behaviour of sandy and clayey soil, a general earth dam built on a layer of liquefiable soil is modelled in OpenSees using FEM that considers the Pressure Depend Multi Yield02 (PDMY02) and the Pressure Independ Multi Yield (PIMY) models. From the NGA-West2 database, two suites of near-fault ground motions, one pulse-like and the other ordinary, are chosen. Comparative findings show that the pulse-containing ground motions are more likely to cause liquefaction in the loose-sand layer than the typical near-fault motions. An earth dam in a location where liquefaction risk exists can experience increased post-liquefaction deformation and damage when subjected to pulse-like ground vibrations.

Dinesh et al. (2022) used the PM4Sand constitutive model in the FLAC 2D to carry out a non-linear seismic deformation analysis of an earthen embankment built on liquefiable soil. The cyclic behaviour of Nevada 120 sand provided the basis for calibrating the PM4Sand model. For the simulation of an untreated sand deposit supporting an embankment, the temporal variations of sand permeability were considered. To account for the shear-induced dilatation of the foundation soil beneath the embankment, various classes of simulations were taken into consideration. Study simulated three distinct liquefaction mitigation strategies (dense sand columns under the foundation soil, gravel berms along the embankment slopes, and vertical sheet piles below the toes) and compared with actual data.

Nonlinear deformation assessments of an embankment on a spatially variable, liquefiable foundation soil reinforced with a spatially variable soil-cement (SC) wall were performed by Zaregarizi and Khosravi (2022). The objective of this research was to compare the benefits of deterministic analysis with homogeneous parameters for the soil and SC wall to stochastic modelling techniques, such as

spatially linked random fields. The findings showed that in order to predict the median of crest and berm displacement in a spatially variable SC wall-supported embankment, a uniform model based on the representative percentile of unconfined compressive strength (q_{ucs}) in the range of 35^{th}–50^{th} percentile was required.

Saade et al. (2023) adopted PM4Sand constitutive model under the framework of FEM to simulate liquefaction induced failure of an embankment constructed on a liquefiable sand. Performance of the numerical model was validated against the centrifuge test results. The verified numerical model is refined to include two improved boundaries. The potential boundary effects in centrifuge and numerical models have been addressed.

To increase the accuracy of the risk assessment of transport infrastructure systems, Zhou et al. (2023) proposed seismic fragility assessment or embankments on liquefiable soils. FLAC 2D and the PM4sand model were used to perform nonlinear dynamic assessments of embankments on liquefiable soils. Ten input motions are chosen and scaled to assess the embankment reaction under escalating shaking intensity levels for the construction of seismic fragility curves. To determine the relative contribution of the investigated liquefaction mitigation measures (soil densification, gravel berm, and sheet-pile enclosure), the embankment responses were compared with the outcomes of the benchmark model.

2.7 CRITICAL APPRAISAL

Based on the above review of literature, following observations are made.

1. To understand the phenomenon of liquefaction, mainly two types of approaches have been studied in the past: empirical approach based on in-situ and experimental test data of soil samples and modeling of field conditions where liquefaction is known to have occurred in the past.
2. In the earlier studies, undrained cyclic laboratory tests had been mainly used to access the liquefaction potential of a soil mass. However, due to difficulties in collecting undisturbed samples of loose sandy soils, most of the studies preferred to use in situ tests such as SPT, CPT, BPT and shear wave velocity results.
3. Empirical field-based methods for determining liquefaction potential have two critical constituents: i) The analytical framework to systematize past experiences, and ii) An appropriate in-situ index which could be able to represent the soil liquefaction characteristics. The original simplified procedure proposed by Seed and Idriss (1971) for estimating earthquake-induced cyclic shear stresses is still to be necessary component of the empirical

and semi-empirical analysis framework. The various parameters of this framework are redefined to include improvements in the in-situ index tests (SPT, CPT, BPT, V_s) and the liquefaction/no-liquefaction cases are compiled accordingly.

4. In a semi-empirical approach, experimental results and the theoretical approach combined together to provide the more confidence in the response analysis of liquefaction phenomenon. It is used to interpolate or extrapolate to areas with inadequate field data to restrain a solely empirical solution.
5. Advanced constitutive models are found to be effective in predicting the liquefaction-induced responses for complex structures which can not be assessed using empirical relations. Adopting such constitutive models for nonlinear dynamic analysis requires proper calibration of material model parameters.
6. Past earthquakes showed that earth structures like embankments are very much vulnerable to earthquake when subjected to liquefaction-induced lateral spreading and settlement. Subsidence of such earth structures can cause disruption of public facilities and transportation facilities. It is important to provide proper mitigation measures for embankments resting on liquefiable deposit.
7. Fragility assessment has been found to be a reliable method for performance-based design of earthen embankments in the recent times. For site specific design of such structures fragility study can provide valuable input for design.
8. A number of terminologies, methods and procedures to study the response of liquefaction phenomena have been proposed. But a reliable approach has to be selected based on available information on domain characteristics and soil properties.

2.8 GAPS AND OBJECTIVE

After studying the key literatures on embankment structures resting on liquefiable soil following major research gaps are identified:

1. Most of the past experimental studies have considered cyclic loading in order to evaluate the dynamic response on embankment. However, based on this earth structures can not be designed in any liquefaction-susceptible zone. Hence, dynamic analysis considering real earthquake ground motions can provide better assessment of embankment response for any earthquake zone.
2. Most of the advancement in numerical analyses are of very recent times. Certainly, literature has gap for calibration of material model parameters for an advanced constitutive model.

3. Embankment response under a wide range of earthquake motions has not been addressed earlier. In order to understand the key factors influential for embankment structures resting on liquefiable soil proper dynamic analyses is required.
4. Effect of main-shock and after-shock in a sequential manner has not been addressed previously. Recent earthquakes in Turkey have shown detrimental effects of after-shock (even of smaller amplitudes) for different structures. Addressing such aspect is very much important for areas bearing history of sequential earthquakes.
5. Most of the numerical studies considered two-dimensional plane strain modeling. A proper three-dimensional analysis is required for better understanding of such complex phenomena.
6. Most of the literature highlighted conventional mitigation measures for embankments on liquefiable soil. Moreover, a comparative study of different mitigation techniques is most requisite in order to understand the efficacy of different mitigation measures under different conditions.
7. Very few literatures have addressed the fragility assessment of embankment structures considering the effect of embankment geometry and foundation soil properties. In order to understand the damage level with increasing earthquake loading amplitude, fragility functions are very much useful.

Based on these available gaps, research objectives of the present study have been identified as given in previous Chapter. Study has been devoted to simulate numerical model of embankment on liquefiable soil in 2D and 3D domain. Various cyclic and seismic ground motions have been applied as base input motion. A detailed finite element formulation with appropriate constitutive model has been outlined in the next Chapter for 2D and 3D domain.

CHAPTER 3
METHODOLOGY

3.1 GENERAL

Studies using physical models have been used to analyze the adverse effects of subsurface liquefaction on embankments. It is necessary to understand the underlying triggering mechanism of liquefaction and ensuing deformations for the creation of the liquefaction remedial design procedure. Numerous research using physical and numerical modeling, including those from large-scale programs like VELACS (1993) and LEAP (2017), have been attempted towards this. The predisposing and triggering elements for liquefaction must be determined in order to assess the potential liquefaction risk of a place. The properties of the soil deposit, such as the size and shape of the particles, the gradation, and the characteristics of plasticity, are the predisposing variables. The triggering variables rely on the magnitude, duration, and peak ground acceleration of the earthquake. Semi-empirical techniques or nonlinear dynamic analyses are available to determine if liquefaction can happen in a particular site subjected to a certain earthquake.

When simulating liquefaction through numerical analysis, an appropriate choice of the soil constitutive model becomes crucial. Significant improvements have been made in the field of soil constitutive models, especially for those that are applicable to the liquefaction study of loose sands (Beaty and Byrne 1998; Yang et al. 2003; Dafalias and Manzari 2004; Taiebat and Dafalias 2008; Andrianopoulos et al. 2010; Beaty and Byrne 2011; Boulanger and Ziotopoulou 2013; Tasiopoulou and Gerolymos 2016). Finite element modeling is already a well-established methodology for solving highly nonlinear behaviour of geological materials under the condition of extreme dynamic loading environment. Finite element modeling considering appropriate material constitutive behaviour along with suitable boundary condition is found to be an efficient framework for solving such complex phenomena. Apart from finite element modeling, finite difference method (FDM), discrete element method (DEM), material point method (MPM) are comparatively new methodologies currently followed by many researchers. In the present study finite element method (2D and 3D) has been adopted for modeling embankment resting above liquefiable soil underlain by a dense sand layer.

3.2 INTRODUCTION TO PLAXIS

PLAXIS is a finite element computer program, which contains different user defined constitutive models for simulating non-linear behaviour of soil. With the use of this program, it is possible to

model structures and the interactions that exist between them and the soil around them, which are essential for simulating many geotechnical issues. In the present study, both 2D and 3D modeling of embankment resting on liquefiable deposit are modeled along with different mitigation approaches. In case of 2D modeling, plane strain or axisymmetric modeling can be performed. Whereas, in 3D modeling full or half geometry of the model can be considered by considering actual model conditions. Users of the program can easily create a geometry model and finite element mesh because to its intuitive graphical user interface. The user must construct a geometry model made up of points, lines, surfaces, volumes, and other components as well as specify the material properties and boundary conditions in order to perform a finite element analysis using the PLAXIS program.

CONSTRUCTION STAGES

Modeling in PLAXIS follows a staged construction sequence. First of all, the soil stratigraphy is defined. Following this structural geometry (in the present study embankment, mitigation approaches), interface, loading, and boundary conditions are defined. Following these steps meshing and analysis steps are defined.

In the *soil mode*, the Borehole function is used to define the soil stratigraphy. Later on, soil layers can be modified depending on the layer properties and configurations. Individual soil layers are given different properties according to the layer configuration using a large set of user-defined material model in the program. In the present study the foundation soil layers are created using this procedure.

The *structures mode* allows for the definition of geometric entities, structural components, and soil boundary conditions. The embankment geometry is modeled in the structure mode. In 2D modeling embankment is modeled considering a surface above the foundation soil. While, in 3D modeling embankment volume is modeled. Alongside different mitigation measures like stone columns, densification, gravel berms, piles are modeled in this phase. Moreover, interface between the rigid inclusion in the foundation soil is also modeled in this phase. The present study mainly dealing with dynamic loading as an input to the base of the model. The dynamic loading is given as *prescribed displacement* function available in this phase. In case of 2D modeling the *prescribed displacement* is given using *line load* and in case of 3D modeling it is given using *surface load*. Material properties of different geometric entities are assigned from the material models selected based on type of materials of the geometries. After this step, meshing of finite domain is carried out which is described in the next section.

MESHING OF FINITE DOMAIN

After creating soil and structural components, meshing of finite domain is carried out. The generation of a suitable Finite Element mesh provides a crucial intermediary step between the stages of geometry definition and construction. The elements need to be small enough to guarantee calculation accuracy, especially in locations where considerable variations in stress or strain are to be anticipated during analysis. Finding the ideal balance between precision and computation time while keeping an eye on mesh quality requires careful consideration. In case of 2D plane strain modeling 15-node triangular elements are considered for higher accuracy of results. In 3D modeling 10-node tetrahedral element is considered. Typical display of elements is shown in Fig. 3.1. Pore pressures are derived from the same number of nodes used to define an element.

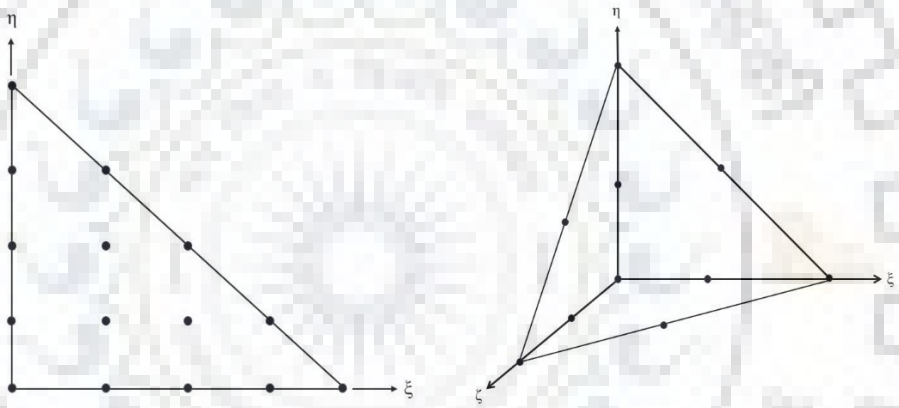

(a) (b)

Fig. 3.1 (a) 15-node triangular element; (b) 10-node tetrahedral element.

DYNAMIC ANALYSIS

Below is a basic equation for movement of a volume over time as a result of a (dynamic) load.

$$\mathbf{M}\ddot{\mathbf{u}}+\mathbf{C}\dot{\mathbf{u}}+\mathbf{K}\mathbf{u}=\mathbf{F} \tag{3.1}$$

Here, **M**, **C** and **K** are mass, damping and stiffness matrices, respectively. **F** is load vector. $(\mathbf{u}, \dot{\mathbf{u}}, \ddot{\mathbf{u}})$ are displacement, velocity, and acceleration vectors.

The mass of the components (soil, water, and any structures) is considered in the matrix **M**. The mass matrix is applied as a consistent matrix in PLAXIS. The damping of the materials is represented by the **C** matrix. In actuality, material damping is brought on by friction or by permanent deformations (plasticity or viscosity). Vibration energy can be dissipated more effectively with more viscosity or plasticity. The matrix **C** can be used to account for damping even if elasticity is

considered. Additional parameters are needed to calculate the damping matrix, which are challenging to obtain from testing. **C** is frequently expressed as a function of the stiffness and mass matrices in finite element formulations as Rayleigh damping (Zienkiewicz and Taylor 1991; Hughes 1987).

$$\mathbf{C}=\alpha_R\mathbf{M}+\beta_R\mathbf{K} \tag{3.2}$$

In light of this, only the Rayleigh coefficients α_R and β_R can be used to determine the damping matrix. For low frequency loading contribution of **M** becomes dominant. Whereas, for high frequency loading **K** becomes dominant.

TIME INTEGRATION

The formulation of the time integration is crucial for both the stability and the accuracy of calculation process in the numerical implementation of dynamics. The two most widely used approaches in time integration are explicit scheme and implicit scheme. Explicit integration has the benefit of being a relatively simple formulation. However, the downside is that the calculating method is less reliable and severely restricts the time step. Although the implicit technique is more complex, it results in a more accurate computation process and is typically more reliable (Sluys 1992).

One approach that is often utilised is Newmark's implicit time integration technique. The displacement and velocity at the moment in time $t+\Delta t$ are expressed afterwards using this method as shown below.

$$u^{t+\Delta t}=u^t+\dot{u}^t\,\Delta t+\left(\left(\frac{1}{2}-\alpha\right)\ddot{u}^t+\alpha\,\ddot{u}^{t+\Delta t}\right)\Delta t^2 \tag{3.3}$$

$$\dot{u}^{t+\Delta t}=\dot{u}^t+\left((1-\beta)\ddot{u}^t+\beta\,\ddot{u}^{t+\Delta t}\right)\Delta t \tag{3.4}$$

The time step is denoted by Δt in the equations above. The precision of time integration is controlled by the coefficients α and β. For a stable solution the condition below needs to be satisfied

$$\beta\geq\frac{1}{2},\ \alpha\geq\frac{1}{4}\left(\frac{1}{2}+\beta\right)^2 \tag{3.5}$$

BOUNDARY CONDITIONS

In a static deformation analysis, specified fixities are introduced at the extreme boundaries. In theory, the borders between dynamics calculations should be significantly farther apart than those between static calculations since otherwise, stress waves will reflect, distorting the computed results.

However, finding the boundaries at a distance necessitates a lot more components, which increases the amount of memory and computation time needed. Various techniques are employed at the boundaries to reduce reflections and prevent spurious waves. Following methods are available in PLAXIS:

1. Adaptation of material properties of boundary elements (low stiffness and high viscosity).
2. Use of viscous boundaries (dampers).
3. Use of free-field and compliant base boundaries (boundary elements).

In our present study the lateral extreme boundaries are considered to be viscous boundary and the base of the model is considered to be compliant base.

3.3 MATERIAL MODELS

A set of mathematical equations that establish a link between stress and strain define a material model. Infinite increments of stress (also known as "stress rates") are frequently described in relation to infinitesimally small increments of strain (also known as "strain rates"). The link among effective stress rates and strain rates is the foundation of every material model used in PLAXIS 3D. The definitions of stresses and strains in PLAXIS 3D are discussed in the section below.

Figure 3.2 illustrates the general system of coordinates and stress sign standard used in PLAXIS 3D. In coordinates, the stress tensor is expressed by the following matrix:

$$\sigma = \begin{bmatrix} \sigma_X & \sigma_Y & \sigma_Z & \tau_{XY} & \tau_{YZ} & \tau_{ZX} \end{bmatrix}^T \tag{3.6}$$

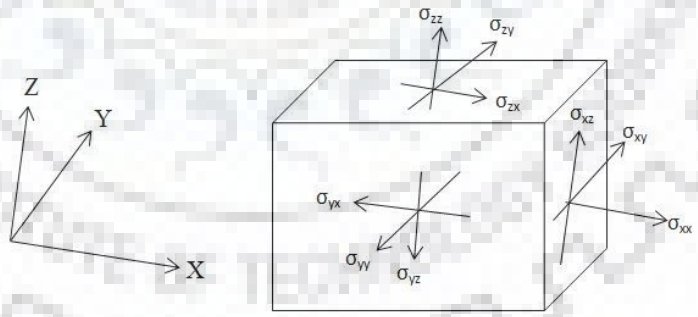

Fig. 3.2 General 3-D coordinate system and sign convention for stresses in PLAXIS 3D.

Terzaghi's Principle states that effective stresses (σ') and pore pressures are two categories of stresses in soil:

$$\sigma = \sigma' + p_w \tag{3.7}$$

Due to the presence of water in the voids, pore pressure develops. The effective shear stresses are equivalent to the total shear stresses because shear forces cannot be sustained in water. Tensile

stresses are viewed as positive in PLAXIS-3D, but compressive stresses are viewed as negative. Pore pressure is defined by a single parameter *p*.

$$p_w = \begin{bmatrix} p & p & p & 0 & 0 & 0 \end{bmatrix}^T \tag{3.8}$$

Stress rates (shown as a dot above the stress symbol) are used to illustrate the correlation between microscopic increments of effective stress.

A matrix having Cartesian coordinates that represents the strain tensor is as follows:

$$\varepsilon = \begin{bmatrix} \varepsilon_X & \varepsilon_Y & \varepsilon_Z & \gamma_{XY} & \gamma_{YZ} & \gamma_{ZX} \end{bmatrix}^T \tag{3.9}$$

Strains, ε_{ij} are the derivatives of the displacement components.

$$\varepsilon_x = \frac{\partial u_x}{\partial x} \qquad \varepsilon_y = \frac{\partial u_y}{\partial y} \qquad \varepsilon_z = \frac{\partial u_z}{\partial z} \tag{3.10}$$

$$\gamma_{xy} = \frac{\partial u_x}{\partial y} + \frac{\partial u_y}{\partial x} \qquad \gamma_{yz} = \frac{\partial u_y}{\partial z} + \frac{\partial u_z}{\partial y} \qquad \gamma_{zx} = \frac{\partial u_z}{\partial x} + \frac{\partial u_x}{\partial z} \tag{3.11}$$

In PLAXIS, a positive normal strain represents extension while a negative normal strain represents compression.

The strain rates (shown by a dot above the strain symbol) are used to depict very small increments of strain when they are taken into consideration.

$$\dot{\varepsilon} = \begin{bmatrix} \dot{\varepsilon}_X & \dot{\varepsilon}_Y & \dot{\varepsilon}_Z & \dot{\gamma}_{XY} & \dot{\gamma}_{YZ} & \dot{\gamma}_{ZX} \end{bmatrix}^T \tag{3.12}$$

The link between small increment of effective stress (also known as "effective stress rates") and small increments of strain (also known as "strain rates") is written as

$$\dot{\sigma}' = \mathbf{D}\dot{\varepsilon} \tag{3.13}$$

D represents material behaviour and is a constitutive matrix. Pore pressures are excluded in this instance while analyzing the stress-strain relationship.

SOIL MODELING

The choice of suitable material modelling for capturing the soil, structure, and soil-structure interaction largely determines accuracy of the FEM simulation. For different kinds of geotechnical problems, numerous mathematical models were developed. In the present study, primarily two non-linear soil models are considered for modeling the embankment and foundation soil conditions. Whereas linear elastic model has been employed in few cases. Detailed description of the non-linear models is given below.

Formulation of the Mohr-Coulomb Model

Real soil behaviour exhibits a significant degree of nonlinearity under many loading scenarios. A straightforward model for describing linear elastic fully plastic behaviour is the Mohr-Coulomb model (MC model). It may be used to get a rough idea of approximate behaviour of soil. Hooke's law of elasticity serves as the foundation for the linear elastic representation of MC model. The Mohr-Coulomb failure criteria serves as the foundation for the completely plastic part. Figure 3.3 depicts the stress-strain relationship for an elastic completely plastic model.

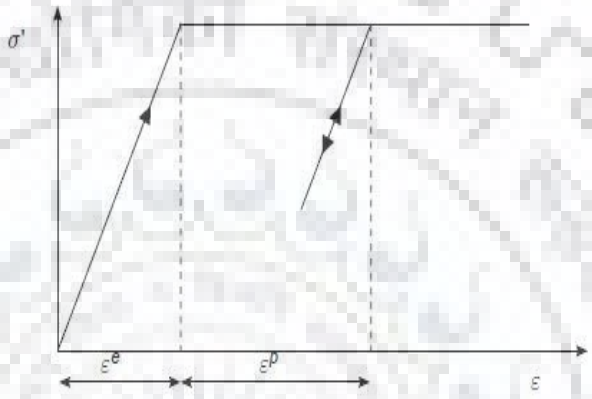

Fig. 3.3 An elastic-perfectly plastic model stress-strain relationship (PLAXIS 3D manual).

Plasticity is the process that generates irreversible strains. In order to evaluate the development of plastic behaviour, a yield function, *f*, is typically defined as a function of both stress and plastic strains. Plasticity yielding is associated with $f = 0$. In principal stress space, this situation can be illustrated as a surface. A constitutive model that has a set yield surface is referred to as a perfectly-plastic model. The yield surface is defined in terms of stress invariants and yield strength parameter. Additionally, it is unaffected by the degree of plastic straining. The behaviour is solely elastic for stresses expressed as points within the yield surface.

The basic concept of elasto-plasticity is the distinction of strains and strain rates into elastic and plastic components.

$$\varepsilon = \varepsilon^e + \varepsilon^p \; ; \qquad \dot{\varepsilon} = \dot{\varepsilon}^e + \dot{\varepsilon}^p \tag{3.14}$$

Where ε^e and ε^p represents elastic and plastic components of strain respectively.

The relationship between elastic strain rates and stress rates is established by Hooke's law. Substituting Eq. (3.14) by Hooke's law leads to:

$$\dot{\sigma}' = \mathbf{D}^e \dot{\varepsilon}^e = \mathbf{D}^e (\dot{\varepsilon} - \dot{\varepsilon}^p) \tag{3.15}$$

According to Hill's (1950) theory, the derivative of yield function and stresses are inversely correlated with the rates of plastic strain. As vectors perpendicular to the yield surface, the plastic strain rate can be depicted. This classical form of the theory is referred to as associated plasticity. The accompanying plasticity assumption for the MC yield function, however, overestimates the dilatancy for sands. In order to account for plastic strain direction, a new plastic potential function *g* is created. Non-associated plasticity is indicated for the condition g ≠ *f*. Generally speaking, through the plastic multiplier λ, a derivative of the plastic potential function in relation to the stresses are linked to the plastic strain rates.

$$\dot{\varepsilon}^p = \lambda \frac{\partial g}{\partial \sigma'} \tag{3.16}$$

Pure elastic behaviour is represented by λ = 0, whereas the plastic behaviour comes into picture when λ is positive

$$\lambda = 0 \quad for; \quad f < 0 \qquad or; \quad \frac{\partial f^T}{\partial \sigma'} \mathbf{D}^e \dot{\varepsilon}^e \leq 0 \ (Elasticity) \tag{3.17a}$$

$$\lambda > 0 \quad for; \quad f = 0 \qquad or; \quad \frac{\partial f^T}{\partial \sigma'} \mathbf{D}^e \dot{\varepsilon}^e > 0 \ (Plasticity) \tag{3.17b}$$

For elastic perfectly-plastic behaviour, the following relationship between the effective stress rates and strain rates may be obtained using these equations (Smith & Griffiths, 1982; Vermeer & Borst, 1984):

$$\dot{\sigma}' = \left(\mathbf{D}^e - \alpha \frac{\mathbf{D}^e \frac{\partial g}{\partial \sigma'} \frac{\partial f^T}{\partial \sigma'} \mathbf{D}^e}{\frac{\partial f^T}{\partial \sigma'} \mathbf{D}^e \dot{\varepsilon}} \right) \dot{\varepsilon} \tag{3.18}$$

The parameter $\alpha = 0$ for elastic behaviour whereas for plasticity $\alpha = 1$.

The MC yield criterion applies broad states of stress to Coulomb's friction law. This requirement ensures adherence to Coulomb's friction law in any plane throughout a material element.

When expressed in terms of primary stresses, the whole MC yield condition consists of six yield functions (Smith & Griffiths, 1982):

$$\begin{aligned} f_{ia} &= \frac{1}{2}\left(\sigma_j' - \sigma_k'\right) + \frac{1}{2}\left(\sigma_j' + \sigma_k'\right)\sin\varphi - c\cos\varphi \leq 0 \\ f_{ib} &= \frac{1}{2}\left(\sigma_k' - \sigma_j'\right) + \frac{1}{2}\left(\sigma_k' + \sigma_j'\right)\sin\varphi - c\cos\varphi \leq 0 \end{aligned} \tag{3.19}$$

$$where, \quad j = i+1; \quad k = j+1 \quad and \quad i = 1,2,3 \quad in \quad cyclic \quad order.$$

Friction angle ϕ and cohesion c are the two plastic model characteristics that are visible in the yield functions. A fixed hexagonal cone is formed in primary stress space by integration for all six yield functions $f_i = 0$ simultaneously (where f_i stands for each yield function), as illustrated in Fig. 3.4.

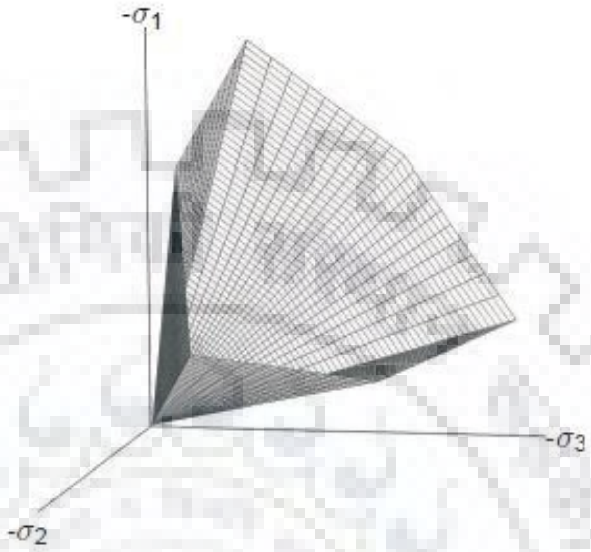

Fig. 3.4 The yield surface of Mohr-Coulomb in the principal stress space (c = 0).

In conjunction with the yield functions, the MC model defines six plastic potential functions:

$$g_{ia} = \frac{1}{2}\left(\sigma_j' - \sigma_k'\right) + \frac{1}{2}\left(\sigma_j' + \sigma_k'\right)\sin\psi$$
$$g_{ib} = \frac{1}{2}\left(\sigma_k' - \sigma_j'\right) + \frac{1}{2}\left(\sigma_k' + \sigma_j'\right)\sin\psi \qquad (3.20)$$

where, $j = i+1$; $k = j+1$ and $i = 1,2,3$ in cyclic order.

A further variable known as the dilatancy angle ψ is included in the plastic potential function. This parameter is crucial to accurately simulating the plastic volumetric strain (positive) increments (dilatancy) that are actually seen in dense sands.

Special consideration is necessary at each of the six corners when applying the MC model to general stress situations. Some programs employ rounded corners to create a smooth transition between one yield surface to another (Smith & Griffiths, 1982). However, employing a sharp change between one yield surface to another, PLAXIS implements the complete MC model in its exact form. Hooke's law for linear elasticity is followed by the behaviour for stress levels within the yield surface. Therefore, information regarding the elasticity modulus E and the Poisson's ratio μ is needed in addition to the plasticity parameters c, φ, and ψ.

Formulation of UBC3D-PLM model

UBC3D-PLM is an effective stress elasto-plastic model and has the capability of simulating the liquefaction phenomenon of sandy soil under dynamic loading conditions. This model is based on the original UBCSAND (University of British Columbia Sand) model developed by Puebla et al. (1997) and Beaty and Byrne (1998). The basic formulation of this model is based on classical plasticity theory with a hyperbolic strain-hardening rule based on the modified Duncan-Chang approach. The original hardening rule of UBCSAND model is shown in Fig. 3.5. A modified non-associative flow rule based on Drucker-Prager plastic-potential function is introduced in the UBC3D-PLM model. The basic difference between the UBCSAND model and the UBC3D-PLM model is the incorporation of the generalized 3-D formulation. The UBC3D-PLM model uses the MC yield condition in 3-D principal stress space. The hardening rule relates the mobilized friction angle (φ_{mob}) to the plastic shear strain at a given stress. The important formulations of this model are described in the following section.

The UBC3D-PLM model incorporated with a non-linear, isotropic law for the elastic behavior. It is defined in terms of the elastic bulk modulus (*K*) and the elastic shear modulus (*G*), which are related to all-round stress *p* using following equations:

$$K = k_B^{*e} p_{ref} \left(\frac{p'}{p_{ref}} \right)^{me} \; ; \; G = k_G^{*e} p_{ref} \left(\frac{p'}{p_{ref}} \right)^{ne} \tag{3.21}$$

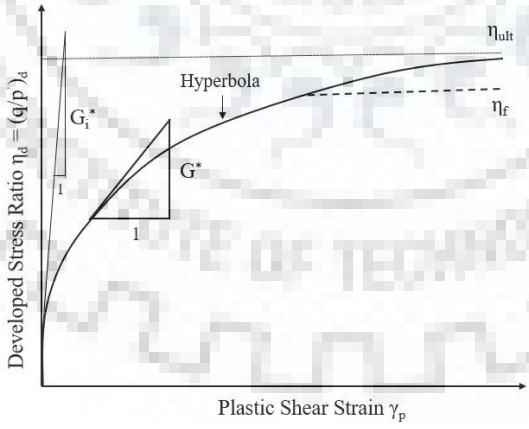

Fig. 3.5 Original hardening rule of UBCSAND model.

Pure elastic behavior is predicted during the unloading process. When the stress state reaches the yield surface, plastic behavior is taken into account until the stress point goes back into the elastic zone. Two yield surfaces are defined as, primary yield surface and secondary yield surface. The

primary yield surface is based on isotropic hardening and becomes active when the mobilized angle of friction becomes equal to the maximum mobilized angle of friction, the soil mass ever reached. In the case of the secondary yield surface, a simplified kinematic-hardening rule is used, which gets activated when the mobilized angle of friction is less than the maximum mobilized angle of friction. From the isotropic stress state, both the yield surfaces get expanded according to the same hardening rule. During the unloading state, the secondary yield surface shrinks, and the elastic behavior of soil becomes dominant. On reloading, the secondary yield surface becomes active and elasto-plastic behavior gets activated. When the mobilized angle of friction reaches the value of the maximum mobilized angle of friction, the primary yield surface becomes active again and soil behavior becomes softer. MC yield function used to define both the yield surfaces is defined in Eq. (3.22).

$$f_m = \frac{\sigma_{\max} - \sigma_{\min}}{2} - \left(\frac{\sigma_{\max} + \sigma_{\min}}{2} + c \cot(\varphi_p) \right) \sin(\varphi_{mob}) \tag{3.22}$$

Plastic hardening based on the principle of strain hardening is used in this model (Hardening Soil model). The hardening rule governs the amount of plastic strain because of the mobilization of the shear strength ($\sin \varphi_{mob}$). In the UBC3D-PLM model, a non-associated flow rule based on the Drucker-Prager plastic potential function is used.

To have higher accuracy in the prediction of EPP, a soil densification rule has been introduced by adopting a secondary yield surface to ensure a smooth transition into the liquefied state of the soil. This approach enables the distinction between the primary and secondary loading states. The secondary yield surface generates lower plastic deformations compared to the primary yield surface. The anisotropic hardening rule adopted for the secondary yield surface is defined in Eq. (3.23).

$$K^{p}_{G,\text{secondary}} = K^{p}_{G}(4 + 0.5\, n_{rev})\, hard\ \ fac_{hard} \tag{3.23}$$

A simple rule based on stress reversals of loading to unloading and vice-versa is used to define the counting of cycles. From the experimental studies, it can be observed that the rate of excess pore pressure (EPP) generation decreases with the increasing number of cycles until the liquefied state is reached. Later, a correction was made for loose sands (Eq. 3.24) following the UBCSAND formulation (Beaty and Byrne, 2011).

$$hard = \min(1; \max(0.5,\ 0.1 N_{1,60})) \tag{3.24}$$

Due to the limitation of the formulation of the flow rule, after the stress path reaches the yield surface defined by peak friction angle (φ_p) becomes constant with the evolution of the plastic volumetric

strains. That implies, φ_{mob} becomes φ_p, and remains constant along with ψ_m. Due to this limitation, stiffness degradation of loose sand during the post-liquefaction stage and cyclic mobility of dense sand can not be modeled. This limitation can be overcome in the UBC3D-PLM model using an equation with decreasing plastic shear modulus as a function of developed plastic deviatoric strain during the dilation phase. Deconstruction of the soil skeleton occurs during dilation, and this leads to a decrease in soil stiffness during the contraction phase following the unloading phase. The formulation of stiffness degradation has been given in Eq. (3.25) and (3.26).

$$K^{*p}_{G,\,post-liq.} = K^{*p}_{G}\, E_{dil} \tag{3.25}$$

$$E_{dil} = \max(e^{-110\varepsilon_{dil}}\,;\, f_{ac,post}) \tag{3.26}$$

The relationship between total stress, effective stress, and pore pressure is based on Terzaghi's theory (1920) as $dp = dp' + dp_w$. Volumetric compatibility under undrained conditions requires that the equivalent volumetric strain of the fluid should be equal to the volumetric strain developed in the soil skeleton.

$$\frac{K_w}{n} = (K_u - K_d) \tag{3.27}$$

Once the value of K_w is determined, EPP in each increment generated during undrained condition can be computed from the following equation:

$$dp_w = (K_w/n)\, d\varepsilon_v \tag{3.28}$$

The Poisson's ratio for the undrained analysis is set as 0.495 implicitly in the model itself, which is close to 0.5 for incompressible material. Due to numerical instability, using a value of 0.5 is avoided (Petalas and Galavi 2013). Using this Poisson's ratio undrained soil bulk modulus is calculated as follows:

$$K_u = \frac{2G^e(1+\nu_u)}{3(1-2\nu_u)} \tag{3.29}$$

The drained soil bulk modulus K_d is also computed similarly. The drained Poisson's ratio can be computed from the relationship $\nu' = \left(3K^e - 2G^e\right)\Big/\left(6K^e + 2G^e\right)$. Hence, by using Eqs. (3.27) and (3.28), during the undrained condition EPP is evaluated in the UBC3D-PLM model. A brief summary of UBC3D-PLM model parameters is given in Table 3.1.

Table 3.1 Summary of UBC3D-PLM parameters.

Function	Formulation	Parameter
Elastic domain	Nonlinear stress dependency of stiffness Unloading elastic	$K_B^e, K_G^e, K_G^p, m_e, n_e$
Failure criteria	Mohr-coulomb criterion	c', ϕ_p
Hardening rule	Hyperbolic: modified from Duncan-Chang	K_G^p, n_p, R_f
Flow rule	Non-associated: modified from Rowe	ϕ_{cv}
Plastic potential	Based on Drucker-Prager plastic potential	$\theta = 30^o$
Densification rule	Considers the number of cycles	n_{rev}, $hard$, fac_{hard}
Post-liquefaction factor	Stiffness degradation parameter	fac_{post}

3.4 ALGORITHM OF PLAXIS

Finite elements calculation process based on the formation of elastic stiffness matrix in PLAXIS. The algorithm used in the program is given below:

Read Input Data

Formation of Stiffness Matrix $\mathbf{K} = \int \mathbf{B}^T \mathbf{D}^e \mathbf{B}\, dV$

New Step $i \rightarrow i + 1$

New load vector $f_{ex}^i = f_{ex}^{i-1} + \Delta f_{ex}$

Formulation of reaction vector $f_{in} = \int \mathbf{B}^T \sigma_c^{i-1}\, dV$

Unbalanced force calculation $\Delta f = f_{ex}^i - f_{in}$

Reset incremental displacement $\Delta U = 0$

New iteration $j \rightarrow j + 1$

Solve for displacements $\delta U = \mathbf{K}^{-1} \Delta f$

Update incremental displacements $\Delta U^j = \Delta U^{j-1} + \delta U\, \mathbf{D}$

Calculate incremental strains $\Delta \varepsilon = \mathbf{B} \Delta U;\ \ \delta \varepsilon = \mathbf{B} \delta U$

Calculate Stresses:

Elastic: $\sigma^{tr} = \sigma_c^{i-1} \mathbf{D}^e \Delta \varepsilon$

Equilibrium: $\sigma^{eq} = \sigma_c^{i-1} \mathbf{D}^e \delta \varepsilon$

Constitutive: $\sigma_c^{i,j} = \sigma^{tr} - \dfrac{\left\langle f(\sigma^{tr}) \right\rangle}{d} \mathbf{D}^e \dfrac{\partial g}{\partial \sigma}$

Formation of reaction vector	$f_{in} = \int \mathbf{B}^T \sigma_c^{i,j} \, dU$
Calculate unbalance forces	$\Delta f = f_{ex}^{i} - f_{in}$
Check for error	$e = \dfrac{\lvert \Delta f \rvert}{\lvert f_{ex}^{i} \rvert}$
Accuracy check	if $e > e_{tolerated} \rightarrow$ new iteration
Update the displacements	$U^i = U^{i-1} + \Delta U$
Write output data (results)	
If not finished → new step	
End	

Where,

B : Strain-displacement matrix

D^e : Elastic stiffness matrix (Hooke's law)

f : Yield function

K : Stiffness matrix

U : Nodal displacement vector

V : Volume

σ : Stress components vector

3.5 CONCLUDING REMARKS

In this chapter, a detailed numerical process used in numerical modelling is described with minor details. Chapter also described two different non-linear constitutive model based on which embankment and foundation soil along with mitigation approaches are modeled. In the subsequent chapters response of a clayey embankment resting on loose saturated cohesionless soil underlain by a dense sand layer along with different mitigation approaches are presented under dynamic loading.

CHAPTER 4
STONE COLUMN MITIGATION

4.1 GENERAL

Construction of embankments on liquefiable soil is very crucial considering different types of damages observed during past significant earthquakes. Among all the physical model testing, shaking table and centrifuge model studies significantly helped to identify the important parameters controlling the dynamic stability of the earthen dams and slopes and provided insights for efficient and economic remedial measures. The significant effects of foundation soil liquefaction on the embankments have been studied via different physical model studies (Koga and Matsuo 1990; Adalier et al. 1998). Among all the physical model testing, shaking table and centrifuge model studies significantly helped to identify the important parameters controlling the dynamic stability of the earthen dams and slopes. These studies provided insights for efficient and economic remedial measures. Particularly, one of the best ways of judging the extent and location of remediation of weak foundation soil is determined based on the observed deformation profile (NRC, 1985). From the previous studies (Koga and Matsuo 1990; Koseki et al. 1994) it can be observed that the soil beneath the embankment does not reach zero effective stress state, whereas soil in the free field approaches zero effective stress condition. The reason behind this difference in the behavior of stress states at two different locations was the spatial variation in stress conditions. Several physical model studies done by different researchers in last few decades and majority of the studies conducted by considering cyclic loading. However, limited studies have been reported on the evaluation of the liquefaction behavior of structures like embankments resting on loose sand layers and its remedial measures, because of variation of stress state in the liquefiable foundation layer. Evaluation of remediated embankment using full-scale testing under the ideal earthquake condition would be the ideal study. However, due to the complexity and expensiveness of such study, numerical modeling becomes a reliable alternative.

From the large-scale dynamic centrifuge study, Adalier (1996) inferred that due to the sideways shear stresses the soil under the toe of the embankment and in front of the embankment, builds up high excess pore pressure (EPP). Consequently, the soil near that region starts losing its shear strength and large deformation occurs. The foundation soil tries to move laterally away from the centerline of the embankment and appears in the form of bulging on the free surface after the toe region. Because of this phenomenon embankment experiences higher values of settlement than the

toe region. Due to this outflow of foundation soil under the embankment, whose effect is more than the change in volumetric strains due to EPP dissipation, surface deformation and settlement of the embankment can be observed. Different soil-treatment techniques and structural inclusion measures were used to reduce the foundation soil liquefaction-induced damage to the embankment. Densification by compaction, soil replacement, soil grouting, gavel berms, and sheet pile walls are the most commonly used remediation measures considered in past studies for reducing the damage to earthen embankments. Past studies revealed that constraining the outflow of foundation soil is the key to an effective remedial measure. However, past studies have reported the effectiveness of gravel drains or stone columns for mitigating the liquefaction phenomenon. Studies showed that gravel drains have two different beneficial aspects in the mitigation of liquefaction and liquefaction-induced damages. The first one is the densification of the surrounding soil during the installation of drains and the latter one is the drainage effect of gravel drains. The former aspect has not been addressed in the current study; however, the later aspect is primarily focused. Moreover, a very limited numerical study is available where stone columns/gravel drains have been considered to mitigate liquefaction-induced damage to embankment-type structures. This Chapter presents numerical study on embankments resting on liquefiable soil with and without mitigation measures. An attempt has been made in order to evaluate the effectiveness of stone column against the liquefaction of embankment foundation soil and the liquefaction-induced settlement of embankment. Plane strain condition has been taken into consideration to analyze an earthen embankment resting on a liquefiable deposit under the application of dynamic/seismic loading.

4.2 VALIDATION OF NUMERICAL MODEL

The efficacy of the present numerical approach must be checked prior to a detailed numerical study. Validation has been carried out in two parts by performing a cyclic element test and comparison with a well-established centrifuge study.

4.2.1 Calibration of UBC3D-PLM Model

The present study considers two sandy layers with different relative densities (R_D). Top layer is liquefiable layer Nevada 120 sand with R_D = 40%. Bottom layer is dense Fraser River sand with R_D = 80%. Properties of these two layers are available from past literature (Arulmoli et al. 1992; Sriskandakumar 2004; Wijewickreme et al. 2005). Basic soil properties of bath sands are reported in Table 4.1. Based on the basic properties of the soil, range of parameters are chosen for UBC3D-PLM model. Further, using iteration process based on best-fit liquefaction strength curve, model

parameters are finalized. Lastly, response of simulated single element cyclic direct simple shear (CDSS) test has been compared with the reported CDSS test results of Arulmoli et al. (1992). Results from published centrifuge study (Adalier 1996; Adalier et al. 1998) have been devised for validating capability and reproducibility of material model. For dense sand, Fraser River sand of 80% relative density (Sriskandakumar 2004) is calibrated for the UBC3D-PLM model and further used in the present study.

Table 4.1 Properties of Nevada 120 sand (Arulmoli et al., 1992) and Fraser River sand (Sriskandakumar, 2004).

Properties	**Nevada 120 sand**	**Fraser River sand**
Relative density	40%	80%
Specific Gravity	2.67	2.71
Dry unit weight (γ_{dry})	15.08 kN/m^3	16.73 kN/m^3
Permeability (k)	6.6E-05 m/s	5.5E-06 m/s*
e_{max}	0.887	0.94
e_{min}	0.511	0.62

* in absence of available data this value has been assumed.

For calibrating the UBC3D-PLM model cyclic test results from different studies have been referred (Arulmoli et al. 1992 for R_D = 40%, and Sriskandakumar 2004 for R_D = 80%). The input parameters of the UBC3D-PLM model are evaluated by Petalas and Galavi (2013) and calibrated using the liquefaction strength curve. Out of different input parameters K_G^p allows the UBC3D-PLM model to be calibrated to target Cyclic Resistance Ratio (CRR). In the single element cyclic test, the number of uniform loading cycles (N_{CYL}) demand to initiate liquefaction are determined for a given CRR. Simulation is repeated for different values of CRR in order to generate CRR versus N_{CYL} curve.

Figures 4.1 and 4.2 illustrate the cyclic shear strength curve from the undrained stress-controlled cyclic simple shear loading of Nevada 120 sand and Fraser River sand respectively along with their numerical predictions from single element simulation of cyclic loading. The soil is K_0 consolidated under an initial vertical effective stress (σ_{v0}) of 100 kPa and zero initial static shear stress ($\alpha = 0$).

The study revealed that K_G^p mainly controls the undrained behavior and liquefaction strength. Three different sets of model parameter (K_G^p) have been introduced to obtain a smooth calibrated liquefaction curve. Calibration of the relationship between the CRR and N_{CYL} needed for liquefaction initiation, is based on the power fit of the form of Eq. 4.1 (Idriss and Boulanger 2008).

$$CRR = a\, N_{CYL}^{-b} \tag{4.1}$$

In which, the parameter *b* for clean sands is typically about 0.34 and factor *a* depends on a wide range of factors. The calibration parameters, particularly K_G^p , have been optimized to satisfy the requirement of the *b* value. It can be observed from Table 4.2 that Type-I calibration of Nevada 120 sand provides good agreement of *b* value with the reported value of Idriss and Boulanger (2008).

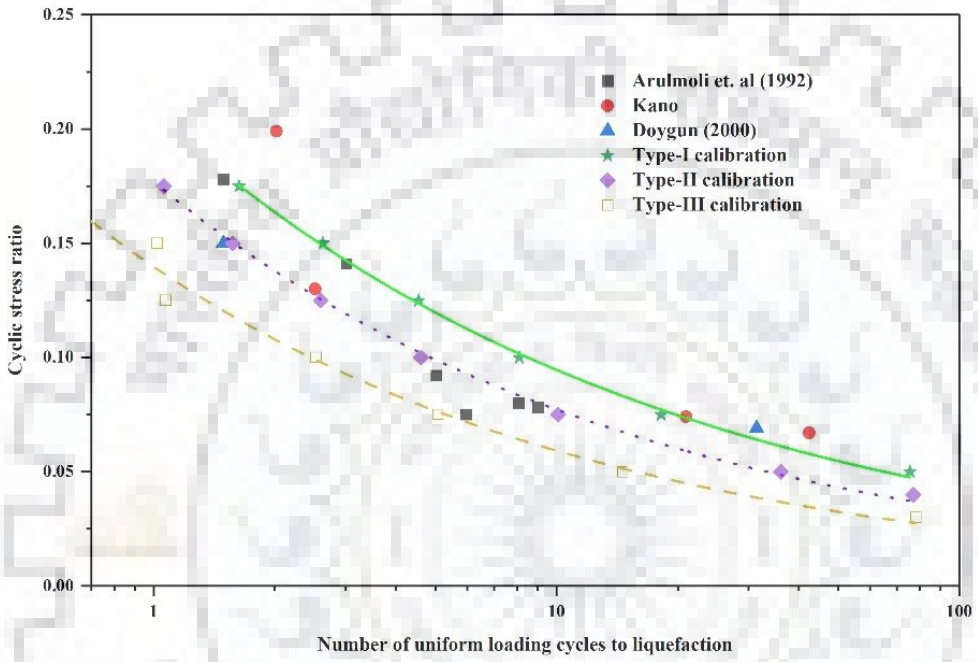

Fig. 4.1 Calibration of UBC3D-PLM model to liquefaction strength curve for Nevada 120 sand from cyclic simple shear element data.

A similar calibration methodology based on liquefaction strength criteria has been adopted by different researchers (Bastidas 2016; Dinesh et al. 2022). In the latest version of the UBC3D-PLM model fac_{post} controls the minimum shear stiffness of the soil. Once the peak yield surface is attained with every load cycle, the shear modulus of soil decreases until it reaches the minimum value. To obtain a pore pressure ratio (r_u) close to unity the fac_{post} factor needs to be very low, otherwise after reaching a minimum shear modulus value, new loading cycles will not be generating any further increment in pore pressures.

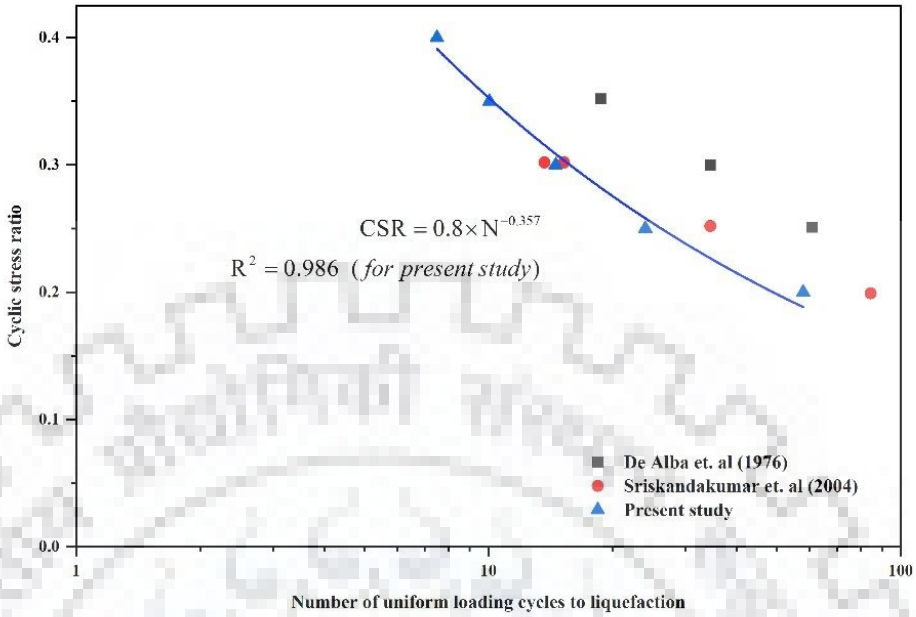

Fig. 4.2 Calibration of UBC3D-PLM model to liquefaction strength curve for Fraser river sand from cyclic simple shear element data.

Table 4.2 Calibration summary based on power fit of Eq. (4.1) for Nevada 120 sand.

Parameters	Type-I Calibration	Type-II Calibration	Type-III Calibration
$K_G^{p\,*}$	350[c]	276.3[c]	202.6 [a, b]
a	0.21	0.18	0.14
b	0.34	0.36	0.37
R^2	0.998	0.998	0.984

[a] Based on Petalas and Galavi, 2013.

[b] Based on Bhatnagar et al., 2015.

[c] Considered based on iteration. A similar approach was adopted by Dinesh et al. (2022) to calibrate the PM4Sand model.

This will prohibit attaining the full liquefaction state. In the case of loose sand, the soil experiences a high pore pressure ratio (close to 100%) as the soil is liquefied before the shear modulus value reaches a minimum. For this reason, the UBC3D-PLM model shows better agreement of shear strain values for low relative density sands with the laboratory test results (Tsegaye 2010; Petalas and Galavi 2013; Antonia 2013). It was assumed that at 85% pore pressure ratio the dense sand (R_D = 80%) has experienced the onset of liquefaction. Based on this criterion, the liquefaction strength curve has been calibrated. It has shown good agreement with the past studies (Sriskandakumar 2004; Idriss and Boulanger 2008).

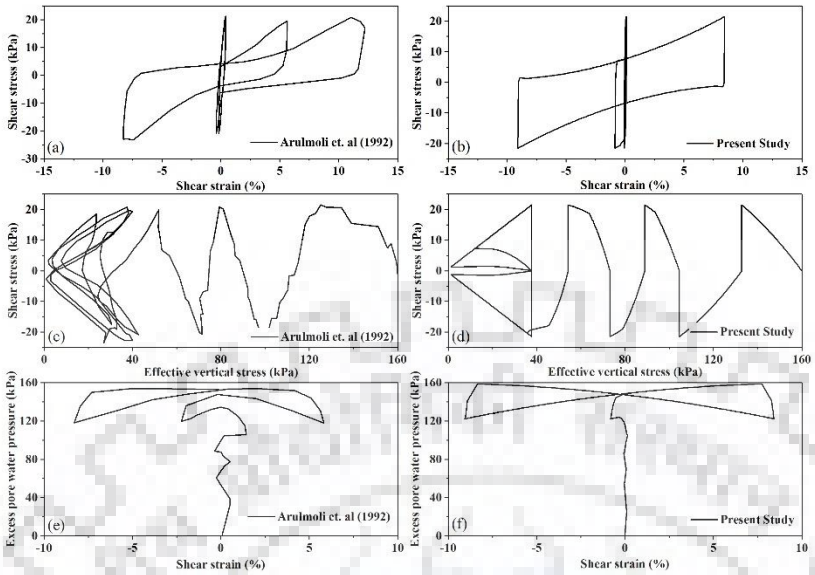

Fig. 4.3 Comparison of CDSS element test results and unit element simulation of CDSS using calibrated UBC3D-PLM model; (a, b) shear stress strain response; (c, d) stress path response and (e, f) development of excess pore pressure.

Analogous stress-controlled loading of cyclic direct shear test (Arulmoli et. al, 1992) has been considered in the single element simulation process for comparison. Figure 4.3 illustrates the comparison of laboratory experimental test results of cyclic loading for Nevada 120 sand with numerical predictions from the single element simulation of cyclic loading. Figures 4.3 (a, c and e) represent the cyclic direct shear test results (Arulmoli et. al, 1992), whereas Figs. 4.3 (b, d and f) represent the single element simulation of cyclic direct shear test using PLAXIS. The model parameters considering Type-I calibration have been used to demonstrate the capability of the calibrated numerical model by plotting shear stress-strain behavior in Figs. 4.3(a and b), stress path response in Figs. 4.3(c and d), and the development of EPP with shear strain in Fig. 4.3(e and f). This calibrated UBC3D-PLM model was then used for the simulation of boundary value problems, which are discussed in the subsequent sections.

4.2.2 Centrifuge Study of Earthen Embankment

Dynamic centrifuge test results of Adalier et al. (1998) conducted at the RPI centrifuge facility are considered in the present study for confirming the ability of the UBC3D-PLM constitutive model to simulate the liquefaction behavior of loose foundation sand layer. Dynamic stability of an earthen embankment supported on a saturated 6 m thick loose sand deposit tested in a 75*g* centrifugal acceleration field was used for the validation of the proposed model developed in PLAXIS 2D.

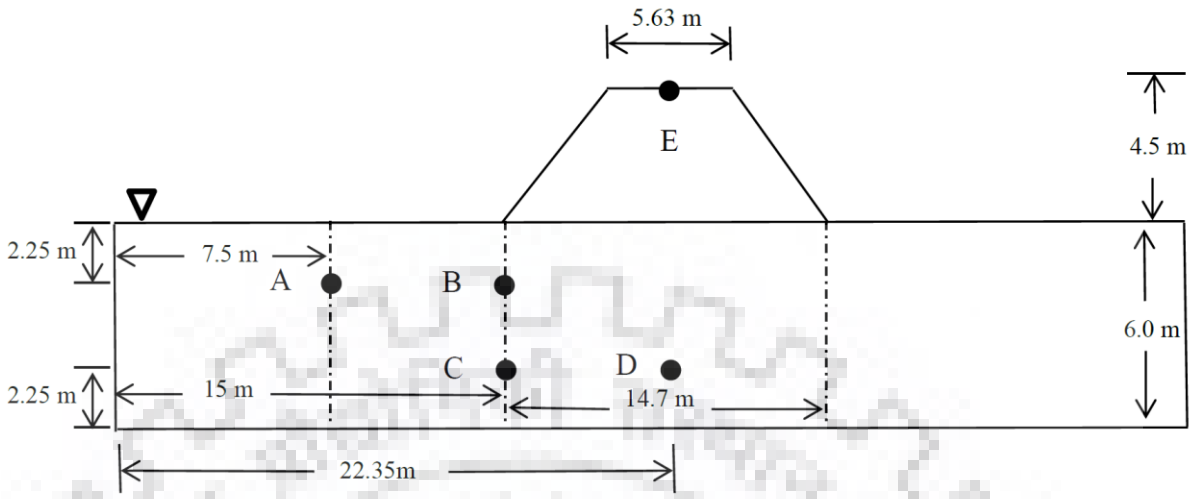

Fig. 4.4 Geometric representation of embankment resting on loose sand (after Adalier, 1996).

The embankment was built with a 1:1 slope made of a mixture of Kaolin clay and Nevada sand (1:4 weight ratio). Figure 4.4 shows the geometry of the centrifuge model considered by Adalier (1996). For the liquefiable foundation soil layer Nevada fine sand with 40% relative density was used. Model parameters are reported in Table 4.3.

Detailed material properties of the embankment are listed in Table 4.4. The initial stresses are calculated using the Mohr-Coulomb model. A similar methodology was adopted by Dinesh et al. (2022) using the PM4Sand model to simulate the liquefaction remedial measures for the embankment. The earthen embankment-foundation system was subjected to 10 cycles of 0.1g acceleration at 1.6 Hz frequency.

At location E, the maximum crest settlement was found to be 11.5 cm and 11.35 cm (Fig. 4.5-e) from the experimental and numerical studies, respectively. However, the numerically predicted acceleration values at location E are found to be slightly lower than the experimental observation (Fig. 4.5-f). From Fig. 4.5(b), it can be noticed that the maximum EPP has been predicted as 20.55 kPa at Point B which is 4.415 kPa higher than the experimental result. Both peaks occurred at 7.9 s which shows a good agreement of the predicted value with the experimental value. At points, A and C predicted EPP values are almost found to be close to the experimental results (Fig. 4.5-a and c).

Table 4.3 Calibrated UBC3D-PLM model parameters.

Parameters	Nevada 120 Sand*	Fraser River sand	Stone column
Relative density	40%	80%	-
γ_{dry} (kN/m^3)	15.08	19.0	18.0
$e_{initial}$	0.736	0.5	0.45
k (m/s)	6.6×10^{-5}	5.5×10^{-6}	0.0524[b]
ϕ_p	33.65^0	38.9^0	48.10^0
ϕ_{cv}	33^o	33^o	40^0
K_B^e	566.6	937.6	744.2[b]
K_G^e	809.4	1339.5	1063.14[b]
K_G^p	350	3597.1	4466.33[b]
m_e	0.5	0.5	0.5
n_e	0.5	0.5	0.5
n_p	0.4	0.4	0.4
R_f	0.83	0.66	0.64
fac_{hard}	0.45	0.45	0.65
fac_{post}	0.1	0.1	0.1
Corrected SPT blow count [$(N_1)_{60}$]	6.5[a]	29.7	37[a]

* Based on Type-I calibration.

[a] Based on Bhatnagar et al. (2016).

[b] for S/D=2.0 , K_B^e is evaluated using Eq. (4.3). For S/D = 2.5 and 3, values of K_B^e are evaluated accordingly.

Table 4.4 Properties of embankment clayey sand (Adalier, 1996).

Properties	Embankment clayey sand
E	20 MPa
γ_{dry}	19 kN/m^3
$\gamma_{saturated}$	21 kN/m^3
$e_{initial}$	0.50
c	22 kPa
ϕ	31^o
k	6.94×10^{-6} m/s

At point D maximum EPP values are found to be 30.49 kPa and 33.33 kPa for experimental and numerical models, but the numerical model predicted the maximum EPP almost 3.0 s earlier compared to the experimental result (Fig. 4.5-d).

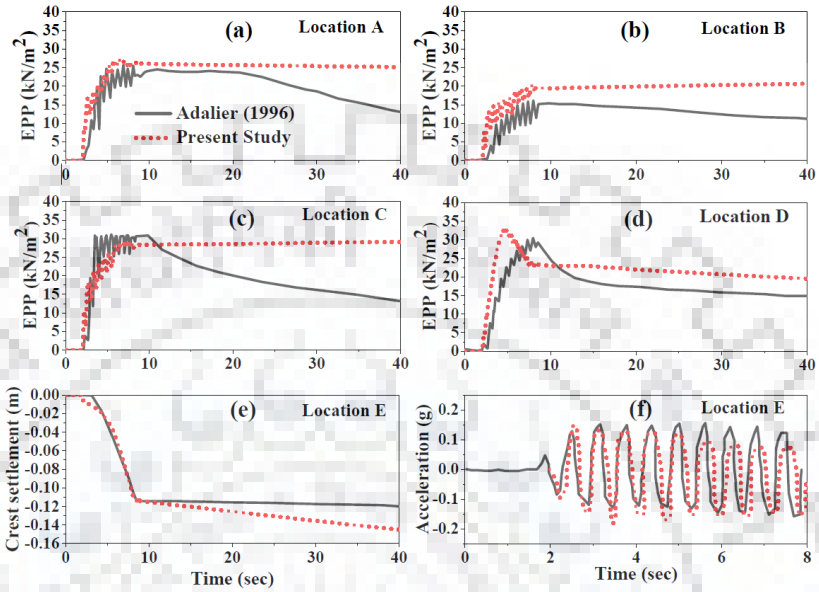

Fig. 4.5 Comparison of simulated and measured time histories of (a-d) excess pore pressure (EPP); (e) settlement and (f) acceleration at various locations.

This implies that the numerical model predicts the early buildup of EPP just beneath the embankment. The plastic state after the dynamic loading shows slower dissipation in the case of the numerical model because UBC3D-PLM does not account for dissipation modeling by default. Differences in buildup and dissipation may be attributed to the assumption of the constant permeability which can change with the change in void ratio.

4.3 EQUIVALENT STRIP APPROACH

The current study has focused on the evaluation of the efficiency of the stone column as a remedial measure. Stone columns are used as a mitigation measure in the foundation soil region under the embankment toe. Stone columns are cylindrical, but for two-dimensional plane strain conditions, an equivalent plane strip is assumed. The permeability and the bulk modulus are important input parameters. Their equivalent values for plain strain condition are determined using the following analytical approach. Figure 4.6 shows the geometric idealization for the equivalent plane strip.

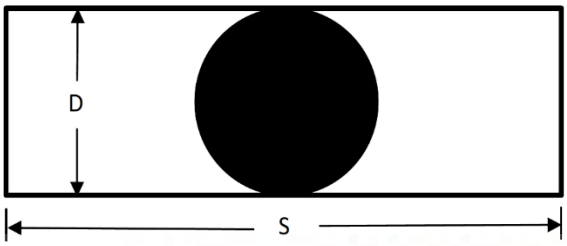

Fig. 4.6 Concept of equivalent plane strip.

The perimeter of the actual stone column is $p_{stonecolumn} = \pi D$, whereas that of the plane strip for single spacing S, $p_{planestrip} = 2(D+S)$. Darcy's law can be applied assuming the unit depth of the soil column. Assuming same discharge through the stone column and the plane strip, following relationship can be derived.

$$Q = kiA = ki\,p_{stonecolumn} \times 1$$

$$k_{equivalent} = \frac{k\,p_{stonecolumn}}{p_{planestrip}} = \frac{k\pi D}{2(D+S)} \tag{4.2}$$

Following a similar approach, equivalent bulk modulus of the plane strip was determined. Total volumetric change from soil and actual stone column has been considered as the equivalent volumetric change of the plane strip.

$$K^e_{B,equivalent} = \frac{S.D}{\frac{A_{soil}}{K^e_{B,soil}} + \frac{A_{stonecolumn}}{K^e_{B,stone\ column}}} \tag{4.3}$$

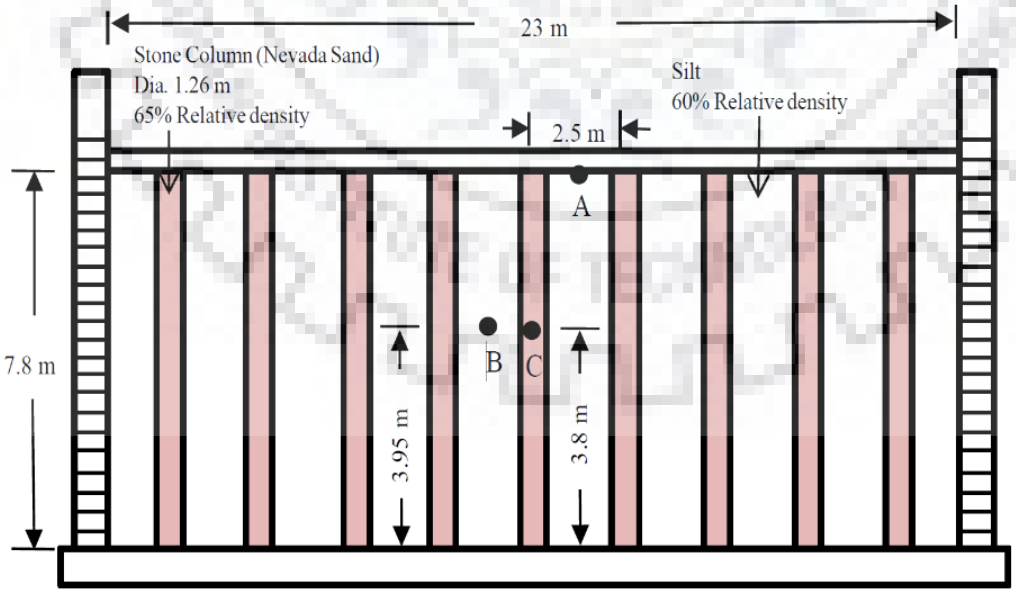

Fig. 4.7 Model of centrifuge testing (after Adalier et al., 2003).

A similar analytical approach has been previously adopted by Kumar et al. (2020). Based on equivalent elastic bulk modulus other two parameters (K_G^e , K_G^p) are evaluated for equivalent plane strip using the empirical correlations of Petalas and Galavi (2013).

Idealizations of equivalent plane strip approach have been confirmed with the centrifuge study (Adalier et al. 2003). The size of prototype model was 23 m × 12.5 m × 7.8 m. It was filled with saturated pure silt. 45 numbers of 1.26 m diameter stone columns were installed with 2.5 m center to center spacing. Stone columns were placed in 5 rows and 9 columns.

The simulated numerical model is represented in Fig. 4.7. The material properties for silt of 60% relative density and stone columns of 65% relative density Nevada sand are reported in Table 4.5. 20 cycles of harmonic motion with increasing amplitude, having a peak excitation of 0.3*g* of 1.8 Hz frequency has been considered in this study. EPP at locations B and C and settlement of point A has been examined.

Table 4.5 UBC3D-PLM parameters for Nevada sand (65% relative density) and Silt (60% relative density).

Parameters	Nevada sand	Silt
Relative density (%)	65	60
γ_{dry} (kN/m^3)	15.76[a]	13.4
$e_{initial}$	0.661[a]	0.7
k (m/s)	1.37×10^{-6}	4.3×10^{-6}
ϕ_p	37^0	25^0
ϕ_{cv}	33^0 [a]	21.7^0 [b]
K_B^e	789.9	773.63
K_G^e	1128.4	1105.2
K_G^p	1378.7	1050
m_e	0.5	0.5
n_e	0.5	0.5
n_p	0.4	0.4
R_f	0.705	0.722
fac_{hard}	0.45	0.45
fac_{post}	0.1	0.1
Corrected SPT blow count [$(N_1)_{60}$]	19.435[b]	16.56[b]

[a] Based on Adalier, 1996.

[b] Based on Petalas and Galavi, 2013.

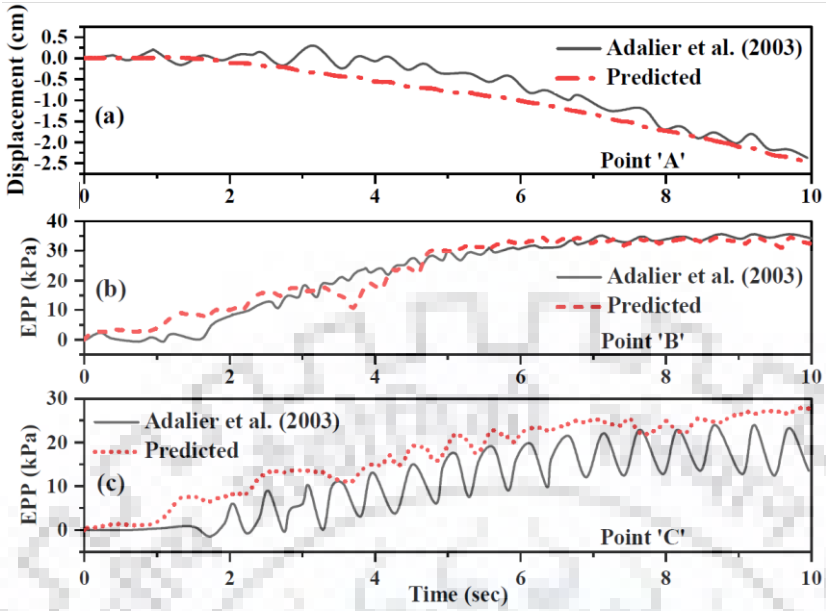

Fig. 4.8 (a) Displacement time history at location 'A', (b) EPP time history at location 'B' and (c) EPP time history at location 'C'.

Figure 4.8 shows the comparison of results of 2D plane strain finite element analysis with the centrifuge test results. A good agreement of results can be observed with some discrepancies in predicted EPP in stone column location C. The reason behind this discrepancy might be due to the use of uncalibrated model parameters, and the unavailability of cyclic element test results for the materials used in this study. However, the primary intention of this analysis was to show the efficacy of the equivalent plain strip consideration which has been used in the next section.

4.4 PARAMETRIC STUDY USING STONE COLUMN MITIGATION

In this present study, a numerical model was simulated to underline the effectiveness of stone columns in reducing the liquefaction-induced detrimental effects of earthen embankments resting on loose sand deposits. A clayey sand embankment founded on a loose saturated sand layer followed by a dense sand layer has been considered in this study. As a benchmark model, the embankment has been considered as 4.5 m thick with a 1:1 slope with a 14.7 m wide base dimension resting on a 6 m thick loose sand layer. It is underlain by a 4 m thick dense sand layer.

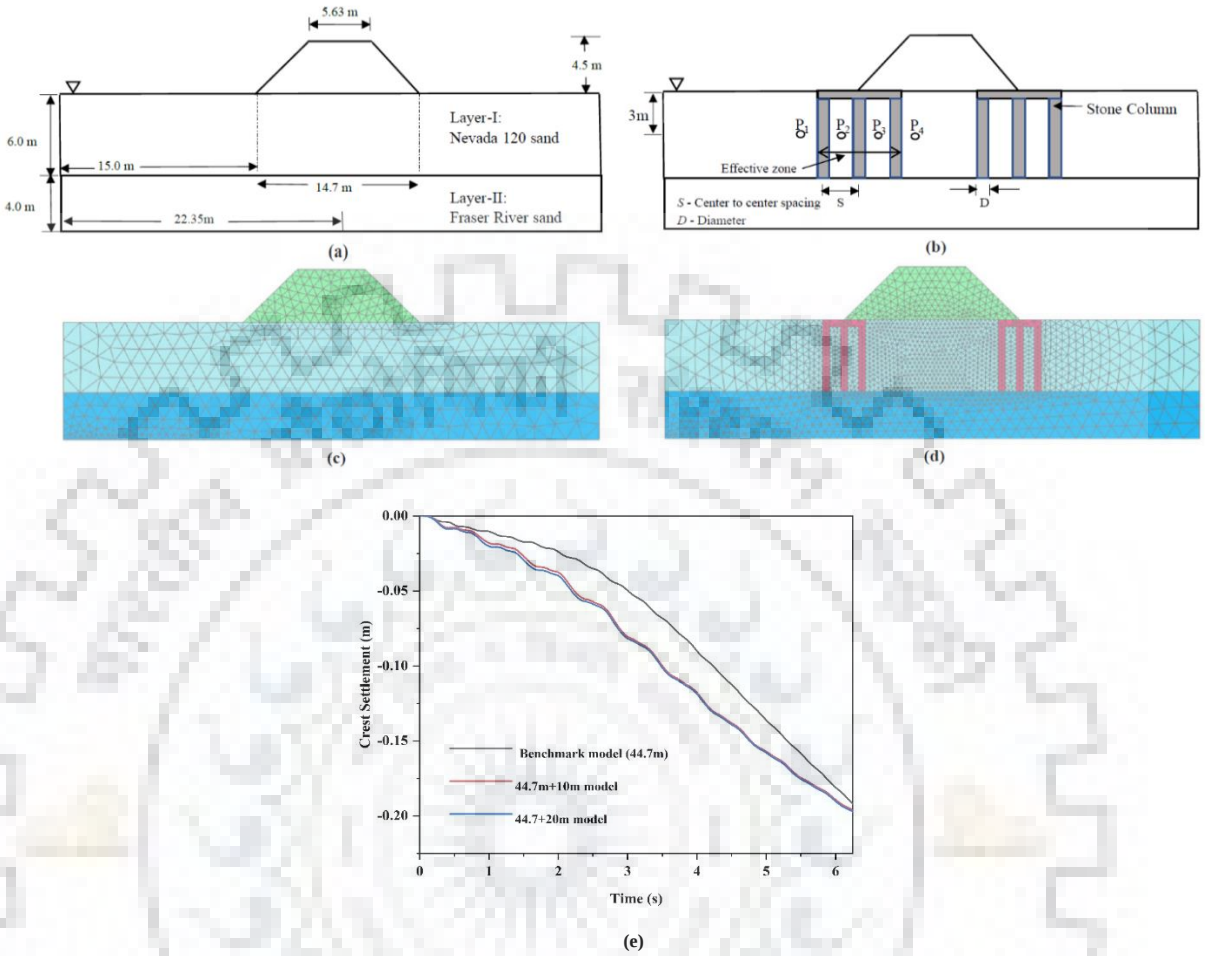

Fig. 4.9 (a) Benchmark model; (b) Benchmark model with stone column; (c) FE mesh of benchmark model; (d) FE mesh of the model with stone column, and (e) effect of lateral boundary distance on embankment settlement.

Figure 4.9 represents the model dimensions taken into consideration for numerical modeling. Figures 4.9(a and b) show the benchmark model and mitigation model with stone columns. The width of the foundation soil layers was considered 44.7 m. Loose and dense sand layer properties are considered as Nevada 120 sand (R_D = 40%), Fraser River sand (R_D = 80%), and Stone column properties are selected from Table 4.3. Similarly, the embankment soil properties are taken from Table 4.4. Embankment clayey sand soil was modeled using the Mohr-Coulomb material model. Fine meshing has been adopted for better accuracy of predicted results in the present numerical model. The finite element mesh for both the benchmark model and model with 3 stone columns on each side below the embankment toe has been shown in Fig. 4.9(c and d). Viscous boundary condition has been considered for vertical boundaries whereas the top surface of soil deposit experiences atmospheric

pressure only. Distance of vertical boundaries from the embankment toe was optimized with a convergence study. The distance of boundary from toe was varied as 15 m, 20 m and 25 m. Results for 20 m and 25 m have shown 2.1 and 2.6 % variation in the crest settlement (Fig. 4.9 e). The bottom boundary was considered to be fully fixed. Viscous boundary generally updates the stress condition at the boundary to nullify the effect of reflected stresses back into the domain. In this manner, it is attempted to simulate the realistic boundary condition with certain accuracy (Yang et al. 2003).

Figure 4.10(a) shows effective vertical stress distribution during the initial soil condition for the benchmark model. Similar stress distribution at the end of reconsolidation (250.0 s) after the application of cyclic loading (amplitude 0.1*g*) is depicted in Fig. 4.10(b). To study the effectiveness of stone column mitigation, a detailed parametric study has been executed to highlight the effect of stone column diameter (*D*), spacing of stone columns (*s*), and input motion.

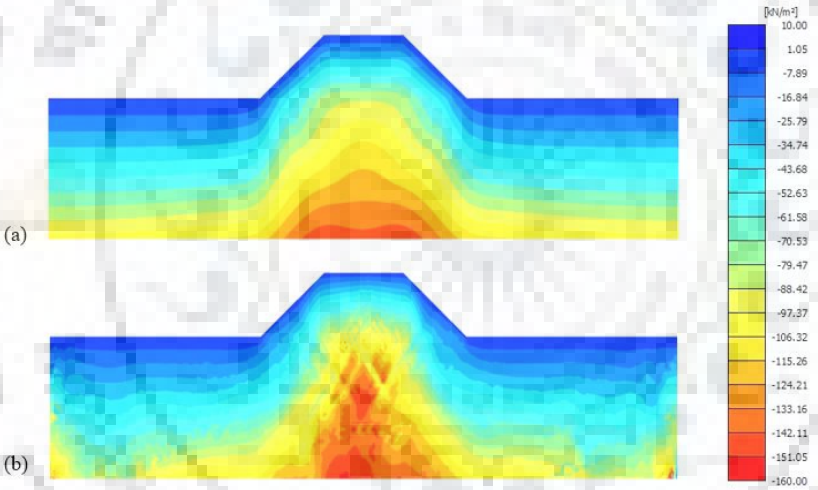

Fig. 4.10 Effective vertical stress distribution during (a) initial soil condition; (b) at the end of reconsolidation after the application of cyclic loading.

4.4.1 Optimization of the number of Stone Columns

To fix the number of stone columns under the embankment toe zone, an optimization study has been conducted. The embankment crest settlement was considered as the governing parameter in this optimization study. The variation in the crest settlement with an increasing number of stone columns was the main focus of this study. As an input motion, 10 cycles of 1.6 Hz frequency were applied with an acceleration of 0.1*g* amplitude. The crest settlement for no stone column condition has been taken as a benchmark.

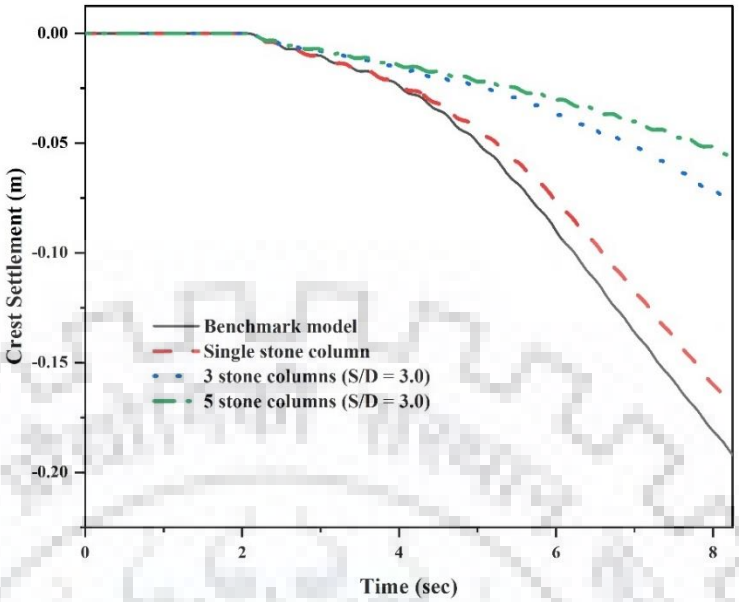

Fig. 4.11 Optimization of number of stone columns for effective mitigation.

It can be observed from Fig. 4.11 that with a single stone column below the toe, settlement reduces nearly by 11.20%, whereas with 3 and 5 stone columns settlement reductions are 60% and 70%, respectively. With an increase in stone column numbers settlement reduces. However, with a minimum of three numbers of stone columns in each region under the embankment toe, a considerable amount of mitigation can be achieved. This may provide an economic solution to such types of geotechnical structures. Hence in the further parametric study, the number of stone columns in each region under the embankment toe was limited to 3.

4.4.2 Effect of Stone Column Diameter

The excess pore pressure ratio (r_u) is expressed in terms of the ratio between the change in pore pressure (Δu) and the initial effective vertical stress ($\Delta\sigma'_{v0}$). In a certain time period of applied dynamic loading condition when the soil experiences the maximum value of change in pore pressure, this condition represents the maximum excess pore pressure ratio ($r_{u,\max}$).

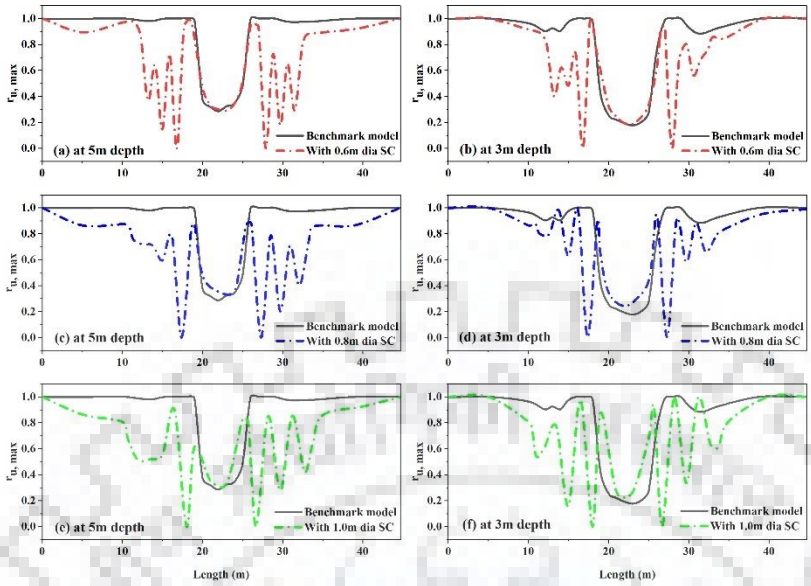

Fig. 4.12 $r_{u,\max}$ profile at different depths of liquefiable foundation soil for $S/D = 3.0$.

Variations in $r_{u,max}$ for different diameters of the stone column throughout the length of the profile of liquefiable foundation soil at 5 m and 3 m depth are compared in Fig. 4.12. For a constant S/D ratio of stone columns, the diameter of stone columns has been varied in this section. Three different diameters (0.6 m, 0.8 m, and 1.0 m) were considered in this study. The stone column encased zone has been demarcated as an *effective zone*. The effect of stone columns in that zone below the embankment toe is the main concern of this study. $r_{u,\max}$ of that zone is categorically named as $r_{u,\max}^{Eff-zone}$. In the case of 0.6 m diameter stone column, a range of $r_{u,\max}^{Eff-zone}$ has been observed from 0 to 0.803 at 3 m depth. At the 5 m depth, this range has been observed as 0 to 0.728. Similarly, for 0.8m diameter stone columns at 3 m depth the range of $r_{u,\max}^{Eff-zone}$ in the *effective zone* was found to be 0 to 0.984, and at 5 m depth the range was within 0 to 0.787.

Lastly, for 1 m diameter stone column, the range for $r_{u,\max}^{Eff-zone}$ at 3 m and 5 m depth in the *effective zone* was observed to be 0 to 0.998 and 0 to 0.854, respectively. It can be inferred that the effectiveness of stone column decreases with increasing diameter of stone column for a constant S/D ratio (at 3 m depth, $r_{u,\max}^{Eff-zone}$ = 0.803, 0.984, 0.998 for 0.6, 0.8, 1.0 m diameter). For S/D = 3.0 the absolute drainage path length for 0.6 m, 0.8 m, and 1.0 m diameter stone columns are 1.2 m, 1.6 m, and 2.0 m, respectively. This indicates that with increasing absolute drainage path length, EPP at the middle of spacing of stone columns increases. With the increasing diameter of stone columns, the stiffness of the region under the toe increases which restrains the soil in between two stone columns,

and the compressibility of soil reduces. At 3 m depth, this phenomenon is more predominant as compared to 5 m depth. At 5 m depth stone columns are more effective than 3 m depth. This may be attributed to the presence of the denser sand layer at 6 m depth. Figure 4.13 shows the effect of the stone column in restraining the lateral outflow deformation of foundation soil below the embankment. The variation in the lateral displacement U_x along the depth of the liquefiable foundation soil layer are compared for all three diameters. In the case of the benchmark model, the maximum outflow horizontal deformation $U_{x,\max}$ right below the embankment toe was found to be 0.171 m at 2 m depth from the ground level. But models with the inclusion of stone column show maximum outflow horizontal deformation ($U_{x,\max}$) at 1 m depth. With an increase in the diameter of stone columns 65.50%, 70.76%, and 77.20% reduction in $U_{x,\max}$ can be observed for 0.6 m, 0.8 m, and 1 m diameter stone columns, respectively.

Stone columns are efficient in reducing the lateral outflow of foundation soil under the embankment. With an increase in diameter (D) of the stone column reduction in $U_{x,\max}$ can be observed. Figure 4.14 shows the embankment crest settlement time history plot for the benchmark model and models with different diameters of stone column.

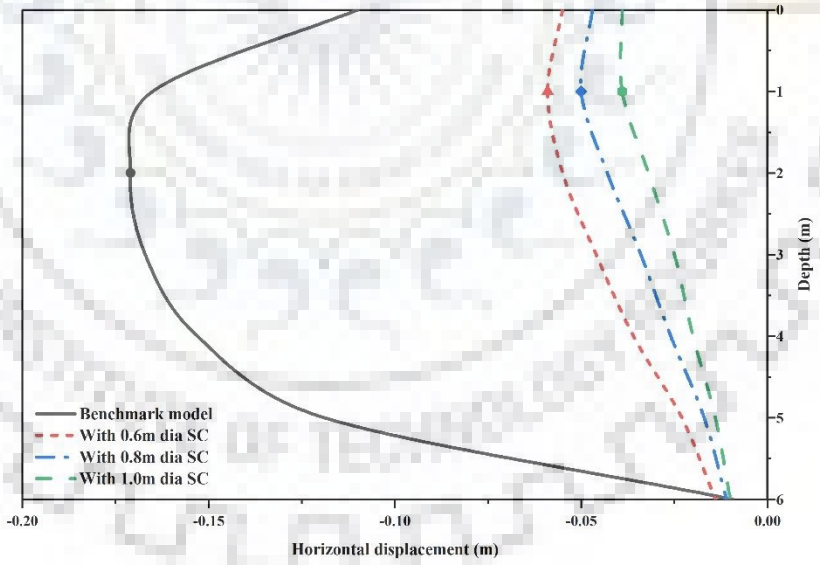

Fig. 4.13 Horizontal outflow deformation (U_x) profile beneath the embankment toe before and after stone column remediation.

At the end of cyclic loading, the crest settlement value was observed to be 0.192 m in the case of the benchmark model. This value has been reduced by 59.8%, 65.52%, and 68.75% for the models with 0.6 m, 0.8 m, and 1 m diameter stone column models. This observation shows a considerable

justification that with the restraining of lateral outflow of embankment foundation soil crest settlement also reduces. With the increase in the diameter, lateral outflow as well as embankment settlement reduce.

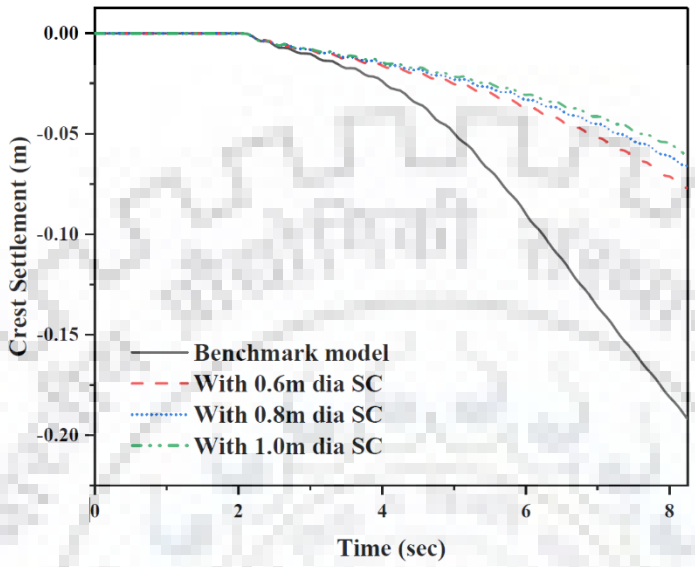

Fig. 4.14 Embankment crest settlement without and with stone column remediation.

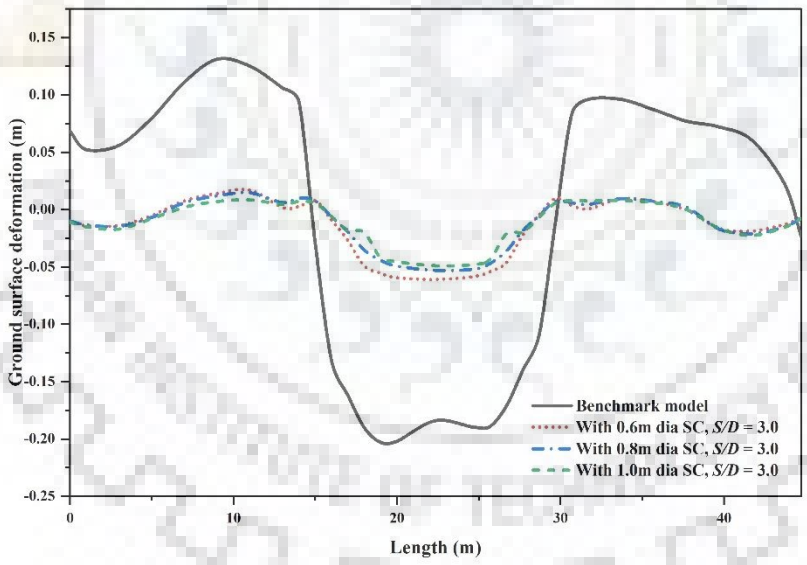

Fig. 4.15 Ground surface deformation profile.

Figure 4.15 shows the profile for the ground surface deformation after the cyclic event. In the case of the benchmark model, considerable heaving has been observed in the free surface region due to the excessive settlement of embankment. The maximum heaving has been noticed at a location 6 m away from the embankment toe. On the other side, heaving occurred 2 m away from the toe. The ground surface deformation also indicated the biasness of the input motion direction. Maximum

heaving can be observed towards the input motion source and the predicted value was approximately 0.131 m. However, the inclusion of stone columns has shown very good improvement in controlling the heaving of the ground surface. Almost 87% heaving has been reduced with the inclusion of 0.6 m diameter stone columns. For 0.8 m and 1 m stone columns, 88.85% and 93.66% reductions in the maximum heaving have been observed, respectively. Moreover, with the inclusion of stone columns below the toe, it can be seen that the central embankment settlement was reduced by 67% using 0.6 m diameter stone columns. The same has been of the order of 71.2% and 73.4% for 0.8 m and 1.0 m diameter stone columns, respectively. Stone column inclusion has improved the deformation behavior of the ground surface and throughout the length of the ground, the surface maintained uniform distribution of deformations. However, with the 0.6 m diameter of stone columns, considerable improvement in embankment responses can be observed. Hence 0.6 m diameter stone columns are focused on in the further study.

4.4.3 Effect of Stone Column Spacing

In this section effect of spacing (S) was taken into consideration by varying S/D ratios as 2, 2.5, and 3. The uniform 0.6 m diameter of the stone column was considered in the parametric study. Variations in $r_{u,\max}$ along the horizontal distance have been compared in Fig. 4.16 for different S/D ratios. The $r_{u,\max}$ below the embankment toe was decreasing with a decrease in the spacing of stone columns. The area enclosed by the stone columns and the nearby surrounding soil was found to be mitigated quite well.

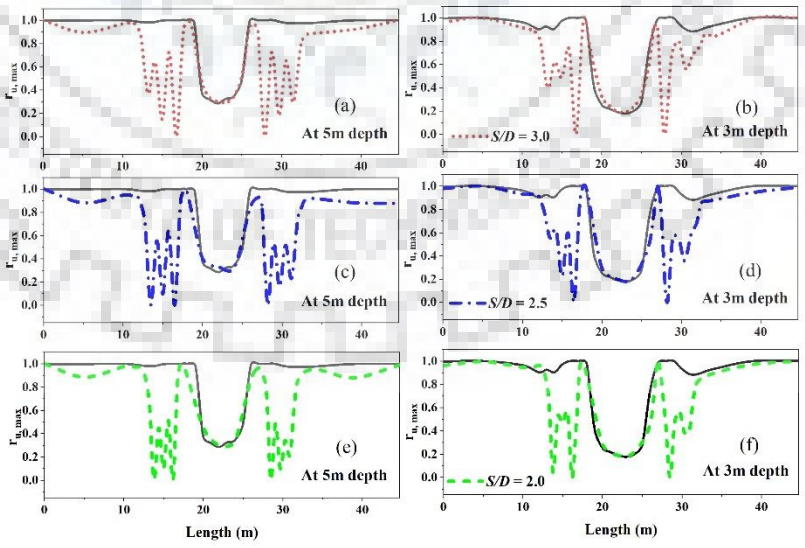

Fig. 4.16 Effect of spacing on $r_{u,\max}$ along embankment profile.

For S/D = 3.0, at 3 m depth the *effective zone* length experiences $r_{u,\max}^{Eff-zone}$ within the range of 0.0 to 0.803, and at 5 m depth, this range was observed to be 0 to 0.728. In the case of S/D = 2.5 at 3 m and 5 m depth, the ranges were observed as 0 to 0.628 and 0 to 0.647, respectively. Lastly, for S/D = 2.0 the ranges of $r_{u,\max}^{Eff-zone}$ at 3 m and 5 m depths are observed as 0 to 0.574 and 0 to 0.512, respectively. Except for the results for S/D = 2.5 for the other two spacings, it can be predicted that the stone columns showed better mitigation with increasing depth. In the case of the benchmark model at 3 m depth below the center of the embankment, the $r_{u,\max}$ value was found to be 0.191. The same has been observed as 0.188, 0.196, and 0.194, for the mitigated model having S/D = 2, 2.5, and 3, respectively. Further, the central region of foundation soil under the embankment was unaffected showing a marginal change in $r_{u,\max}$ values (maximum 2.6%).

Figure 4.17 shows the embankment crest settlement time history after 10 cycles of cyclic loading for various spacing of stone columns under the toe regions along with the benchmark model results. A small marginal difference in the crest settlement has been observed with the variation in spacing for 0.6 m diameter stone column.

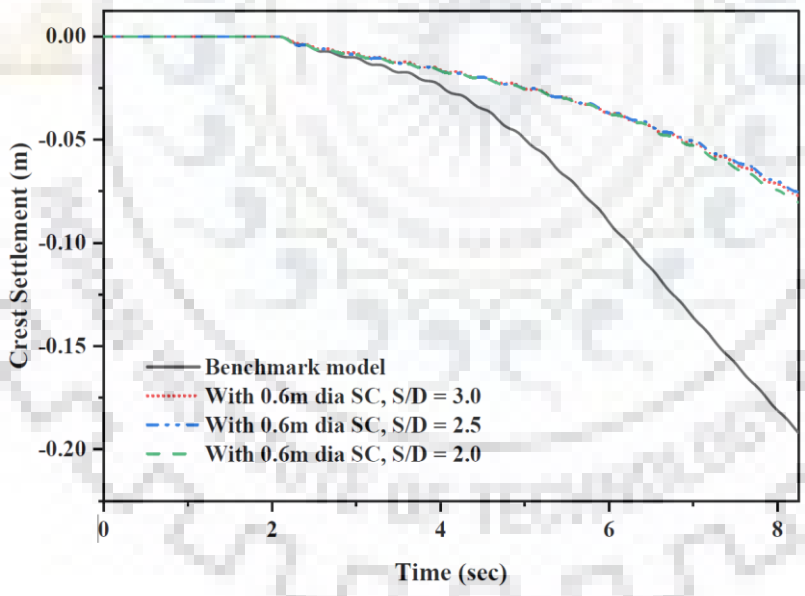

Fig. 4.17 Effect of stone column spacing on crest settlement.

The maximum reduction of 60.77% in crest settlement has been observed for the case of S/D = 2.5. Whereas for S/D = 2.0 and 3.0, reductions in the crest settlement were of the order of 58.19% and 59.83%, respectively. It has been seen that not only the efficiency of reduction of EPP is important for reducing settlement of embankment, but also the effective length of mitigation is important. The

maximum reduction in settlement can only be obtained if mitigation has been done up to the required length of the mitigation zone under the toe of the embankment.

Figure 4.18 shows the time history of the EPP plot for different locations at the mid-depth of the liquefiable layer (S/D = 2.5) for both the benchmark model and the mitigated model. The location P_1 towards the free field shows approximately 13.92% reduction in the maximum EPP value due to the presence of a stone column. However, locations P_2 and P_3 at the middle of stone column spacing show 24.45% and 35.53% reduction in the maximum EPP value by considering the stone column. This indicates that the region between two stone columns has been improved by the stone columns, and mitigation of liquefaction can be achieved. However, the P_4 location shows a marginal reduction of 14.27% in the maximum EPP value.

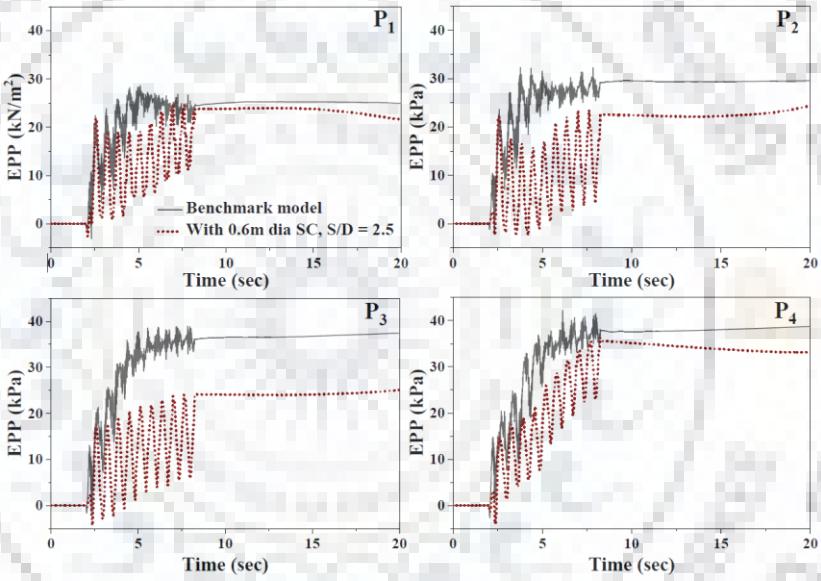

Fig. 4.18 EPP time history at the mid-depth of the liquefiable layer.

Fig. 4.19 Contour of r_u after 10 cycles of loading for (a) benchmark model; (b) model with 0.6 m dia. SC at 2.5D.

However, this study primarily focuses on the region below the embankment toe (*effective zone*), as this location is most critical for the liquefaction-induced settlement of embankments. The contour of r_u after 10 cycles of loading for the benchmark model and the model with 0.6 m diameter stone columns at 2.5*D* spacing has been compared in Fig. 4.19. A clear effect of stone columns in reducing EPP in the area below the embankment toe can be noticed from the contours of r_u. To evaluate the post-liquefaction reconsolidation behavior of the foundation liquefiable soil below the embankment, an additional consolidation stage has been considered for both the benchmark model and the mitigated model. Material properties were kept similar to the dynamic stage only. Contours of r_u after reconsolidation for 41.75 s post-liquefaction are compared in Fig. 4.20 for the benchmark model and the model with 0.6 m diameter stone column. A clear effect is noticed in the values of r_u below the embankment.

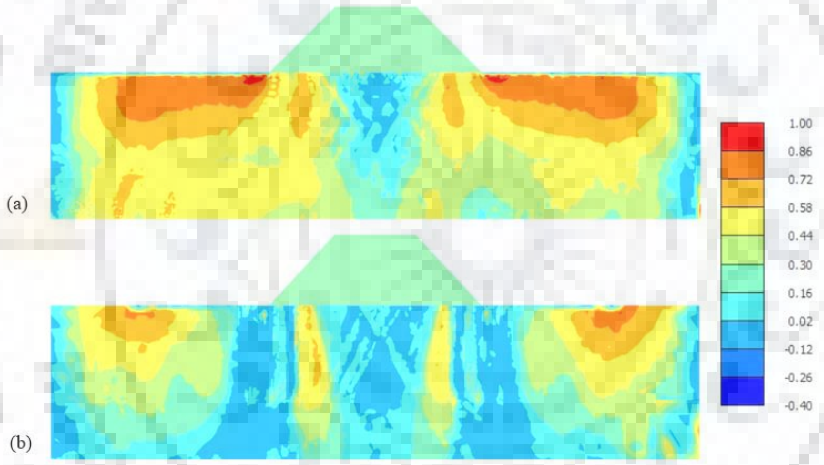

Fig. 4.20 Contour of after consolidation for 41.75 seconds post-liquefaction for (a) benchmark model; (b) model with 0.6m diameter stone column.

Figure 4.21 depicts 41.75 s post-liquefaction reconsolidation EPP time history for locations P_1 to P_4. It can be easily interpreted that the stone column was efficient enough to dissipate the EPP in a short span of time which was built up during the dynamic loading stage. At location P_1 in the case of the benchmark model, the maximum EPP can be observed as 28.61 kN/m^2, whereas with mitigation maximum EPP has been calculated as 24.64 kN/m^2. Almost a 13.87% reduction in the maximum EPP has been noticed in the case of the stone column model. After 41.75 s post cyclic loading reconsolidation, the EPP was found to be 19.80 kN/m^2 which resulted in an almost 30% reduction in EPP in case of the benchmark model. But in the case of the stone column mitigated model EPP

after 41.75 s post cyclic reconsolidation was found to be only 1.71 kN/m^2, which shows an almost 93% reduction in EPP.

Similarly, at location P_2, the maximum EPP of 30.32 kN/m^2 has been observed during the cyclic loading in the benchmark model. But in the case of the mitigated embankment model maximum EPP is estimated as 23.78 kN/m^2. Almost a 21% reduction in EPP can be observed during cyclic loading conditions in the middle of spacing between the stone columns facing towards the free field from the embankment toe. After the reconsolidation of 41.75 s, in the case of the benchmark model 34.8% reduction in EPP can be observed. However, just after 2.5 s of reconsolidation in the case of the mitigated model EPP has been reduced by more than 95%.

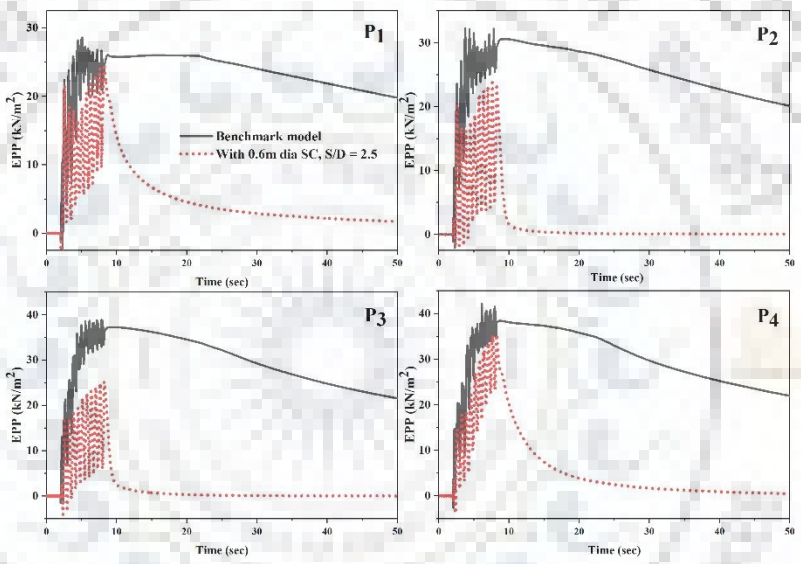

Fig. 4.21 Post-liquefaction EPP dissipation due to consolidation at different locations.

This shows permeability of the stone column has effectively increased the rate of dissipation of the soil placed in between the spacing of two stone columns. Likewise, at the P_3 location, EPP has been reduced by 95% after 5 s of reconsolidation and at location P_4 it took 21.25 s of reconsolidation to reduce the EPP below 95%. This also shows that the dissipation of EPP in the foundation below the embankment slope has been reduced in comparison to the free surface side. However, the central embankment foundation soil showed complete dissipation after a few seconds of consolidation only. The self-weight of the embankment structure worked as a surcharge which has quickly dissipated EPP in the soil just beneath the central portion of the embankment. However, the area beneath the slope after the effective zone has shown some residual EPP. This might be attributed to a lesser surcharge as compared to the central region.

4.4.4 Effect of Cyclic Loading Input

Three different amplitudes of acceleration input motion (0.1*g*, 0.15*g*, and 0.2*g*) have been considered in this study to show the effectiveness of stone columns under various loading conditions. Each loading amplitude has been considered for 10 cycles of harmonic motion with 1.6 Hz frequency. In the case of 0.1*g* amplitude of loading, the region under the embankment experienced $r_{u,\max}$ a value of 0.324. From Fig. 4.22, it can be observed that with increasing loading amplitude, the soil under the embankment experiences increases in the EPP.

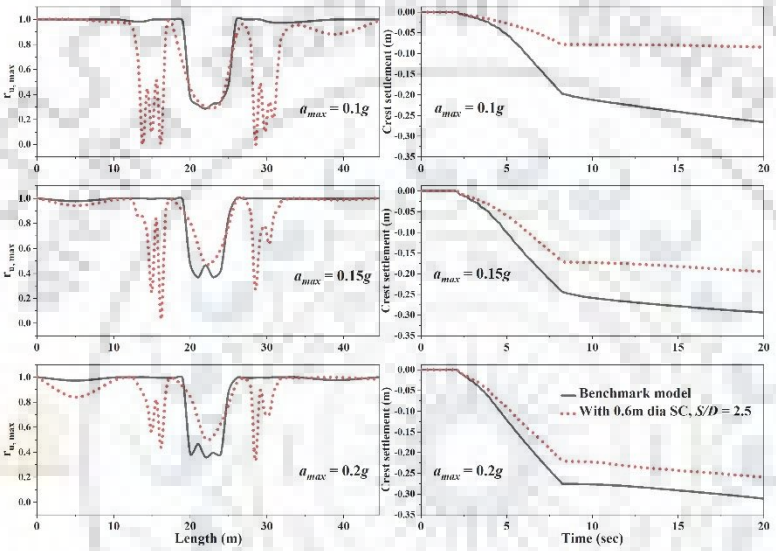

Fig. 4.22 Effect of loading amplitude on the response of foundation soil and embankment.

The $r_{u,\max}$ values increased to 0.369 and 0.396 for 0.15*g* and 0.2*g* amplitude, respectively. Consequently, the *effective zone* region also develops higher EPP with increasing amplitude but has shown certain resistance against full liquefaction. In the case of 0.1*g* amplitude of loading, the *effective zone* experiences $r_{u,\max}^{Eff-zone}$ within the range from 0 to 0.512. However, for 0.15*g* and 0.2*g* amplitude of cyclic loading, the range increased to 0.03 to 0.858 and 0.33 to 0.887, respectively. This shows that the efficiency of mitigating EPP of *effective zone* region decreases with the increase in the amplitude of cyclic loading. However, in all three amplitudes of cyclic loading, it can be observed, that the *effective zone* length of the stone column has never reached the full liquefaction ($r_{u,\max}$ = 1.0).

The increment in $r_{u,\max}^{Eff-zone}$ increases the settlement of the embankment (Fig. 4.22). Concerning the benchmark model, the stone column mitigated embankment model reduced the settlement by 60%, 30%, and 20% for 0.1*g*, 0.15*g*, and 0.2*g* input amplitude acceleration, respectively. However, stone

columns showed good mitigation and prevented $r_{u,\max}$ reaching unity near the toe region. This study also suggests that this configuration of the stone column system may not be adequate for higher amplitude dynamic loading above 0.2*g*. Hence, a detailed study with a higher configuration of mitigation model (a greater number of stone columns) can provide some deeper insights.

4.5 RESPONSE UNDER SEISMIC CONDITIONS

To evaluate the efficiency of the stone columns under real ground conditions, 10 different earthquake input motions have been considered. Figure 4.23 represents the 5% damped acceleration spectra of all the ground motions. Figure 4.24 represents the acceleration time history and Fourier amplitude spectra of the ground motions considered for seismic analysis in the present study. Table 4.6 shows the parameters for important characteristics of the ground motions namely, peak ground acceleration (PGA), time-period, predominant frequency (f_p), and arias intensity (I_a). Responses were obtained for the benchmark model and the stone column mitigated embankment model for all the earthquake ground motions considered in this study.

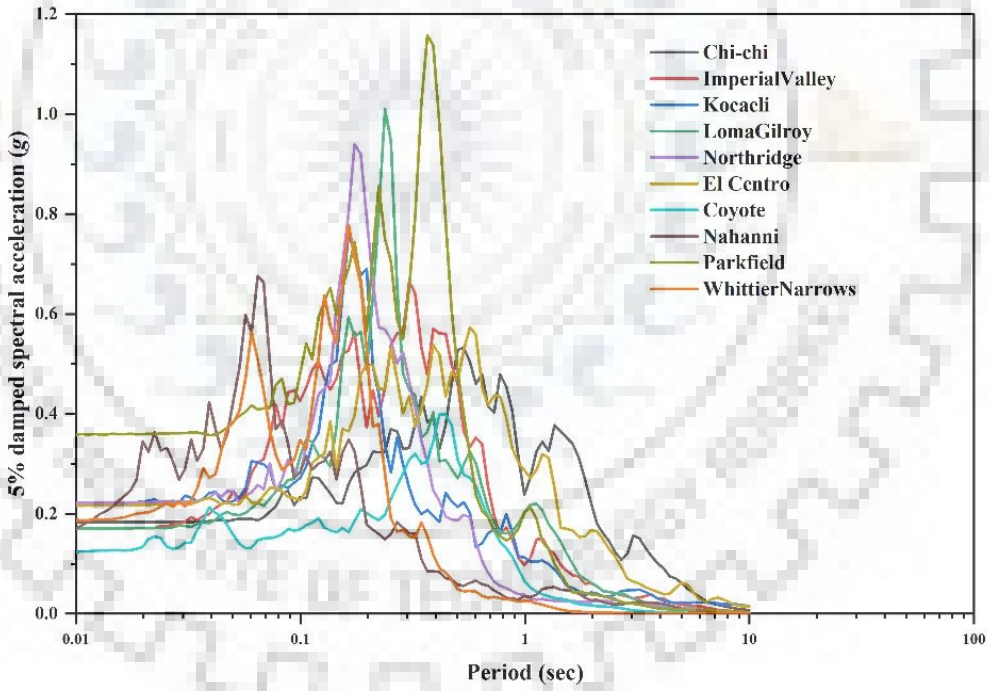

Fig. 4.23 Response spectra plot of input ground motions.

Figure 4.25 shows $r_{u,\max}$ profiles along the length at the mid-depth of the liquefiable layer. Figure 4.26 shows the embankment crest settlement for different earthquake motions. Maximum values of settlement and maximum values of pore pressure coefficient in the *effective zone* enclosed by stone columns $r_{u,\max}^{Eff-zone}$ are reported in Table 4.7. Maximum settlements are predicted in the case of the

Imperial Valley, Chi-chi, and El Centro earthquakes. $r_{u,\max}^{Eff-zone}$ values show a similar trend for these three earthquakes.

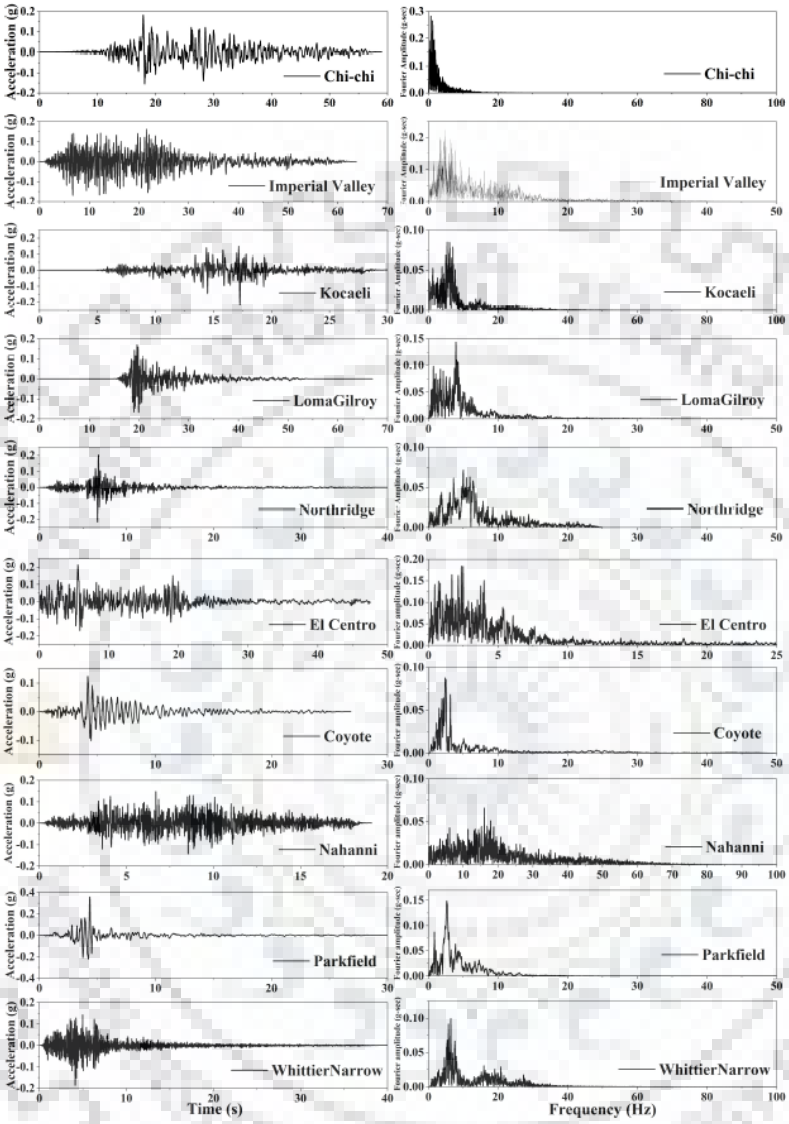

Fig. 4.24 Acceleration time history and Fourier amplitude plot of different earthquake ground motions.

Excess pore pressure (EPP) time history for the Northridge ground motion has been shown in Fig. 4.27 for both the benchmark model and mitigated model at P_1 to P_4 locations. It can be seen that stone columns have improved the vicinity of the embankment toe region and successfully reduced the generation of EPP. At 6.76 s the ground motion approaches the PGA value. Accordingly, in both models, a sharp rise in the EPP value can be observed. However, from this time onwards dissipation

of EPP can be observed in the stone column mitigated model. This indicates that the permeability of stone columns played a vital role in the mitigation of EPP.

Table 4.6 Earthquake ground motions selected for the nonlinear seismic analysis of embankment for the present study.

#	Earthquake	Station (year)	PGA (m/s^2)	T_p (s)	f_p (Hz)	I_a (m/s)
1	Imperial Valley, USA	Aeropuerto, Mexicali (1979)	1.67	0.31	2.36	1.22
2	Loma Gilroy, USA	Gilroy Array #2 (1989)	1.67	0.24	3.94	0.44
3	Chi-chi, Taiwan	CHY092 (1999)	1.77	0.53	0.70	0.96
4	Kocaeli, Turkey	Arcelik (1999)	2.16	0.16	5.36	0.29
5	Northridge, USA	Bell Gardens, Jaboneria (1994)	2.16	0.19	5.01	0.23
6	El Centro, USA	El Centro, Los Angeles (1940)	2.06	0.60	2.49	0.84
7	Coyote, USA	Gilroy Array #1 (1979)	1.22	0.44	2.40	0.12
8	Nahanni, Canada	Nahanni Site #3 (1985)	1.47	0.06	16.06	0.28
9	Parkfield, USA	Cholame - Shandon Array #8 (1966)	3.53	0.37	2.63	0.45
10	WhittierNarrow, USA	Beverly Hills - 14145 Mulhol (1987)	1.86	0.16	6.41	0.26

Table 4.7 Embankment crest settlement details of benchmark model and mitigated embankment model.

#	Ground motion	Embankment Crest Settlement (m)			$r_{u,\max}^{Eff-zone}$
		Benchmark model	Mitigated model	% Reduction	
1	Imperial Valley, USA	0.913	0.604	33.84	0.869
2	Loma Gilroy, USA	0.40	0.267	33.34	0.805
3	Chi-chi, Taiwan	0.662	0.590	10.81	0.881
4	Kocaeli, Turkey	0.286	0.109	61.87	0.798
5	Northridge, USA	0.232	0.036	84.45	0.537
6	El Centro, USA	0.593	0.591	0.30	0.903
7	Coyote, USA	0.192	0.041	78.70	0.467
8	Nahanni, Canada	0.109	0.025	77.52	0.343
9	Parkfield, USA	0.257	0.187	27.49	0.84
10	Whittier Narrow, USA	0.156	0.077	50.48	0.794

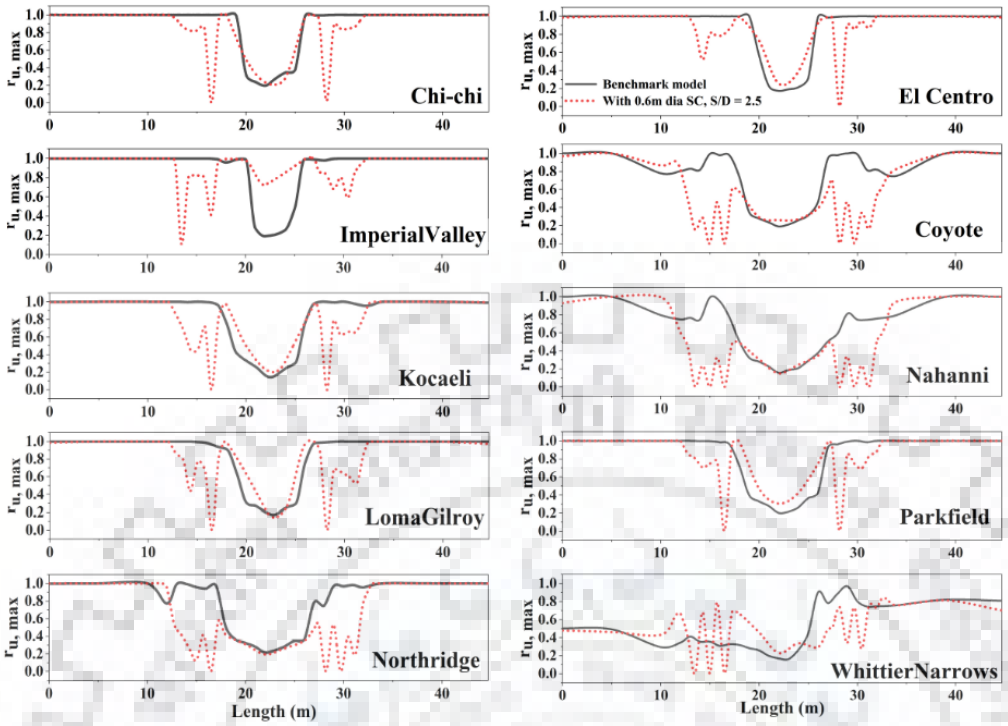

Fig. 4.25 $r_{u,max}$ profile at the mid depth of liquefiable layer for different earthquake motions.

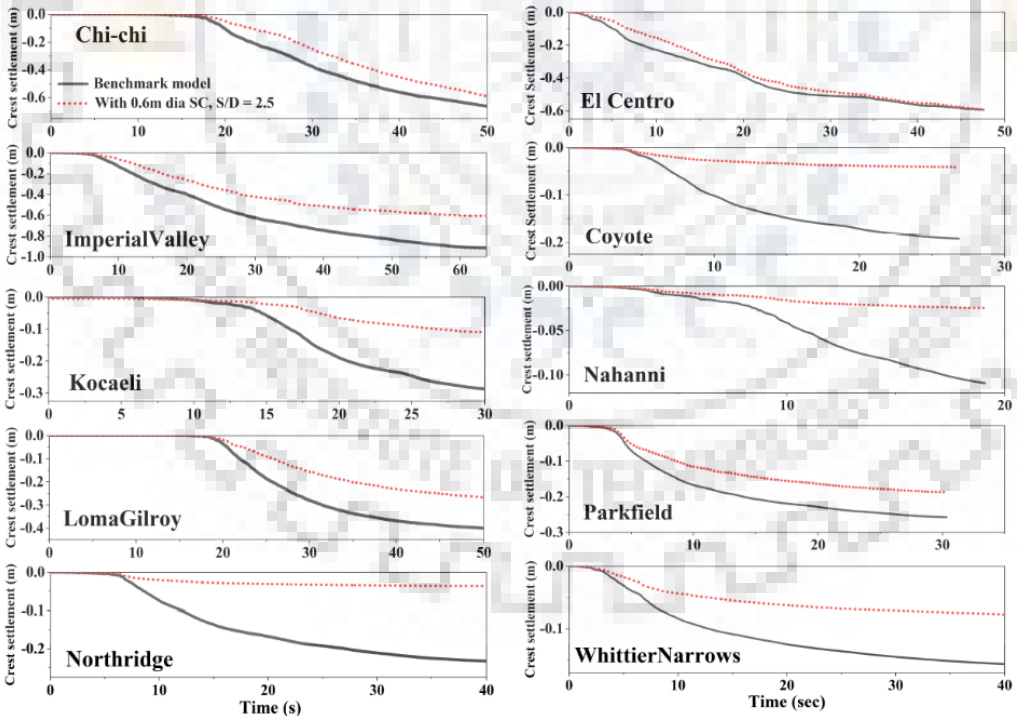

Fig. 4.26 Embankment crest settlement for different earthquake motions.

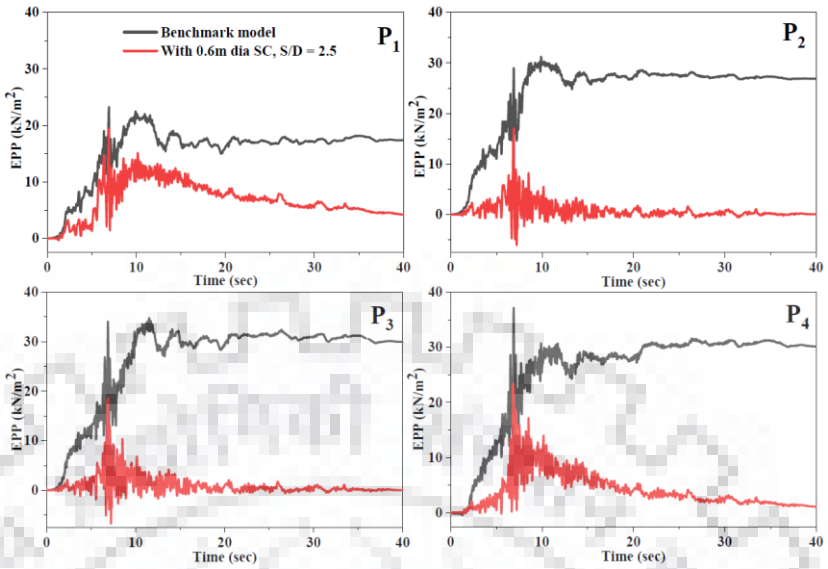

Fig. 4.27 EPP time history at different locations for Northridge earthquake input motion.

Arias Intensity of an input ground motion has been preferred as a most important synthetic parameter which reflects three important major ground motion characteristics namely, the amplitude of the motion, frequency content, and the duration of the motion (Kramer 1996). From past studies, it can be seen that arias intensity (I_a) has been considered an efficient way of representing ground motion intensity measure which can efficiently quantify record-to-record variability of earthquake-induced displacements (Wang 2012; Huang and Wang 2017; Cascone et al. 2021). It can be observed in Fig. 4.28 that for different earthquake input motions the embankment crest settlement increases linearly with the increase in arias intensity (I_a) of the ground motion. A similar trend of response was reported by Sica and Pagano (2009).

Imperial Valley motion containing the maximum value of arias intensity (I_a) resulted in a maximum embankment crest settlement of 0.913 m. Whereas the Coyote ground motion containing the minimum value of arias intensity (I_a) showed an embankment crest settlement of 0.192 m. An exception of result can be observed in the Nahanni ground motion, which has a higher value of arias intensity (I_a) compared to Coyote but caused the least embankment crest settlement. However, the peak frequency value of Nahanni ground motion is too higher than the peak frequency value of Coyote input motion. It is also evident from Fig. 4.25 that, Nahanni input motion resulted in a smaller $r_{u,\max}^{Eff-zone}$ value near the embankment toe in the mitigated model. This might be a potential reason for a lesser embankment settlement compared to the Coyote input motion.

Figure 4.28 shows a reduction in the intercept value of the linear relationship (almost 3.6 times) between embankment crest settlement and arias intensity (I_a) value of earthquakes. Best fits to both plots suggested an intercept difference (settlement) of 0.107 m. However, both the linear relationship of the benchmark model and the mitigated embankment model with the arias Intensity (I_a) have a negligible difference in the slope (almost 6%).

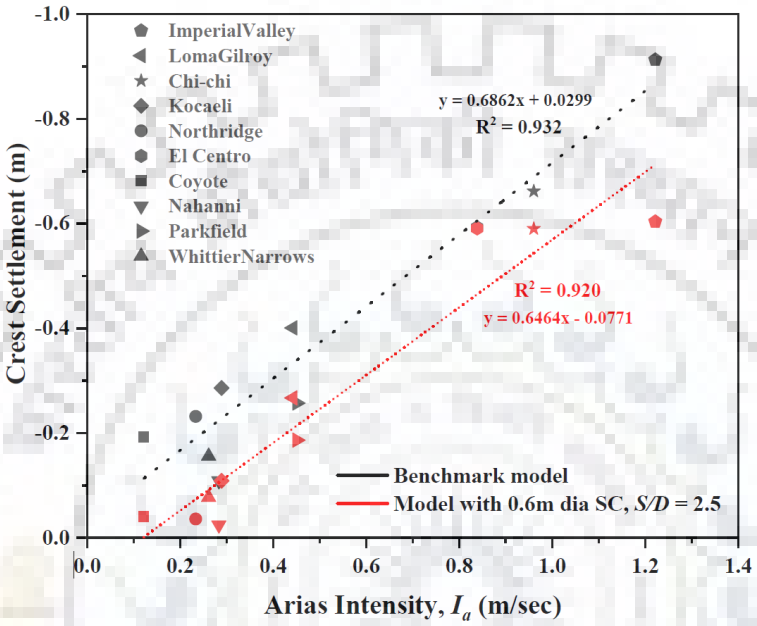

Fig. 4.28 Plot of earthquake-induced embankment crest settlement versus arias intensity (I_a) of the earthquakes.

This shows mitigation using a stone column near the embankment toe is quantitatively efficient enough to reduce the embankment crest settlement. In the case of El Centro ground motion, the mitigation showed the least improvement in the embankment crest settlement. However, a reduction in EPP near the toe can be observed. It can be observed from Table 4.6 that the El Centro ground motion contains the longest time period (T_p) of 0.6 s. This longest time period of motion may have developed temporary plastic mechanisms near the mitigated embankment toe which was activated by transient mobilization of the shear strength. This might have caused excessive settlement in the mitigated embankment model.

4.6 CONCLUDING REMARKS

In the present study, initially, the soil constitutive model UBC3D-PLM has been calibrated for two different soil layers using well-established element and physical test results reported in the past literature. Later, stone column mitigation has been adopted as a mitigation technique and the efficacy of stone column mitigation below the embankment toe was investigated. A thorough parametric

investigation was carried out on varying stone column diameter, spacing, and input motion. Lastly, a seismic investigation of the mitigation model was carried out for 10 different ground motions. Based on the results obtained from this study following conclusions were drawn.

1. The calibrated soil model was able to capture the beneficial effects of shear-induced dilation of the soil resting below the central part of the embankment, which never attains full liquefaction (r_u = 1) and contributes stability to the embankment. However, the toe regions of the embankment liquefy which is mainly responsible for the excessive settlement of the embankment due to the lateral outflow of soil beneath the embankment.
2. The optimization study for the optimum number of stone columns below the embankment toe concluded that three stone columns have been found effective in reducing embankment crest settlement by 60%. Stone columns below the embankment toe have shown efficacy in reducing the EPP near the toe region. A clear effect of stone columns can be seen from the results reported in the present study.
3. For a constant *S*/*D* ratio, smaller diameter stone columns were more effective in reducing the EPP below the embankment toe due to shorter drainage path. This is evident from the reduction in the values of $r_{u,\max}^{Eff-zone}$ with decrease in the diameter of the stone column. However, larger diameter stone columns are effective in reducing the embankment settlement as compared to smaller diameter stone columns.
4. Variation of spacing showed a marginal difference in the embankment settlement. In the case of *S*/*D* = 2.5, for 0.6 m diameter stone columns, maximum reduction of embankment crest settlement of approximately 61% was achieved. However, smaller spacings mitigated the EPP of the zone encased by stone columns under the embankment toe. For *S*/*D* = 2.0, the foundation soil beneath the embankment toe experiences $r_{u,\max}^{Eff-zone}$ 0.574 and 0.512 at 3 m and 5 m depth, respectively.
5. In reducing the maximum outflow horizontal deformation $U_{x,\max}$, 1 m diameter stone columns have shown the maximum effectiveness (77.20% reduction). However, 0.6 m and 0.8 m diameter stone columns have been reduced $U_{x,\max}$ by 65.50% and 70.76%, respectively. Accordingly, the maximum heaving of the ground surface was also reduced effectively by the inclusion of stone columns.
6. The time history plot of EPP for the Northridge earthquake has revealed that after $a_{\max}$ onwards, the drainage effect of stone columns can be seen in faster dissipation. This shows the effect of

permeability of stone columns, which played a key role in dissipating the excess pore pressure (EPP).

7. The embankment settlement shows a linearly increasing relationship with the arias Intensity I_a. From the best fit plot of untreated and treated embankment model, a reduction of 0.107 m intercept in embankment crest settlement was observed which shows stone columns are efficient under real ground conditions. However, for the higher arias Intensity ground motions, the optimized stone column number was not sufficient. A further study exploring all the possible configurations can reveal the optimum configuration of stone columns.
8. The results presented in this study are entirely based on existing experimental data from the past literature along with certain assumptions. Further laboratory studies are warranted to capture the effect of EPP near the toe region and the consequent effect on the embankment crest settlement, for improving the numerical predictions for both types of models.

After exploring a detailed study on stone column mitigation, it is planned to explore effectiveness of other mitigation measures. The detailed study has been presented in next Chapter.

CHAPTER 5

EVALUATION OF A HYBRID MITIGATION STRATEGY

5.1 INTRODUCTION

Due to the rapid urbanization, it has become very common for field engineers to encounter liquefiable soil deposits. However, vulnerability study of a city can give vital information regarding the expected liquefiable zones in a city. Hence, it becomes very crucial to design an effective foundation mitigation for important geotechnical structures situated in an expected liquefaction zone. Past studies have shown catastrophic damage to important geotechnical structures due to the liquefaction of underlying foundation soil. Along with previous earthquakes, river dike foundations were also reported to have liquefied during the El Centro earthquake in 1940 (Seed 1968) and the Nipponkai-Chubu earthquake in 1983 (Tani 1991).

Total settlement of any structure under the dynamic loading can be described using two phases as co-shaking settlement and post-shaking settlement (Dobry and Liu 1992; Kokusho 1999). The co-shaking settlement is dominated by the shear induced settlement and the post-shaking settlement found to be affected by change is soil density, volumetric strain and permeability of soil (Ishihara and Yoshimine 1992; Liu and Dobry 1997). From the centrifuge study, Adalier (1996) emphasized how an earth embankment resting on the liquefiable soil behaved and demonstrated various mitigating strategies (dense sand columns, gravel berms alongside slopes, vertical sheet piles right below the toe) to reduce the liquefaction-induced embankment settlement. Similar mitigation strategies employing physical model tests have been described by Okamura and Matsuo (2002). Koga and Matsuo (1990) also conducted a series of experiments in 1*g* shake table and centrifuge shaking. Study revealed that the densification of foundation soil near the embankment toe effectively reduces the settlement. In a series of 1*g* shaking table tests, Takeuchi et al. (1991) examined the deformation mechanisms of dykes built on loose saturated sand deposits and assessed the efficacy of compaction as a corrective measure. According to past test results, there might be an ideal depth of treatment beneath an earth dam, beyond which the reduction of earthquake induced deformations is only marginally effective (Adalier and Sharp 2004). Studies showed that rather of using a safety factor against liquefaction, remedial measures should be based on displacement criteria. However, determining the appropriate size and distribution of such zones can be challenging in certain situations.

Limited studies have focused on the impact of various ground motions. Most of them have been restricted to simple cyclic loading conditions due to difficulty in simulation of real ground motions in physical models. In such case, the numerical analysis remains the only possible method for forecasting how such significant structures will behave under earthquake loading.

One of the prime approaches for controlling liquefaction is the installation of gravel drain piles (Seed and Booker 1977; Baez and Martin 1993; Adalier et al. 2003). Experimental investigations in field and laboratory have verified the competence of gravel drains against small to moderate magnitude earthquakes (Baez and Martin 1993; Adalier et al. 2003; Brennan and Madabhushi 2006). But this may substantially increase EPP dissipation rate after the liquefaction. This can badly affect the post-liquefaction settlement of the foundation. Previous Chapter 4 summarized that an arrangement of three numbers of 0.6 m diameter stone columns with 2*D* spacing are efficient enough to reduce the EPP and settlement for lower to moderate earthquake loading. However, a higher configuration of stone columns can be beneficial for higher-intensity ground motions. Few studies have explored hybrid mitigation strategies against the liquefaction-induced effects on shallow foundations. Kumar et al. (2019) suggested a hybrid foundation in a centrifuge testing facility employing a combination of the gravel drainage system and friction piles under the footing. The hybrid foundation has effectively reduced the settlement of shallow foundations brought on by liquefaction during strong ground motion. Qin et al. (2021) carried out a study on a 1*g* shake table testing program for evaluating a new, economical countermeasure method for existing and future road embankments on a liquefiable foundation soil. The hybrid pile-stone column foundation was effective for maintaining the overall safety of embankment. Very limited study has been reported till now, which shows a comparative analysis between different mitigation methods for an embankment structure resting on liquefiable deposit for a wide range of dynamic loading condition. The effectiveness of three alternative mitigation techniques has been assessed in the current study under seismic loading scenarios. Densification of the area beneath the embankment toe, mitigation using stone columns, and a hybrid foundation utilizing both stone columns and piles have been investigated for their effectiveness against liquefaction. These remediation techniques were chosen after taking into account: (1) their suitability as a retrofitting option for existing earth embankments; (2) their affordability and construction efficiency; and (3) their dependability and anticipated efficacy. Liquefaction behaviour of sandy soil was modelled using effective stress based elasto-plastic model UBC3D-PLM followed by a proper calibration methodology.

5.2 NUMERICAL MODEL DEVELOPMENT SCHEME

Three different mitigation techniques have been introduced in the current study as shown in Fig. 5.1. Model 1 represents the benchmark model which provides valuable understanding about the behaviour of earth embankment resting on a liquefiable soil deposit having a dense sand layer at the bottom. In Model 2, the areas beneath the toe of embankment have been provided densification as a mitigation approach. In case of Model 3, the area beneath the toe has been provided with a mitigation using stone columns. Finally, a hybrid pile-stone column mitigation under the toe has been proposed in Model 4.

Table 5.1 Properties of different sands.

Properties	**Nevada 120 sand**	**Fraser River sand**	**Toyoura sand**	**Silica sand no. 3**
Relative Density (R_D)	40%	80%	50%	30%
Specific Gravity	2.67	2.71	2.65	2.63
Dry density (γ_{dry})	15.08 kN/m^3	16.73 kN/m^3	14.52 kN/m^3	13.50 kN/m^3
Permeability (k)	6.6×10^{-5} m/s	5.5×10^{-6} m/s*	2×10^{-4} m/s	6.6×10^{-3} m/s
e_{max}	0.887	0.94	0.973	1.009
e_{min}	0.511	0.62	0.609	0.697

* in absence of available data this value has been assumed.

The benchmark model in Fig. 5.1a represents an embankment resting on a liquefiable soil layer (Nevada 120 sand) followed by a dense sand medium (Fraser River sand). The material properties of different sands are reported in Table 5.1.

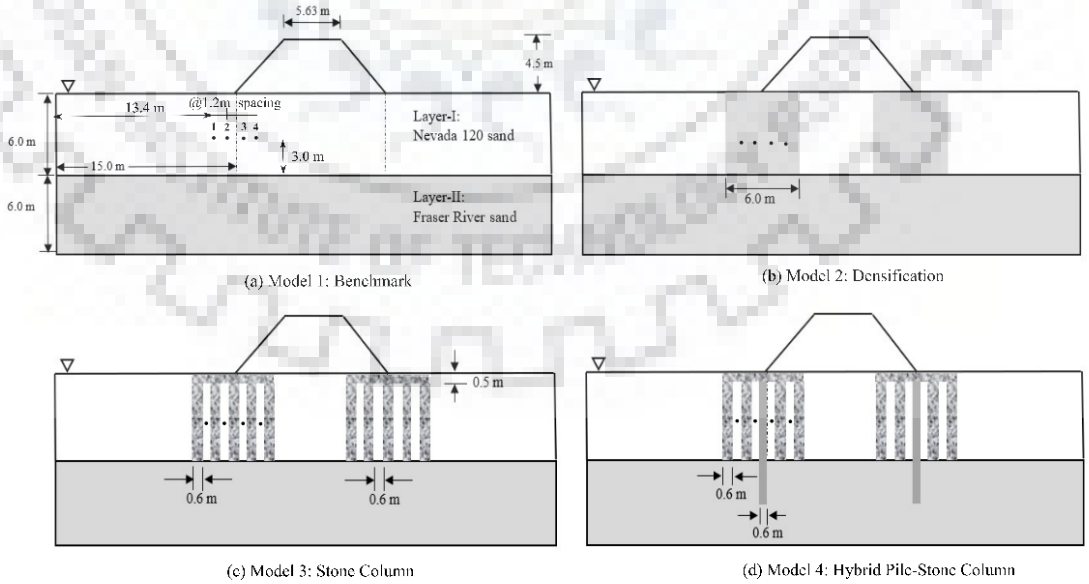

N.B: In Model 2-4 embankment and soil layer properties and dimensions are kept similar to Model 1.

Fig. 5.1 Different model configurations considered in the present study.

The embankment material has been modelled as Mohr-Coulomb model with material properties reported by Bhatnagar et al. (2016): modulus of elasticity E = 20 MPa, Poisson's ratio μ = 0.3, cohesion c = 22 kPa, angle of friction ϕ = 31°, permeability $k = 6.94\times10^{-6}$ m/s, dry unit weight γ_{dry} = 19 kN/m^3. In case of Model 2 (Fig. 5.1b), the width of the densification area considered to be 6.0 m (Adalier 1996; Okamura and Matsuo 2002). The embankment model dimensions are identical to the study conducted by Adalier et al. (1998). Hence, a densification width of 6.0 m is only considered on both sides of the embankment toe. In Model 3 (Fig. 5.1c), 5 numbers of the stone column have been provided beneath the embankment toe area as stone column mitigation based on the observations of previous Chapter. It was observed that 0.6 m diameter (D) stone columns with 2D spacing are efficient enough to reduce both the EPP beneath the toe region and the settlement of the embankment. Hence, a similar configuration with a larger number of stone columns has been considered in the present study. Model 4 consists of a pile exactly below toe with 2 stone columns on either side (Fig. 5.1d). The 0.6 m diameter concrete piles are considered to be 10 m in length with elastic properties (E = 30 GPa, μ = 0.2). Though the densification method is a conventional liquefaction-induced damage mitigation method for embankment structures, it does not provide an economical solution to an effective mitigation approach in every scenario. However, from the literature it can be seen that, the stone column mitigation provides very much satisfactory result against low to moderate magnitude earthquakes. In case of higher magnitude earthquake, stone columns found to be exceeding the gravel drainage system. Moreover, due to the presence of gravel drains, the large rate of EPP dissipation after the liquefaction may adversely increase the post-liquefaction settlement (Kumar et al. 2019). With keeping this viewpoint in consideration, a hybrid mitigation has been introduced in this study considering a pile-stone column combined mitigation method. However, the location and width of mitigation is based on the observations from past studies (Adalier et al. 1998; Okamura and Matsuo 2002) and the judgment depending on the overall performance of embankment under dynamic loading.

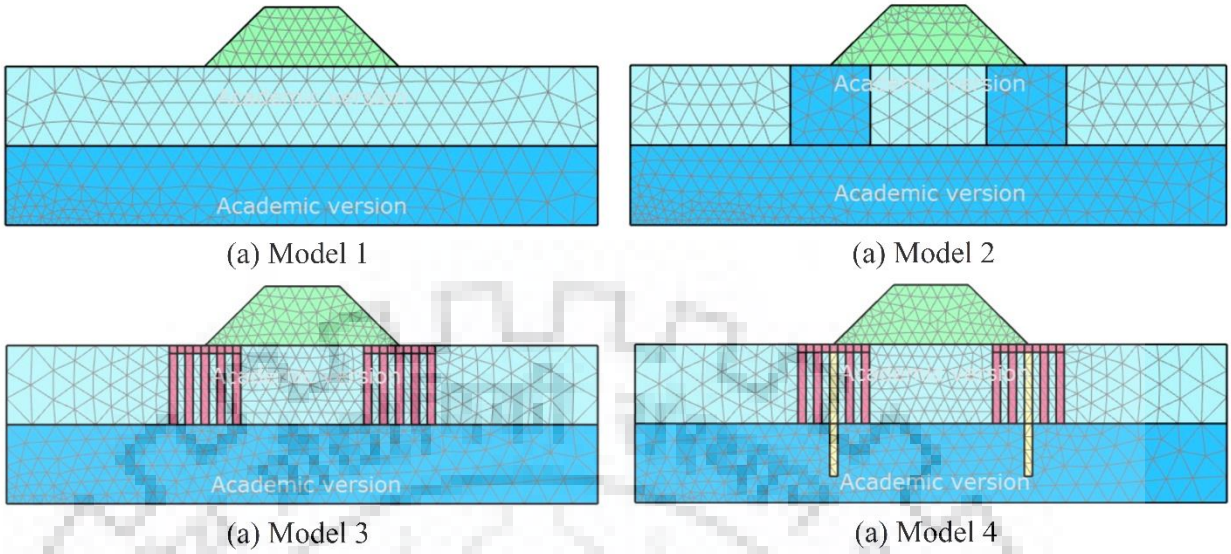

Fig. 5.2 Finite element mesh of different models.

The stone columns and the pile has been modeled in structure mode in PLAXIS 2D. For plane strain idealization equivalent plane strip analytical approach has been used. Model 3 and 4 represent stone columns and piles in 2D plane strain condition as equivalent strip. Jellali et al. (2005) suggested yield design homogenization approach to compute equivalent strength parameters for soils reinforced with stone columns. Kumar et al. (2020) assumed plane strip approach to evaluate equivalent permeability and strength parameters. For the plane strain idealization, these structural elements have been modeled considering an analytical approach, by evaluating different equivalent input parameters. Input parameters such as, modulus of elasticity of pile, permeability and the bulk modulus of stone columns have been computed using equivalent plane strip approach. Equivalent permeability and bulk modulus are calculated using Eq. 4.2 and 4.3. Finite element meshes of four models have been shown in Fig. 5.2.

However, as the pile material is considered to be linear elastic, hence, the equivalent modulus of elasticity can be found out using Eq. 5.1 (Kumar et al. 2020).

$$E_{equivalent} = \left[E_{soil}\left(\frac{S\,D^3}{12} - \frac{\pi\,D^4}{64} \right) + E_{pile}\left(\frac{\pi\,D^4}{64} \right) \right] \Big/ \frac{S\,D^3}{12} \tag{5.1}$$

These approximations are exact for linear elastic behaviour. In the yielded zone the assumption of constant soil modulus and permeability is approximate. However, variation with time is not possible in the program.

5.3 CALIBRATION OF MODEL PARAMETERS

An effective stress elasto-plastic model, UBC3D-PLM can simulate the liquefaction of sandy soil when subjected to dynamic loading conditions. In the present study two different layers of sand have been chosen (Fig. 5.1). The relative density (R_D) of the upper sand layer (layer 1) has been considered as 40%. The lower sand layer (layer 2) has been set as 80% R_D. For layer 1 and layer 2 sand deposits, the properties of Nevada 120 sand and Fraser River sand (Table 5.1) are used, respectively.

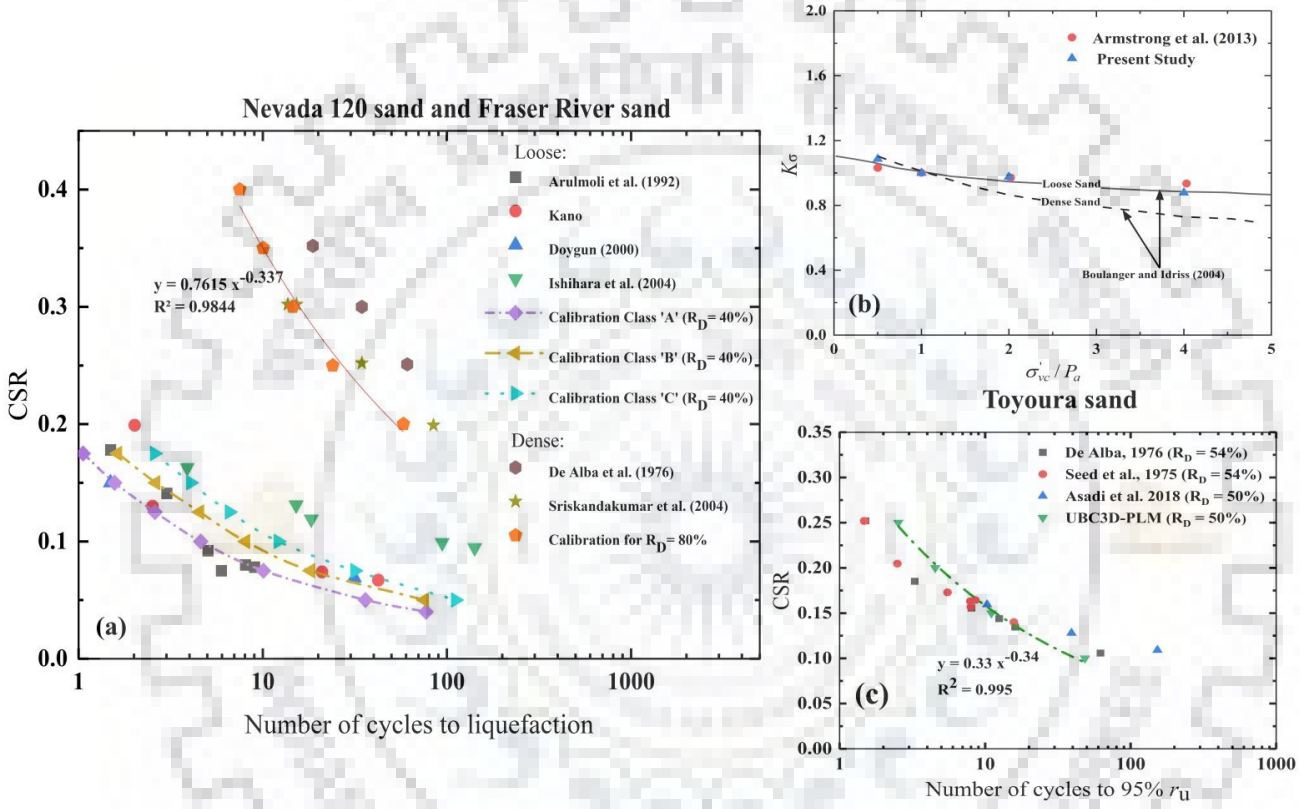

Fig. 5.3 Calibration of cyclic behaviour of UBC3D-PLM model.

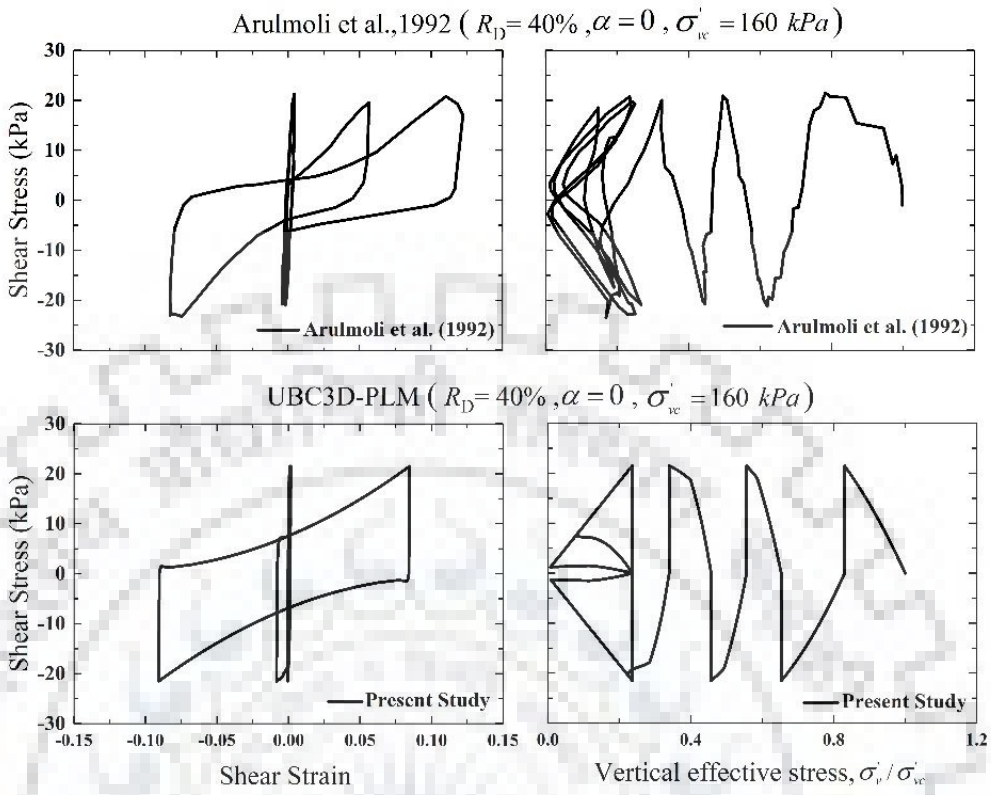

Fig. 5.4 Undrained cyclic direct simple shear test of loose Nevada sand (R_D = 40%) measured by Arulmoli et al. (1992) and predictions using UBC3D-PLM.

In order to calibrate the UBC3D-PLM model for cyclic response, a single element under simple shear stress was used to conduct a number of assessments using various model parameters. In accordance with the limitations set forth by the data, the parameters were changed until a reasonable match was made for the liquefaction triggering and the confinement effects (Figs. 5.3-a and 5.3-b). The laboratory and simulation data are based on number of cycles to r_u = 95% for loose sand and 1.5% shear strain for dense sand condition (Armstrong et al. 2013).

An example comparison of cyclic element response of UBC3D-PLM using the properties given in Table 5.2 (Class 'B' calibration) and the laboratory test results from Arulmoli et al. (1992) are shown in Fig. 5.4 for loose Nevada 120 sand. Comparison shows how the UBC3D-PLM model can simulate a realistic development of pore water pressure and accumulation of shear strain comparable to that reported in the laboratory testing. To assess the efficacy of numerical model in the simulation of different mitigation measures, the centrifuge study by Kumar et al. (2019) has been devised. This centrifuge study examines several different aspects of a hybrid foundation system to reduce the effects of liquefaction on shallow foundations.

Table 5.2 Calibrated UBC3D-PLM model parameters.

Parameters	Nevada 120 Sand*	Fraser River sand	Stone column	Toyoura Sand	Silica sand no. 3
R_D	40%	80%	-	50%	30%
γ_{dry} (kN/m^3)	15.08	16.73	18.0	14.52	13.50
$e_{initial}$	0.736	0.5	0.45	0.791	0.9154
k (m/s)	6.6×10^{-5}	5.5×10^{-6}	5.24×10^{-2} [b]	2×10^{-4}	3.46×10^{-3} [b]
ϕ_p	33.65^0	38.9^0	48.10^0	34.15^0	37^0
ϕ_{cv}	33^o	33^o	40^0	33^0	33^0
K_B^e	566.6	937.6	744.2[b]	685.2	617.7[b]
K_G^e	809.4	1339.5	1063.14	978.8	882.4
K_G^p	350	3597.1	4466.33	700	2500
m_e	0.5	0.5	0.5	0.5	0.5
n_e	0.5	0.5	0.5	0.5	0.5
n_p	0.4	0.4	0.4	0.4	0.4
R_f	0.83	0.66	0.64	0.763	0.852
fac_{hard}	0.45	0.45	0.65	0.45	0.45
fac_{post}	0.1	0.1	0.1	0.1	0.1
Corrected SPT blow count [$(N_1)_{60}$]	6.5[a]	29.7	37[a]	11.5[c]	5.5[c]

* based on Class 'B' calibration

[a] based on Bhatnagar et al. (2016)

[b] for (spacing/diameter) ratio = 2.0, k and K_B^e values are evaluated using Eqs. (4.2) and (4.3).

[c] Petalas and Galavi (2013)

The effectiveness of a hybrid foundation is examined using a friction pile and gravel drainage system test model. The model is framed by a flexible laminar container with inner dimensions of 600×250×438 mm (model scale) in length, width, and height, respectively at the Tokyo Institute of Technology. At the Tokyo Tech Mark III centrifuge facility, which has a radius of 2.45 m and a centrifugal acceleration of 40*g*, dynamic centrifuge tests are conducted. The model ground was prepared using Toyoura sand (R_D = 50%). Silica sand no. 3 (R_D = 30%) was used to model the gravel drainage of 0.6 m diameter. Material properties for Toyoura sand, Silica sand no. 3 are reported in Table 5.1. SUS304 material based frictional piles have been used in the experiment. The centrifuge experiments represent a prototype saturated soil deposit with a depth of 10 m and a water table that

was 1.8 m below the surface. The Buffer Tank and Flare Stack, temporary structures that place average bearing pressures of 51.2 kPa and 71.2 kPa, respectively, at 0.8 m below the surface of the model ground in the prototype scale, are used to assess the viability and effectiveness of the hybrid foundation. Figure 5.5 shows the diagram of the typical test setup of the dynamic centrifuge test (Kumar et al. 2019) along with the Tokachi-Oki earthquake ground motion observed at Hachinohe Port in 1968 (NS component) used as base motion.

In the numerical modeling of the dynamic centrifuge model, the Buffer Tank and Flare Stack has been considered as surcharge at the footing level. The equivalent properties of stone column are provided in Table 5.2. Figure 5.3(c) shows the calibration of CSR vs number of cycles to liquefaction plot for Toyoura sand (R_D = 50%). Figure 5.6 shows the comparison of EPP time histories at different locations. Fair comparisons have been observed at locations 3 to 6. Figure 5.7 shows the contour diagram of $r_{u,\,max}$ for the simulation of centrifuge study conducted by Kumar et al. 2019.

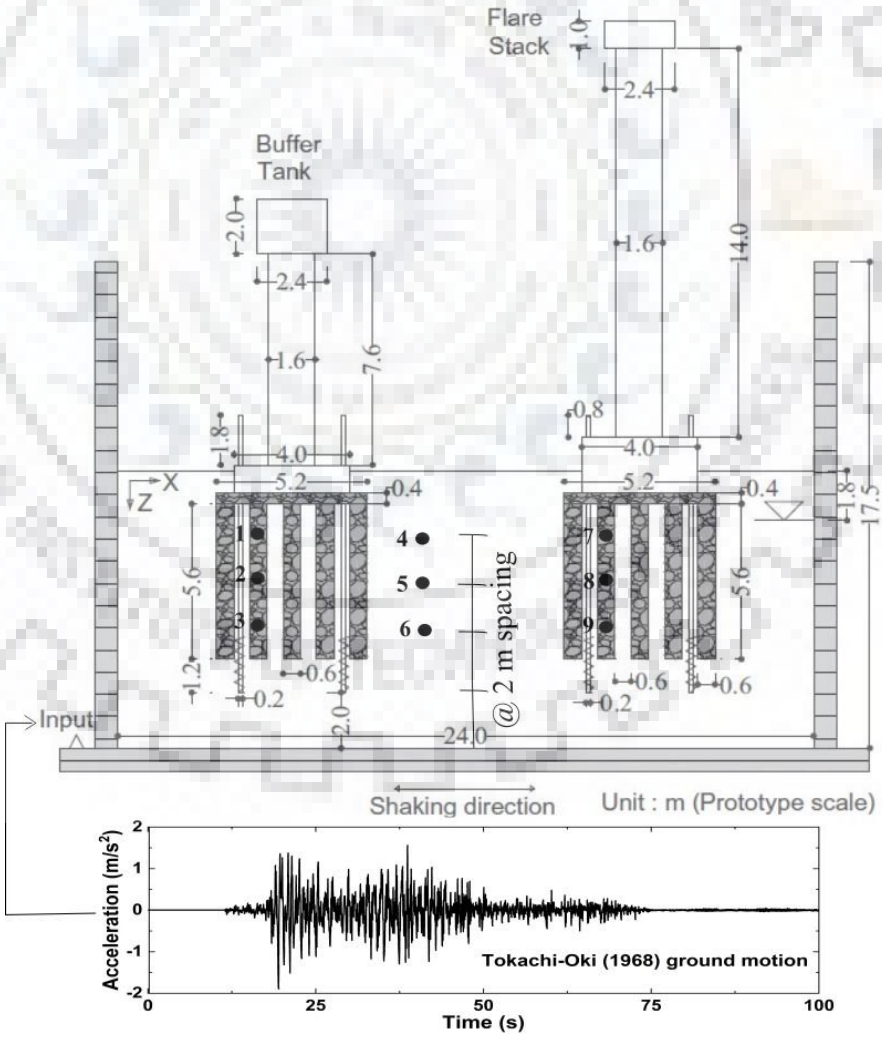

Fig. 5.5 Hybrid foundation system used in the centrifuge study (after Kumar et al. 2019).

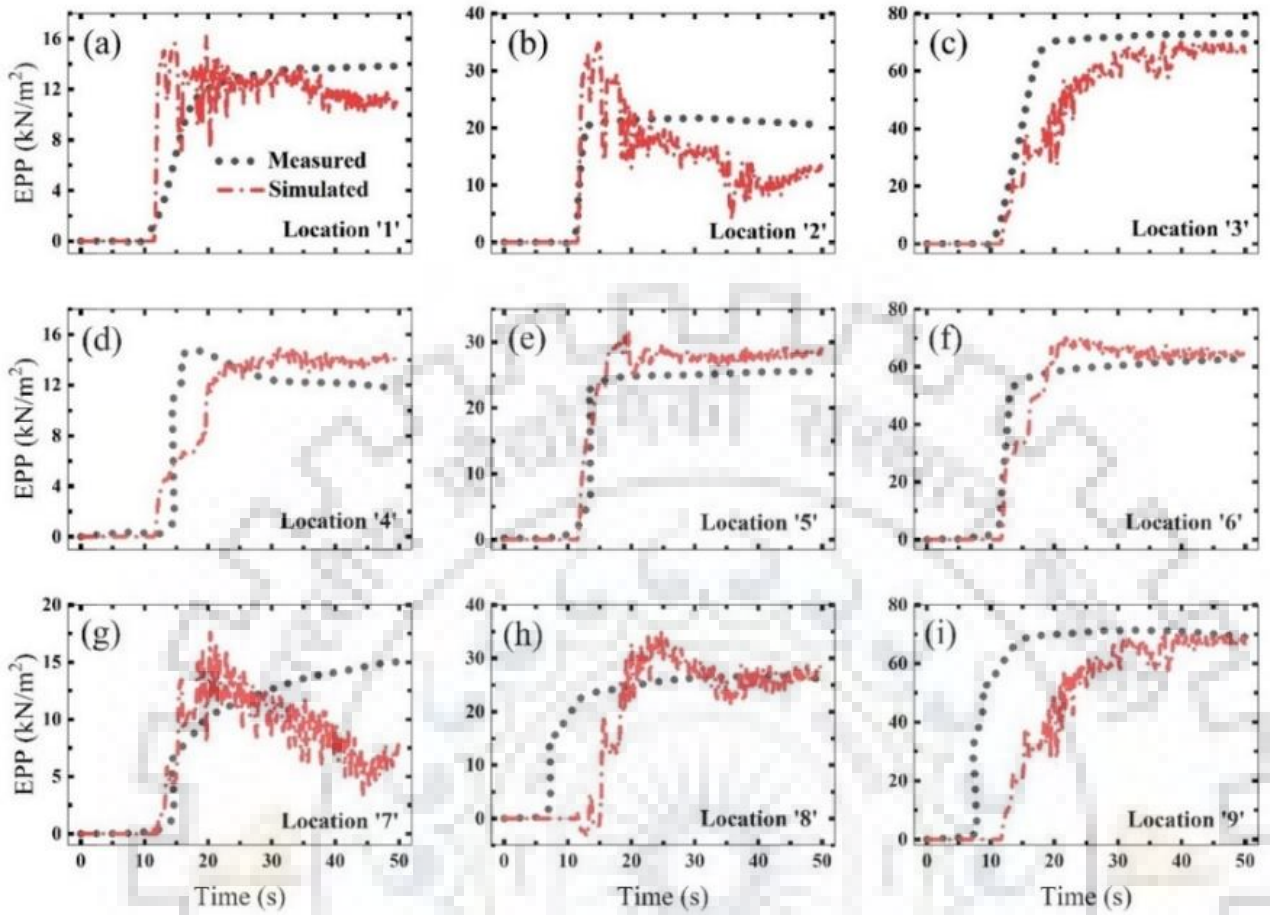

Fig. 5.6 EPP time histories at different locations for Tokachi-Oki (1968) acceleration time history.

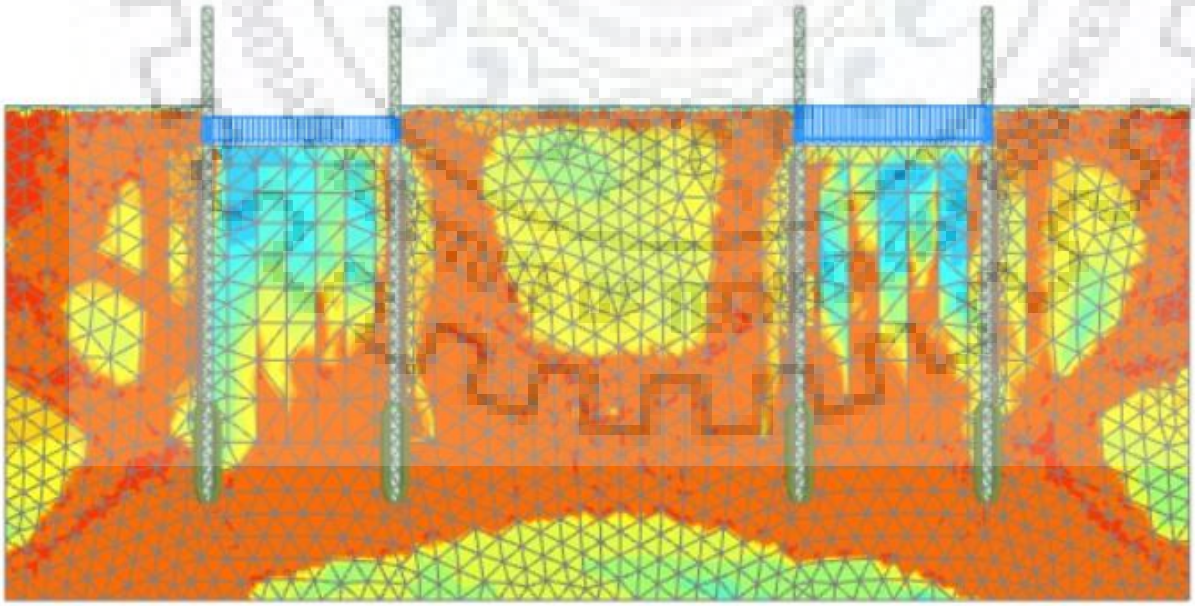

Fig. 5.7 $r_{u,\,max}$ contour of simulation of centrifuge study by Kumar et al. (2019).

5.4 ANALYSIS UNDER DIFFERENT SEISMIC LOADING CONDITIONS

Effect of nature of earthquake ground motions on the embankment settlement has been evaluated for 4 different models considered in the present study. The nature of the earthquake is characterized by the peak ground acceleration (PGA), Arias Intensity (I_a), Moment Magnitude (M_w) and Predominant Frequency (f_p). A total of 25 earthquake ground motion records have been considered in order to study the behaviour of ground motions on the embankment response and how different mitigation performs in order to reduce the embankment crest settlement. All the ground motion records have been obtained from PEER ground motion database and the details of the ground motions are presented in Table 5.3.

Time history analyses of the four models have been carried out for the above mentioned 25 ground motions. Categorically the embankment crest settlement values have been reported for all the four models (Table 5.3). Figure 5.8 shows the variation of embankment crest settlement with the predominant frequency of 25 ground motions. It can be observed that only at smaller frequency ground motions, larger embankment crest settlement occurred. The maximum settlement has been observed during Imperial Valley (1979) ground motion (0.9295 m for benchmark model 1), which has predominant frequency (f_p) of 2.36 Hz. However, it can be inferred that, not only f_p but other important parameters are also associated with a ground motion.

Figure 5.9 shows the variation of equivalent dynamic shear stress along the depth of the liquefiable soil deposit below the embankment toe of Model 1 and Model 2. Since the most significant ground motion factors are amplitude, frequency content, or duration, a parameter that reflects more than one of the aforementioned parameters is particularly useful to understand the nature of the earthquake.

As the most crucial synthetic parameter, Arias intensity I_a of a ground motion has been chosen. It integrates three major crucial ground motion characteristics, amplitude, frequency content, and duration (Kramer 1996). Its value is independent of the technique used to define the duration of strong motion because it is produced by integration over the total time rather than the duration of the strong motion. I_a is closely related to the rms acceleration (Arias 1970) and can be defined as

$$I_a = \frac{\pi}{2g}\int_0^{\infty}\left[a(t)\right]^2 dt \tag{5.2}$$

Table 5.3 Details of selected Earthquake ground motions and predicted Embankment crest settlement of different models.

#	Earthquake	Station (year)	PGA (m/s^2)	I_a (m/s)	M_w	f_p (Hz)	Crest Settlement (m) for Model			
							1	2	3	4
1	Imperial Valley, USA	Aeropuerto, Mexicali (1979)	1.67	1.22	6.53	2.36	0.9295	0.6948	0.7160	0.6020
2	Loma Gilroy, USA	Gilroy Array #2 (1989)	1.67	0.44	5.2	3.94	0.4286	0.2606	0.2209	0.2140
3	Chi-chi, Taiwan	CHY092 (1999)	1.77	0.96	7.62	0.70	0.6777	0.6550	0.5749	0.5057
4	Kocaeli, Turkey	Arcelik (1999)	2.16	0.29	7.51	5.36	0.3016	0.1455	0.0864	0.0823
5	Northridge, USA	Bell Gardens, Jaboneria (1994)	2.16	0.23	6.69	5.01	0.2345	0.0953	0.0452	0.0507
6	El Centro, USA	El Centro, Los Angeles (1940)	2.06	0.84	6.9	2.49	0.6450	0.4522	0.4757	0.4330
7	Coyote, USA	Gilroy Array #1 (1979)	1.22	0.12	5.74	2.40	0.1852	0.0582	0.0433	0.0474
8	Nahanni, Canada	Nahanni Site #3 (1985)	1.47	0.28	6.76	16.06	0.1534	0.0833	0.0388	0.0376
9	Parkfield, USA	Cholame - Shandon Array #8 (1966)	3.53	0.45	6.19	2.63	0.2754	0.1616	0.1445	0.1432
10	Whittier Narrow, USA	Beverly Hills - 14145 Mulhol (1987)	1.86	0.26	5.99	6.41	0.1875	0.0895	0.1449	0.110
11	Darfield	RKAC (2010)	1.67	0.5	7.0	1.32	0.6100	0.2618	0.2141	0.2070
12	Helena Montana-01	Carroll College (1935)	1.58	0.1	6.0	2.48	0.0496	0.0246	0.0153	0.0161
13	Holister-01	Hollister City Hall (1961)	0.58	0.2	5.6	1.81	0.3338	0.0975	0.05436	0.0568
14	Holister-03	Hollister City Hall (1974)	0.922	0.2	5.14	9.09	0.1734	0.0518	0.0354	0.0327
15	Kalamata	Kalamata-bsmt (1986)	1.197	0.3	5.4	3.46	0.0794	0.0316	0.0284	0.0310
16	Kern County	Taft Lincoln School (1952)	1.56	0.6	7.36	1.37	0.6470	0.4503	0.4273	0.1935
17	Kobe	HIK (1995)	1.47	0.4	6.9	1.72	0.4416	0.2108	0.23006	0.2146
18	Loma Prieta	Coyote Lake Dam -Downst (1989)	1.57	0.5	6.93	2.68	0.3991	0.2294	0.1837	0.1820
19	San Fernando	LA - Hollywood Stor FF (1971)	2.205	0.7	6.61	0.75	0.5472	0.4466	0.3540	0.3390
20	Superstition Hills	Calipatria Fire Station (1987)	1.86	0.5	6.54	5.99	0.3246	0.1594	0.1042	0.1120
21	Borrego Mtn.	El Centro Array #9 (1968)	1.302	0.2	6.63	0.61	0.6344	0.4267	0.29578	0.2100
22	Lytle Creek	Devil's Canyon (1970)	1.69	0.1	5.33	6.17	0.0424	0.0216	0.01693	0.0176
23	Northern Calif-03	Ferndale City Hall (1954)	1.59	0.5	6.5	0.62	0.4964	0.3826	0.3564	0.3360
24	Managua Nicaragua-02	Managua ESSO (1972)	2.58	0.4	5.2	2.25	0.3588	0.2665	0.2483	0.2390
25	Mammoth Lakes-04	Convict Creek (1980)	3.645	1.0	5.7	3.33	0.3034	0.1533	0.1277	0.1284

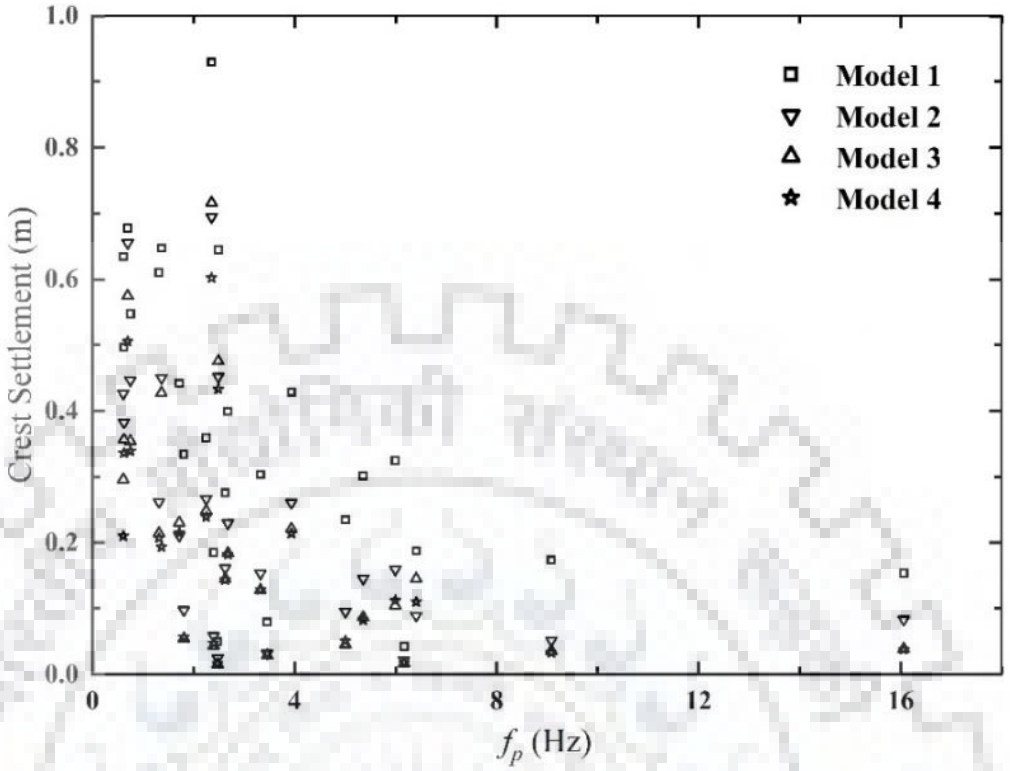

Fig. 5.8 Variation of embankment crest settlement with f_p of different ground motions.

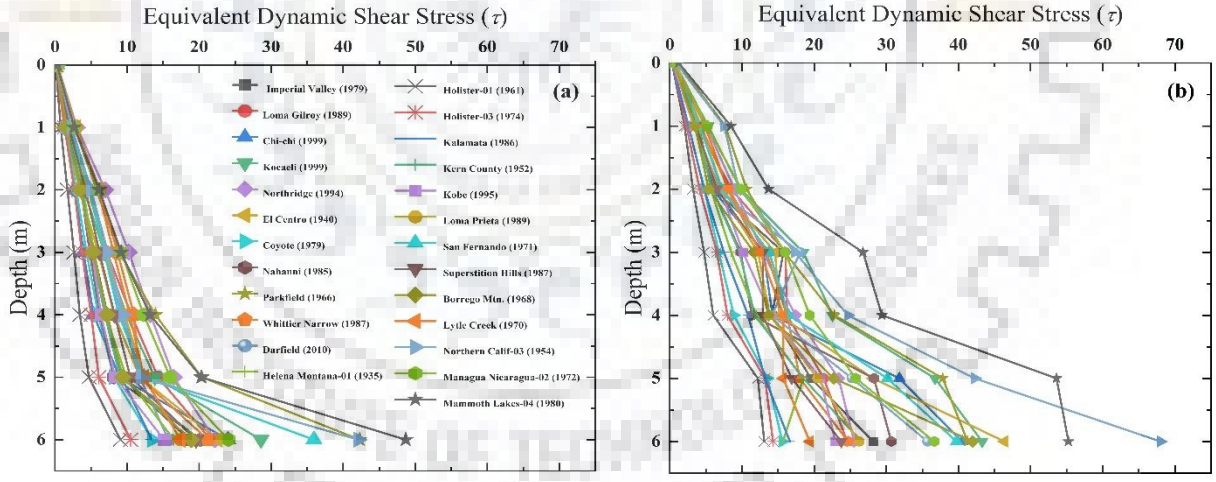

Fig. 5.9 Equivalent dynamic shear stress (τ) along the depth of liquefiable layer for (a) Model 1 and (b) Model 2.

Figure 5.10 shows the plots between the embankment crest settlement and I_a of different models. A nearly linear relationship exists between the I_a and the embankment crest settlement. The embankment crest settlement increases with I_a. A similar kind of response was reported by Sica and Pagano (2009).

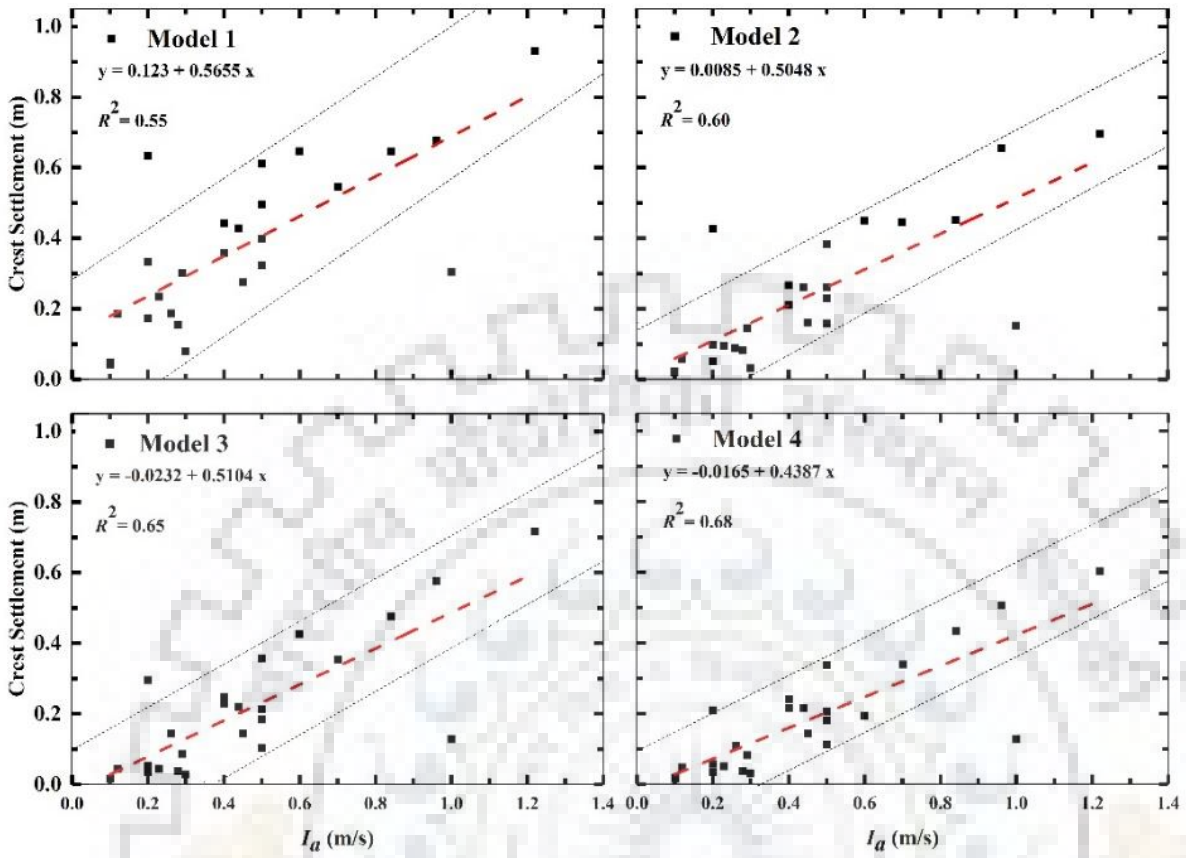

Fig. 5.10 Variation of embankment crest settlement with I_a of different ground motions.

Out of 25 ground motions it can be seen a total of 23 motions follow a certain band width. The band width for Model 1 is found to be maximum. In the models with mitigation, the band width reduces. In case of hybrid mitigation (Model 4) the bandwidth found to be minimum out of all the models. However, for Borrego Mtn. (1968) and Mammoth Lakes-04 (1980) ground motion, the crest settlements found to be more scatter and at a distance from the band. The maximum embankment crest settlement has been occurred in the Imperial Valley (1979) ground motion which also has the maximum value of I_a. In case of Model 1, the crest settlement found to be 0.9295m. By using densification of the toe region (Model 2) this settlement has been reduced by 25.3%. Stone column mitigation has reduced the settlement by 23%. Maximum reduction of 35.23% in settlement has been observed using the hybrid mitigation (Model 4). Figure 5.11 shows the I_a-M_w-Crest settlement plot for four different models.

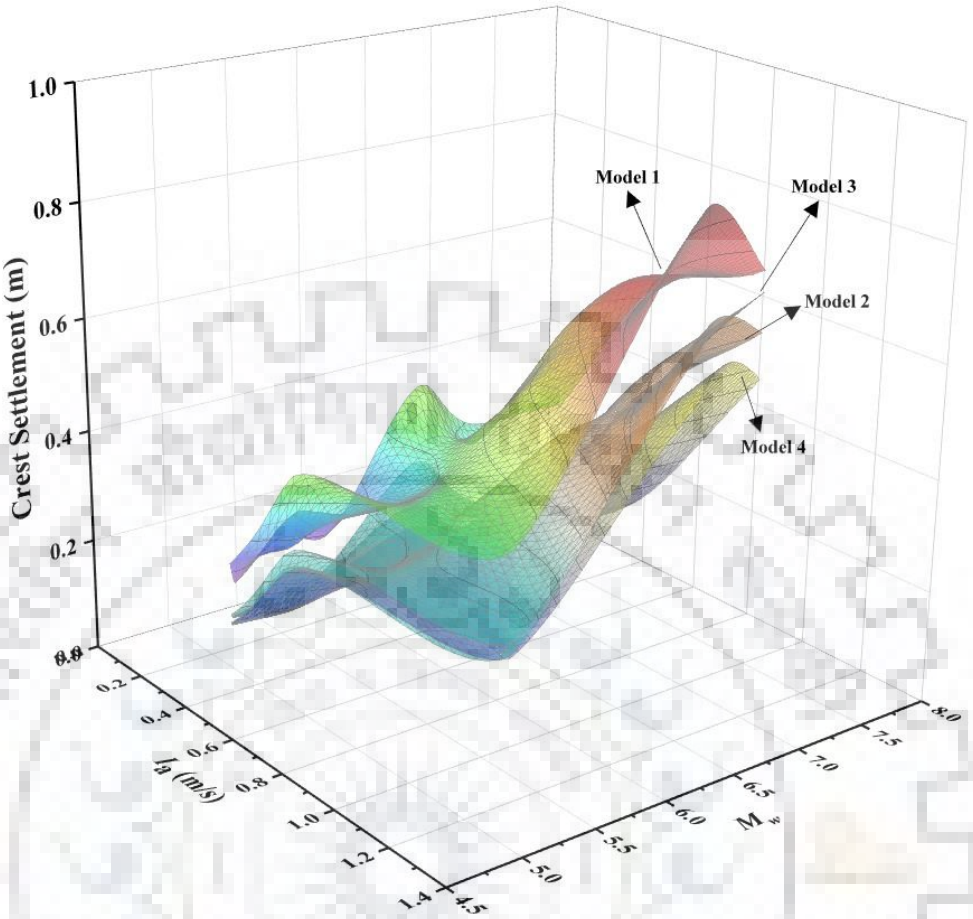

Fig. 5.11 I_a - $r_{u,\,max}$ - Crest Settlement plot for 25 different ground motions.

Quantitively it can be observed that out of 25 ground motions, the hybrid mitigation has shown better performance in 15 ground motion cases. Models 2 and 3 had been found to be proficient in 3 and 7 ground motion cases, respectively. The stone column mitigation had been observed competent for low to medium intensity ground motions. Similar observation had been reported in past studies (Baez and Martin 1993; Adalier et al. 2003; Brennan and Madabhushi 2006). Barring the Chi-chi ground motion (1999), the hybrid mitigation (Model 4) technique has been found to be more effective than other two mitigation models in higher intensity ground motions.

Figure 5.12 shows the variation of $r_{u,max}$ in the region of mitigation for three different models (Model 2, Model 3 and Model 4) with respect to the I_a of different ground motions. It is clearly visible that the model without any mitigation (Model 1) shows maximum value of $r_{u,max}$ at the location below embankment toe. In case of all the models, $r_{u,max}$ found to be increasing with the increase in I_a of ground motions.

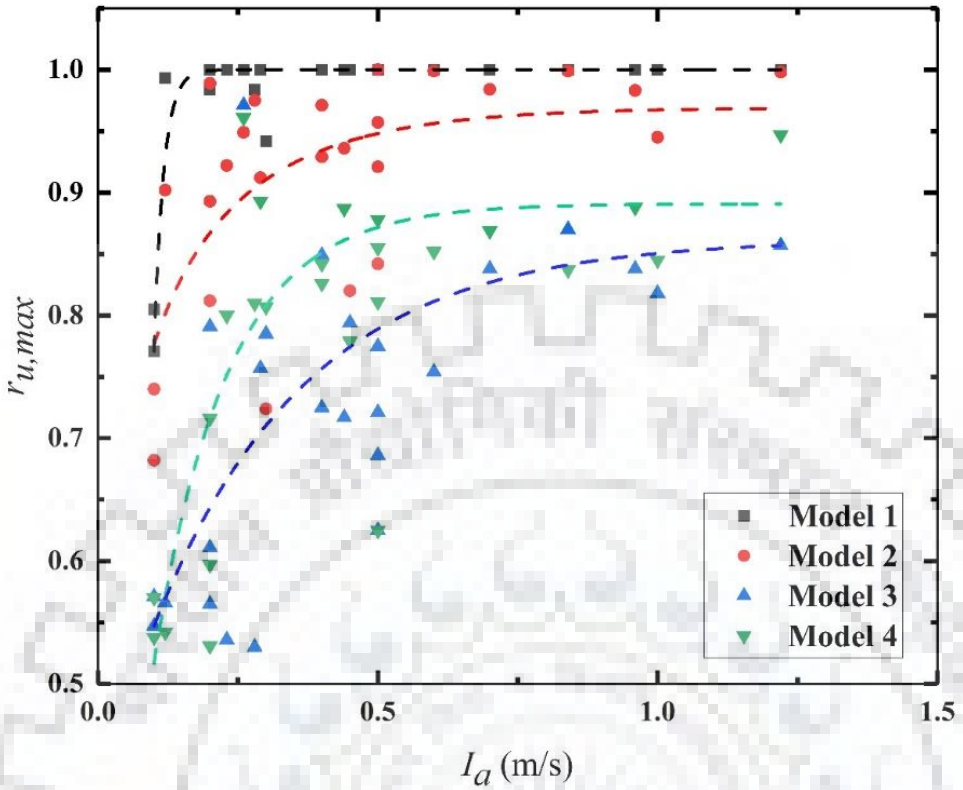

Fig. 5.12 Variation of $r_{u,max}$ with I_a for different ground motions.

Out of three different mitigation models, stone column mitigation has shown better performance in reducing the $r_{u,max}$ value. However, hybrid mitigation (Model 4) also shown better performance compared to densification model (Model 2). In this case, the maximum values of $r_{u,max}$ have been observed near the pile surface. This may be attributed to the reduction of drainage due to the existence on non-porous material (Pile). Densification model has revealed least mitigation to liquefaction showing maximum $r_{u,max}$ values at the region towards the free field. Average curves represented for all models are asymptotic in nature. Average asymptotic values are 1.0 for Model 1, 0.95 for Model 2, 0.84 for Model 3 and 0.87 for Model 4. Average curves are becoming flatter at I_a = 0.2 for Model 1, I_a = 0.6 for Model 2, I_a = 1.0 for Model 3 and I_a = 0.7 for Model 4. It can be inferred that $r_{u,max}$ values increase with I_a. Model 3 and Model 4 perform much better under seismic condition in respect of maximum EPP.

In order to evaluate the detailed response of all the models under a particular ground motion, a detailed time history analysis is presented for Darfield (2010) ground motion. Acceleration time history of Darfield (2010) input ground motion and at the embankment crest of different models are presented in Fig. 5.13.

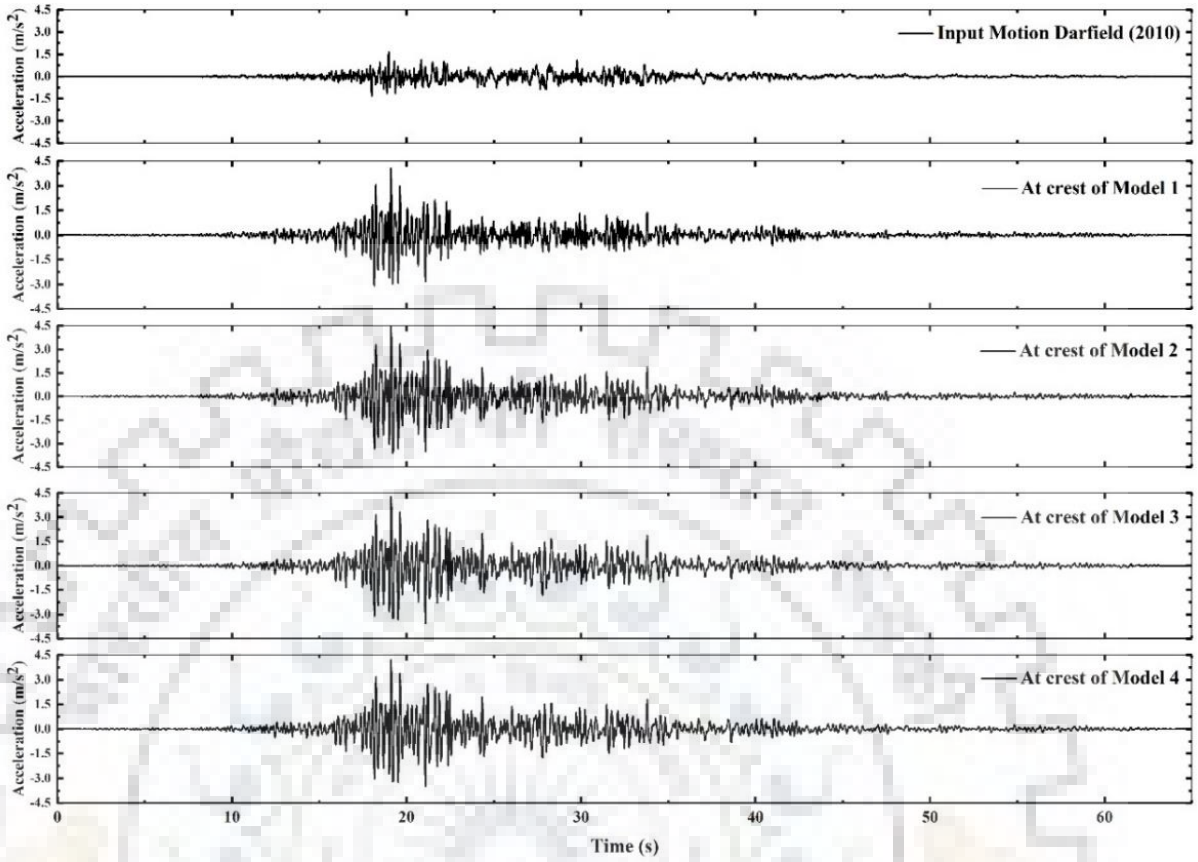

Fig. 5.13 Acceleration time history of input motion and at the crest of different models.

Excess pore pressure ratio (r_u) contour plots for all the models at the end of Darfield (2010) ground motion have been shown in Fig. 5.14. Figure 5.14 (a) represents the r_u contour plot for the model without any mitigation. It can be observed that the foundation soil region away from the embankment liquefied within few cycles. The densification measure in Model 2 shows effective mitigation for a certain region of soil beneath the toe, however the densified zone away from the toe towards the free field liquefies (Fig. 5.14-b). That shows two important concerns about the mitigation using densification: (i) the migration of pore water into the densified zone from the nearby (loose) liquefied ground can cause pore pressure to increase in the densified zone, which could lead to a potential loss of strength in the densified zone; (ii) there is a possibility of sliding of the densified zone (at least a portion of it) as the surrounding liquefied soil flows. Similar observation has been reported by Adalier (1996).

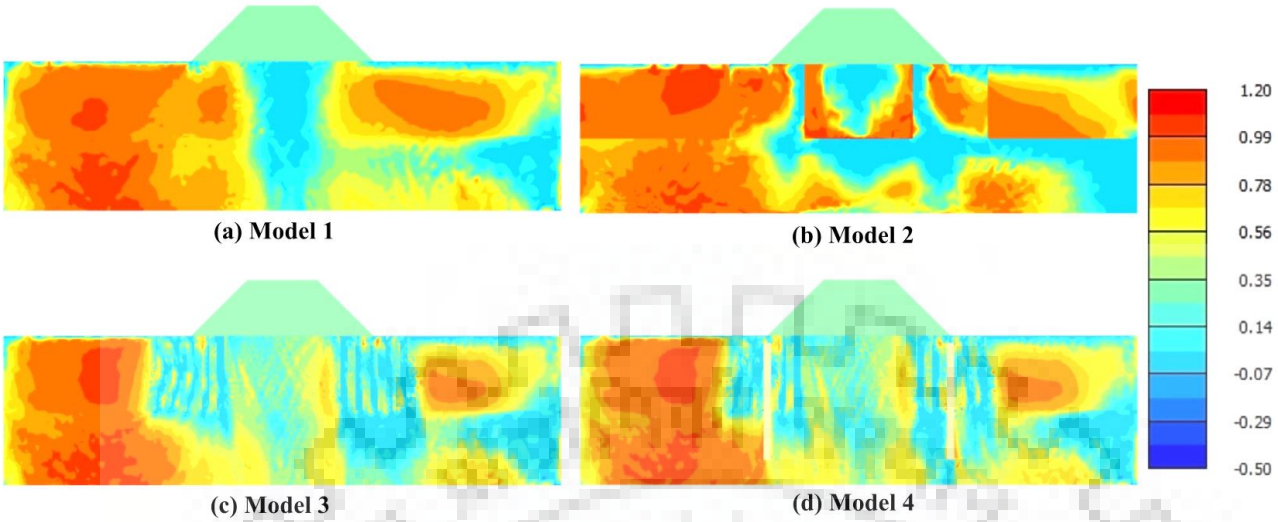

Fig. 5.14 r_u contour at the end of Darfield (2010) ground motion for different models.

Figures 5.14-c and 5.14-d show r_u contour of Model 3 and Model 4, respectively. At the end of the ground motion, Model 3 and Model 4 have shown similar plots of r_u contour. Both models have shown better dissipation of excess pore pressure (EPP) at the end of loading.

Figure 5.15 shows EPP time history at different locations (1, 2, 3, and 4 shown in Fig. 5.1) of liquefiable foundation soil layer for the applied ground motion of Darfield (2010). At location '1', the maximum value of EPP in Model 1 found to be 30.18 kN/m^2 at 21.284 s. Whereas, in case of Model 2, it was 32.415 kN/m^2 at 50.90 s at the same location. This shows that at later duration when dissipation is more predominant, the densified zone restricts the flow of EPP which increased the EPP of the densified zones adjacent to the free field. Similarly, during the post-seismic period also consequent rise of EPP found to be occurring at this location. However, in case of Model 3 and Model 4, consequent contractive and dilatative behaviour of sand can be observed. The maximum EPP in case of Model 3 and Model 4 have been observed to be 6.73 kN/m^2 and 7.39 kN/m^2 at 27.924 s.

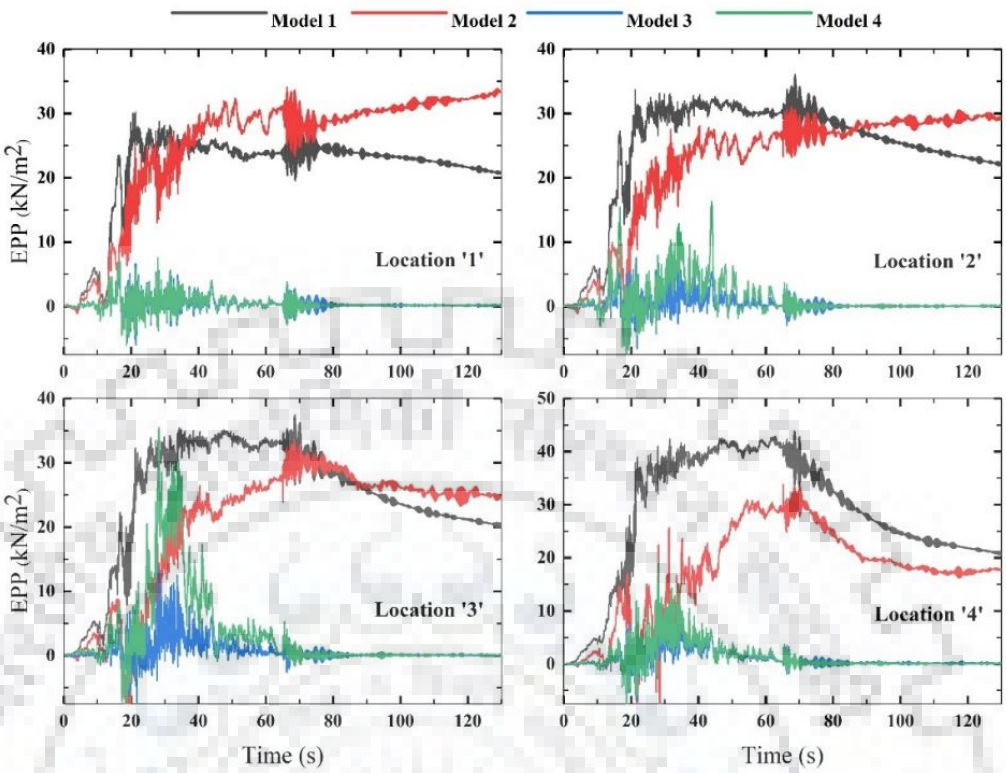

Fig. 5.15 EPP time histories of different models during Darfield (2010) ground motion.

At location '2', the maximum value of EPP in Model 1 observed to be 33.68 kN/m^2 at 21.28 s. It was 28.07 kN/m^2 at 40.42 s for Model 2. In case of Model 3 and Model 4, maximum EPP values were found to be 8.45 kN/m^2 and 16.33 kN/m^2 at 33.78 s and 44 s, respectively. At location '3', Model 1, Model 2, Model 3, and Model 4 showed maximum EPP values 35.47 kN/m^2, 28.13 kN/m^2, 13.68 kN/m^2, and 35.40 kN/m^2 during the co-seismic period at 34.30 s, 65.02, 28.25 s, and 28.25 s, respectively. In case of Model 2, 20.7% reduction of EPP can be observed in comparison to Model 1. Maximum reduction of 61.43% can be observed in Model 3. However, in case of Model 4, negligible mitigation in the peak EPP value has been observed at the location '3'. But, a considerable mitigation of EPP can be observed during the entire period. At location '4', maximum EPP value in Model 1 can be observed as 42.9 kN/m^2 at 62.61 s. Model 2 showed maximum EPP value as 30.94 kN/m^2 at 54.48 s. In Model 3, maximum reduction has been observed with maximum EPP value of 15.94 kN/m^2 at 28.25 s. In case of hybrid mitigation (Model 4), the maximum EPP value can be observed as 18.94 kN/m^2 at 28.25 s.

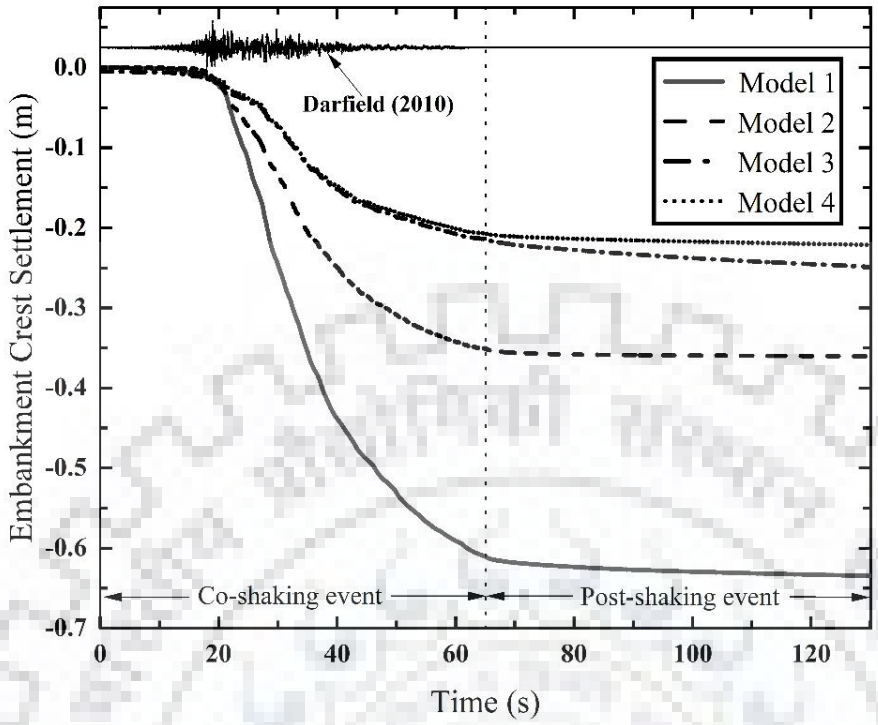

Fig. 5.16 Embankment Crest Settlement Time Histories of different models during Darfield (2010) ground motion.

Figure 5.16 shows embankment crest settlement time history for the co-seismic and post-seismic event. At the end of the co-seismic event, the final embankment crest settlement of Model 1 can be observed to be 0.6104 m. In Model 2, the settlement has been reduced by 57%. In case of Model 3 and Model 4, settlement reduced by 64.95% and 66%, respectively. However, at the end of post-seismic event, Model 4 showed a maximum reduction of crest settlement by 65.12%. Model 2 and Model 3 reduced the crest settlement by 54.40% and 60.81%. Maximum slope of time vs settlement plot can be observed in Model 3. This might be due to large rate of dissipation during the post-seismic event. However, Model 4 has shown better performance during post-seismic event as well. The hybrid mitigation approach has shown desirable performance for reduction of overall liquefaction-induced embankment settlement.

5.5 CONCLUDING REMARKS

An attempt has been made to study the effectiveness of three different mitigation approaches for earth embankment resting on liquefiable foundation soil. Three different mitigation techniques; (i) densification, (ii) stone column, and (iii) hybrid pile-stone column, have been incorporated in numerical model considering equivalent plane strip for simplifying into a plane strain problem. Based on the key observations from this study, few conclusions have been drawn.

1. Study shows that well calibrated UBC3D-PLM constitutive model can efficiently simulate the liquefaction phenomenon as well as shear induced dilation of a liquefiable soil. Due to liquefaction of foundation soil below the toe region, the shear induced dilated soil below the crest of embankment moves laterally.
2. Larger embankment crest settlement has been occurred at smaller frequency ground motions. The maximum settlement has been observed during Imperial Valley (1979) ground motion, which has predominant frequency of 2.36 Hz.
3. A nearly linear relationship exists between the Arias Intensity (I_a) and the embankment crest settlement. The embankment crest settlement increases with I_a. The maximum embankment crest settlement has been occurred in the Imperial Valley (1979) ground motion having ximum Arias Intensity I_a. Moreover, the $r_{u,max}$ value in the mitigation zone below embankment toe found to be increasing with I_a.
4. From the analyses of 25 ground motions for 4 different models, the hybrid mitigation was found to be more effective in reducing the embankment crest settlement than other two mitigation approaches for the higher intensity ground motions. Densification and stone column mitigation were found to be effective in the cases of low to medium intensity ground motions.
5. The time history analysis of Darfield (2010) ground motion for mitigation model using densification indicated possible development of progressive liquefaction in the densified zone facing the free ground. This may cause potential failure of the mitigation system. Further study by addressing this issue needs to be carried out.
6. The liquefaction of the soil beneath the embankment toe mainly affects the embankment settlement behaviour. The densification measure in Model 2 shows effective mitigation for a certain region of soil beneath the toe, however the densified zone away from the toe towards the free field liquefies.
7. The stone column mitigation model (Model 3) and hybrid pile-stone column mitigation model (Model 4) have shown better dissipation of EPP at the end of loading.
8. The higher dissipation rate due to stone columns may lead to the excess settlement. The hybrid mitigation method has been found to be most effective in reducing the shear induced settlement of embankment during the co-shaking event as well as during the post-shaking event.
9. The results presented in this study are based on calibration of a material model using existing experimental studies and validation against certain assumptions. Physical model testing is further

required to understand completely the whole phenomenon and to design a better mitigation approach.

A comparative study on effectiveness of different mitigation models had been presented for 25 ground motions. Study highlights the effectiveness of hybrid model (stone column - pile). Analysis was based on plain strain assumptions. Mitigation features like stone column and pile had converted to equivalent 2D sub-domains. Next Chapter deals with three-dimensional analysis for sequential ground motion. Effect of after-shock motion has been explored in detail.

CHAPTER 6

EFFECT OF RE-LIQUEFACTION UNDER SEQUENTIAL LOADING

6.1 GENERAL

Recent studies have focused to understand the behaviour of earth embankment foundations under seismic loadings and identifying the appropriate remedial measures in these situations. Densification of embankment toe region, gravel berm at the embankment slopes, stone column mitigation, sheet pile below the toes of an embankment, and deep soil mixing are some of the previously explored ground-improvement techniques (Adalier 1996; Okamura and Matsuo 2002). Adalier (1996) reported the effectiveness of the gravel berm technique using dynamic centrifuge testing. However, the study was limited to only cyclic loading conditions.

An earth embankment without any mitigation measure can be idealized with 2D plane strain assumption appropriately. But when discrete mitigation measures have been included with desired spacing, it is no longer remain ideal 2D domain. Earlier studies have considered these measures in the form of equivalent strip as explored in previous Chapters. Considering nonlinear behaviour of soil, the assumption of equivalent strip with homogeneous properties renders to be approximate.

Only limited studies have been reported on gravel berm and stone column mitigation incorporating 3D analysis on liquefaction-induced effects on embankment response. Moreover, experimental investigation for such a complex physical model is very complicated to conduct. This attracted full-scale numerical modeling in recent decades. Very few studies have been reported on full-scale 3D finite element numerical modeling on the stone column and gravel berm mitigation techniques. The resistance of the liquefiable ground to liquefaction is eventually increased by the stone columns. The satisfactory performance of gravel drainage against small to moderate-magnitude earthquakes has been supported by physical model tests and field studies carried out by several researchers (Priebe 1989; Baez and Martin 1993; Adalier et al. 2003; Brennan and Madabhushi 2006). Moreover, it has been observed that the addition of gravel berms on the embankment slopes would increase the resistance of the embankment to excess settlement (Adalier 1996). Additionally, the berm would act like a surcharge, increasing the liquefaction resistance of the foundation sandy soil. Due to increased overburden stress from the gravel berm, the loose sand foundation responded better to earthquakes in the case of the gravel berm (Adalier 1996). However, the efficacy of this technique has not been evaluated under rigorous dynamic loading events.

In several earthquakes, aftershock events have been observed repeatedly occurring after the main shock over brief time intervals. In a recent event, on February 6th, 2023 an M7.8 earthquake struck the Giazantep province of Turkey, which triggered almost 1200 aftershock events recorded up to Feb. 10th (Baltzopoulos et al. 2023). The range of magnitude of main shock events has been recorded to be M6.6 to M7.8. However, multiple major aftershocks of M5.0+ are also observed within the next 90 minutes of the main shock event. In order to provide a point of reference, the same number of M5.0+ events were observed across five months of the prolonged 2016 - 2017 central Italy seismic sequence (Iervolino et al., 2021). Under main shock followed by series of aftershock seismic sequences, the already-damaged structure from the main shock that has not been fixed may collapse or become totally vulnerable since it will not be able to withstand the excitation of the intense aftershocks (Zhang et al. 2013). Previous research has shown that low-amplitude aftershocks can build significant lateral deformation following a main shock event (Okamura et al. 2001; Meneses-Loja et al. 1998). Ye et al. (2007) investigated the mechanical behaviour of liquefiable foundations during repeated shaking and consolidation by performing shaking table tests and numerical studies on saturated sandy soil. Xia et al. (2010) also presented a numerical study on an earthen embankment on liquefiable soil under the application of a repeating shake-consolidation process. However, most of the past research was carried out considering a single shaking event by ignoring repeated shaking events. The 2011 Great East Japan Earthquake caused the liquefaction-vulnerable buildings to tremor for over two minutes after the soil started to liquefy (Maharjan and Takahashi, 2014). Sasaki et al. (2012) discovered that the presence of aftershocks contributed to the more severe deformation and subsidence of levees during the reconnaissance survey following the 2011 Great East Japan Earthquake. Moreover, a very limited study has been reported for embankments resting on deposits susceptible to liquefaction under the application of sequential ground motions. It is important to assess the response of embankment structures under both the main shock and aftershock events. However, no such studies have been reported for embankments on liquefiable soil considering full 3D numerical simulation using a well-calibrated dynamic constitutive model under the application of sequential ground motion.

An attempt has been made to understand the dynamic behaviour of embankment on liquefiable soil, considering ten different sequential ground motions as input motion. Three-dimensional numerical models have been simulated for embankment resting in liquefiable soil with and without different mitigation measures. Effectiveness of stone column and gravel berm mitigation measures have been explored under cyclic and 10 different sequential ground motions.

6.2 3D FINITE ELEMENT MODELS

Three different embankment models have been modeled where the 4.5 m high embankment rests on loose cohesionless foundation sand. The embankment is modeled considering Mohr-Coulomb material model. But the foundation soil is modeled considering UBC3D-PLM model.

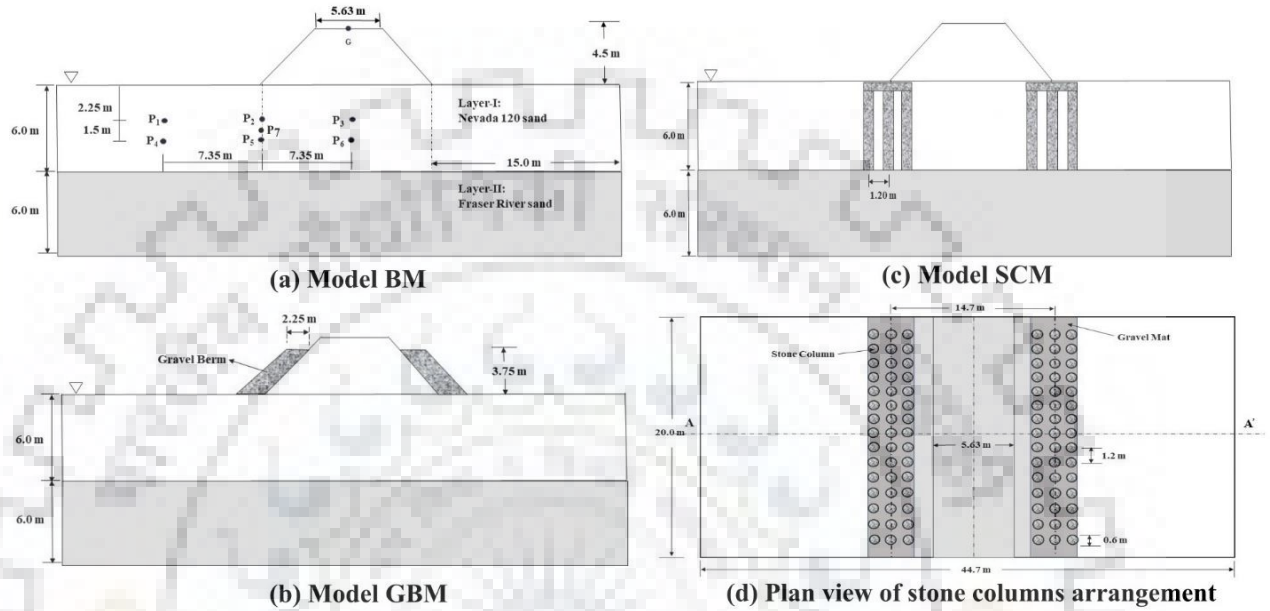

Fig. 6.1 Configuration of different embankment models.

The embankment is having 1:1 side slope. Foundation soil has been considered of layers of two different relative densities (R_D). Layers 1 and 2 have R_D = 40% and R_D = 80%, respectively. Each layer has been chosen to be 6 m in depth. The first model is a benchmark model without any mitigation denoted as model BM (Fig. 6.1a). In the second model, gravel berm along the slopes of the embankment has been considered. This model is named as GBM. A cross-sectional view of the model GBM is shown in Fig. 6.1b. The last model consists of stone column mitigation beneath the toes of the embankment denoted as SCM. A cross-sectional view is given in Fig. 6.1c. The plan view of the arrangement of stone columns is shown in Fig. 6.1d. This arrangement of stone columns has been selected from study presented in Chapter 4. Stone columns are created using volume elements, with a spacing to diameter ratio (S/D) equal to 2.

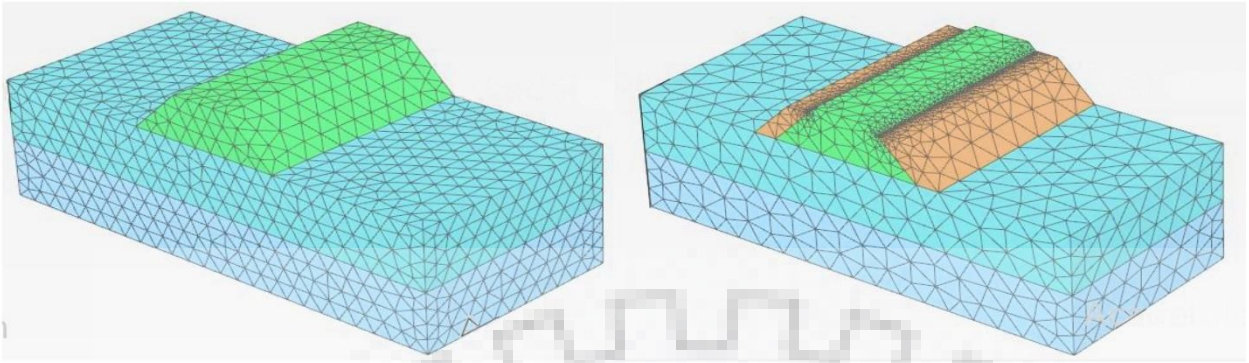

(a) Model BM (b) Model GBM

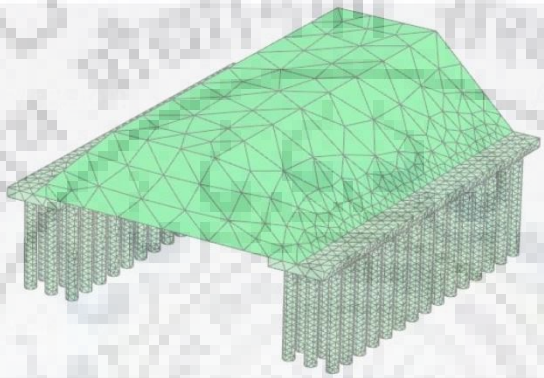

(c) Model SCM

Fig. 6.2 FE mesh of different embankment models.

The gravel berms are generally provided for increasing the effective stress near the toe region so that it provides additional safety to the embankment. Figure 6.2 shows a schematic representation of FE mesh of three different models. Figure 6.2a shows the 3D FE mesh of the benchmark model (BM). Figure 6.2b shows the isometric view of FE mesh for the gravel berm model. Figure 6.2c represents the FE mesh model of stone columns under the embankment toes. Stone columns are placed below gravel mats of 0.5 m thickness. Refined meshing has been adopted in the stone columns and the adjacent soil volumes because of the expected higher stress concentrations in these regions.

6.3 MATERIAL PROPERTIES

The earth embankment has been built with a 1:1 slope using a mixture of Nevada sand and Kaolin clay in a 4:1 weight ratio (Adalier 1996). In the present study, the material of the embankment has been modeled considering the Mohr-Coulomb model. Layer I and Layer II have basic properties of Nevada 120 sand (R_D = 40%) and Fraser River sand (R_D = 80%). The basic sand properties are reported in Table 6.1.

Table 6.1 Properties of Nevada 120 sand (Arulmoli et al., 1992) and Fraser River sand (Sriskandakumar, 2004).

Properties	**Nevada 120 sand**	**Fraser River sand**
Relative density	40%	80%
Specific gravity	2.67	2.71
Dry Unit Weight (γ_{dry})	15.08 kN/m^3	16.73 kN/m^3
Permeability (k)	6.6×10^{-5} m/s	5.5×10^{-6} m/s[a]
e_{max}	0.887	0.94
e_{min}	0.511	0.62

The foundation soil layers (layer I and layer II) have been modeled using the UBC3D-PLM material model. The material model properties are considered from the calibration study reported in Chapter 4. However, in the case of model GBM, the gravel berms are considered linear elastic (Dinesh et al. 2022). The stone columns are modeled using the UBC3D-PLM model. The basic soil properties are taken from Arulmoli et al. (1992). Material properties of embankment and gravel berm are listed in Table 6.2.

Table. 6.2 Material properties of embankment and gravel berm.

Properties	**Embankment**	**Gravel Berm**[*]
Elastic modulus E (MPa)	20	375
Dry Unit Weight (kN/m^3)	19	20
Cohesion (kPa)	22	-
ϕ_{cv} (^{o})	31	-
Poisson's ratio	0.3	0.25

[*] Data from Dinesh et al. (2022)

6.4 VALIDATION

In order to evaluate the performance of the UBC3D-PLM model under the static loading condition, the model has been tested against the monotonic direct, simple shear test (DSS) performed by Arulmoli et al. (1992) for the Nevada 120 sand (R_D = 40%) considering the undrained condition. Model parameters are shown in Table 6.3. The testing has been conducted by applying 80 kPa effective vertical stress (σ_v'). A single-element test has been carried out considering the same loading condition. Comparison of shear strain versus shear stress and shear strain versus σ_v' have been shown

in Figs. 6.3 a and b, respectively. It can be assessed that the UBC3D-PLM model very closely follows the trend of laboratory test results (Arulmoli et al., 1992). Further assessment of performance under undrained cyclic loading conditions has been performed. A comparison has been made against the study reported by Arulmoli et al. (1992). An undrained cyclic simple shear test (CDSS) was carried out under the initial vertical effective stress of 160 kPa, considering the isotropic condition. Similar conditions have been considered during the single-element testing. Comparison of EPP time history (Fig. 6.3c) and σ_v' vs shear stress (Fig. 6.3d) has been reported.

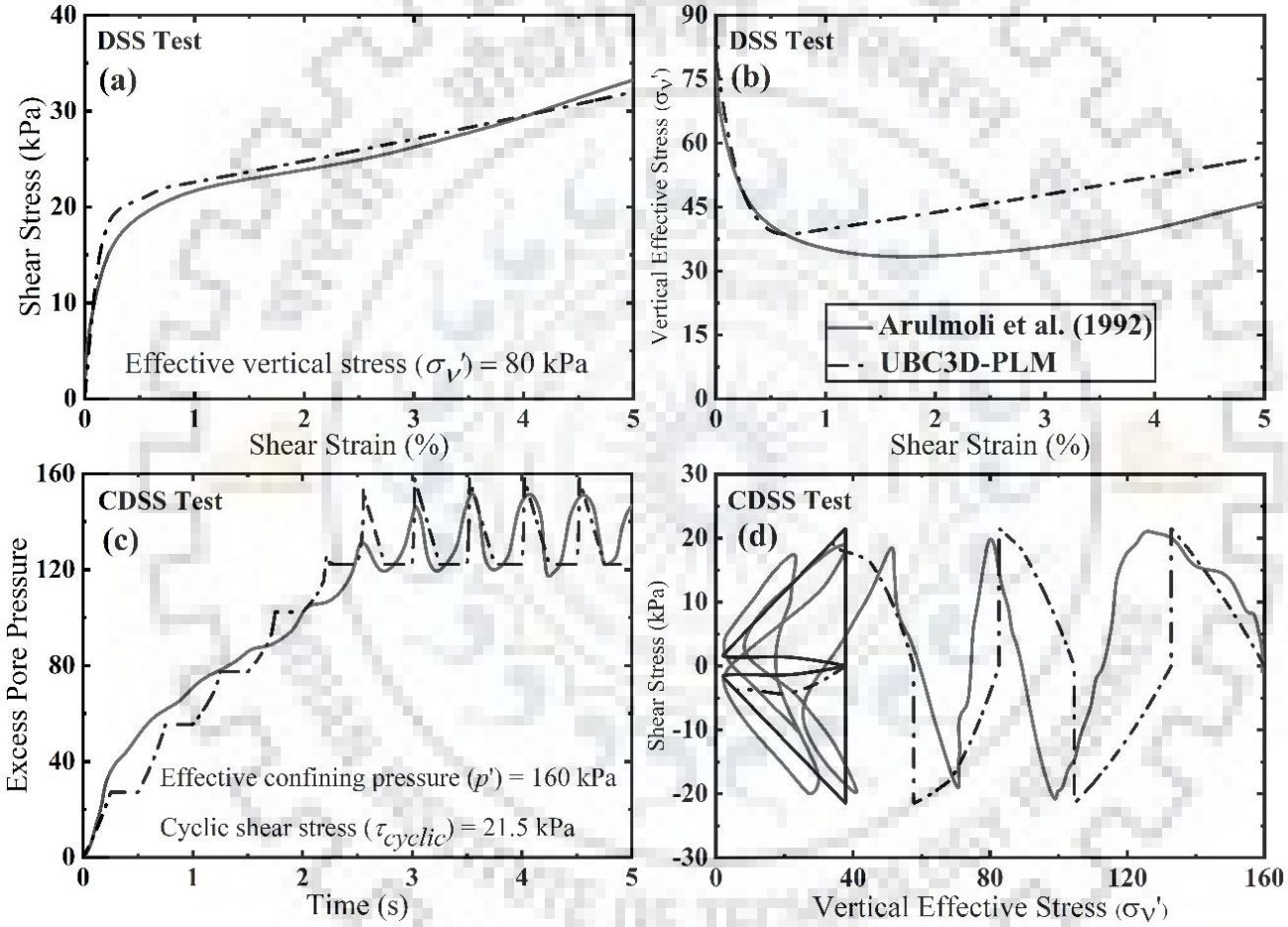

Fig. 6.3 Calibration of UBC3D-PLM model for Nevada 120 sand under monotonic direct simple shear loading (DSS) and cyclic simple shear loading (CDSS).

Table 6.3 Calibrated UBC3D-PLM model parameters.

Parameters	Nevada 120 Sand	Fraser River sand	Stone column
Relative density	40%	80%	-
γ_{dry} (kN/m^3)	15.08	19.0	18.0
$e_{initial}$	0.736	0.5	0.45
k (m/s)	6.6×10^{-5}	5.5×10^{-6}	0.10
ϕ_p	33.65 º	38.9 º	48.10 º
ϕ_{cv}	33 º	33 º	40 º
K_B^e	566.6	937.6	1011
K_G^e	809.4	1339.5	1444
K_G^p	350	3597.1	6032
m_e	0.5	0.5	0.5
n_e	0.5	0.5	0.5
n_p	0.4	0.4	0.4
R_f	0.83	0.66	0.64
fac_{hard}	0.45	0.45	0.65
fac_{post}	0.1	0.1	0.1
Corrected SPT blow count ($N_{1,60}$)	6.5	29.7	37

The efficacy of a material model is justified by given comparisons. A well-documented dynamic centrifuge test performed by Adalier (1996) has been simulated in the present study using 3D finite element modeling for evaluating the performance of the UBC3D-PLM model. Figure 6.4 shows the cross-sectional view of the embankment model resting on a liquefiable sand deposit considered in the study of Adalier (1996). The testing was conducted in the laboratory of the RPI centrifuge facility under a 75g centrifugal acceleration field. The foundation liquefiable soil was Nevada 120 sand with R_D = 40%. The embankment was 4.5 m high with a 1:1 slope. The embankment was made of a mixture of Nevada 120 sand and Kaolin clay (4:1 by weight). The embankment-foundation liquefiable soil system was subjected to 0.1g amplitude cyclic loading for ten cycles with a 1.6 Hz loading frequency.

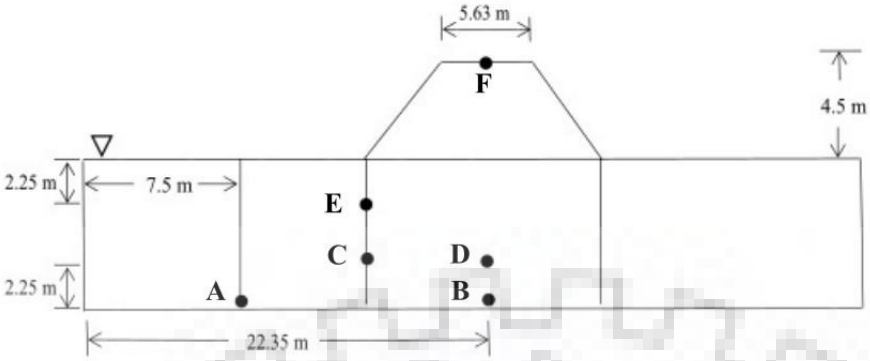

Fig. 6.4 Geometric presentation of embankment on liquefiable soil (after Adalier, 1996).

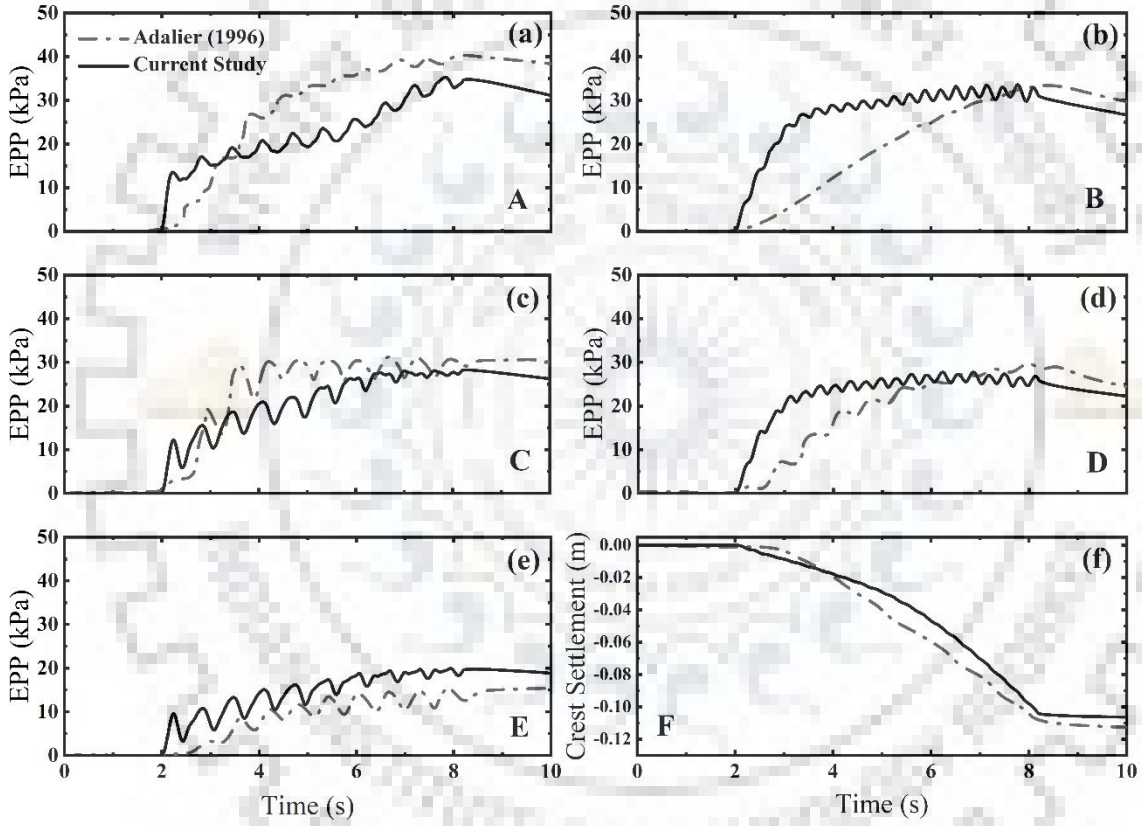

Fig. 6.5 Comparison of time histories of (a-e) excess pore pressure (EPP) time history and (f) settlement time history at different locations.

Figure 6.5a-e compares EPP time histories at different locations in foundation soil below the embankment, and Fig. 6.5f compares embankment crest settlement time histories. A close agreement between the experimental test results and simulated results has been observed. At location A, a 9% difference between the experimental and simulated maximum EPP values can be observed. Locations B, C, and D show 1.1%, 9.31%, and 9.41% difference between the experimental and

simulated maximum EPP values, respectively. However, at location E, a noticeable difference can be observed between the experimental and numerical maximum EPP values, but the resulting trend shows good agreement. Moreover, a marginal difference of 3.5% can be seen between the experimental and simulated embankment crest settlement (location F).

6.5 RESPONSE UNDER CYCLIC LOADING CONDITION

The effectiveness of two different mitigations has been analyzed under the application of simple cyclic loading conditions. This section presents the parametric study on the effect of loading amplitude on the embankment and foundation soil response. Three different amplitudes of cyclic loading (PGA_{Cyclic}) have been considered (0.1g, 0.2g, and 0.3g). All three cyclic loadings are having a frequency of 1.6 Hz. Ten cycles of loading have been applied along the base of the numerical models. Figure 6.6 shows the cyclic loading time histories.

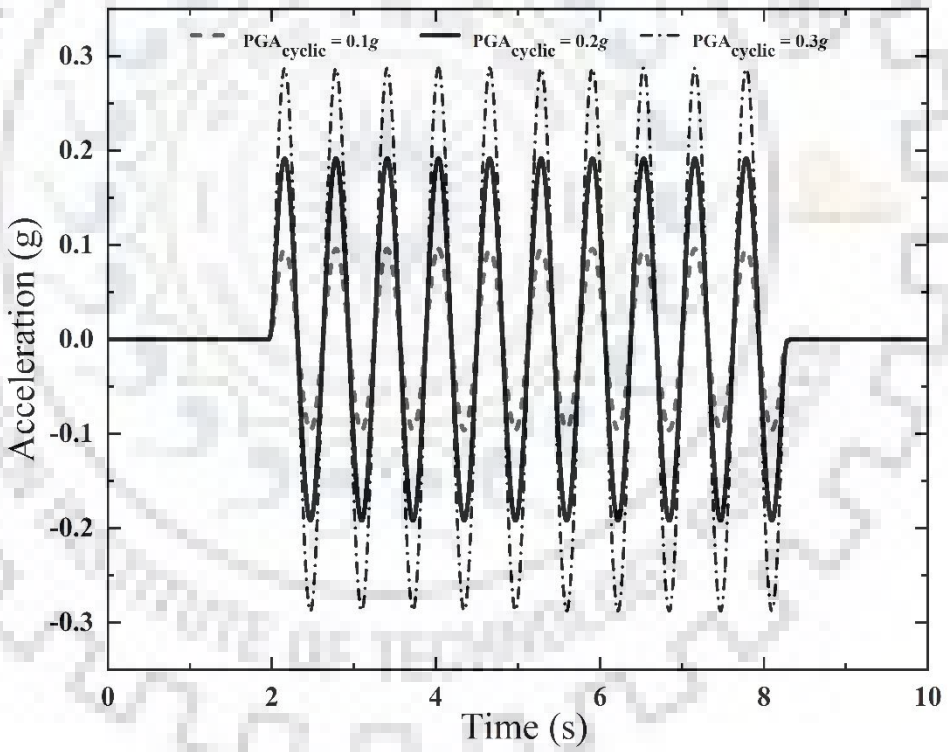

Fig. 6.6 Input cyclic loading time histories of different amplitudes.

It can be observed that with an increase in cyclic loading amplitude level (PGA_{Cyclic}), the embankment crest settlement also increases for all the models (Fig. 6.7). Increase in r_u values in the foundation liquefiable soil is also observed. However, mitigated models (GBM and SCM) have shown resistance to foundation soil to reach full liquefaction conditions (r_u = 1.0).

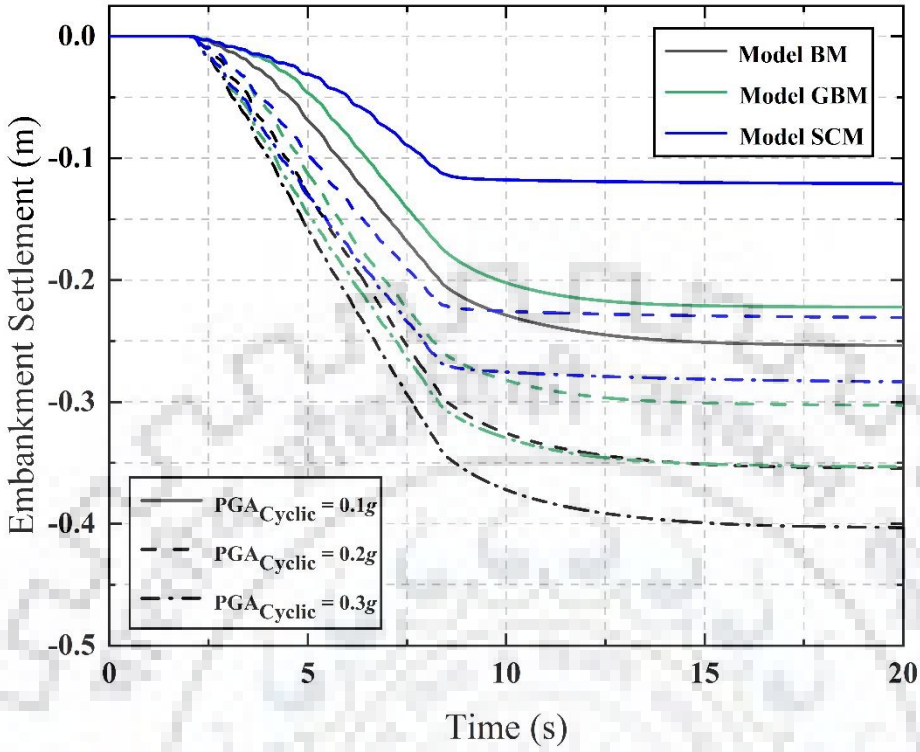

Fig. 6.7 Crest settlement at different cyclic loading for different embankment models.

Figures 6.8 and 6.9 show the r_u time history of different locations of foundation soil at 2.25 m and 3.75 m depth, respectively. In the case of PGA$_{Cyclic}$ = 0.1g, model GBM, and SCM have shown a 14.21% and 44.67% reduction in the crest settlement, respectively, compared to the model BM. Also, below the embankment toe (at 3.75 m depth), 36.93% and 83.66% reduction in $r_{u,max}$ can be observed (Fig. 6.9) in the case of model GBM and SCM, respectively.

In comparison to model BM, reductions in the embankment crest settlement for model GBM were 12.46% and 10.51% under PGA$_{Cyclic}$ = 0.2g and 0.3g. Similarly, reductions were 25.26% and 21.02% for model SCM. Again, the model GBM has shown 32.86% and 35% reduction in the $r_{u,max}$ value for 0.2g and 0.3g PGA$_{Cyclic}$. Similar reductions in the $r_{u,max}$ were 54.95% and 46.36% for the model SCM. Reductions in the values of $r_{u,max}$ can be attributed to an increase in the effective stress for the GBM model due to the additional surcharge.

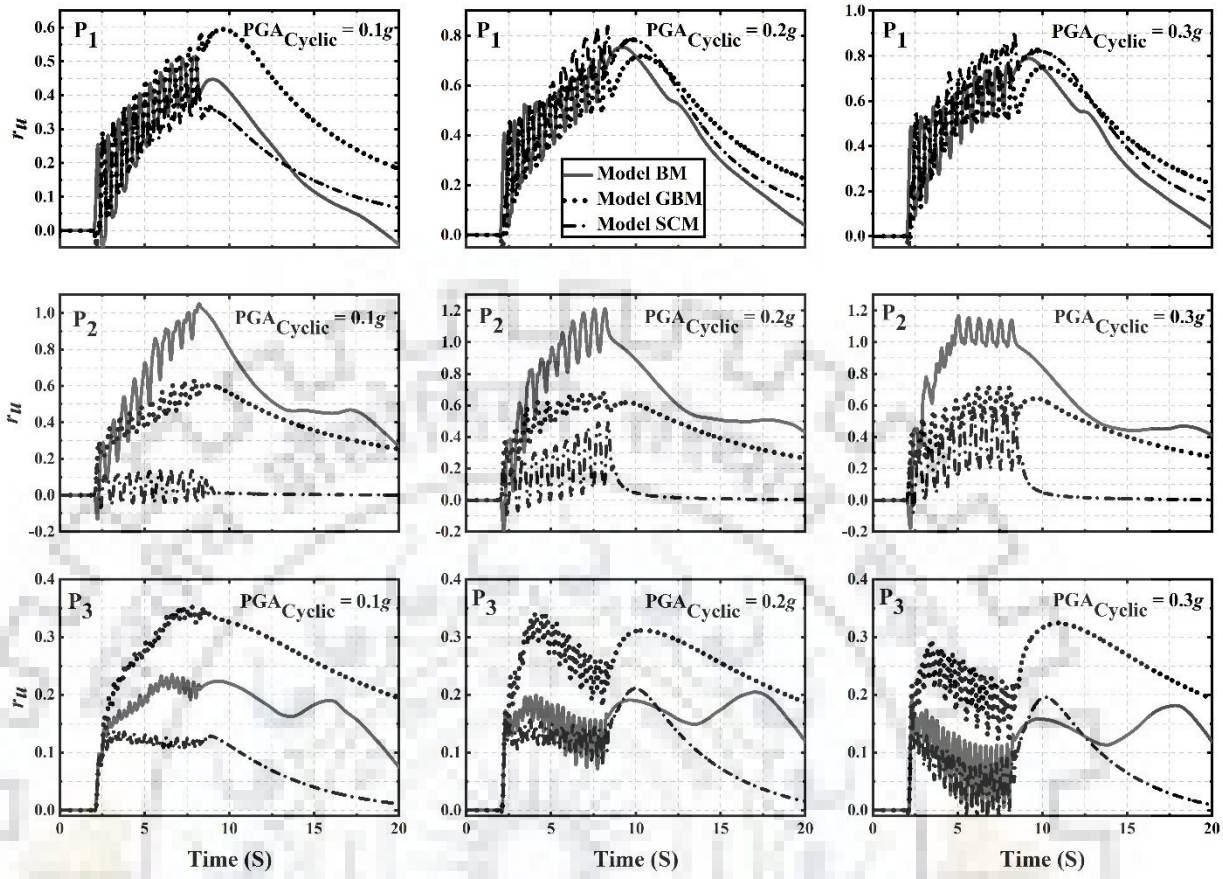

Fig. 6.8 r_u time history at 2.25m depth for P_1, P_2 and P_3 location after 10 cycles of different PGA_{cyclic}.

In the case of SCM, the permeability and stiffness of stone columns are contributing factors. Reductions in $r_{u,max}$ resulted in lesser crest settlement as compared to model BM. Details of the embankment crest settlement and $r_{u,max}$ in the foundation soil are reported in Table 6.4. Figure show r_u time histories at 2.25 m and 3.75 m depths of different locations (P_1 to P_6) under the application of different level of cyclic loading amplitude. Model SCM has shown better efficacy in terms of liquefaction reduction. One aspect that needs to be highlighted from the study is that with an increase in cyclic loading amplitude effectiveness of mitigation is reducing. It can also be seen that the foundation soil region below the embankment crest never attains liquefaction condition, and $r_{u,max}$ never exceeds the value 0.4. A similar observation has also been reported by Adalier (1996). Figure 6.10 shows embankment crest acceleration time histories of three different models under 0.3*g* cyclic amplitude loading. Details of the final embankment settlement, $r_{u,max}$ (at 3.75 m depth), and the maximum crest acceleration for different PGA_{cyclic} levels are reported in Table 6.4.

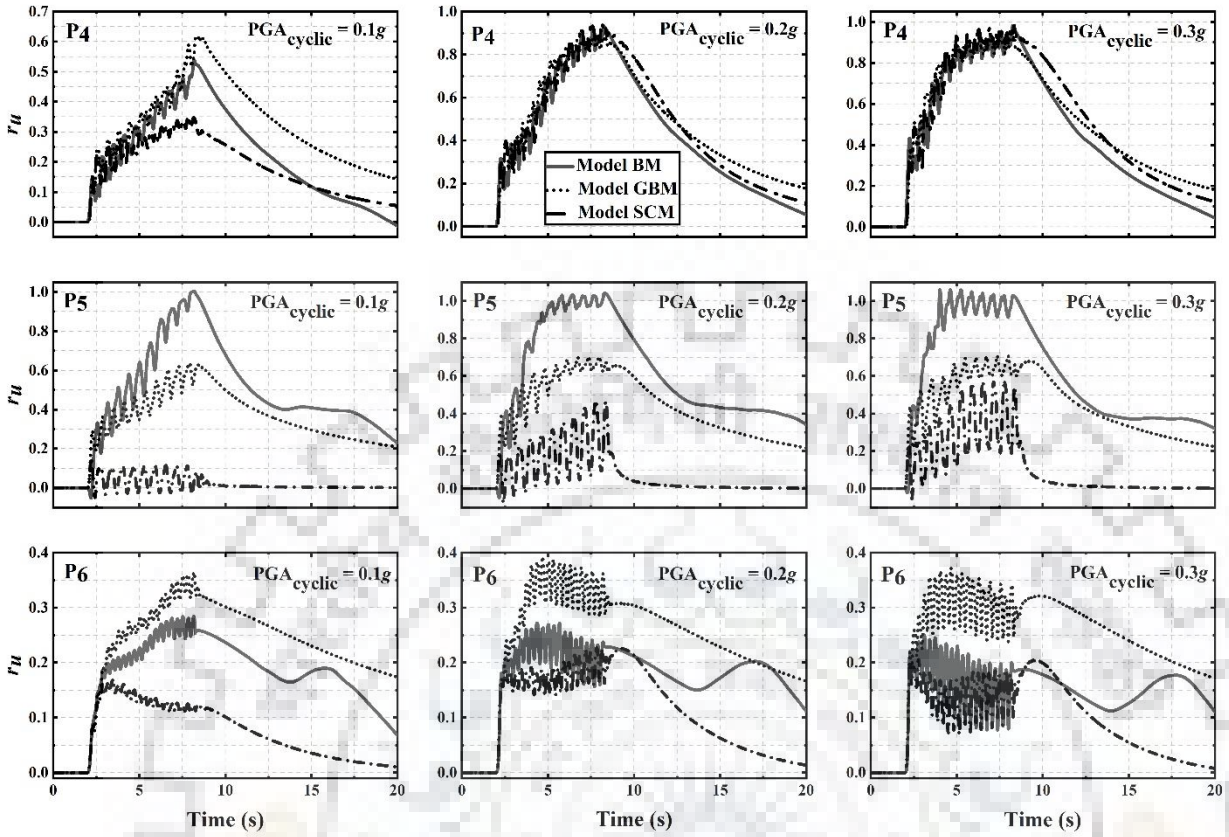

Fig. 6.9 r_u time history at 3.75 m depth for P_4, P_5 and P_6 location after 10 cycles of different PGA_{cyclic}.

Table 6.4 Details of crest settlement, r_u of foundation soil below embankment toe, and maximum crest acceleration for different cyclic loading amplitude (PGA_{cyclic}).

PGA_{Cyclic} (g)	**Crest Settlement (m)**			**$r_{u,max}$ below toe (3.75 m depth)**			**Max. crest acceleration (g)**		
	BM	**GBM**	**SCM**	**BM**	**GBM**	**SCM**	**BM**	**GBM**	**SCM**
0.10	0.197	0.169	0.109	1.01	0.637	0.165	0.155	0.131	0.162
0.20	0.289	0.253	0.216	1.05	0.705	0.473	0.269	0.287	0.279
0.30	0.333	0.298	0.263	1.10	0.715	0.590	0.411	0.469	0.383

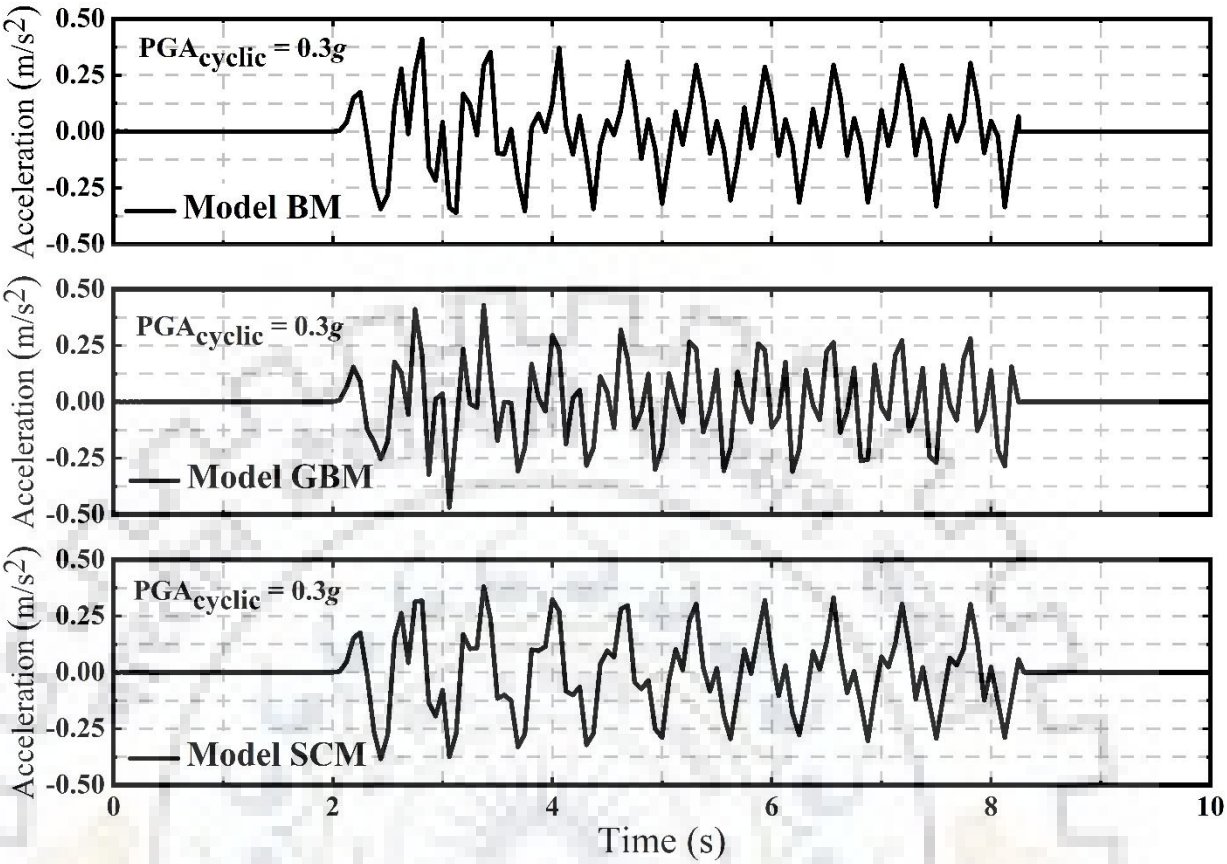

Fig. 6.10 Typical Crest acceleration time-histories of different embankment models under 0.3g cyclic amplitude.

6.6 RESPONSE UNDER SEQUENTIAL EARTHQUAKE GROUND MOTION

In the present section, an attempt has been made to understand the dynamic behaviour of embankment on liquefiable soil, considering ten different sequential ground motions as input motion. These ground motions are taken from the database of the COSMOS virtual data center. Table 6.5 shows the important characteristics of the ground motions along with the occurrence time and station details. The acceleration time-histories of ten ground motions are shown in Fig. 6.11.

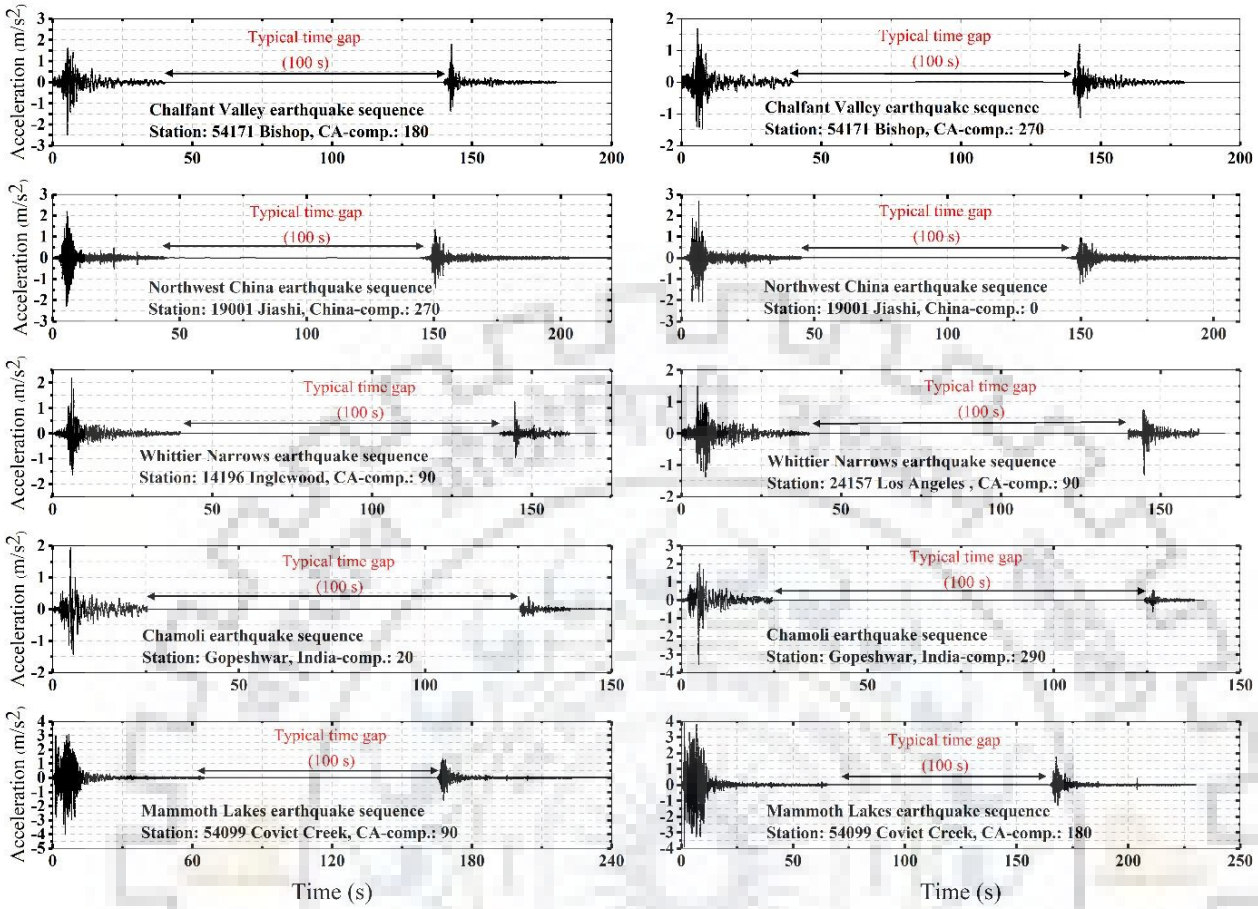

Fig. 6.11 Acceleration time-histories of different sequential earthquakes considered in the present study.

Each of the sequential earthquake motions has been separated into two different motions considering 100 s time gap between the main shock and the aftershock events (Fig. 6.11). Similar time gap has been considered in a study by Zhang et al. (2013). The gap period of 100 s has been considered to be of zero acceleration which will lead to the consolidation of foundation soil layers. It has been observed that no significant change in the embankment settlement occurred during the consolidation stage in comparison to the main shock events. However, the minimum r_u below the embankment toe has been found to be nearly 0.30 at the end of the consolidation period for the model BM and GBM. However, complete dissipation of EPP has been observed in the case of model SCM. Figure 6.12 shows the 5% damped spectral acceleration plots over the period for both the main shock and aftershock events. The final settlement of embankment models (BM, GBM, and SCM) are also reported in Table 6.5. In the case of the embankment model BM, the maximum settlement can be observed during all the earthquake events. However, model SCM has shown a maximum reduction

in the embankment settlement almost in all earthquake events except Mammoth Lakes 1980 earthquake (comp. 180).

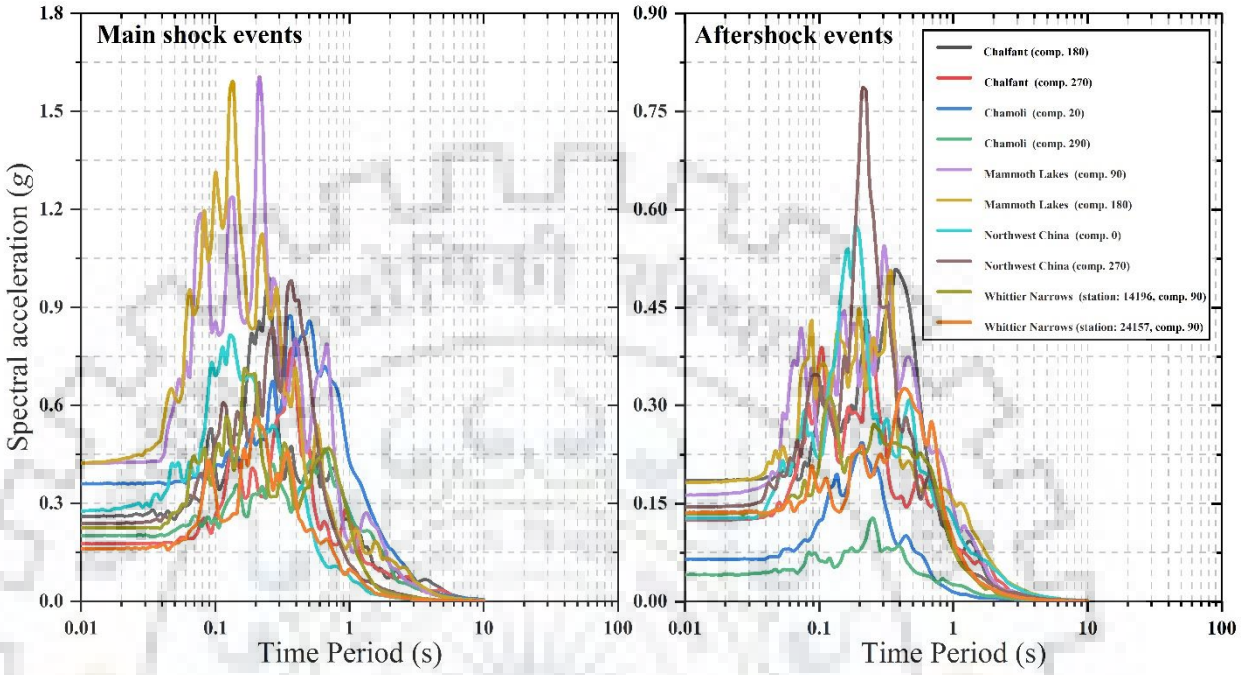

Fig. 6.12 Elastic pseudo-acceleration response spectra (5% damped) of the seismic sequences considered in the present study.

Figure 6.13 shows r_u time-history of three different embankment models at the middle of the liquefiable soil layer beneath the embankment toe (location P_7) due to the application of sequential earthquake motions.

Table 6.5 List of as-recorded main shock and aftershock sequences considered in this study.

No	Earthquake event	Station	Comp	Date	Magnitude	PGA (cm/s^2)	Final Settlement (m)		
							SCM	GBM	BM
01.	Chamoli	Gopeshwar, India	20	1999-03-28 (19:05:11)	6.6 (Mw)	352.83	0.629	0.530	0.444
				1999-03-28 (19:36:06)	5.4	63.40	0.863	0.706	0.627
0.2.	Chamoli	Gopeshwar, India	290	1999-03-28 (19:05:11)	6.6 (Mw)	195.07	0.531	0.474	0.342
				1999-03-28 (19:36:06)	5.4	40.06	0.751	0.627	0.469
03.	Whittier Narrows	24157, Los Angeles, CA	90	1987-10-01 (14:42:20)	6.1 (Mw)	149.60	0.625	0.516	0.404
				1987-10-04 (10:59:38)	5.3	130.10	1.089	0.885	0.695
04.	Whittier Narrows	14196, Inglewood, CA	90	1987-10-01 (14:42:20)	6.1 (Mw)	219.30	0.636	0.524	0.426
				1987-10-04 (10:59:38)	5.3	127.10	1.046	0.851	0.712
05.	Northwest China	19001 Jiashi, China	0	1997-04-05 (23:46:00)	5.9	268.34	0.509	0.362	0.343
				1997-04-06 (04:36:00)	5.9	122.47	1.035	0.774	0.753
06.	Northwest China	19001 Jiashi, China	270	1997-04-05 (23:46:00)	5.9	229.23	0.590	0.459	0.416
				1997-04-06 (04:36:00)	5.9	140.98	1.251	0.954	0.887
07.	Chalfant Valley	54171 Bishop, CA	270	1986-07-21 (14:42:26)	6.4 (ML)	169.00	0.730	0.617	0.484
				1986-07-31 (07:22:40)	5.8 (ML)	121.14	1.407	1.141	0.977
08.	Chalfant Valley	54171 Bishop, CA	180	1986-07-21 (14:42:26)	6.4 (ML)	249.10	0.750	0.639	0.502
				1986-07-31 (07:22:40)	5.8 (ML)	179.66	1.425	1.149	0.997
09.	Mammoth Lakes	54099 Convict Creek	180	1980-05-25 (16:33:44)	6.1 (ML)	392.09	1.047	0.794	0.840
				1980-05-25 (16:49:27)	6.0 (ML)	176.79	1.689	1.296	1.371
10.	Mammoth Lakes	54099 Convict Creek	90	1980-05-25 (16:33:44)	6.1 (ML)	402.19	0.750	0.639	0.503
				1980-05-25 (16:49:27)	6.0 (ML)	158.33	1.425	1.149	0.997

From studies reported in previous two Chapters and past studies (Adalier 1996; Okamura and Matsuo 2002), it has been observed that the embankment settlement behavior is closely related to the liquefaction behaviour of the region below the embankment toe. As the toe region starts losing shear strength due to the increased excess pore pressure (EPP), the foundation soil below the embankment crest moves laterally towards the free field due to the increased sideways shear stresses of the toe region. Hence, examining this region due to the dynamic loading event becomes more important than the free field region. However, the central region below the embankment never attains the initial liquefaction (r_u = 1.0) condition.

In the case of model BM, the soil below the embankment toe attains maximum r_u value (close to unity) during the main shock and aftershocks. This observation is worth to be noted that there is a high possibility of re-liquefaction of foundation soil, which may cause additional damage to the structures resting on liquefiable soil. In the case of Chalfant (comp. 180), Northwest China (comp. 0 and comp. 270), and Whittier Narrows (stn. 24157) earthquakes, $r_{u\text{-}as,max}$ ($r_{u,max}$ during the aftershock event) found to be exceeding the $r_{u\text{-}ms,max}$ ($r_{u,max}$ during the main shock event). However, it is worth to be mentioned that the complete dissipation of EPP was not considered after the main shock event.

Most of the past research is mainly focused on main shock events, and design guidelines are also based on this concept only. However, sequential ground motions can lead to a severe detrimental condition when there is a possibility of re-liquefaction of the foundation soil deposit. However, noticeable effectiveness of mitigation can be observed in the case of model GBM and SCM. Figure 6.14 shows a comparison of the maximum excess pore pressure ratio during main shock ($r_{u\text{-}ms,max}$) and aftershock ($r_{u\text{-}as,max}$) at the middle of the liquefiable layer beneath the embankment toe (location P_7). The $r_{u\text{-}ms,max}$ (main shock) for model BM, GBM, and SCM for all 10 sequential input motions range from 0.878 to 1.083, 0.570 to 0.723, and 0.270 to 0.518, respectively. Whereas the range of $r_{u\text{-}as,max}$ (aftershock) is found to be 0.782 to 0.967 for model BM, 0.496 to 0.742 for model GBM, and in the case of model SCM the range is found to be 0.162 to 0.40. It can be seen in both shock events that stone column mitigation was more efficient than the gravel berm technique. However, the upper limit of $r_{u\text{-}as,max}$ was found to be increasing compared to $r_{u\text{-}ms,max}$ in the case of model GBM. This also indicates the effect of surcharge on liquefaction resistance marginally reduces when subjected to sequential earthquake motions.

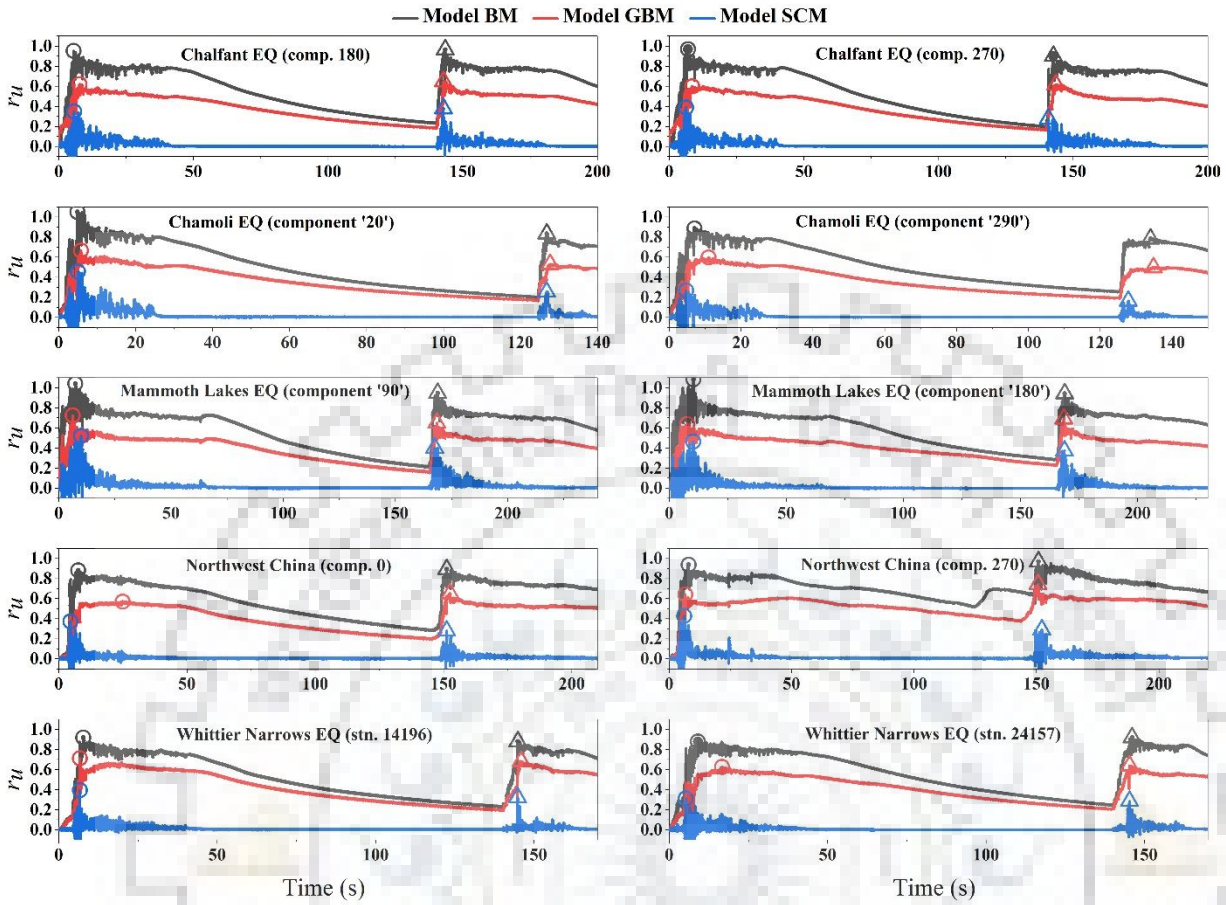

Fig. 6.13 r_u time-history at middle of the liquefiable layer beneath the toe (location P_7) for different ground motions.

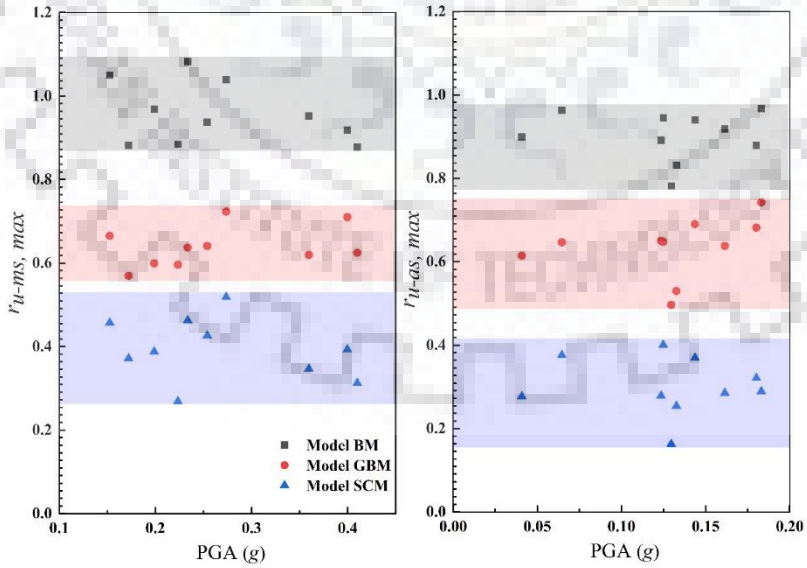

Fig. 6.14 $r_{u,max}$ at mid-depth of the liquefiable layer beneath toe of different embankment models.

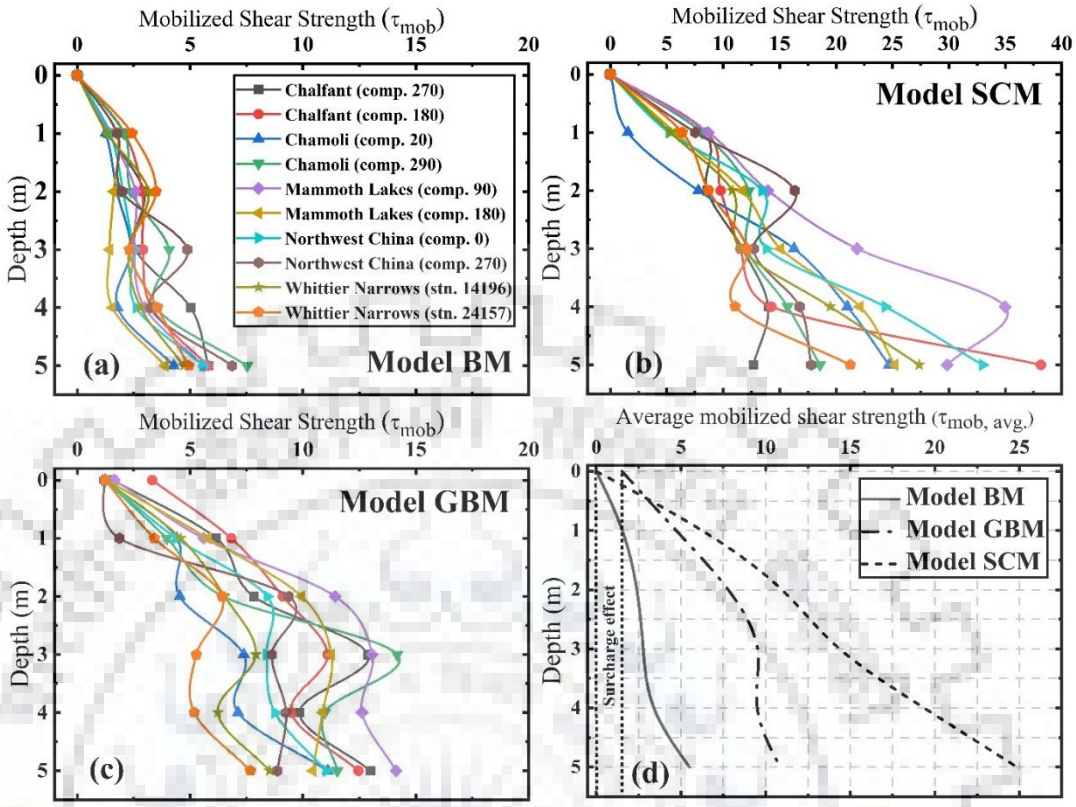

Fig. 6.15 Variation of dynamic shear stress in the liquefiable layer under ten different ground motions.

Figure 6.15 reports variation in the maximum mobilized shear stress τ_{mob} with depth. It is increasing with depth owing to an increase in effective stress with depth. It can be seen that Chamoli (comp. 290) earthquake has produced the maximum stress for BM and GBM models. For the SCM model, Mammoth Lakes (comp. 90) has produced the maximum stress. Stress ground levels are lower in BM and SCM models (close to zero) as compared to the GBM model (1.524 kPa average value). The average maximum shear stresses mobilized ($\tau_{mob,avg.}$) at 5 m depth are about 5.5, 10.9, and 24.9 kPa for BM, GBM, and SCM. But effect of GBM and SCM is clear with increasing depth. Mobilized shear stresses in SCM are higher due to lesser development of EPP as drainage path gets shortened in the presence of stone columns. Improvement in the GBM model is by virtue of an increase in the effective stress due to additional surcharge of gravel berm. A typical representation of I_a - $r_{u,max}$ - embankment settlement has been shown in Fig. 6.16 for both main shock and aftershock events.

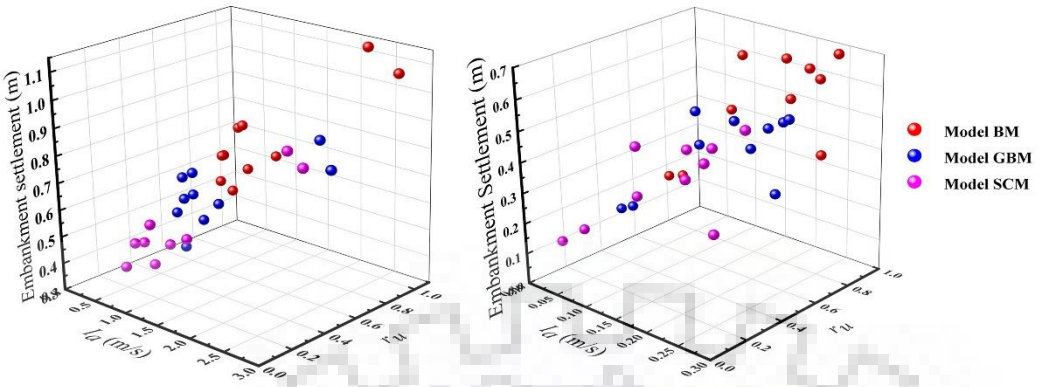

Fig. 6.16 I_a - r_u - embankment settlement plot under ten ground motions.

Figures 6.17a and b represent the bar diagram of the final embankment crest settlement due to main shock and aftershock events of considered 10 sequential ground motions. In case of Mammoth Lake sequential earthquake motions (comp. 90 and 180), the effectiveness of stone column mitigation has been reduced compared to gravel berm mitigation.

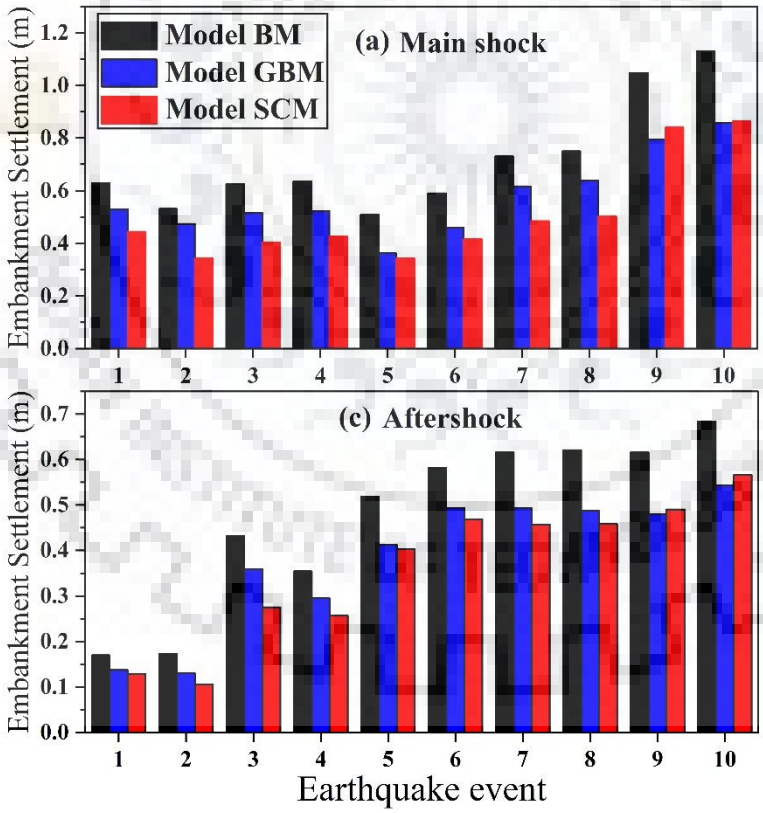

Fig. 6.17 (a) Embankment settlements due to the main shock; (b) embankment settlements due to the aftershock.

These two sequential ground motions have maximum Arias intensity (I_a) of 2.475 m/s and 2.787 m/s, respectively. This might be a potential reason that stone column mitigation showed less effectiveness in mitigation than gravel berm.

The seismic response of models has been evaluated against ten different sequential ground motions. These ground motions have different PGA, frequency content, and time duration of a shock event. Arias intensity (I_a) can be the best intensity measure which reflects three major ground motion characteristics like PGA, frequency content, and time duration of motion (Kramer 1996). It integrates PGA and frequency content over a time duration. Moreover, it can efficiently quantify record-to-record variability of earthquake-induced displacements (Wang 2012; Huang and Wang 2017; Cascone et al. 2021). The present study uses the 1-D wave propagation program DEEPSOIL V7.0 to compute the Arias intensity of 10 sequential ground motions. It can be used as a parameter for comparing both $r_{u,\max}$ and settlement under different motions. Table 6.5 reports the final settlement of three different embankment models under ten sequential earthquake motions. In general, it can be concluded that both $r_{u,\max}$ and settlement increase with Arias intensity (I_a), which is also evident from Fig. 6.16. In the aftershock motions, Arias intensity (I_a) is less than 10 % of corresponding main shock events in most of the motions. In spite of having lesser intensity, both $r_{u,\max}$ and settlement are attaining values closer to the main shock response. The average settlement ratios (aftershock response/main shock response) for each model are 0.681(BM), 0.689(GBM), and 0.744(SCM), with an overall average 0.704. The similar average $r_{u,\max}$ ratio for each model are 0.952(BM), 0.986(GBM), and 0.766(SCM). It can be seen that aftershock events are nearly generating EPP closer to the main shock.

Relative settlements are crucial in the performance of a super-structure. It should be as minimum as possible. In the present study, the difference in the maximum settlement in the central region and crest settlement is normalized with respect to the maximum settlement. It is considered a relative embankment settlement parameter ($\Delta_{e,dif}$). Figure 6.18a shows a typical display of relative embankment settlement. Figure 6.18b shows the plot of the percentage relative embankment settlement parameter $\Delta_{e,dif}$ for different input motions. An average value of 15 % for $\Delta_{e,dif}$ can be observed in the case of model BM.

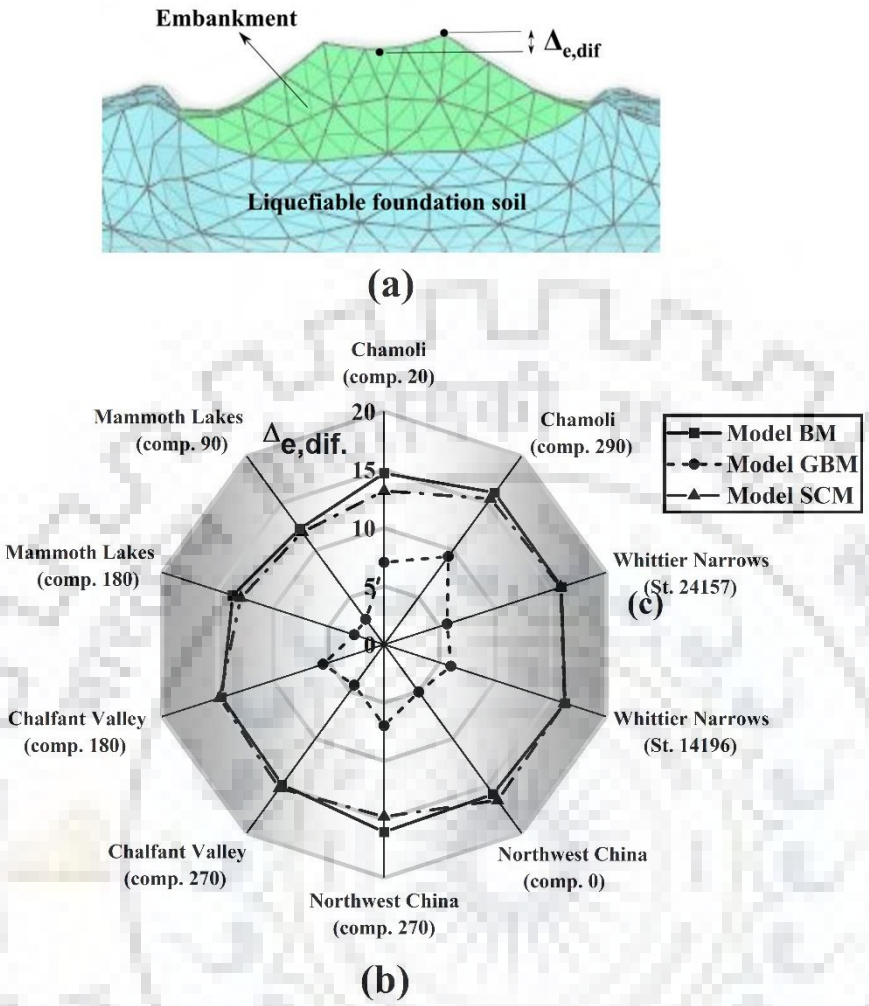

Fig. 6.18 (a) A typical display of relative settlement of embankment crest; (b) plot for estimated relative settlement of three embankment models.

However, a marginal reduction in the relative embankment settlement can be seen with the improved stone column model. An average value of 14.7% has been observed for $\Delta_{e,dif}$. This might be attributed to the combination of the shock-absorbing nature of the stone column and marginally affected wave propagation at the embankment level in the shaking event. But a noticeable reduction in the relative embankment settlement can be observed with the gravel berm mitigation. The maximum value of 9.3% (average 5.5%) for $\Delta_{e,dif}$ has been noticed in the case of the GBM model. Gravel berms provide additional side restraints resulting in additional stability to the embankment slopes. That may result in a lesser relative embankment settlement value.

The settlement ratio $S_{r,i}^{main/after}$ can be considered to assess the effect of mitigation. It can be defined in the mathematical form considering the ratio of settlement $U_{z,i}^{GBM/SCM}$ of the mitigated model for the i^{th} event to the corresponding settlement $U_{z,i}^{BM}$ in the BM model as

$$S_{r,i}^{main/after} = \frac{U_{z,i}^{GBM/SCM}}{U_{z,i}^{BM}} \tag{6.1}$$

Figure 6.19 shows settlement ratios for the mitigated model GBM and SCM with reference to a settlement in the BM model in order.

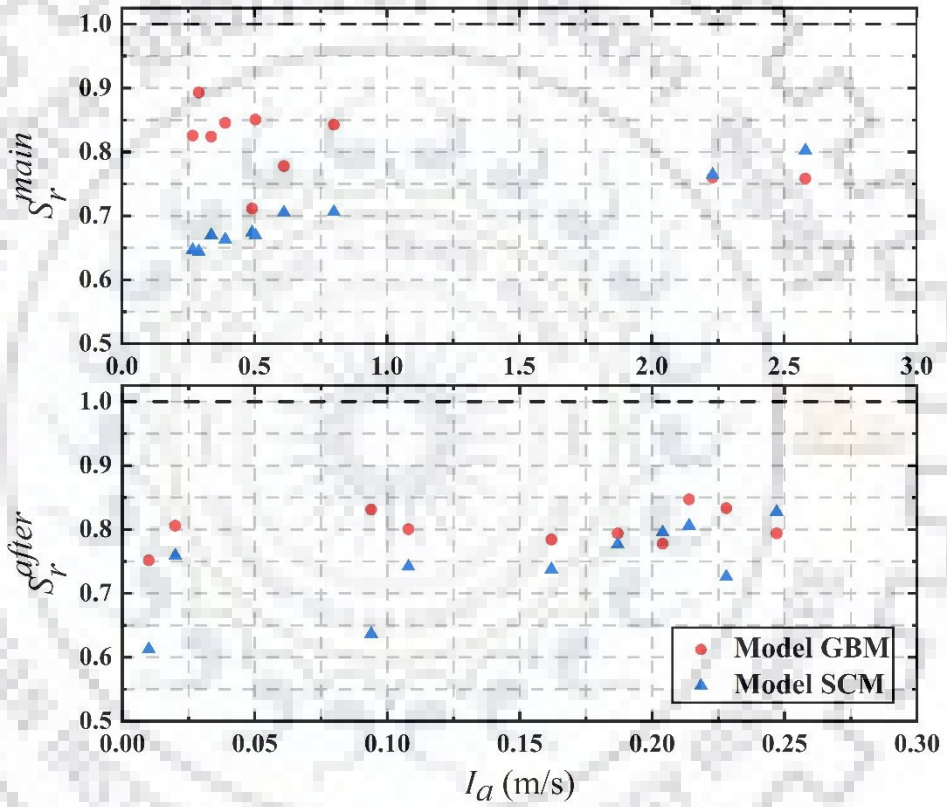

Fig. 6.19 Settlement ratio of model GBM and SCM with respect to model BM.

To get a better understanding of effect of both the mitigations during the aftershock events, ratios of Arias intensity, $r_{u,max}$ and settlement (S) of all aftershock and main shock events are evaluated for models BM, GBM, and SCM. Settlement ratio and $r_{u,max}$ ratio were computed from taking ratio with the respective value of the main shock response for given model as defined in Eq. (6.2).

$$Ratio_{ru} = \frac{r_{u,as}^{Model}}{r_{u,ms}^{Model}} \quad and \quad Ratio_S = \frac{S_{as}^{Model}}{S_{ms}^{Model}} \tag{6.2}$$

Table 6.6 summarizes $r_{u,max}$ ratio and settlement ratio for a range of aftershock to main shock events along with Arias intensity ratio. The average Arias intensity ratio is 0.26. The average values of $r_{u,max}$ *ratio* are 0.94, 0.99 and 0.77 for BM, GBM and SCM models respectively. Similarly, average values of the settlement ratio are 0.67, 0.68 and 0.73 for BM, GBM and SCM models respectively. Comparing with the average ratio of input arias intensity (0.26), settlement and r_u responses are factored by (3.6, 3.8, 3.0) and (2.6, 2.6, 2.8) times respectively for BM, GBM and SCM models. For Northwest China earthquake (0 and 90 components), settlement ratios are observed greater than one. Similarly, in case of Whittier Narrows and Northwest China earthquakes summarizes $r_{u,max}$ *ratio* were found to be greater than one for GBM models.

Table 6.6 Summary of $Ratio_{ru}$ and $Ratio_S$ due to the main shock and aftershock events.

#	I_a (MS)	I_a (AS)	$Ratio_{ru}$ **(BM)**	$Ratio_{ru}$ **(GBM)**	$Ratio_{ru}$ **(SCM)**	$Ratio_S$ **(BM)**	$Ratio_S$ **(GBM)**	$Ratio_S$ **(SCM)**	I_a ratio
1	0.267	0.094	0.9087	0.8963	0.7722	0.8213	0.7508	0.9761	0.3521
2	0.290	0.010	0.9432	0.9315	0.6846	0.3258	0.2743	0.3099	0.0345
3	0.337	0.228	0.8954	1.1648	0.6255	0.6058	0.6329	0.6559	0.6766
4	0.390	0.108	0.9594	0.9594	0.6502	1.0196	1.1381	1.1749	0.2769
5	0.492	0.187	0.9171	0.9729	0.8228	0.5931	0.6134	0.5452	0.3804
6	0.504	0.162	0.9643	1.0307	0.8237	0.9864	1.0741	1.1274	0.3214
7	0.611	0.214	0.9711	1.1519	0.9536	0.8438	0.7990	0.9442	0.3502
8	0.800	0.020	0.8907	0.7936	0.5192	0.2703	0.2585	0.2905	0.0250
9	2.230	0.247	0.9706	0.9155	0.7099	0.6792	0.6851	0.6455	0.1108
10	2.580	0.204	0.9943	1.1443	1.1933	0.5664	0.5717	0.6361	0.0791
Avg.			0.9415	0.9961	0.7755	0.6712	0.6798	0.7306	0.2607

During the main shock event, the stone column mitigation (SCM) shows a lower settlement ratio except in the case of a higher intensity level (I_a). With an increasing level of Arias intensity (I_a) the effectiveness of stone column mitigation reduces, which has been reported in previous chapters. In case of an aftershock event up to 0.162 m/s Arias intensity (I_a) level, stone column mitigation gave a lower settlement ratio compared to the gravel berm mitigation. Afterward, a marginal difference in settlement ratio can be seen between both the mitigation model. Comparison of settlement ratios

in the main shock and aftershock events for the SCM model reveals a small reduction in the effectiveness of stone column mitigation aftershock, as apparent from slightly higher values.

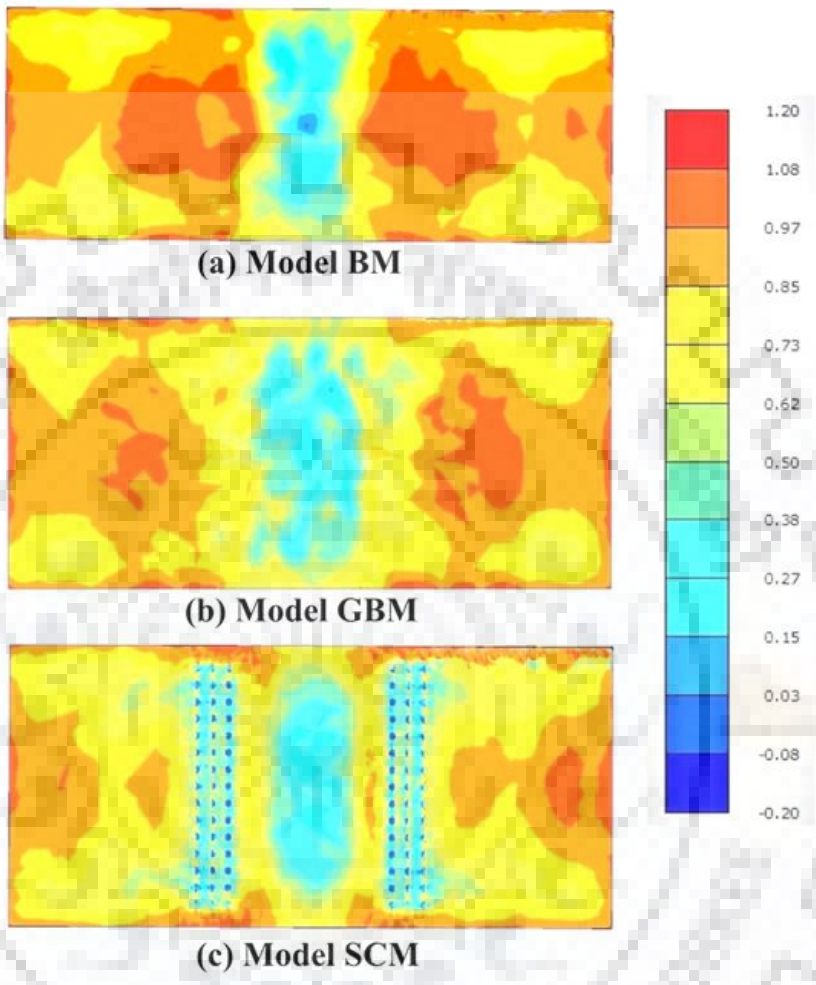

Fig. 6.20 Contour plot of $r_{u,max}$ of different models for Chamoli earthquake (comp. 290) at 3 m depth of foundation liquefiable soil.

Figure 6.20 shows the plan view of the mid-section of the liquefiable foundation soil layer for the contour of $r_{u,\,max}$ distribution during the Chamoli (comp. 290) earthquake for the models BM, GBM, and SCM. The central foundation soil region below the embankment never attains the initial liquefaction condition in three embankment models. In model BM, $r_{u,max}$ can be observed to be nearly 1.0 around the toe region. Whereas, model GBM and SCM show approximately the $r_{u,max}$ value below 0.80 and below 0.40. This again shows the effectiveness of mitigations in reducing the excess pore pressure ratio (r_u) below the embankment toe region.

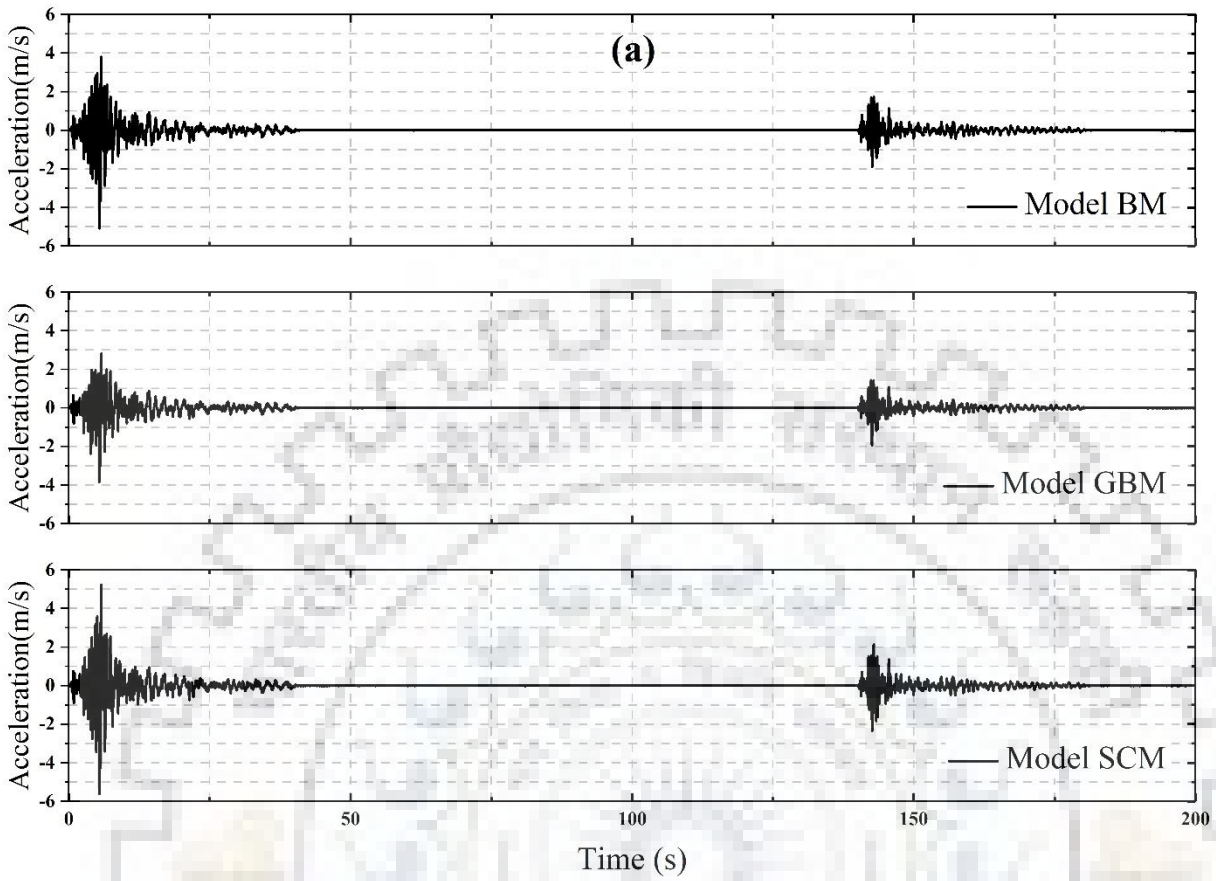

Fig. 6.21 Embankment crest acceleration of different models during Chalfant Valley (comp. 180 and 270) sequential earthquake.

Figure 6.21 shows the acceleration time history at the embankment crest point for three different models subjected to the Chalfant Valley (comp. 180 and 270) time histories. For the BM model, the maximum acceleration was observed to be -5.09 m/s^2 (comp. 180) and 4.16 m/s^2 (comp. 270). It can be observed that the gravel berm technique effectively reduces the acceleration of the embankment structure (-3.82 m/s^2 and 3.86 m/s^2). This might be attributed to the increased inertia due to the presence of gravel berms. At the same time, the stone column mitigation resulted in an increased acceleration in the embankment structure (-5.62 m/s^2 and 5.21 m/s^2) due to the increased stiffness of foundation soil beneath the embankment toes.

Figure 6.22 shows embankment settlement time histories of 3 embankment models under the same Chalfant sequential earthquakes (comp. 180 and 270). The embankment model without any mitigation (model BM) showed 1.425 m and 1.407 m final settlement. Those have been reduced by almost 19% and 30% by gravel berm and stone column mitigations. This also indicates that for earth

structures resting on liquefiable deposits, the mitigation of foundation soil is more effective in reducing the settlement.

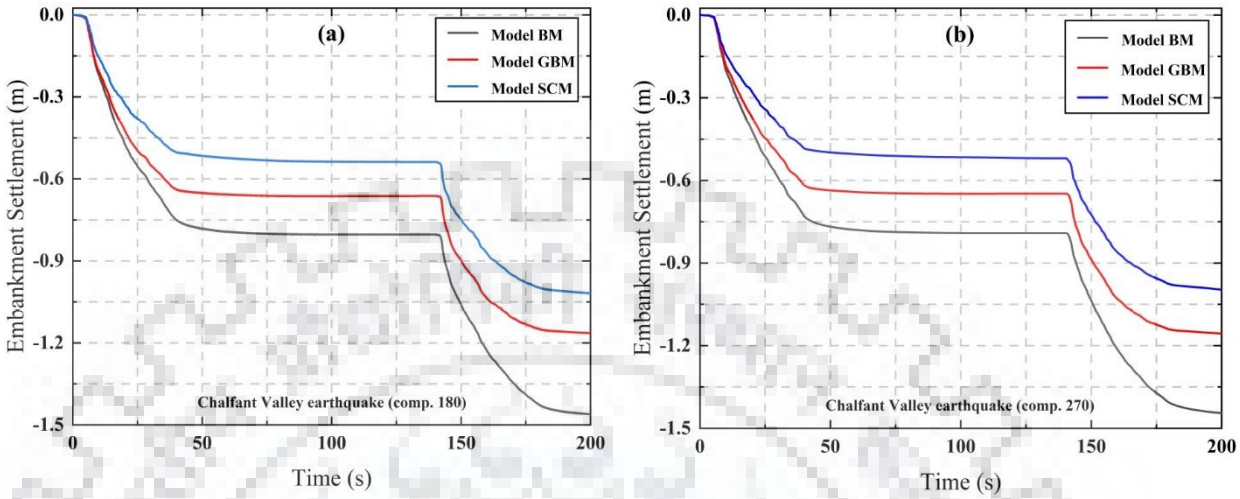

Fig. 6.22 Settlement time-history different embankment models during (a) Chalfant Valley (comp. 180) and (b) Chalfant Valley (comp. 270).

Figure 6.23 shows the plot of the intensity of input motion versus that at embankment crest for three embankment models. The Arias intensity of the embankment crest has been obtained from the acceleration time history at the crest during ten sequential ground motions. A linear relationship can be observed between the intensities of input motion and at the crest of embankments.

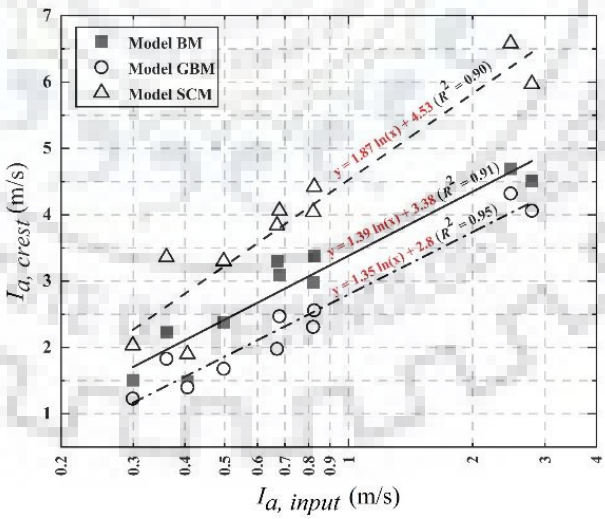

Fig. 6.23 Variation of I_a of embankment crest for different models.

As earlier, it was observed that gravel berms resulted in a reduction of acceleration amplitude; hence, a lower intercept value of linear relation can be observed. Moreover, higher values can be seen in

the case of model SCM. It can be inferred from the slope of best-fit lines that the Arias intensity of the embankment crest in SCM is increasing with an increase in the input Arias Intensity.

6.7 SUMMARY AND CONCLUDING REMARKS

Numerical analyses presented in this study considered the liquefaction-induced settlement behaviour of embankment resting on loose foundation soil with two different mitigation approaches. Three-dimensional FEM modeling has been carried out using PLAXIS 3D program. Foundation soil layers have been modeled using calibrated UBC3D-PLM material model. Calibration of the material model has been conducted using a single-element cyclic loading test with the laboratory test results of Arulmoli et al. (1992), and validation of the embankment model under dynamic loading has been done against the centrifuge study reported by Adalier (1996). Initially, cyclic ground motions have been applied to three different embankment models with varying PGA. Both $r_{u,max,}$ and crest settlement increase with an increase in PGA_{cyclic}. Stone column mitigation measure is more effective in reducing $r_{u,max,}$ and the crest settlement as compared to gravel berm mitigation. After assessing the efficacy of the numerical model for a dynamic response, ten different sequential earthquake motions were applied to highlight the effect of mitigation and aftershock motions. Based on the results obtained from the study, the following key conclusions have been drawn:

1. In the case of the BM model, the soil below the embankment toe attains the maximum r_u value (close to unity) during both the main shock and aftershock events. There is a high possibility of re-liquefaction of foundation soil during the aftershock, which may cause additional damage to the structures resting on liquefiable soil. For both shock events, stone column mitigation was more efficient than the gravel berm technique.
2. Mobilized shear stresses in liquefiable soil are more for mitigated models. It is roughly twice as for the GBM model and 4.5 times for the SCM model. In SCM, higher shear stresses can be mobilized in liquefiable soil due to the lesser development of EPP owing to shortened drainage paths in the presence of stone columns. GBM model can resist higher shear stress due to the surcharge effect of gravel berm, leading to an increase in the effective stress.
3. Both $r_{u,max}$ and the embankment settlement increase with the Arias intensity (I_a) of ground motion. Though Arias intensity (I_a) is less than 10% of corresponding main shock events in most of the aftershock motions, both $r_{u,max,}$ and the embankment settlement are attaining values closer to the main shock response. Average response ratios are 0.704 and 0.902 for settlement and $r_{u,max}$.

4. An average relative embankment settlement of 15% was observed for the BM model due to the sequential ground motions. A marginal reduction was observed for the SCM model. A noticeable reduction in relative embankment settlement can be observed with the gravel berm mitigation due to lateral stability offered by gravel berms.
5. The settlement ratio $S_{r,i}^{main/after}$ can be considered as a measure of the effect of mitigation. In main shock events, the stone column mitigation shows a lower settlement ratio except for higher intensity level (I_a). With an increasing level of the Arias intensity (I_a) the effectiveness of stone column mitigation reduces. Marginal reduction in the effectiveness of stone column mitigation is noticed during the aftershock as apparent from slightly higher values.
6. A linearly increasing relationship can be observed between the Arias intensity of input motion ($I_{a,input}$) and the Arias intensity generated at the embankment crest ($I_{a,crest}$). The gravel berms resulted in a reduction of acceleration amplitude due to increased inertia on the embankment structure. On the contrary, stone columns increase acceleration levels at the embankment crest due to the increased stiffness of the foundation soil beneath the embankment.

The primary objective of this study was to evaluate the response of embankment structures considering effect of sequential earthquake motions, to evaluate the main shock and aftershock response of an earthen embankment built on liquefiable soil. This study highlights the effect of aftershock events and consequent associated damages like re-liquefaction. It can be suggested that considering only the main shock effect in the design of earth structures is not adequate. Design should also consider the past earthquake history of aftershocks in the desired region. There is always an inherent uncertainty in the Input seismic motion. Next chapter tries to address the issue by developing fragility curves considering different uncertainties in the modeling.

CHAPTER 7

FRAGILITY ASSESSMENT OF HIGHWAY EMBANKMENT

7.1 INTRODUCTION

Highway embankments resting on loose soil deposits are highly susceptible under seismic motions. This can substantially impact the transportation facility for certain period. During an earthquake event, the ability of various lifeline facilities like transportation is very much essential to move individuals and goods. Recent catastrophic earthquakes in Japan and New Zealand have shown that damage to the geotechnical infrastructure of roadway networks. It is frequently noticeable and just as significant as structural damage (Argyroudis and Kaynia, 2015). When such geotechnical structures are situated in seismically active regions over loose saturated sandy deposits, an earthquake shaking might result in soil liquefaction leading towards serious damage (Ledezma et al., 2012; Cubrinovski et al., 2012; Yamaguchi et al., 2012; Lombardi and Bhattacharya, 2014). It is crucial to investigate the vulnerability of such geotechnical structures while assessing the seismic risk of the transportation network.

One of the essential components of the probabilistic seismic risk assessment of the existing structures and life support systems is the fragility curve. They relate the intensity of an earthquake to the likelihood of each element at risk exceeding a particular damage condition (like minor, moderate, extensive, and collapse). The fragility curves can be created in a variety of approaches, including analytical, judgmental, hybrid, and empirical (Argyroudis and Kaynia, 2015). Di Ludovico et al. (2020) carried out an empirical study based on 1000 private residential masonry structures spread throughout multiple municipalities that were affected by liquefaction during the 2012 Emilia earthquake. A comparison of the empirical damage revealed that liquefaction had a significant impact on the buildings, demonstrating its applicability to damage scenarios under particular subsurface circumstances. Numerical fragility curve procedures have recently gained popularity because they are easily adaptable to various types of structures and geographical locations where there is a lack of information about the damage records. Most techniques reported fragility assessment for the majority of lifeline components and transportation facilities, although embankments are not thoroughly investigated (HAZUS-MH, 2004). Khalil et al. (2017) evaluated numerical fragility curves for embankments resting on liquefiable soil using an elastoplastic multi-mechanism model. Study considered the embankment settlement as a damage variable and PGA of ground motions as intensity measure (*IM*). A similar study has been reported by Oblak et al. (2020),

where fragility assessment of a traffic embankment resting on a layered liquefiable soil ground has been conducted using PM4Sand material model for simulating liquefiable soil condition. Study considered permanent vertical settlement of embankment middle point of top surface as the damage index (*DI*) and PGA as the intensity measure (*IM*). Past studies (Bhatnagar et al. 2016) have shown the efficacy of UBC3D-PLM material model to simulate the embankment response due to liquefaction phenomenon of foundation soil and the dilation of dense sand under dynamic loading. Argyroudis and Kaynia (2015) have recently studied the fragility assessment of earthen embankment for highway infrastructure. In the majority of empirical or statistical fragility studies, soil characteristics or embankment geometry is not well characterized. Maruyama et al. (2010) derived fragility functions for the expressway embankments based on damage datasets from recent earthquakes in Japan. There are two functions offered: one for severe damage, which affects traffic serviceability, and the remaining one for all damage to highway embankments.

However, seismic liquefaction of foundation sandy soil is a critical aspect in geotechnical investigation. The last few decades have seen a major advancement in the field of soil constitutive models for sands (Yang et al., 2003; Taiebat and Dafalias, 2008; Andrianopoulos et al., 2010; Boulanger and Ziotopoulou, 2013; Ye et al., 2012; Galavi, 2021). Hosseinejad et al. (2019) numerically simulated the failure of lower San Fernando dam under 1971 earthquake. A generalized plasticity theory has been adopted to simulate the elasto-plastic behavior of the soil under seismic loading and dynamic analysis of through Darcy and non-Darcy flow models. It is worth to be mentioned that constitutive models such CycLiq (Wang et al., 2014; Wang et al., 2021), Ta-Ger (Tasiopoulou and Gerolymos, 2016), and Sanisand-Msf (Yang et al., 2022) have shown significant development in the field of simulation of liquefaction and post-liquefaction behaviour.

In the present study, an attempt has been carried out to develop numerical fragility curves for earth embankments resting on loose saturated sand due to earthquake events. To simulate the behaviour of liquefaction, a well-calibrated UBC3D-PLM material model (Galavi et al., 2013) has been used. Based on several parameters, the performance of the embankment is subsequently assessed. This methodology is based on the method described by Argyroudis et al. (2013) and Argyroudis and Kaynia, (2015).

7.2 METHODOLOGY

Figure 7.1 provides the key steps involved in deriving analytical fragility curves. A typical soil profile and different input ground motions are selected to account for the effect of ground motion characteristics and soil conditions on the performance of the embankment.

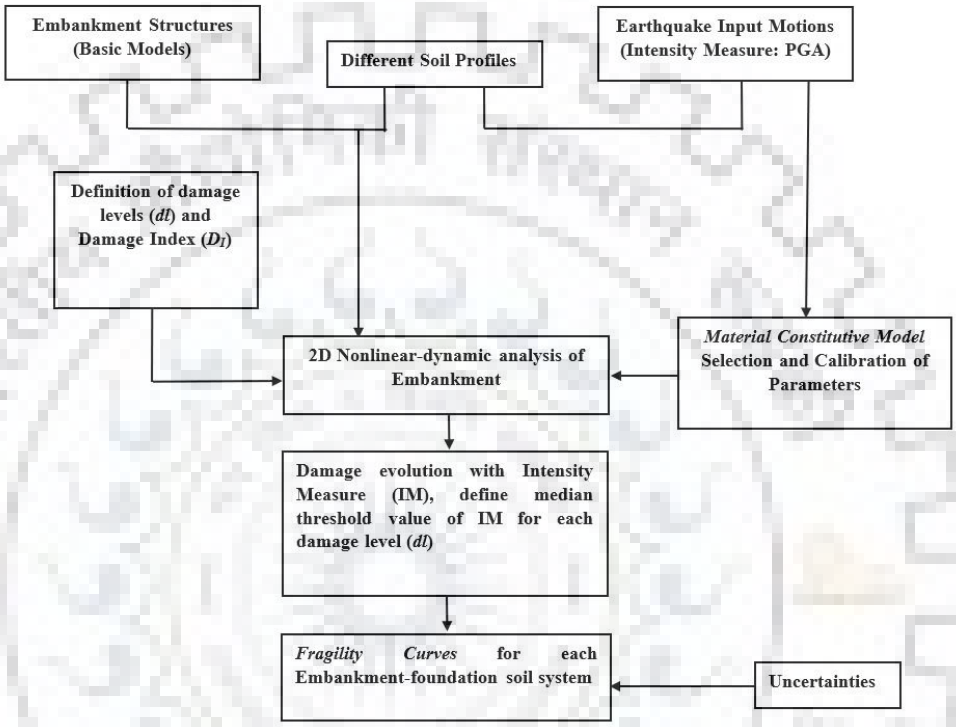

Fig. 7.1 Approach deriving numerical fragility curves for embankments resting on the liquefiable ground.

For the nonlinear dynamic finite element analysis, an effective stress-based elasto-plastic UBC3D-PLM material model was chosen for this study. The main reason is its capability to model liquefaction as well as shear-induced dilation behaviour of the foundation soil below the embankment. An extensive calibration analysis has been conducted for the various soil types taken into consideration in the study to anticipate the compatible level of strains during dynamic loading events. The fragility curves might be generated as a function of the magnitude of seismic excitation by defining the damage level using an appropriate damage index. This technique makes it possible to evaluate the fragility curves of different geotechnical structures by taking into account distinctive properties like the geometries, the input motions, and the properties of the surrounding soil (Argyroudis et al., 2013).

7.2.1 Definition of Damage Levels

Earthquakes have historically had varying degrees of impact on embankments, as well as fills for roads and railroads. For the damage to be promptly repaired, it is crucial that the induced deformation is smaller than the permitted limit because an earth embankment can be easily fixed in contrast to steel and concrete constructions. The effect of an earthquake on earth structures is generally grouped into two different categories: (1) ground shaking event and (2) failure of ground due to liquefaction, fault deformation, and development of slip surface, etc (Argyroudis et al. 2013). The geometry of the structure (shape and dimensions), the characteristics of the nearby ground, and the severity of the ground failure all have an impact on how seismically resistant a structure is. The following criteria are directly related to an embankment's damage: (a) the age of the embankment; (b) topographical factors, including the embankment geometry (Ikehara, 1970). Sometimes embankments are built on liquefiable deposits of soil, and due to seismic events, the foundation soil underlying the embankment loses its bearing capacity, which may lead to excessive settlement and lateral spread (from a few centimeters to many meters). Due to this, embankment structures face severe damage (subsidence), and cracks may appear on the road surface built on that embankment. Based on the description of damage, functionality, and cost for repairing, different studies have proposed different damage levels for various elements of a highway system network (HAZUS-MH, 2004; Werner et al., 2006; Maruyama et al., 2010). The damage levels (dl_i) defined by the European project SYNER-G (2013) are used in the current study (Table. 7.1). The levels are based on peak embankment settlement (PES) of the embankment surface, which defines the damage index (DI) of the embankment system. Based on a wide range of observed values, the mean PES value has been calculated, in particular for minor, moderate, and significant damage states (minimum, maximum).

Table 7.1 Definition of different damage states.

Damage Level	**Permanent Vertical Settlement (m)**			**Serviceability**
	Minimum	**Maximum**	**Mean**	
Minor (dl_1)	0.02	0.08	0.05	Open, reduced speed or partially closed
Moderate (dl_2)	0.08	0.22	0.15	Closed or partially closed
Extensive (dl_3)	0.22	0.58	0.40	Closed

These damage level definitions are congruent with the existing systems and are based on expert opinion. The chosen criteria have an impact on how well the road will function. These limits are also

in line with research by Tokida (2012), who used driving experiments with small and big vehicles to determine the maximum settlement states for road embankments in relation to driving speed.

7.2.2 Definition of Parameters for Fragility Curve

Fragility functions express the likelihood of surpassing different limit states for a given ground shaking level. A number of earthquake parameters can be used to describe the level of shaking, depending on the structure in concern. Spectral acceleration, velocity, displacement, peak ground acceleration (PGA), and permanent ground displacement (PGD) are a few of these. Fragility curves are often defined by a lognormal probability distribution function, which is given below:

$$P_f\ (dl \geq dl_i \mid S) = \Phi\left[\frac{1}{\beta_{tot}}.\ln\left(\frac{IM}{IM_{mi}}\right)\right] \tag{7.1}$$

P_f is the likelihood that a specific damage level (dl) will be exceeded for a specific intensity level specified by the intensity measure (IM) of an earthquake (for example, PGA), and Φ is the typical cumulative probability function. The median threshold value of IM necessary to produce the i^{th} damage level is denoted by the symbol IM_{mi}, and the entire lognormal standard deviation is denoted by β_{tot}. Hence, for defining the fragility curves as per Eq. (7.1) requires two parameters, IM_{mi} and β_{tot}.

A damage index (DI) that indicates when a limit state has been surpassed defines the state of damage (of embankment in the current study) (Table 7.1). Fragility curves are evaluated using the evolution of the damage index (DI) with increasing earthquake intensity (IM) while taking into account the related uncertainty. A representation of several points representing the outcomes of a study in terms of the damage index (DI) at various degrees of earthquake intensity is shown in Fig. 7.2. Based on the description of the total variability linked to each fragility curve and the best fit line from the regression analysis, the solid line shows the estimate of the median threshold value of the intensity measure (IM_{mi}) needed to cause the i^{th} damage level (dl_i). It is necessary to estimate a lognormal standard deviation (β_{tot}) that captures all the variability connected to each fragility curve. The description of record-to-record collapse uncertainty (β_{RTR}), the design requirement-based collapse uncertainty (β_{DR}), material test data-related uncertainty (β_{TD}), and the modeling-related uncertainty (β_{MDL}) are the main sources of uncertainties that are taken into consideration (FEMA P695, 2009). The total variability (β_{tot}) is calculated using the combination of the above-mentioned uncertainties (Eq. 7.2) assuming that all of them are statistically independent as well as lognormally distributed.

$$\beta_{tot} = \sqrt{\beta_{RTR}^2 + \beta_{DR}^2 + \beta_{TD}^2 + \beta_{MDL}^2} \tag{7.2}$$

The uncertainty parameters have been considered based on the literature FEMA P695 (2009) because a more accurate estimation is not available. The standard deviation of the DI, which have been determined for the various input motions at each level of PGA, however, can characterize the final source of uncertainty, which is related to seismic demand.

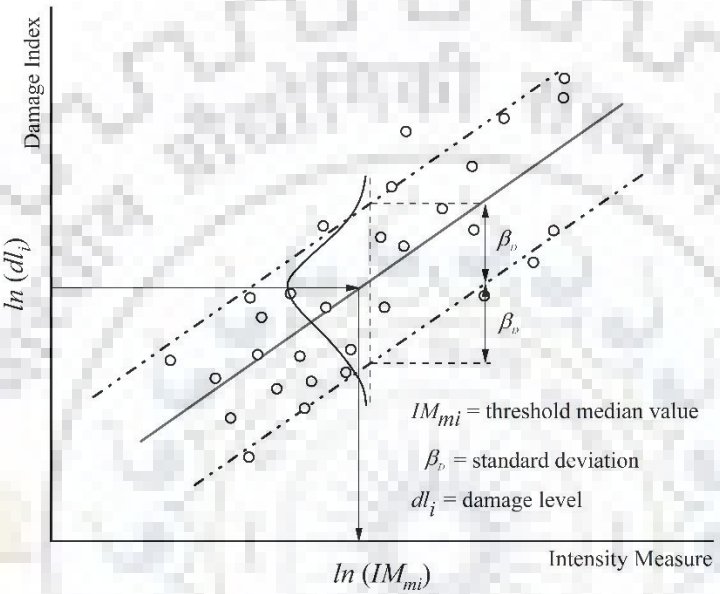

Fig. 7.2 An example of the development of damage with the increasing intensity measure.

7.3 DEVELOPMENT OF FRAGILITY CURVES

For the analyses, a representative geometry of the embankment resting on liquefiable soil is considered (Fig. 7.3). Different dimensions of the embankment geometry (W and h) have been considered in the present study to evaluate the effect of the shape of the embankment. Two different configurations of embankment models have been considered in the current study. Initially, fragility analysis of embankment without any mitigation (Benchmark Model) has been carried out for different geometrical variations. Later, mitigation by densification considering a dense sand column in the foundation soil has been considered in this study. Past studies have shown that effective mitigation can be achieved by densifying the toe region with different mitigation techniques (Kumar et al. 2020, Bhatnagar et al. 2016). Hence, an attempt has also been taken into consideration for the fragility analysis of a mitigated embankment resting on loose foundation soil system. The extent of the densification zone has been kept constant with 6.0 m width in the foundation soil below the embankment by changing the position of the dense column. Based on three different location of

dense column the models are named as (i) dense column outside of the toe (model DCO), (ii) dense column below the toe (model DCT), and (iii) dense column inside the toe (model DCI). Past studies have shown this width of densification for an earth embankment resting on liquefiable soil provide desired mitigation under the application of cyclic loading condition (Adalier 1996; Okamura and Matsuo 2002).

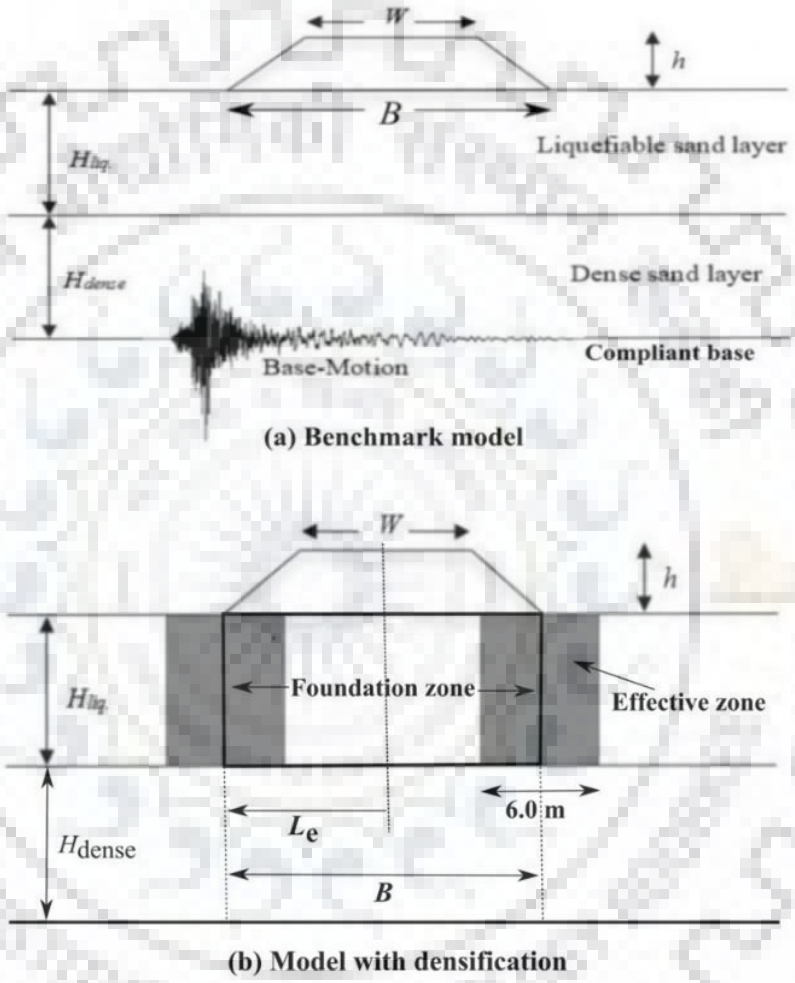

Fig. 7.3 Embankment geometry and properties under the study.

7.3.1 Input Motions

As the outcrop motion for the current study, nine real acceleration time histories from various earthquakes recorded on rock (Class A) or stiff soil (Class B) of Eurocode 8 (2004) were chosen for 2D nonlinear analyses of embankment-liquefiable soil system (Table 2). The acceleration time histories are taken from PEER ground motion database. The frequency content, amplitude, and large duration errors that are naturally present in seismic motion are addressed by the records that are chosen. No particular soil amplification factors are considered because this is clearly taken into

account in the numerical computations and the various soil models, where the seismic motion is applied as outcrop tectonic motion at the base of the numerical model.

Table 7.2 Ground motions selected for the present study.

#	Earthquake	Station (year)	PGA (*g*)	M_w
1	Chi-chi, Taiwan	CHY092 (1999)	0.180	7.62
2	Borrego Mtn.	El Centro Array #9 (1968)	0.133	6.63
3	Northern Calif-03	Ferndale City Hall (1954)	0.162	6.50
4	El Centro	Los Angeles (1940)	0.210	6.90
5	Darfield	RKAC (2010)	0.180	7.00
6	Loma Prieta	Coyote Lake Dam, downst. (1989)	0.160	6.93
7	San Fernando	LA - Hollywood Stor FF (1971)	0.225	6.61
8	Kern County	Taft Lincoln School (1952)	0.160	7.36
9	Imperial Valley, USA	Aeropuerto, Mexicali (1979)	0.170	6.53

However, several seismic codes recommend use of spectrum matching method (Katsanos et al., 2010; Iervolino et al., 2010, 2011). Past studies have shown using spectrum-compatible earthquake motion, a minimum variation in the response can be achieved (Ghosh and Bhattacharya, 2008).

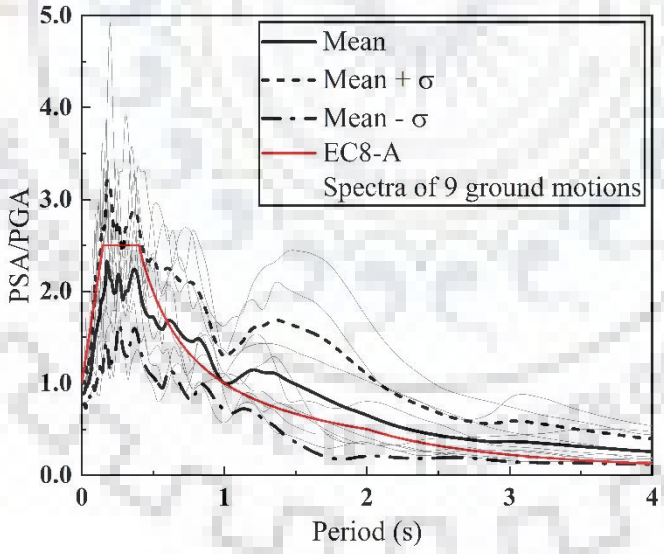

Fig. 7.4 Different spectra of the input motions along with EC8 (2004) spectrum for soil type A.

The nine ground motions were chosen to be real earthquakes in order to represent the dependability of the seismic parameters and characteristics. No particular measure has been taken for fault characteristic, which has been a different aspect and out of the scope of this study. In Fig. 7.4, the EC8 spectrum for soil class A is displayed with the normalized mean and ± one standard deviation

of the response spectra for the chosen motions. For spectral matching, no particular scaling of PGA has been considered. To estimate the vulnerability for a specific PGA value, the user can simply estimate the PGA at the surface and then directly use the pertinent set of fragility curves. Difference between the maximum value of normalized target spectrum and mean spectra is found to be almost 7% which is considerable. However, for a wide range of dynamic analyses, time histories are scaled from 0.02 to 0.90*g* considering 16 divisions to capture all the damage levels for different models considered in this study.

7.3.2 Material Properties

Two different sand layers have been considered in the present study, which consists of a liquefiable layer followed by a dense sand layer. In order to study the variation of relative density of the liquefiable layer, four distinct soil condition has been considered to represent the loose state to medium dense state of foundation soil, which represents 30, 40, 50, and 60% relative density (R_D). The dense sand layer has been considered to have 80% relative density (R_D). In the case of mitigated model, the dense columns have also been considered to have 80% relative density (R_D).

Table 7.3 Basic properties of different sands used in this study.

Properties	**Nevada Sand[a]**	**Ottawa F-65 Sand[b]**	**Toyoura Sand[c]**	**Fraser Sand[d]**
Relative Density, R_D (%)	40, 60	30	50	80
Max. Void ratio (e_{min})	0.887	0.766	0.977	0.94
Min. Void ratio (e_{min})	0.511	0.486	0.597	0.62
Specific Gravity (G_s)	2.67	2.65	2.65	2.71
Mean particle size, D_{50} (mm)	0.15	0.21	0.20	0.26

[a] Data from Arulmoli et al. (1992); [b] Data from ElGhoraiby et al. (2020); [c] Data from Wu and Kiyota (2019); [d] Data from Sriskandakumar (2004)

Grain size distribution of all the sands used in this study along with the boundary of liquefiable soil condition has been shown in Fig. 7.5. All these sand layers have been modeled using elasto-plastic effective stress-based UBC3D-PLM model. The basic properties of the sands considered in the present study are listed in Table 7.3. The embankment material has been modeled using the Mohr-Coulomb model with material properties reported by Bhatnagar et al. (2016) as cohesion, c = 22 kPa; angle of friction, ϕ = 31°; dry unit weight, γ_{dry} = 19 kN/m^3. Initial stress conditions have been simulated considering the Mohr-Coulomb material model. For the dynamic analyses, UBC3D-PLM model has been employed for the sand layers.

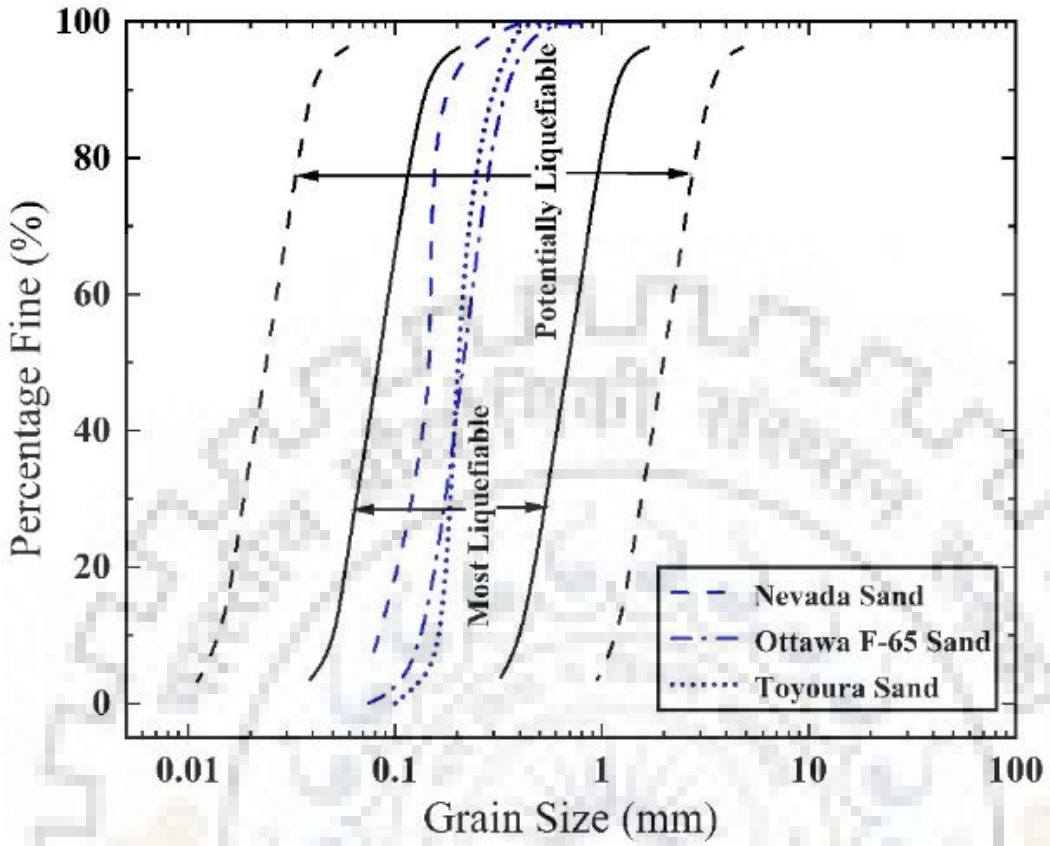

Fig. 7.5 Grain size distribution of different sands and the boundaries of the liquefaction susceptible sand (Adapted from Arulmoli et al. 1992; ElGhoraiby et al. 2020; Wu and Kiyota 2019; Sriskandakumar 2004; Obermeier 1996).

7.3.3 Calibration of Different Sands

Past studies have significantly shown the importance of calibration of a constitutive model for simulating a highly nonlinear dynamic analysis for liquefaction phenomenon where high strain levels can be observed in material under the application of a rapid dynamic loading like an earthquake. Based on the similar calibration procedure done by previous Chapters, material parameters are listed in Table 7.4. The criteria to consider whether the material has reached a liquefaction state are based on the number of cycles to reach the r_u value of 95% or the shear strain value of 1.5% (Armstrong et al., 2013). In the case of loose to medium dense sand, the former criteria were found to be more realistic. In the case of dense sand, the dilation behaviour is more predominant, and hence the later criterion was followed.

Table 7.4 Calibrated UBC3D-PLM model parameters.

Parameters	Type of sand				
	Ottawa-F65 sand	Nevada sand		Toyoura sand	Fraser River sand
R_D (%)	30%	40%	60%	50%	80%
γ_{dry} (kN/m^3)	15.76	15.08	15.76	14.89	19.0
$e_{initial}$	0.682	0.736	0.658	0.718	0.5
k (m/s)	2.2×10^{-4}	6.6×10^{-5}	5.6×10^{-5}	6×10^{-5}	5.5×10^{-6}
ϕ_P	31.2^0	33.65^0	34.32^0	33.4^0	38.9^0
ϕ_{cv}	30.7^0	33^0	33^0	31.1^0	33^o
K_B^e	519.2	566.6	717.4	685.2	937.6
K_G^e	741.7	809.4	1024.8	978.8	1339.5
K_G^p	213.2	350	635.68	550	3597.1
m_e	0.5	0.5	0.5	0.5	0.5
n_e	0.5	0.5	0.5	0.5	0.5
n_p	0.4	0.4	0.4	0.4	0.4
R_f	0.864	0.83	0.75	0.763	0.66
fac_{hard}	0.45	0.45	0.45	0.45	0.45
fac_{post}	0.1	0.1	0.1	0.1	0.1
$[(N_1)_{60}]$	5	6.5	13.2	11.5	29.7

The cyclic shear strength curves from the undrained stress-controlled cyclic simple shear loading of various sands are shown in Figure 7.6, along with numerical predictions from the cyclic loading simulation using a single element.

Sandy soil is K_0 consolidated with zero initial static shear stress ($\alpha=0$) under an initial vertical effective stress (σ_{v0}) of 100 kPa. Figure 7.6 shows a comparison of liquefaction strength curves of sand for three different relative densities, along with the laboratory CSR values with the

corresponding number of cycles to liquefaction. Prior to the application of a constitutive model for nonlinear dynamic analysis, the accuracy of the model under simple cyclic loading should be inspected. For this, the single-element simulation technique has been adopted considering similar stress-controlled loading of cyclic direct, simple shear (CDSS) test by Arulmoli et al. (1992).

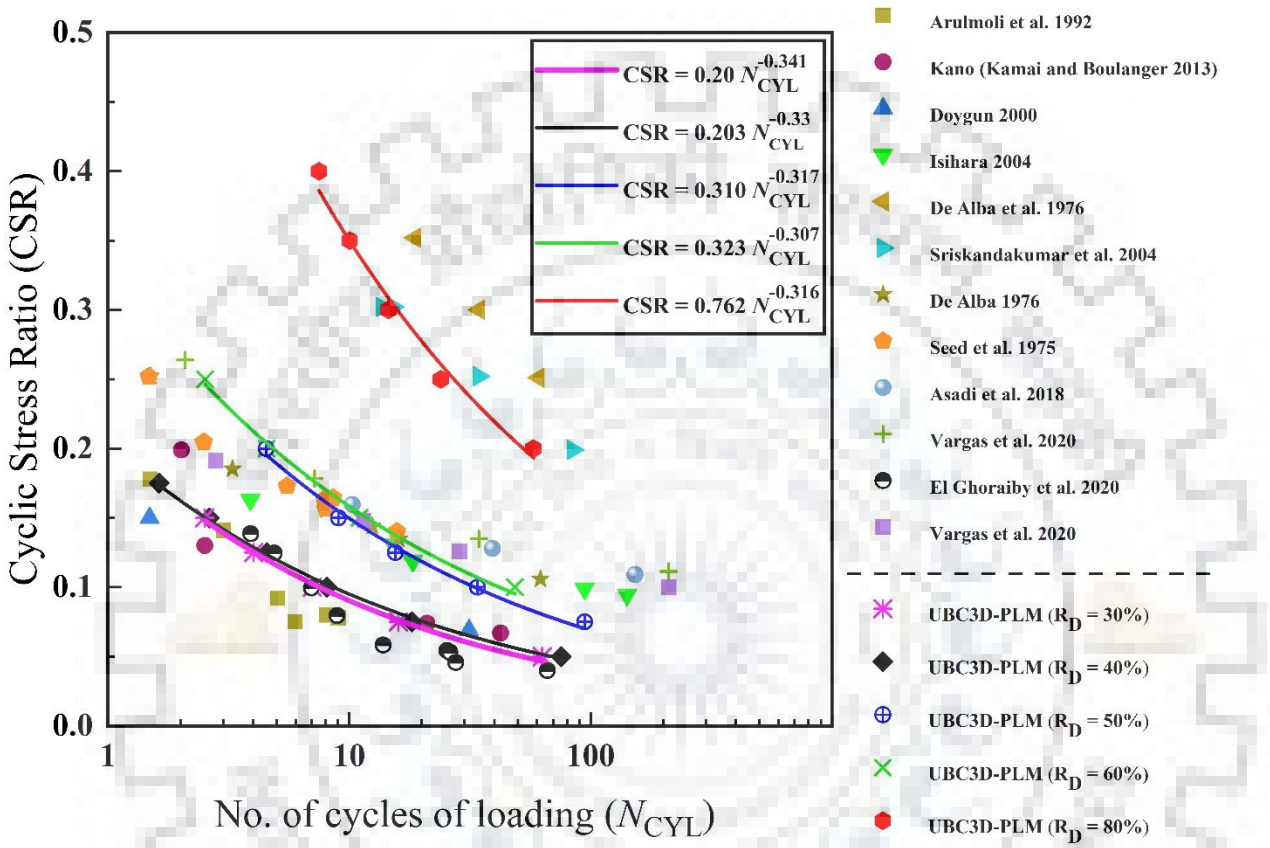

Fig. 7.6 Calibration of liquefaction strength curve of the clean sands considered in the study.

Figures 7.7 and 7.8 show a comparison of the cyclic response of a single element under the same loading environment adopted by Arulmoli et al. (1992) for 40% and 60% relative densities, respectively. A comparison of cyclic responses has shown the effectiveness of this material constitutive model. It can be envisaged that the model can perform with certain accuracy under the application of earthquake loading.

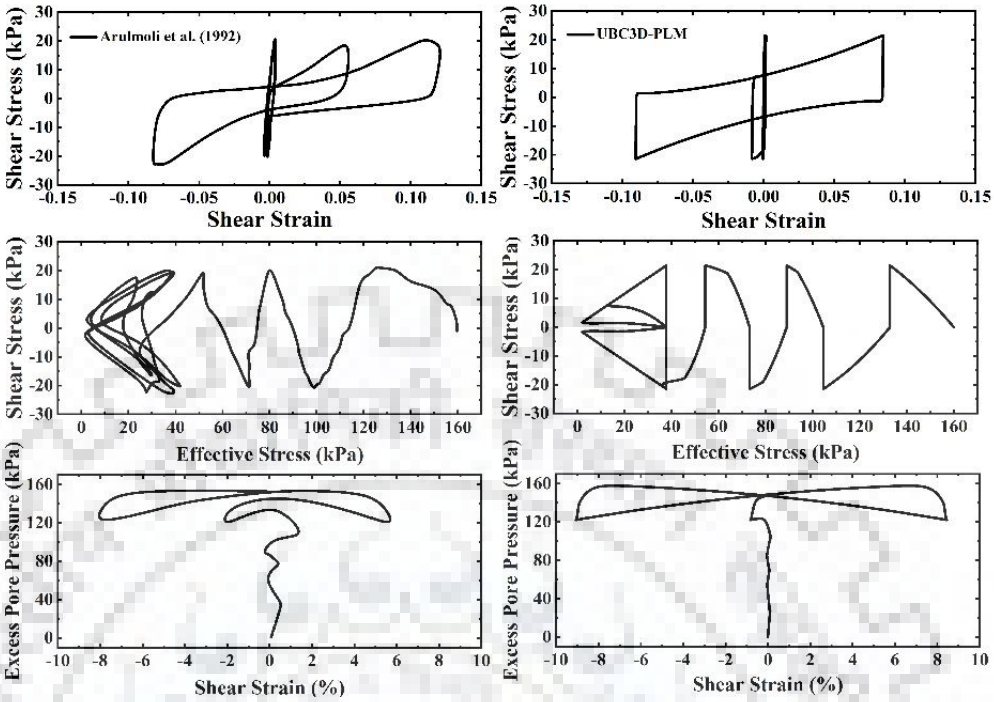

Fig. 7.7 Comparison of CDSS test response of loose sand (R_D = 40%) with numerical prediction using single element testing.

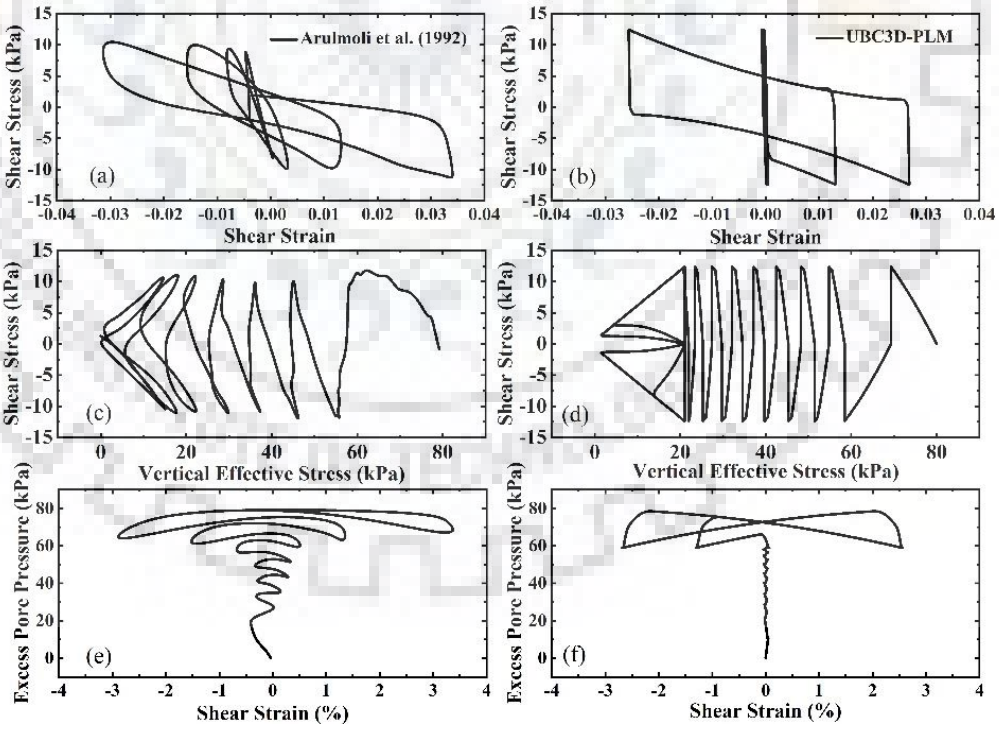

Fig. 7.8 Comparison of CDSS test response of medium dense sand (R_D = 60%) with numerical prediction using single element testing.

7.4 FEM ANALYSIS

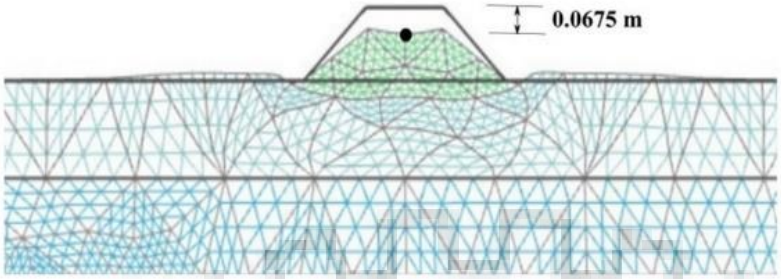

Fig. 7.9 Deformed mesh under Loma Prieta (1989) ground motion (PGA = 0.10*g*, *h* = 4.5 m, R_D = 40%).

Figure 7.9 shows the deformed mesh of embankment under 1989 Loma Prieta ground motion (PGA scaled to 0.1*g*). Which shows the subsidence of embankment and heaving of foundation soil. Fine meshing is adopted in the entire domain.

To evaluate the effect of excess pore pressure (EPP) on the peak embankment settlement (PES), the excess pore pressure ratio (r_u) below the embankment toe has been observed. Figure 7.10 (a) and (b) show the PGA-r_u-PES plots for 40% and 60% relative density of foundation soil. It can be observed that r_u is increasing asymptotically, whereas a linear best fit can be observed in the case of PES. For 40% R_D, the asymptotic plot of r_u is approaching the value of unity at 0.10*g*, whereas for 60% R_D of foundation soil, the corresponding value has been observed to be 0.16*g*.

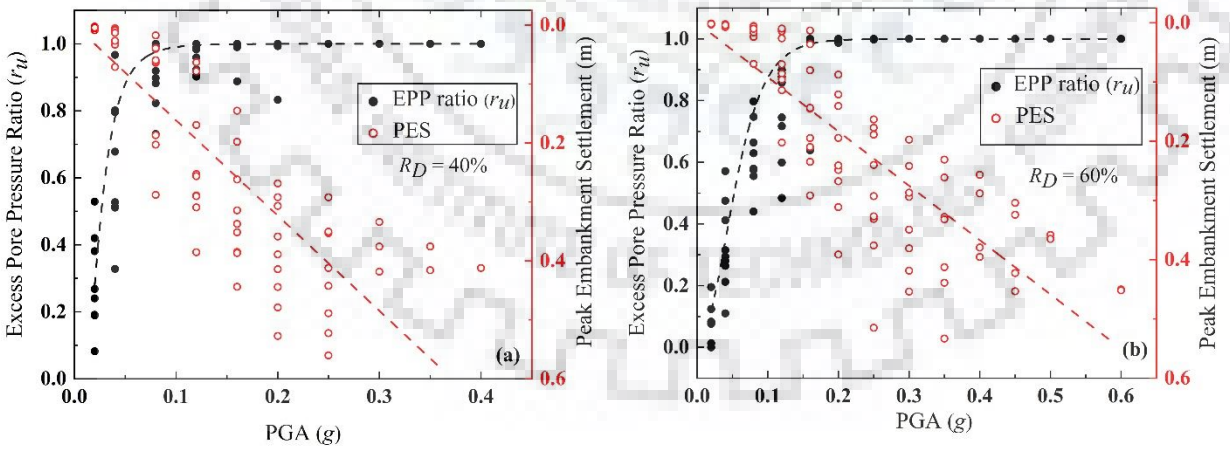

Fig. 7.10 Evolution of embankment crest settlement with increase in r_u below embankment toe for foundation soil relative density (a) 40%, and (b) 60%.

With the increase in the r_u below the toe, regions resulted increase in the embankment settlement. The PGA- r_u-PES plots given in Fig. 7.10 are based on the benchmark embankment model with *W*

= 5.63 m, h = 4.5 m, and H_{liq} = 6.0 m. The study shows that due to the presence of the liquefiable layer immediately below the embankment, higher settlements can be observed at low intensity of loading (PGA). However, a detailed parametric study based on different geometry configurations has been performed for fragility assessment for a better understanding of the phenomenon. Moreover, this study also reveals the evaluation of mitigation of embankment resting on liquefiable soil based on further extensive r_u-PES correlation, which is out of the scope of the present study.

7.5 FRAGILITY CURVES

The median threshold value of PGA for various damage levels serves as the foundation for the fragility curve definition. However, the development of a curve for the computed damage indices in terms of peak embankment settlement (PES) at the surface of the embankment with the increasing PGA values yields the median threshold value of PGA. The PES obtained from the analysis reflects the average total settlement seen at the center and embankment crests (both side). The curves produced in this manner describe the progression of the damage as the intensity of the earthquake increases. The independent variable is PGA, and the dependent variable is PES. The intensity measure at the required damage level has been interpolated from the constructed correlation between the PGA and PES. The present study is mainly concerned with a special case where the ground below the embankment is liquefiable. It has been observed in the preliminary study that the embankment reaches the extensive damage state even under low to medium intensity measures depending on the relative density of soil and geometry of the embankment. Due to the existence of the liquefiable ground directly below the embankment, the lateral outflow of foundation soil can be observed below the embankment crest during ground motion. Past studies also highlighted this aspect (Adalier 1996; Okamura and Matsuo 2002). The embankment settles quickly due to the lateral outflow of foundation soil (Adalier, 1996). The median threshold value of PGA at each damage level listed in Table 7.1 serves as the key parameter of the lognormal probability function, which primarily defines the fragility curve. It is necessary to compute a lognormal standard deviation (β) that describes the overall variability that is correlated with each fragility curve. Quantitative values of uncertainty based on the scale good (B) based on FEMA P695 (2009) are translated from quality ratings for design specifications, test data, and nonlinear models. Hence a value of 0.2 for β_{DR}, $\beta_{TD,}$ and β_{MDL} is considered for this study. However, the last source of uncertainty associated with the record-to-record variability (β_{RTR}) is defined by the variability in embankment response due to the variability of input motion. In the present study, a wide range of parameters have been selected for

understanding the response of embankment resting on the liquefiable ground. Relative density (R_D) of the liquefiable layer, embankment width (W), embankment height (h), and liquefiable layer thickness (H_{liq}) are the parameters that have been taken into consideration. A comparative study of a mitigation model (densification of toe region) has been conducted.

7.5.1 Relative Density

Different relative densities (varying from 30 to 60 %) of the liquefiable layer have been considered for replicating loose (30, 40 %) and medium dense conditions (50, 60 %). Relevant properties of these soils to represent constitutive behaviour are reported in Table 7.3. The depth of the liquefiable layer is 6.0 m thick, which is resting on a 6.0 m thick, dense sand layer (R_D = 80 %). The embankment height (h) and width (W) are 4.5m and 5.63m, respectively.

Figure 7.11 shows the fragility curves for different relative density of foundation soil. As expected, embankments resting on loose saturated sand (R_D = 30% and 40%) are more vulnerable because the loose saturated sand can develop full liquefaction even at lower intensity values of input motion compared to the medium dense soil (R_D = 50% and 60%). This shows that the relative density is of paramount influence in liquefaction phenomenon. With an increase in the R_D of the foundation soil, the seismic demand for embankment structure increases. The estimated parameters of the fragility curves are given in Table. 7.5.

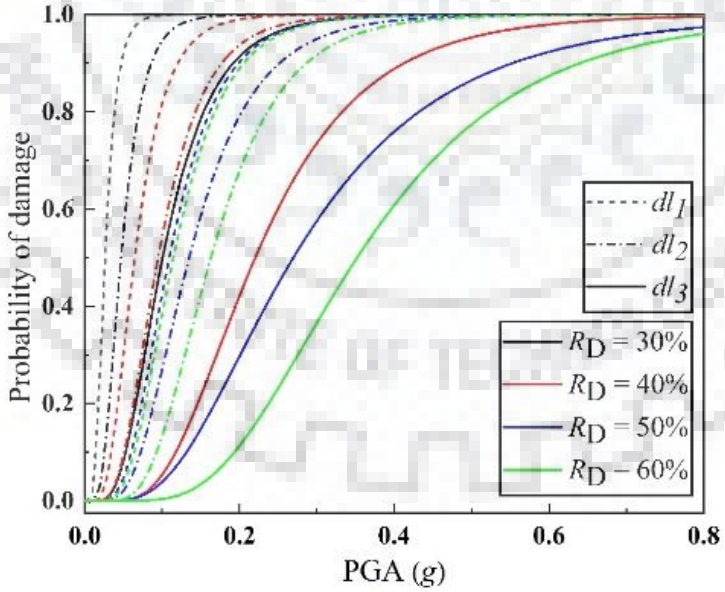

Fig. 7.11 Numerical fragility curve for embankment for different relative densities (R_D) of foundation soil.

Table 7.5 Numerical fragility curve parameters of embankment for varying soil type (h = 4.5 m, W = 5.63 m, H_{liq} = 6.0 m).

Typology	Damage level	Relative Density (R_D)							
		30%		40%		50%		60%	
		μ (g)	β_{tot}	μ (g)	β_{tot}	μ (g)	β_{tot}	μ (g)	β_{tot}
Highway (Benchmark model)	Minor (dl_1)	0.026	0.458	0.065	0.487	0.110	0.467	0.115	0.455
	Moderate (dl_2)	0.047	0.471	0.095	0.486	0.135	0.486	0.163	0.439
	Extensive (dl_3)	0.101	0.503	0.221	0.489	0.270	0.560	0.352	0.467

Figure 7.12 compares the mean values of PGA essential for three different damage levels. For damage level dl_1, the demand for mean PGA increases almost linearly up to 50% relative density and thereafter increases marginally. For damage level dl_2, the demand for mean PGA increases almost linearly up to 50% relative density and thereafter reveal moderate increment at R_D = 60 %. However, for the third damage level dl_3, the demand for mean PGA increases till 60% relative density. Significant increment in demand can be seen between 30 to 40 % relative density. There after linear trend has been observed with approximate 25 % increment.

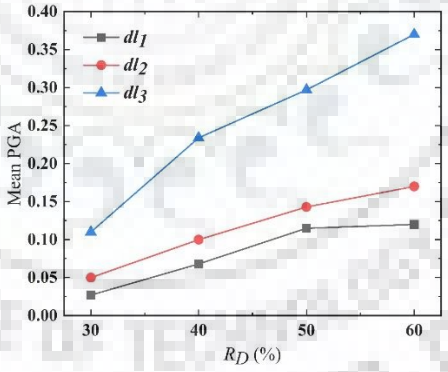

Fig. 7.12 Variation of mean PGA at different damage level (dl_i) with R_D of foundation soil.

7.5.2 Width of Embankment

The influence of embankment width (W) has been studied for a 4.5 m high embankment resting on a 6.0 thick loose saturated sand (R_D =40%) layer. Three different values of W have been considered based on multiples of 5.63 m width of embankment. It can be inferred from the fragility curves presented in Fig. 7.13 that the vulnerability of the embankment slightly reduces with increasing the embankment width (W). From the preliminary analyses also, it has been observed that for the larger

width of the embankment, the central settlement of the embankment surface is reduced compared to the lesser width of embankments. This can be attributed to the increment in effective stress over larger area in foundation soil with increasing width of embankment.

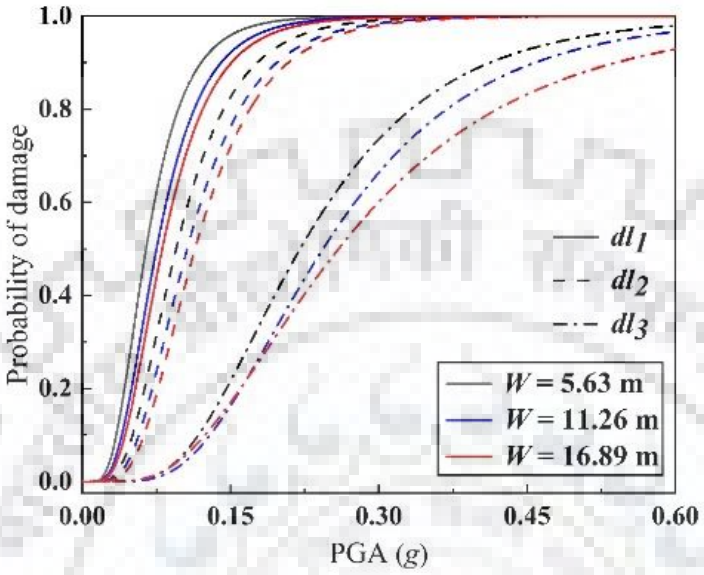

Fig. 7.13 Numerical fragility curves for embankment for different embankment width (W).

Table 7.6 Numerical fragility curve parameters of embankment for varying W (h = 4.5 m, H_{liq} = 6.0 m, R_D = 40%).

Fragility curve parameters	Embankment crest width (W)								
	5.63 m			11.26 m			16.89 m		
	dl_1	dl_2	dl_3	dl_1	dl_2	dl_3	dl_1	dl_2	dl_3
μ (g)	0.065	0.095	0.221	0.075	0.106	0.244	0.081	0.114	0.260
β_{tot}	0.487	0.486	0.489	0.488	0.482	0.493	0.486	0.470	0.573

Details of the fragility parameters are given in Table. 7.6. It is worth to be noticed that with increasing width of the embankment (W), settlement of the embankment surface at the center is found to be lower compared to the edges. The increasing width of the embankment provides more stability to the embankment structure.

7.5.3 Height of Embankment

Figure 7.14 shows the fragility curves for embankment with different heights (2.5 m, 4.5 m, and 6.5 m) resting on 6.0 m thick foundation soil with 40% relative density for a constant embankment width of 11.26 m. It is noticeable that with the reduction of height, the vulnerability of the embankment has been reduced significantly.

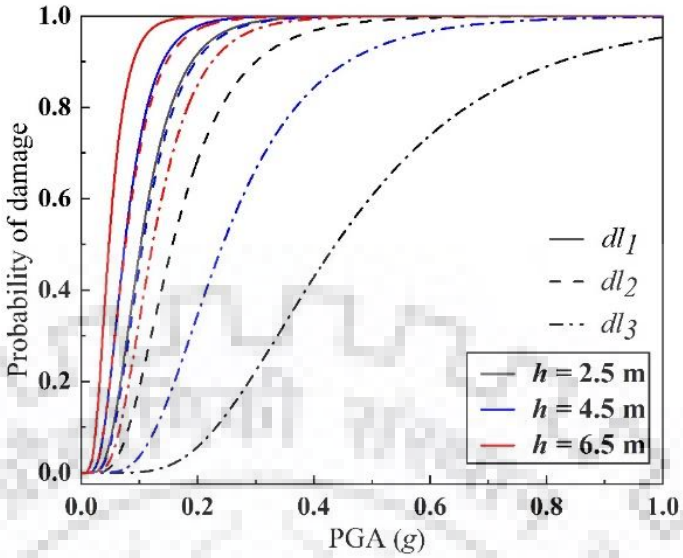

Fig. 7.14 Numerical fragility curves for embankment for varying embankment height (*h*).

This can be attributed to the reduction in the drainage path with smaller heights. Another factor is slope-stability of the embankment which increases with smaller heights. In the case of 2.5 m height least vulnerability can be observed. It can be seen that, in the case of an embankment height (*h*) of 2.5 m, the fragility curve for dl_3 has been shifted towards the right and shows the lower vulnerability of the embankment.

Table 7.7 Numerical fragility curve parameters of embankment for varying *h* (W = 11.26 m, H_{liq} = 6.0 m, R_D = 40%).

Fragility curve parameters	**Embankment height (*h*)**								
	2.5 m			**4.5 m**			**6.5 m**		
	***dl*₁**	***dl*₂**	***dl*₃**	***dl*₁**	***dl*₂**	***dl*₃**	***dl*₁**	***dl*₂**	***dl*₃**
μ (g)	0.103	0.157	0.438	0.075	0.106	0.244	0.048	0.076	0.123
β_{tot}	0.483	0.506	0.494	0.488	0.482	0.493	0.488	0.511	0.473

Table 7.7 shows the parameters of the fragility curve for the varying embankment height. In the case of *h* = 2.5 m, a sharp rise of 79.51% and 256.10% in median value (μ) of seismic demand can be observed in comparison to 4.5 m and 6.5 m embankment height (*h*) for the extensive damage level (dl_3). This can be an important aspect of constructing the embankments in such soil conditions.

7.5.4 Thickness of the Liquefiable Layer

In order to evaluate the influence of liquefiable layer thickness on embankment response, two different layer thicknesses (4.0 m and 6.0 m) have been considered. In this case, the embankment width (W) and embankment height (*h*) are 11.26 m and 4.5 m, respectively. Whereas the liquefiable

foundation layer is having 40% relative density. A significant reduction in vulnerability in the embankment settlement can be observed with the reduction of liquefiable layer thickness (Fig. 7.15).

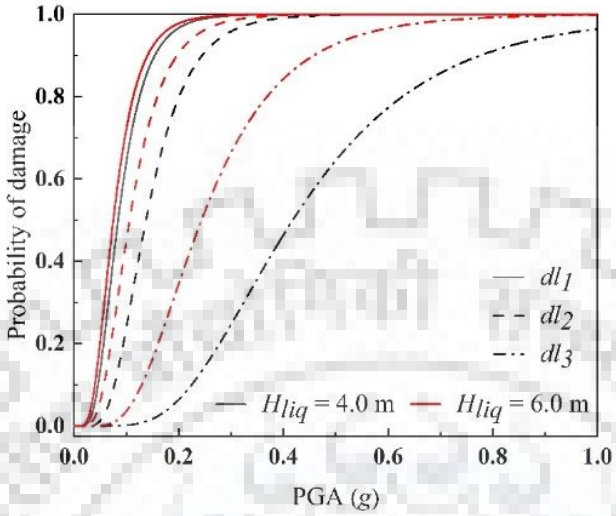

Fig. 7.15 Numerical fragility curves for embankment with variation of liquefiable layer thickness (H_{liq}).

Table 7.8 Numerical fragility curve parameters of embankment for varying H_{liq} (h = 4.5 m, W = 11.26 m, R_D = 40%).

Fragility curve parameters	**Thickness of liquefiable layer (H_{liq})**					
	4.0 m			**6.0 m**		
	***dl*₁**	***dl*₂**	***dl*₃**	***dl*₁**	***dl*₂**	***dl*₃**
μ (g)	0.084	0.138	0.418	0.075	0.106	0.244
β_{tot}	0.472	0.449	0.483	0.488	0.482	0.493

It can be linked with a reduction in the associated drainage path, which facilitates the dissipation of the excess pore pressure. A negligible difference in the case of dl_1 can be observed. However, the maximum difference can be observed in the case of dl_3. In the case of extensive collapse state (dl_3), a 71.31% increase in the median (μ) value of seismic demand can be observed with a reduction of 2.0 m of liquefiable layer thickness. The fragility curve parameters are provided in Table 7.8.

7.5.5 Effect of Densification

In this section, a mitigation technique has been introduced by providing a strip of dense sand in the foundation soil at three different locations in order to investigate the effect of densification with respect to the position. Analyses have been carried out for foundation soil with R_D = 40%, embankment width W = 5.63 m, embankment height h = 4.5 m and thickness of liquefiable layer H_{liq}

= 6.0 m . Considerable improvement can be observed in the embankment response from the preliminary analyses.

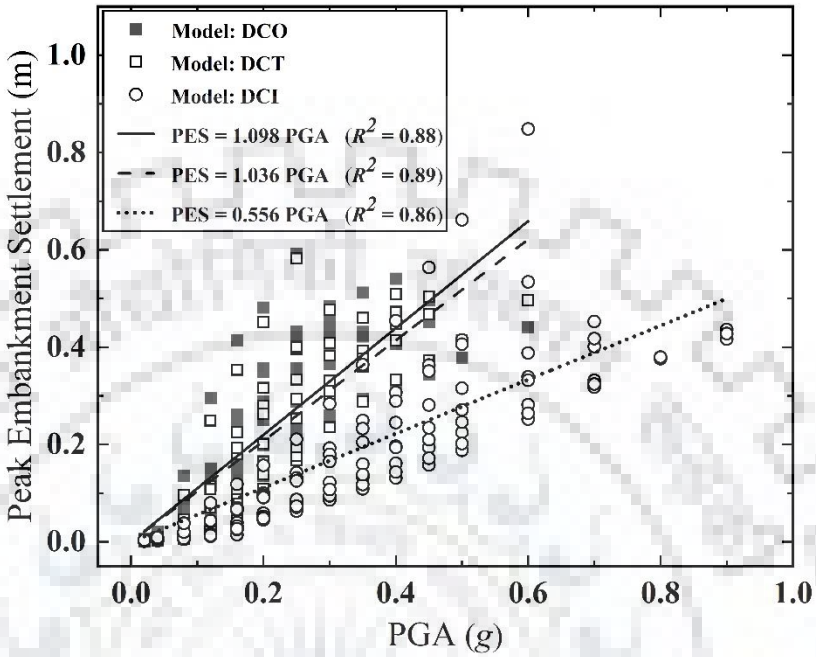

Fig. 7.16 Damage evolution in mitigated embankment with increasing intensity (PGA).

In dense sandy strips, soil grains in the saturated soil matrix will share more load, and less will be transferred to the water present in voids. Figure 7.16 shows the damage evolution of three different mitigated model. It can be seen that densification outside the toe has shown minimum reduction in embankment settlement. However, model DCT has shown marginal reduction in intensity-settlement slope (θ_{is}). Model DCI has shown maximum reduction in settlement of embankment and resulted in minimum intensity-settlement slope (θ_{is}). Based on the position of dense column area replacement ratio (A_r) has been calculated for three different models using the formula given below:

$$A_r = \frac{Area\ of\ dense\ column\ in\ the\ foundation\ zone}{Area\ of\ foundation\ zone} \tag{7.3}$$

The distance of center of dense column from the centerline of embankment has been defined as effective densification distance (L_e). This distance is presented in terms of normalized form using the embankment base width (L_e/B) in Fig. 7.17. It is obvious that with decreasing normalized effective densification distance (L_e/B), area replacement ratio (A_r) increases below the embankment (foundation zone). Figure 7.18 shows that, with increase in L_e/B ratio, A_r increases and this resulted in reduction of θ_{is}.

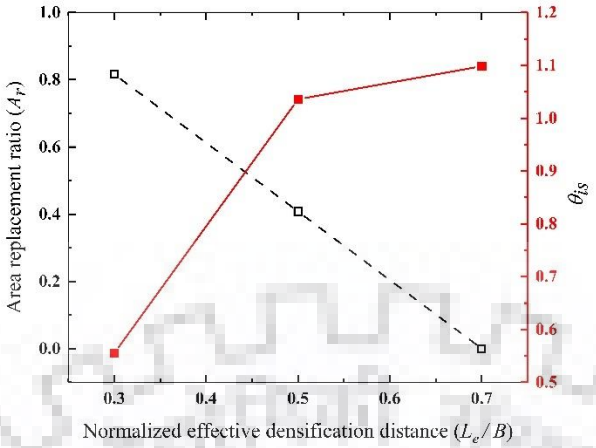

Fig. 7.17 Variation of intensity-settlement slope (θ_{ls}) with the effective densification distance.

Figures 7.18 shows the comparison of fragility curves for benchmark model and models with densification, resting on liquefiable ground conditions. In the case of extensive damage condition (dl_3), model DCO and DCT have shown 30.32% and 40.30% increase in the mean (μ) value, respectively. Whereas, model DCI has shown a sharp jump of 185.52% increase in the mean value (μ) with respect to the benchmark model. This shows that with increase in the densification of the foundation zone the embankment seismic demand increases and results in more safety to the embankment structure.

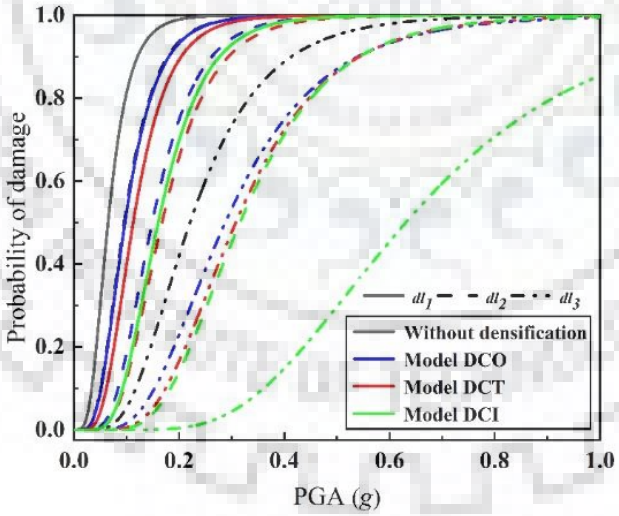

Fig. 7.18 Numerical fragility curves for the benchmark and densified model (R_D = 40%).

The parameters of the numerical fragility curves for the densification models have been shown in Table 7.9. However, the present study was limited to the densification of the 6.0 m width of the area below the embankment. Depending on the requirement, by increasing the width of densification also, the fragility study can be conducted.

Table 7.9 Numerical fragility curve parameters of embankment with densification (h = 4.5 m, W = 5.63 m, H_{liq} = 6.0 m).

Typology	Damage level	Densification Model					
		Model DCO		Model DCT		Model DCI	
		μ (g)	β_{tot}	μ (g)	β_{tot}	μ (g)	β_{tot}
Highway	Minor (dl_1)	0.097	0.484	0.113	0.462	0.160	0.426
	Moderate (dl_2)	0.149	0.442	0.167	0.439	0.316	0.423
	Extensive (dl_3)	0.288	0.491	0.308	0.443	0.631	0.436

7.6 PGA-PES RELATIONSHIP FOR EMBANKMENT

The relationship between PGA and PES is an outcome of the earlier analyses presented for different parameters influencing the embankment response. Effects of different parameters (R_D, W, and h, H_{liq}) have been discussed in this section. The relationships could be useful for design purposes where insufficient safety factors are indicated by pseudo-static stability methods. As the ground is liquefiable, at small to medium intensity ground motions, higher settlements can be observed. Hence, these linear best-fit equations are applicable only for situations identical to the current problem where permanent ground settlement at the embankment surface can be predicted for a specific range of PGA. At the higher intensity of ground motion, large lateral displacement can be observed from the preliminary study and hence avoided depending on the damage criteria for the fragility assessment.

Figure 7.19a depicts a PGA-PES response for a 4.5 m high embankment for different relative densities of foundation liquefiable layer. An average linearly increasing trend can be considered for all soil conditions. Associated intensity-settlement slope (θ_{is}) values are found to be 3.163, 1.403, 0.965, and 0.917 for 30, 40, 50, and 60% R_D of foundation soil. A greater value of θ_{is} indicates loose soil condition. This is obvious considering the compressibility of loose soil. Seismic displacement estimates are typically only approximate because of the varied earthquake ground motion and the complexity of the dynamic response of the associated soil elements with drainage path. The computed seismic displacement is, however, successfully employed in practice for design purposes when seen as a prospective seismic performance index (Bray and Travasarou, 2007).

Figure 7.19b shows the effect of embankment width (W) on the PGA-PES relationship. A similar linearly increasing trend can be noticed for all widths. As from the earlier section, it can be observed that with increasing width (W) of the embankment, the intensity demand (PGA) slightly increases to achieve a particular damage state, which is also seen in the PGA-PES relationship. This can be attributed to the increase in the effective stress over larger area of foundation soil with the width of the embankment.

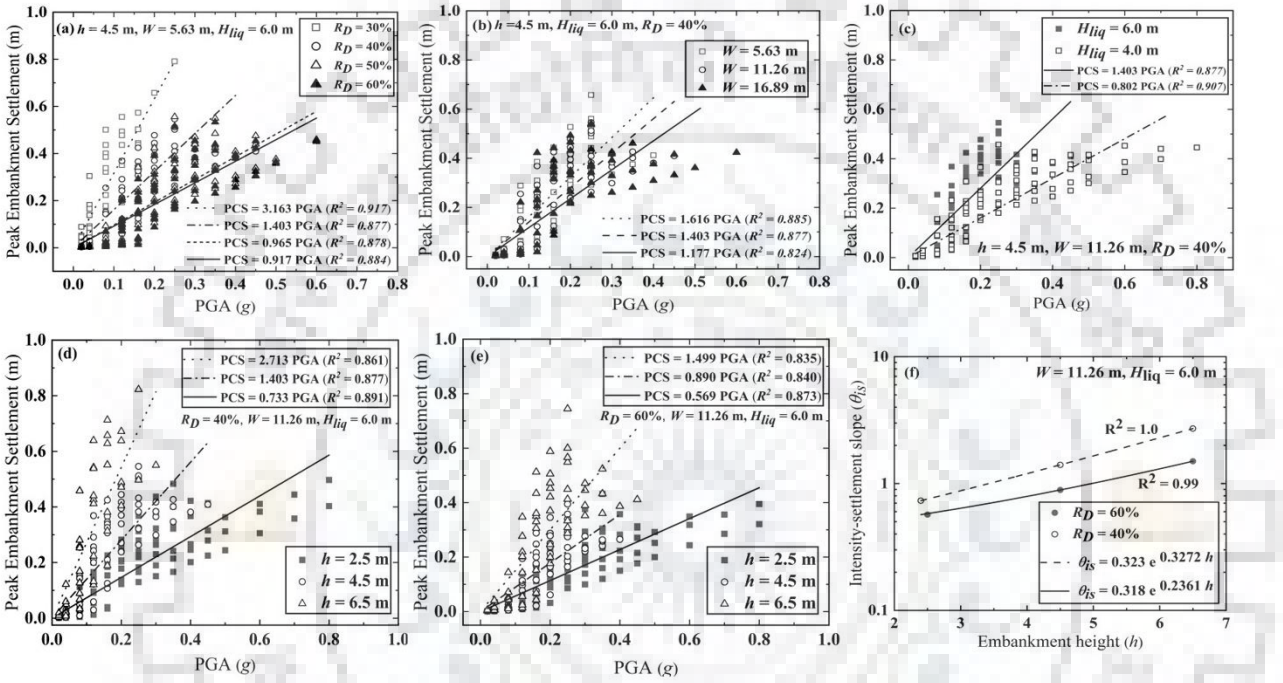

Fig. 7.19 Damage evolution in embankment with increasing intensity (PGA) for (a) varying R_D; (b) varying W; (c) varying H_{liq}; (d) varying h for R_D = 40%; (e) varying h for R_D = 60%; (f) best-fit plot between h and θ_{is}.

The effect of liquefiable layer thickness (H_{liq}) on the PGA-PES relationship is presented in Fig. 7.19c. With a decrease in H_{liq} the settlement of embankment (PES) reduces owing to the effect of the drainage path and thickness of the deformable layer.

Out of the different parameters considered in the present study, the height of the embankment has been found to be one of the major influencing parameters (after relative density) for the fragility assessment. The similar observation has been reported by earlier studies (Maruyama et al. 2010; Argyroudis and Kaynia 2015; Oblak et al. 2020). Figures 7.19d and 7.19e show the effect of embankment height (h) on the PES for 40% and 60% R_D of foundation soil, respectively. For two different relative densities (R_D = 40% and 60%) of foundation liquefiable soil layer, best-fit linear

correlation can be observed with satisfactory R^2 values for three different heights of embankment (h). Further regression has been carried out in between intensity-settlement slope (θ_{is}) and height of embankment (h) and an exponential best-fit correlation can be observed (Fig. 7.19f) for both the relative density. Final equations are provided for both the foundation soil conditions, which can be readily applicable to approximately estimate PES based on PGA and embankment height (h).

$$PES = 0.323 e^{0.3272\,h}\, PGA \quad ; \quad (for\ R_D = 40\%) \tag{7.4a}$$

$$PES = 0.318 e^{0.2361\,h}\, PGA \quad ; \quad (for\ R_D = 60\%) \tag{7.4b}$$

Where the units of PES and h are in meters, and PGA is in the unit of g. This relationship has been derived based on embankment width W = 11.26 m and thickness of loose sand layer H_{liq} = 6.0 m. This relation is established based on the linear regression of PES as the dependent variable whereas h and PGA are the input variable.

In a similar way, for other soil conditions also PGA-PES relationship can be established. However, this study primarily focused on a specific case of embankment-liquefiable foundation soil condition; hence its use is limited to the dimensions not too different from the present values and the soil condition considered.

7.7 VERIFICATION OF NUMERICAL FRAGILITY CURVES

Recent earthquakes have caused several roads to fail on embankments as a result of seismic activity. Recent earthquakes frequently result in road surface cracking or track displacement owing to soil settlement (Kayen et al., 2006; Maruyama et al., 2010). Although damaged embankments do not pose a threat to life, the length of time it takes for repair can have a significant impact on nearby emergency traffic and other activities. Most of the damages observed widely, description of the extent of damage, material properties of the embankment and surrounding soil, and intensity of seismic activity are rarely reported.

7.7.1 Validation 1

For verification of the present numerical fragility curves, a comparison was made with empirical data reported by Maruyama et al. (2010) depending on the damage of embankments in Japan. The fragility functions of expressway embankments in terms of damage ratio R_{rate} (number of damage events per kilometer) as a function of PGV are provided by Maruyama et al. (2010). A spatial Poison function developed by Duenas-Osorio et al. (2007) is provided below to evaluate the likelihood of having at least one damage, d, along a certain length of embankment, l.

$$P(d>0)=1-e^{-R_{rate}*l} \quad (7.5)$$

Damage is reported in the dataset on which these empirical curves are based regarding the kilometer post. The analytical fragility curve for *all damages* has been used for comparison where empirical curves are applicable to embankments having heights of approximately 5–10m. The intensity measure has been reported in the study based on PGV, which is also converted into PGA based on the ratio of PGV to PGA at the surface given by Power et al. (1998) for soft soil considering the magnitude of the earthquake (M) of 7.5 and source-to-site distance 0 to 20 km. The numerical fragility curve with h = 6.5 m is shown for comparison in Fig. 7.20.

Due to the lack of information about soil properties of the empirical fragility curves, 40% and 60% relative densities have been considered for foundation soil. It has been observed that the reference length (l) has a significant effect on the damage probability of embankment. The likelihood of damage increases with the length of the embankment. Using the previously discussed assumptions, the curves were generated for lengths of 1.0 km and 0.1 km for all damages. These two fragility curves bracket the numerical fragility curve at higher shaking levels very well.

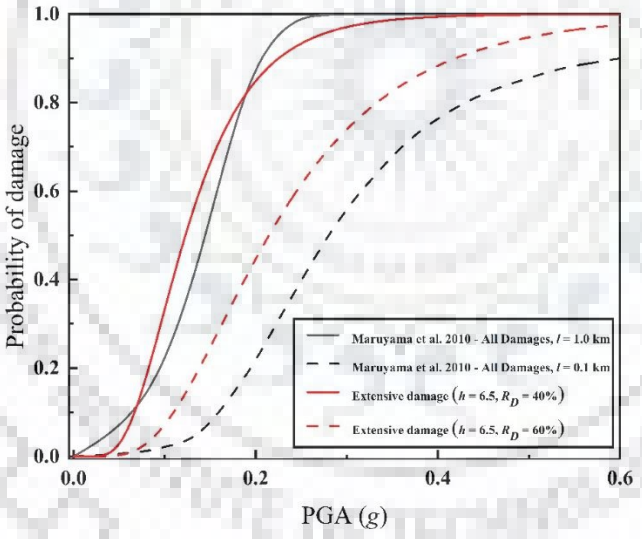

Fig. 7.20 Comparison of present study with the empirical fragility curves (after Maruyama et al. 2010).

7.7.2 Validation 2

For further verification of the present study, the numerical study proposed by Khalil et al. (2017) has been taken into consideration. In their study, embankment of 9 m height and 73 m width with 1:3 (V:H) side slopes resting on 4 m thick liquefiable soil followed by 6 m thick dense sand layer has been considered. However, detailed soil properties have not been reported in the study. Finite

element analysis has been carried out considering embankment settlement as a damage index and PGA as the intensity measure. Two different damage conditions (moderate and extensive) have been taken into consideration for the comparison with the present study. In the present study a 6.5 m high embankment (1:1 side slope) with W = 11.26 m, resting on 4 m thick liquefiable layer of 40% relative density (R_D) has been considered. However, the comparison presented here (Fig. 7.21) is not quantitative but still similar trend of fragility curves can be observed. The primary intention of this comparison is to ensure the validity of the present study despite of several dissimilarities being present in the comparison.

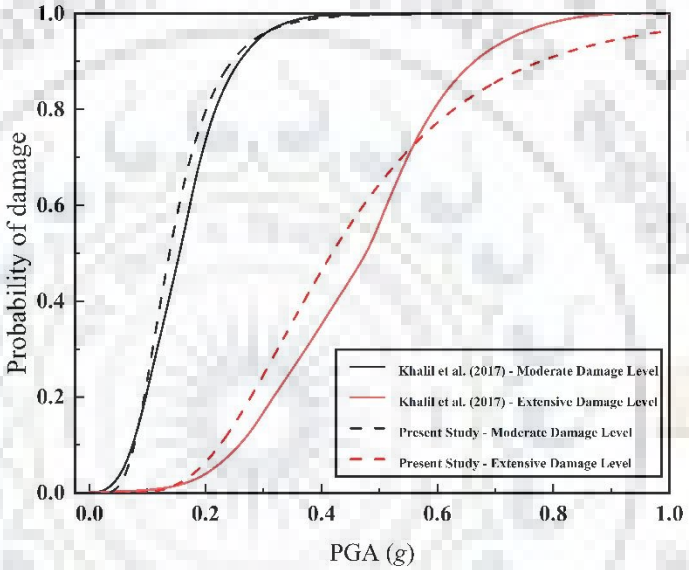

Fig. 7.21 Comparison of present study with the study of Khalil et al. (2017).

However, a lot of uncertainties are related to the comparison described here. The definition of damage levels, the soil property, embankment features, and conversion of damage ratio to the probability of damage of the empirical fragility curve are uncertain. Moreover, the comparison is an approximate analysis and qualitative in nature. Results show a similar trend with the empirical curves despite having several uncertainties in the analysis. The present study shows the derived numerical fragility curves can represent the seismic vulnerability of embankment structures for road network infrastructure.

7.8 CONCLUDING REMARKS

This study has proposed an approach for developing a numerical fragility curve for embankments resting on liquefiable soil. The seismic response of the embankment is assessed using dynamic 2D finite element analysis in Plaxis 2D. Different frequency-content ground motions have been scaled to various levels of earthquake loading (PGA). Where the dense sand layer is followed by a

liquefiable layer, two separate sand layers have been taken into consideration. Four different relative densities of liquefiable soil layer were considered.

There are very limited fragility models available for the vulnerability assessment of highway embankments. Further, available fragility curves are based on empirical data without proper soil characteristics and embankment geometry. The present study highlights a wide range of factors that influence the vulnerability of an embankment structure resting on liquefiable soil. The effect of relative density (R_D) of the foundation soil, embankment geometry (h, W), liquefiable layer thickness (H_{liq}), and densification of the toe region has been presented in a systematic way. The fragility curves show an increase in seismic demand with increasing both width of the embankment and the relative density of the liquefiable layer. With reducing the height of the embankment and liquefiable layer thickness, the seismic demand increases. A linear relationship has been established for estimating the normalized PES for a given PGA. The numerical fragility curves are qualitatively compared with the empirical fragility functions from Japan. Study revealed that not only relative density and thickness of liquefiable layer are very important, but embankment geometry also has significant effect on vulnerability. Further, densification at three different locations have been considered in the foundation soil. Maximum seismic demand of embankment has been observed when the location of densification is considered inside the toe region below the embankment.

The assumptions and selected parameters in the numerical models have certain limitations on the applicability of the fragility functions that were developed. These include the overall depth of the foundation soil, the characteristics of the soil layers, and the geometry of the soil embankment. As a result, the resulting fragility curves can be utilized in particular to provide a preliminary assessment of the vulnerability of embankments with similar geometries and soil with relative density 30 to 60%. Additionally, future enhancements can be made by randomizing the soil parameters and layer thickness in order to solve the inherent uncertainties in modeling.

Next Chapter summarizes the emergent conclusions and outcomes from the present study.

CHAPTER 8
CONCLUSIONS AND FUTURE SCOPE

8.1 GENERAL

Present study has been focused on developing numerical simulations for embankments resting on liquefiable soil with and without mitigation measures. A well-calibrated material constitutive model UBC3D-PLM has been introduced for simulating liquefaction phenomena. The seismic response of the embankment has been assessed using dynamic 2D and 3D FE analysis in PLAXIS 2D and 3D program. Foundation soil is considered to be liquefiable layer followed by a dense layer. Study mainly focused on different mitigation approaches of embankment under different dynamic loading conditions. Liquefaction-induced embankment settlement countermeasures like stone column, hybrid pile-stone column, densification, gravel berms are considered. Their performance in terms of EPP and embankment crest settlement are evaluated under different earthquake loading. Effect of sequential ground motion on the embankment response is also considered in the present study. Moreover, fragility assessment of embankment structures is carried out considering a wide range of parameters along with effect of location of effective mitigation. Emergent conclusions are presented below in four parts depending on the objectives of the present study.

8.2 STONE COLUMN MITIGATION

An attempt has been made to evaluate the effectiveness of stone columns in mitigating liquefaction of foundation soil and embankment crest settlement. Based on the past literature and the preliminary study, stone columns are considered below embankment toe regions. For the plane strain idealization, stone columns are modeled considering an equivalent plane strip approach. Parametric study in terms of diameter of stone column, *S*/*D* ratio, effect of cyclic loading amplitude and response under earthquake ground motions are considered. Based on the observations from the analyses following major conclusions are drawn:

1. The calibrated UBC3D-PLM constitutive model was able to capture the beneficial effects of shear-induced dilation of the soil immediately below the embankment. This portion of soil never attains full liquefaction condition and contributes stability to the embankment. However, the regions below toe of the embankment liquefy which is primarily responsible for excessive settlement of the embankment due to the lateral outflow of soil beneath the embankment.

2. For a constant *S*/*D* ratio, smaller diameter stone columns were found to be more effective in reducing the EPP below the embankment toe due to shorter drainage path (proportional to diameter). This is evident from the reduction in the values of $r_{u,max}^{Eff-zone}$ with decrease in the diameter of the stone column for constant *S*/*D* ratio. However, larger diameter stone columns are more effective in reducing the embankment settlement owing to greater stiffness in comparison to smaller diameter stone columns.

3. Variation of spacing showed a marginal difference in the embankment settlement. In the case of *S*/*D* = 2.5, for 0.6 m diameter stone columns, the maximum reduction of embankment crest settlement of approximately 61% was achieved. However, smaller spacings mitigated the EPP of the zone encased by stone columns under the embankment toe. For *S*/*D* = 2.0 the foundation soil beneath the embankment toe experiences $r_{u,max}^{Eff-zone}$ 0.574 and 0.512 at 3 m and 5 m depths, respectively.

4. In reducing the maximum outflow horizontal deformation $U_{x,max}$, 1.0 m diameter stone columns have shown the maximum effectiveness (77.20% reduction) in comparison with the benchmark model. However, 0.6 m and 0.8 m diameter stone columns have reduced $U_{x,max}$ by 65.50% and 70.76%, respectively. Accordingly, the maximum heaving of the ground surface was also reduced effectively by the inclusion of stone columns.

5. The time history plot of EPP for the Northridge earthquake has revealed that after a_{max} onwards, the drainage effect of stone columns can be seen in faster dissipation. This shows the effect of permeability of stone columns, which played a key role in dissipating the excess pore pressure (EPP).

6. The embankment settlement shows a linearly increasing relationship with the arias Intensity Ia. From the best fit plot of untreated and treated embankment model, a reduction of 0.107 m intercept in embankment crest settlement was observed which shows stone columns are efficient under real ground conditions. However, for the higher arias Intensity ground motions, the optimized stone column number was not sufficient. A further study exploring all the possible configurations can reveal the optimum configuration of stone columns.

8.3 EVALUATION OF HYBRID MITIGATION

The efficiency of three alternative mitigation strategies for earth embankments sitting on liquefiable foundation soil has been investigated. Three different mitigation strategies as densification, stone

columns, and hybrid pile-stone columns have been included in a 2D numerical model. It considers an analogous plane strip approach in order to reduce the complexity to a plane strain issue. A wide range of earthquake ground motions have been considered in this study to evaluate the effect of earthquake motions. Few inferences made based on the main findings of this study are as follows:

1. Larger embankment crest settlement has been occurred at smaller frequency ground motions. The maximum settlement has been observed during Imperial Valley (1979) ground motion, which has predominant frequency of 2.36 Hz.
2. A nearly linear relationship exists between the Arias Intensity (I_a) and the embankment crest settlement for all the embankment models. The embankment crest settlement increases with I_a. The maximum embankment crest settlement has been occurred in the Imperial Valley (1979) ground motion which also has the maximum value of I_a. Moreover, the $r_{u,max}$ value in the mitigation zone below embankment toe found to be increasing with I_a.
3. From the analyses of 25 ground motions for 4 different models, the hybrid mitigation was found to be more effective in reducing the embankment crest settlement than other two mitigation approaches for the higher intensity ground motions. Densification and stone column mitigation were found to be effective in the cases of low to medium intensity ground motions.
4. The time history analysis of Darfield (2010) ground motion for mitigation model using densification indicated possible development of progressive liquefaction in the densified zone facing the free ground. This may cause potential failure of the mitigation system. Further study by addressing this issue needs to be carried out.
5. The liquefaction of the soil beneath the embankment toe mainly affects the embankment settlement behaviour. The densification measure shows effective mitigation for a certain region of soil beneath the toe, however the densified zone away from the toe towards the free field liquefies.
6. The stone column mitigation model and hybrid pile-stone column mitigation model have shown better dissipation of EPP at the end of loading.
7. The higher dissipation rate due to stone columns may lead to the excess settlement. The hybrid mitigation method has been found to be most effective in reducing the shear induced settlement of embankment during the co-shaking event as well as during the post-shaking event.

8.4 EFFECT OF SEQUENTIAL GROUND MOTION

Numerical analyses presented in this study considered the liquefaction-induced settlement behaviour of embankment resting on loose foundation soil with two different mitigation approaches. Three-

dimensional FEM modeling has been carried out using PLAXIS 3D program. Initially, cyclic ground motions have been applied to three different embankment models with varying PGA. Both $r_{u,max}$, and crest settlement increase with an increase in PGA_{cyclic}. After assessing the efficacy of the numerical model for a dynamic response, ten different sequential earthquake motions were applied to highlight the effect of after-shock motions and mitigation. Based on the results obtained from the study, the following key conclusions have been drawn:

1. In the case of model without any mitigation, the soil below the embankment toe attains maximum r_u value (close to unity) during both the main shock and aftershock events. There is a high possibility of re-liquefaction of foundation soil during aftershock, which may cause additional damage to the structures resting on liquefiable soil. For both shock events, stone column mitigation was more efficient than the gravel berm technique.
2. Mobilized shear stresses in liquefiable soil are more for mitigated models. It is roughly twice as for the gravel berm mitigated model and 4.5 times for the stone column mitigated model. In stone column mitigated model, higher shear stresses can be mobilized in liquefiable soil due to the lesser development of EPP owing to shortened drainage paths in the presence of stone columns. Gravel berm mitigated model can resist higher shear stress due to the surcharge effect of gravel berm, leading to an increase in the effective stress.
3. Both $r_{u,max,}$ and embankment settlement increase with Arias intensity (I_a) of ground motion. Though Arias intensity (I_a) is less than 10% of corresponding main shock events in most of the after-shock motions, both $r_{u,max,}$ and embankment settlement are attaining values closer to the main-shock response. Average response ratios are 0.704 and 0.902 for settlement and $r_{u,max}$.
4. An average differential embankment settlement of 15% was observed for the model without any mitigation due to the sequential ground motions. A marginal reduction was observed for the stone column mitigated model. A noticeable reduction in differential embankment settlement can be observed with the gravel berm mitigation due to lateral stability offered by gravel berms.
5. The settlement ratio $S_{r,i}^{main/after}$ can be considered as a measure of the effect of mitigation. In main-shock events, the stone column mitigation shows a lower settlement ratio except for higher intensity level (I_a). With an increasing level of Arias intensity (I_a) the effectiveness of stone column mitigation reduces. Marginal reduction in the effectiveness of stone column mitigation is noticed during the aftershock as apparent from slightly higher values.

6. The gravel berms resulted in a reduction of acceleration amplitude due to increased inertia on the embankment structure. On the contrary, stone columns increase acceleration levels at the embankment crest due to the increased stiffness of the foundation soil beneath the embankment.

8.5 FRAGILITY ASSESSMENT OF HIGHWAY EMBANKMENT

This study has proposed an approach for developing a numerical fragility curve for embankments resting on liquefiable soil. The seismic response of the embankment is assessed using dynamic 2D finite element analysis in PLAXIS 2D. Different frequency-content ground motions have been scaled to various levels of earthquake loading (PGA). Four different relative densities of liquefiable soil layer were considered. Sand specific calibration of material model parameters are carried out based on laboratory test results from the past literature. There are very limited fragility models available for the vulnerability assessment of highway embankments. Further, available fragility curves are based on empirical data without proper soil characteristics and embankment geometry. The present study can be useful for future aspects in terms of implementation of advanced constitutive model and reliability study of embankment structures resting on liquefiable deposit. However, the key conclusions are listed below:

1. It has been observed from the analyses that embankments resting on loose saturated sand (R_D = 30% and 40%) are more vulnerable because the loose saturated sand can develop full liquefaction even at lower intensity values of input motion compared to the medium dense soil (R_D = 50% and 60%). This shows that the relative density is of paramount influence in liquefaction phenomenon.
2. Significant increment in demand can be seen between 30 to 40 % relative density. For damage levels dl_1 and dl_2, the demand for mean PGA increases almost linearly up to 50% relative density and thereafter increases marginally. However, for the third damage level dl_3, the demand for mean PGA increases till 60% relative density.
3. Analysis showed that the vulnerability of the embankment slightly reduces with increasing the embankment width (W). With increasing width of the embankment (W), settlement of the embankment surface at the center is found to be lower compared to the edges. The increasing width of the embankment provides more stability to the embankment structure.
4. It is noticeable that with the reduction of height, the vulnerability of the embankment has been reduced significantly. In the case of 2.5 m embankment height, a sharp rise of 79.51% and 256.10% in median value (μ) of seismic demand can be observed in comparison to 4.5 m and 6.5

m embankment height (h) for the extensive damage level (dl_3). This can be an important aspect of constructing the embankments in such soil conditions.

5. A significant reduction in vulnerability in the embankment settlement can be observed with the reduction of liquefiable layer thickness. In the case of extensive collapse state (dl_3), a 71.31% increase in the median (μ) value of seismic demand can be observed with a reduction of 2.0 m of liquefiable layer thickness.
6. Densification at three different locations have been considered in the foundation soil. Maximum seismic demand of embankment has been observed when the location of densification is considered inside the toe region below the embankment.

8.6 LIMITATIONS AND FUTURE SCOPE

Present study has been devoted to numerical modeling of liquefaction-induced settlement of embankment using a well calibrated effective stress-based UBC3D-PLM constitutive model. The material model is found to be efficient in modeling free-field liquefaction and shear-induced dilation behaviour below embankment. However, few assumptions and limitations are there which are discussed below.

8.6.1 Limitations of Present Study

Despite efforts to consider the majority of the factors, time constraints and computing challenges prevented consideration of all factors. Some of the limitations are listed below.

1. The findings of this study are solely based on experimental data that has already been published in the prior literature as well as certain presumptions. In order to improve the numerical predictions for both types of models, further laboratory investigations are necessary to fully understand the impact of the EPP near the toe area and the subsequent impact on the embankment crest settling.
2. The densification effect due to the installation of stone columns or piles has not been addressed in the present study. Future studies can be carried out by considering the beneficial aspect of effective influential zone of installed stone columns using 3D FEM modeling.
3. Assumption of constant permeability results slower dissipation of EPP in the prediction during post-liquefaction stage. Variations in the permeability with volume changes need to be established in the further studies.
4. Aspects like densification and change in permeability must be addressed in physical studies with measurement before incorporating in numerical model.

5. The assumptions and selected parameters in the numerical models have certain limitations on the applicability of the present study. Overall depth of the foundation soil, the characteristics of the soil layers, and the geometry of the soil embankment are considered based on past literature and assumptions.
6. To reduce the inherent errors associated with modelling, future improvements can be achieved by randomizing the soil characteristics and layer thickness.

8.6.2 Future Scope

Based on the limitations of the present study future scopes can be suggested as follows:

1. Future experimental study (shake table or centrifuge modeling) should be carried out in order to investigate the discrepancy between the numerical modeling and the actual performance of stone columns in mitigating EPP below embankment toes.
2. A proper design guideline can be a better outcome of the present research. A more extensive study can be carried out in providing design chart or guidelines for field practitioners for different mitigations considered in this study.
3. State-dependent bounding surface constitutive models can be further introduced in modeling the liquefiable soil behaviour. Moreover, different material of embankment structure can be considered considering advanced constitutive models.
4. In case of fragility assessment, addition of further ground motions can be considered to get better output in terms of seismic demand of such geotechnical structures. However, site-specific vulnerability or hazard analysis can be beneficial for performance-based design of such important life-line infrastructures.
5. Variation of permeability during liquefaction and post-liquefaction stage can be considered in future study.
6. Study can be extended to consider the effect of depth of bedrock from ground surface.

REFERENCES

1. A1-Homoud, A. S. (2000). "Geologic Hazards of an Embankment Dam Constructed Across a Major, Active Plate Boundary Fault." Environmental and Engineering Geoscience, VI(4): pp. 353-382.
2. A1-Homoud, A. S., Taqieddin, S. A. and Ahmad, F. H. (1995). "Geologic problems related to dam sites in Jordan and their solutions." Engineering Geology 39: 233-263.
3. Adalier, K. (1996). "Mitigation of earthquake induced liquefaction hazards." Ph.D. thesis, Dept. of Civil and Environmental Engineering, Rensselaer Polytechnic Institute.
4. Adalier, K. and Aydingun, O. (2003). "Numerical analysis of seismically induced liquefaction in earth embankment foundations. Part II. Application of remedial measures." Canadian Geotechnical Journal, 40(4): 766–779.
5. Adalier, K. and Sharp, M. K. (2004). "Embankment dam on liquefiable foundation-dynamic behaviour and densification remediation." J Geotech Geoenviron Eng; 130(11): 1214-24.
6. Adalier, K., Elgamal, A. W., Martin, G. R. (1998). "Foundation liquefaction countermeasures for earth embankments." J. Geotech Geoenviron Eng. 124(6):500-17. https://doi.org/10.1061/(ASCE)1090-0241(1998)124:6(500).
7. Adalier, K., Elgamal, A., Meneses, J. and Baez, J. I. (2003). "Stone columns as liquefaction countermeasure in non-plastic silty soils." Soil Dyn. Earthq. Engg. 23 (7), 571–584. https://doi.org/10.1016/S0267-7261(03)00070-8.
8. Andrianopoulos, K. I., Papadimitriou, A. G. and Bouckovalas, G. D. (2010). "Bounding surface plasticity model for the seismic liquefaction analysis of geostructures." Soil Dynam Earthq Eng. 30(10):895–911. https://doi.org/10.1016/j.soildyn.2010.04.001.
9. Andrus, R. D. and Stokoe, K. H., II. (1997). ''Liquefaction resistance based on shear wave velocity.'' Proc., NCEER Workshop on Evaluation of Liquefaction Resistance of Soils, Tech. Rep. NCEER-97-0022,T.L.Youd and I. M. Idriss, eds., National Center for Earthquake Engineering Research, Buffalo, 89–128.
10. Andrus, R. D. and Stokoe, K. H., II. (2000)."Liquefaction resistance of soils from shear-wave velocity."J. Geotech. Geoenviron. Eng., 126(11),1015–1025.
11. Antonia, M. (2013). "Evaluation of UBC3D-PLM constitutive model for prediction of earthquake induced liquefaction on embankment dams." Msc Graduation Thesis. Delft University of Technology.

12. Argyroudis, S., Kaynia, A. M. (2015). “Analytical seismic fragility functions for highway and railway embankments and cuts.” Earthq. Eng. Struct. Dyn. 44, 1863–1879. https://doi.org/10.1002/eqe.2563.
13. Argyroudis, S., Kaynia, A. M., Pitilakis, K. (2013). “Development of fragility functions for geotechnical constructions: Application to cantilever retaining walls.” Soil Dynamics and Earthquake Engineering 50: 106–116. http://dx.doi.org/10.1016/j.soildyn.2013.02.014.
14. Arias, A. (1970). “A measure of earthquake intensity. In R. J. Hansen, ed. Seismic Design for Nuclear Power plants.” MIT Pres, Cambridge, Massachusetts, pp. 438-483.
15. Armstrong, R. J., Boulanger, R. W. and Beaty, M. H. (2013). “Liquefaction effects on piled bridge abutments: centrifuge tests and numerical analyses.” J. Geotech. Geoenviron. Eng., 139(3): 433-443, ASCE. DOI: 10.1061/(ASCE)GT.1943-5606.0000780.
16. Arulanandan, K. and Scott, R. F. (1993). “Verification of numerical procedures for the analysis of soil liquefaction.” In: Proc. of International conference on the verification of numerical procedures for the analysis of soil liquefaction problems. Rotterdam: Balkema Press.
17. Arulmoli, K., Muraleetharan, K. K., Hossain, M. M. and Fruth, L. S. (1992). VELACS: verifications of liquefaction analyses by centrifuge studies. Laboratory testing program. Soil Data Report.
18. Athanasopoulos-Zekkos, A. and Seed, R. B. (2013). “Simplified Methodology for Consideration of Two-Dimensional Dynamic Response of Levees in Liquefaction-Triggering Evaluation.” Journal of Geotechnical and Geoenvironmental Engineering, 139(11). https://doi.org/10.1061/(ASCE)GT.1943-5606.0000913.
19. Aydingun, O. and Adalier, K. (2003). “Numerical analysis of seismically induced liquefaction in earth embankment foundations. Part I. Benchmark model.” Can Geotech J;40(4):753–65.
20. Baez, J.I. and Martin, G.R. (1993). “Advances in the design of vibro systems for the improvement of liquefaction resistance.” International Symposium for Ground Improvement, pp. 1–16. Canadian Geotechnical Society, Vancouver.
21. Baltzopoulos, G., Baraschino, R., Chioccarelli, E., Cito, P. and Iervolino, I. (2023). “Preliminary engineering report on ground motion data of the Feb. 2023 Turkey seismic sequence.” V2.0 – 10/02/2023.
22. Bastidas, P. (2016). “*Ottawa F-65 sand characterization*.” Doctoral dissertation. University

of California at Davis.

23. Beaty, M. H. and Byrne, P. M. (2011). "UBCSAND constitutive model version 904aR." Itasca.

24. Beaty, M. H. and Byrne, P. M. (2011). "UBCSAND constitutive model version 904aR." Itasca.

25. Beaty, M., Byrne, P. M. (1998). "An Effective Stress Model for Predicting Liquefaction Behavior of Sand." Geotechnical Earthquake Engineering and Soil Dynamics III, ASCE. Vol. 1, pp766 - 777.

26. Bhatnagar, S., Kumari, S. and Sawant, V. A. (2016). "Numerical analysis of earth embankment resting on liquefiable soil and remedial measures." International Journal of Geomechanics 16(1), 04015029-1 to 13. https://doi.org/10.1061/(ASCE)GM.1943-5622.0000501.

27. Boulanger, R. W., Khosravia, M., Khosravia, A. and Wilson, D. W. (2018). "Remediation of liquefaction effects for an embankment using soil-cement walls: Centrifuge and numerical modeling." Soil Dynamics and Earthquake Engineering, 114:38–50. https://doi.org/10.1016/j.soildyn.2018.07.001.

28. Boulanger, R.W. and Ziotopoulou, K. (2013). "Formulation of a sand plasticity plane-strain model for earthquake engineering applications." Soil Dynam Earthq Eng. 53:254–67. https://doi.org/10.1016/j.soildyn.2013.07.006.

29. Bray, J. and Travasarou, T. (2007). "Simplified procedure for estimating earthquake-induced deviatoric slope displacements." Journal of Geotechnical and Geoenvironmental Engineering 133(4):381–392.

30. Brennan, A. J. and Madabhushi, S. P. G. (2006). "Liquefaction remediation by vertical drains with varying penetration depths." Soil Dyn. Earthq. Eng. 26 (5), 469–475. https://doi.org/10.1016/j.soildyn.2005.10.001.

31. Byrne, P. M., Park, S., Beaty, M., Sharp, M., Gonzalez, L. and Abdoun, T. (2004). "Numerical modeling of liquefaction and comparison with centrifuge tests." Can. Geotech. J. 41, 193–211.

32. Byrne, P. M., Puebla, H., Chan, D. H., Soroush, A., Morgenstern, N. R., Cathro, D. C., Gu, W. H., Phillips, R., Robertson, P. K., Hofmann, B. A., Wride, C. E. (Fear), Sego, D. C., Plewes, H. D., List, B. R. and Tan, S. (2011). "CANLEX full-scale experiment and modelling." Canadian Geotechnical Journal. 37(3): 543-562. https://doi.org/10.1139/t00-

042.

33. Carey, T. J., Chiaradonna, A., Love, N. C., Wilson, D. W., Ziotopoulou, K., Martinez, A., DeJong, J. T. (2022). "Effect of soil gradation on embankment response during liquefaction: A centrifuge testing program." Soil Dynamics and Earthquake Engineering, 157:107221. https://doi.org/10.1016/j.soildyn.2022.107221.
34. Cascone, E., Biondi G., Aliberti, D. and Rampello, S. (2021). "Effect of vertical input motion and excess pore pressures on the seismic performance of a zoned dam." Soil Dyn. Earthquake Eng.142: 106566. https://doi.org/10.1016/j.soildyn.2020.106566.
35. Cascone, E., Biondi,G., Aliberti, D. and Rampello, S. (2021). "Effect of vertical input motion and excess pore pressures on the seismic performance of a zoned dam." Soil Dynamics and Earthquake Engineering, 142:106566. https://doi.org/10.1016/j.soildyn.2020.106566.
36. Chen, L. and Kimoto, S. (2018). "Numerical Analysis of Damaged River Embankment during the 2011 Tohoku Earthquake Using a Multiphase-Coupled FEM Analysis Method." Geofluids, Hindawi. Article ID 5191647. https://doi.org/10.1155/2018/5191647.
37. Chern, S. and Chang, T. (1995). "Simplified procedure for evaluating soil liquefaction characteristics." Journal of Marine Science and Technology, 3(1), 35-42.
38. Chiaradonna, A., Tropeano, G., d'Onofrio, A. and Silvestri, F. (2019). "Interpreting the deformation phenomena of a levee damaged during the 2012 Emilia earthquake." Soil Dynamics and Earthquake Engineering, Volume 124, 2019, Pages 389-398, https://doi.org/10.1016/j.soildyn.2018.04.039.
39. Cooke, H. G. (2000). "Ground improvement for liquefaction mitigation at existing highway bridges." PhD Thesis, Virginia Polytechnic Institute and State University.
40. Cox B. R., Boulanger R. W., Tokimatsu K., Wood C., Abe A., Ashford S. A., Donahue J., Ishihara K., Kayen R. E., Katsumata K., Kishida T., Kokusho T., Mason H. B., Moss R. E. S., Stewart J. P., Tohyama K. and Zekkos D. (2013). "Liquefaction at strong motion stations in Urayasu City during the 2011 Tohoku-oki earthquake." Earthquake Spectra 29, S55–S80.
41. Cubrinovski, M., Robinson, K., Taylor, M., Hughes, M. and Orense, R.P. (2012). "Lateral spreading and its impacts in urban areas in the 2010–2011 Christchurch earthquakes." New Zealand J. Geol. Geophys. 55, 255–269. https://doi.org/10.1080/00288306.2012.699895.
42. Dafalias, Y. F. and Manzari, M. T. (2004). "Simple plasticity sand model accounting for fabric change effects." J Eng Mech. 130(6):622–34. https://doi.org/10.1061/(ASCE)0733-9399(2004)130:6(622).

43. Dashti, S. and Bray, J. (2013). “Numerical Simulation of Building Response on Liquefiable Sand.” J. Geotech. Geoenviron. Eng., 139(8), 1235–1249.
44. Di Ludovico, M., Chiaradonna, A., Bilotta, E., Flora, A. and Prota, A. (2020). “Empirical damage and liquefaction fragility curves from 2012 Emilia earthquake data.” Earthquake Spectra. https://doi.org/10.1177/8755293019891713.
45. Di, Y. and Sato, T. (2003). “Liquefaction analysis of saturated soils taking into account variation in porosity and permeability with large deformation.” Computers and Geotechnics, 30: 623–635. doi:10.1016/S0266-352X(03)00060-0.
46. Dinesh, N., Banerjee, S. and Rajagopal, K. (2022). “Performance evaluation of PM4Sand model for simulation of the liquefaction remedial measures for embankment.” Soil Dynam Earthq Eng., 152: 107042. https://doi.org/10.1016/j.soildyn.2021.107042.
47. Dobry, R. and Liu, L. (1992). “Centrifuge modeling of soil liquefaction.” Proc., 10th World Conf. on Earthquake Engineering, pp. 6801–6809, Rotterdam; Brookfield, VT: A.A. Balkema.
48. Duenas-Osorio, L., Craig, J. I. and Goodno, B. J. (2007). “Seismic response of critical interdependent networks.” Earthquake Engineering and Structural Dynamics 36 (4) :285–306.
49. Elgamal, A., Parra, E., Yang, Z., and Adalier, K. (2002). Numerical Analysis of Embankment Foundation Liquefaction Countermeasures.” Journal of Earthquake Engineering, 6:4, 447-471, DOI: 10.1080/13632460209350425.
50. ElGhoraiby, M. A., Park, H. and Manzari, M. T. (2020). “Stress-strain behavior and liquefaction strength characteristics of Ottawa F65 sand.” Soil Dynamics and Earthquake Engineering 138: 106292. https://doi.org/10.1016/j.soildyn.2020.106292.
51. EN 1998-1 Eurocode 8: Design of structures for earthquake resistance-part 1: general rules, seismic actions and rules for buildings. CEN, Bruxelles, 2004.
52. Enomoto, T. and Sasaki, T. (2015). “Several factors affecting seismic behaviour of embankments in dynamic centrifuge model tests.” Soils and Foundations, 55(4):813–828. http://dx.doi.org/10.1016/j.sandf.2015.06.013.
53. FEMA P695. (2009). “Quantification of Building Seismic Performance Factors.” APPLIED TECHNOLOGY COUNCIL 201 Redwood Shores Parkway, Suite 240 Redwood City, California, NEHRP.
54. Feng, K., Wang, G., Huang, D. and Jin, F. (2021). “Material point method for large

deformation modeling of coseismic landslide and liquefaction-induced dam failure." Soil Dynamics and Earthquake Engineering, 150:106907. https://doi.org/10.1016/j.soildyn.2021.106907.

55. Finn, W. D. L. (1988). "Dynamic analysis in geotechnical engineering." In Proc. Earthquake Engineering and Soil Dynamics II - Recent Advances in Ground Motion Evaluation, ASCE Geotechnical Engineering Division, Park City, Utah, June, 523-91.
56. Finn, W. D. L. (1991). "Estimating how embankment dams behave during earthquakes." Water Power and Dam Construction, London, April, 17-22.
57. Finn, W. D. L. (1998). "Estimating Post-Liquefaction Displacements in Embankment Dams and Prioritizing Remediation Measures." Proceedings: Fourth International Conference on Case Histories in Geotechnical Engineering, St. Louis, Missouri.
58. Finn, W. D. L., Lee, K. W. and Martin, G. R. (1977). "An effective stress model for liquefaction." J. Geotech. Engrg. Div. ASCE, 103, 513–533.
59. Galavi, V. (2021). "DeltaSand: A state dependent double hardening elasto-plastic model for sand: Formulation and validation." Computers and Geotechnics 129: 103844. https://doi.org/10.1016/j.compgeo.2020.103844.
60. Galavi, V., Petalas, A. and Brinkgreve, R. B. J. (2013). "Finite element modelling of seismic liquefaction in soils." Geotechnical Engineering 44(3): 55-64.
61. Ganesalingam, D., Read, W. and Sivakugan, N. (2013). "Consolidation Behavior of a Cylindrical Soil Layer Subjected to Nonuniform Pore-Water Pressure Distribution." International Journal of Geomechanics 13(5):665-671. https://doi.org/10.1061/(ASCE)GM.1943-5622.0000249.
62. Ghaboussi, J. and Wilson, E. L. (1973). "Flow of compressible fluid in porous elastic media." International Journal for Numerical Methods in Engineering, 5(3), 419–442.
63. Ghosh, B. and Bhattacharya, S. (2008). "Selection of appropriate input motion for foundation design in seismic areas." In: Proceedings of the 14th world conference on earthquake engineering, Beijing, China, October 12–17.
64. Gingery, J. R. (2003). "Embankment failure from liquefaction and other damage in the 20 April2002 Au Sable Forks, NY earthquake." Proceedings, 12th Pan-American Conference on Soil Mechanics and Geotechnical Engineering, Cambridge, MA.
65. Grasso, S., Massimino, M. R. and Sammito, M. S. V. (2021). "New Stress Reduction Factor for Evaluating Soil Liquefaction in the Coastal Area of Catania (Italy)." Geosciences 2021,

11(1), 12; https://doi.org/10.3390/geosciences11010012.

66. Green, R.A., Cubrinovski, M., Cox, B., Wood, C., Wotherspoon, L., Bradley, B. and Maurer, B. W. (2014). "Select liquefaction case histories from the 2010-2011 Canterbury earthquake sequence." Earthquake Spectra 30(1): 131-153.

67. Groot, M. B. de, Adel, H. den, Stoutjesdijk, T. P., Westenbrugge, C. J. van. (1995). "Risk of dike failure due to flow slides." Coastal Engineering, 26: 241-249.

68. Gu, L., Wang, Z., Zhu, W., Jang, B., Ling, X. And Zhang, F. (2021). "Numerical analysis of earth embankments in liquefiable soil and ground improvement mitigation." Soil Dynamics and Earthquake Engineering, 146:106739. https://doi.org/10.1016/j.soildyn.2021.106739.

69. Gu, L., Zheng, W., Zhu, W., Wang, Z., Ling, X. and Zhang, F. (2022). "Liquefaction-induced damage evaluation of earth embankment and corresponding countermeasure." Front. Struct. Civ. Eng. 16(9): 1183–1195. https://doi.org/10.1007/s11709-022-0848-7.

70. Ha, I. S., Oh, I. T. and Yoo, M. (2023). "Analysis of Factors Affecting Railway Settlement of Embankment Section due to Liquefaction Using 1-g Shaking Table Model Tests." KSCE Journal of Civil Engineering 27, pp. 2822–2833. DOI 10.1007/s12205-023-2133-2.

71. Harada, Y., Goto, H and Sawada, S. (2022). "Initiation process of tension cracks in soil embankment on liquefied sandy ground investigated from centrifuge model test." Soil Dynamics and Earthquake Engineering, 161:107444. https://doi.org/10.1016/j.soildyn.2022.107444.

72. HAZUS-MH: User's Manual and Technical Manuals. National Institute of Building Sciences. report prepared for the Federal Emergency Management Agency, Washington, D.C. USA, 2004.

73. Hill, R. (1950). "The Mathematical Theory of Plasticity." Clarendon Press, Oxford.

74. Hosseinejad, F., Kalateh, F. and Mojtahedi, A. (2019). "Numerical Investigation of liquefaction in earth dams: A Comparison of Darcy and Non-Darcy flow models." Computers and Geotechnics 116: 103182. https://doi.org/10.1016/j.compgeo.2019.103182.

75. Huang, D. and Wang, G. (2017). "Energy-compatible and spectrum-compatible (ECSC) ground motion simulation using wavelet packets." Earthquake Eng. Struct. Dyn. 46: 1855–1873. https://doi.org/10.1002/eqe.2887.

76. Huang, Y., and Zhu, C. Q. (2016). "Safety Assessment of Antiliquefaction Performance of a Constructed Reservoir Embankment. I: Experimental Assessment." Journal of Performance of Constructed Facilities, 31(2). https://doi.org/10.1061/(ASCE)CF.1943-5509.0000965.

77. Huang, Y., Yashima, A., Sawada, K., Zhang, F. (2008). "Numerical assessment of the seismic response of an earth embankment on liquefiable soils." Bull Eng Geol Environ 67, 31–39. https://doi.org/10.1007/s10064-007-0097-y.

78. Huang, Y., Yashima, A., Sawada, K., Zhang, F. (2009). "A case study of seismic response of earth embankment foundation on liquefiable soils." J. Cent. South Univ. Technol. 16: 0994−1000. DOI: 10.1007/s11771−009−0165−5.

79. Huang, Y., Zhang, W., Dai, Z. and Xu, Q. (2013). "Numerical simulation of flow processes in liquefied soils using a soil–water-coupled smoothed particle hydrodynamics method." Nat Hazards, 69:809–827. DOI 10.1007/s11069-013-0736-5.

80. Hughes, T. J. R. (1987). "The finite element method: linear static and dynamics finite element analysis." Prencice Hall Int.

81. Hynes-Griffin, M. E., Franklin, A. G. (1984). "Rationalizing the seismic coefficient method." Misc. PaperGL-84-13 U.S. Army Waterway Experiment Station, Vicksburg, Mississipi.

82. Idriss, I. M. and Boulanger, R. W. (2008). "Soil liquefaction during earthquakes." Monograph, Earthquake Engineering Research Institute 136(6): 755.

83. Iervolino, I., Cito, P., Felicetta, C., Lanzano, G. and Vitale, A. (2021). "Exceedance of design actions in epicentral areas: insights from the ShakeMap envelopes for the 2016–2017 central Italy sequence." Bulletin of Earthquake Engineering; 19(13), 5391–5414. https://doi.org/10.1007/s10518-021-01192-z.

84. Iervolino, I., Galasso, C. and Cosenza, E. (2010). "REXEL: computer aided record selection for code-based seismic structural analysis." Bulletin of Earthquake Engineering 8: 339–62.

85. Iervolino, I., Galasso, C., Paolucci, R. and Pacor, F. (2011). "Engineering ground motion record selection in the Italian Accelerometric Archive." Bulletin of Earthquake Engineering 9: 1761–78.

86. Ikehara, T. (1970). "Damage to railway embankments due to the Tokachioki earthquake." The Japanese Geotechnical Society X(2):52–71. https://doi.org/10.3208/sandf1960.10.2_52.

87. Inagaki, H., Iai, S., Sugano, T., Yamazaki, H. and Inatomi, T. (1996). "Performance of caisson type quay walls at Kobe." Soils and Foundations, Special Issue on Geotechnical Aspects of the January 17 1995 Hyogoken-Nambu Earthquake, pp. 119-136. https://doi.org/10.3208/sandf.36.Special_119.

88. Inagaki, H., Iai, S., Sugano, T., Yamazaki, H. and Inatomi, T. (1996). "Performanceof caisson type quay walls at kobe port." Soils Found.36: 119–136. Special Issue on

Geotechnical Aspects of the January 17 1995 Hyogoken-NambuEarthquake.https://doi.org/10.3208/sandf.36.Special_119.

89. IS 1893 (Part 1): 2016. “Criteria for Earthquake Resistant Design of Structures.” Indian Standard.

90. Ishihara, K. and Yoshimine, M. (1992). “Evaluation of settlements in sand deposits following liquefaction during earthquakes.” Soils Found. 32 (1), 173–188. https://doi.org/10.3208/sandf1972.32.173.

91. Jakura, K. and Abghari, A. (1994). “Mitigation of liquefaction hazards at three California bridge sites.” 5th US-Japan Workshop, Snowbird, Utah, October.

92. Jaya, V., Dodagoudar, G. R. and Boominathan, A. (2008). “Seismic Soil Structure interaction of tall slender structures.” Int. J. of Geotechnical Engineering, 2(4), 381-393.

93. Jaya, V., Dodagoudar, G. R. and Boominathan, A. (2012). “Seismic soil-foundation structure interaction analysis of deeply embedded ventilation Stack.” Journal of Earthquake and Tsunami, 6(1), (doi: 10.1142/S1793431112500030).

94. Jellal,i B., Bouassida, M. and P., de Buhan (2005). “A homogenization method for estimating the bearing capacity of soils reinforced by columns.” Int. J. Numer. Anal. Meth. Geomech., 29:989–1004, DOI: 10.1002/nag.441

95. Kartha, U., Beena, K. S. and Mohamed, T. C. P. (2016). “Shake Table Studies on Embankments on Liquefiable Soil.” Indian Geotechnical Conference IGC2016. 15-17, IIT Madras, Chennai, India.

96. Katsanos, E. I., Sextos, A. G., Manolis, G. D. (2010). “Selection of earthquake ground motion records: a state-of-the-art review from a structural engineering perspective.” Soil Dynam. Earthq. Eng. 30 (4), 157–169.

97. Kawakami, F. and Asada, A. (1966). “Damage to the Ground and Earth Structures by the Niigata Earthquake of June 16, 1964.” Soils and Foundations, 6(1): 14-30. https://doi.org/10.3208/sandf1960.6.14.

98. Kayen, R. E., Mitchell, J. K., Seed, R. B., Lodge, A., Nishio, S. and Coutinho, R. (1992). “Evaluation of SPT-, CPT-, and shear wave-based methods for liquefaction potential assessment using Loma Prieta Data.” Proc., 4th U.S.-Japan Workshop on Earthquake Resistant Design of Lifeline Facilities and Countermeasures Against Soil Liquefaction,Honolulu, HI NCEER.

99. Kayen, R., Collins, B., Abrahamson, N., Ashford, S., Brandenberg, S.J. and Cluff, L. (2006).

"Investigation of the M6.6 Niigata-Chuetsu Oki, Japan, earthquake of July 16." US Department of the Interior & US Geological Survey, Open File Report 2007-1365.

100. Kaynia, A. M. (2013). (ed.). "Guidelines for deriving seismic fragility functions of elements at risk: buildings, lifelines, transportation networks and critical facilities." Publications Office of the European Union. https://10.2788/19605. (SYNER-G)

101. Khalil, C. and Lopez-Caballero, F. (2021). "Survival analysis of a liquefiable embankment subjected to sequential earthquakes." Soil Dynamics and Earthquake Engineering 140: 106436. https://doi.org/10.1016/j.soildyn.2020.106436.

102. Khalil, C., Rapti, I. and Lopez-Caballero, F. (2017). "Numerical Evaluation of Fragility Curves for Earthquake-Liquefaction-Induced Settlements of an Embankment." Geotechnical Special Publication 0(GSP 283), 21-30. https://doi.org/10.1061/9780784480700.003.

103. Kim, H. J., Dinoy, P. R., Reyes, J. V., Kim, H. S., Park, T. W. and Choi, H. S. (2023). "Seismic Characteristics of a Geotextile Tube-Reinforced Embankment and Shallow Foundations Laid on Liquefiable Soil." Appl. Sci. 13, 785. https://doi.org/10.3390/app13020785.

104. Kimura, T., Takemura, J., Hiro-Oka, A., Okamura, M. and Matsuda, T. (1995). "Countermeasures against liquefaction of sand deposits with structures." Proc. 1 st Int. Conf. Earthquake Geotechnical Engineering, Tokyo, 163-184.

105. Koga, Y. and Matsuo, O. (1990). "Shaking table tests of embankments resting on liquefiable sandy ground." Soils Found. (30):162-74. https://doi.org/10.3208/sandf1972.30.4_162.

106. Kokusho, T. (1999). "Water film in liquefied sand and its effect on lateral spread." J. Geotech. Geo-Environ. Eng. 125 (10), 817–826. https://doi.org/10.1061/(ASCE)1090-0241(1999)125:10(817).

107. Koseki, J., Koda, M., Matsuo, S., Takasaki, H. and Fujiwara, T. (2012). "Damage to railway earth structures and foundations caused by the 2011 off the Pacific Coast of Tohoku Earthquake." Soils and Foundations, 52(5):872–889. http://dx.doi.org/10.1016/j.sandf.2012.11.009.

108. Koseki, J., Koga, Y. and Takahashi, A. (1994). "Liquefaction of sandy ground and settlement of embankments." Proc., Int. Conf. Centrifuge 94, Singapore, Balkema, Rotterdam, Netherlands, 215–220.

109. Koseki, J., Sasaki, T., Wada, N., Hida, J., Endo, M., Tsutsumi, Y. (2006). "Damage to Earth Structures for National Highways by the 2004 Niigata-Ken Chuetsu Earthquake." Soils and

Foundations, 46(6): pp. 739-750. https://doi.org/10.3208/sandf.46.739.

110. Kramer, S. L. (1996). "*Geotechnical Earthquake Engineering*." Prentice-Hall Inc., New Jersey.

111. Krinitzsky, E. L. and Hynes, M. E. (2002). "The Bhuj, India, earthquake: Lessons learned for earthquake safety of dams on alluvium." Eng. Geol. (Amsterdam),66(3–4), 163–196. https://doi.org/10.1016/S0013-7952(02)00049-2.

112. Krinitzsky, E. L. and Hynes, M. E. (2002). "The Bhuj, India, earthquake: lessons learned for earthquake safety of dams on alluvium." Engineering Geology, 66: 163–196.

113. Kumar, A., Kumari, S. and Sawant, V. A. (2020). "Numerical Investigation of Stone Column Improved Ground for Mitigation of Liquefaction." International Journal of Geomechanics. 20(9):04020144. https://doi.org/10.1061/(ASCE)GM.1943-5622.0001758.

114. Kumar, R., Sawaishi, M., Horikoshi, K. and Takahashi, A. (2019). "Centrifuge modeling of hybrid foundation to mitigate liquefaction-induced effects on shallow foundation resting on liquefiable ground." Soils and Foundations 59: 2083–2098. https://doi.org/10.1016/j.sandf.2019.11.002.

115. Kumari, S. and Sawant, V. A. (2021). "Numerical simulation of liquefaction phenomenon considering infinite boundary." Soil Dynam Earthq Eng. 142:106556. https://doi.org/10.1016/j.soildyn.2020.106556.

116. Kwak, D. Y., Stewart, J. P., Brandenberg, S. J. and Mikami, A. (2016). „Characterization of Seismic Levee Fragility Using Field Performance Data." Earthquake Spectra, 32(1):193-215. doi:10.1193/030414EQS035M.

117. Ledezma, C., Hutchinson, T., Ashford Scott, A., Moss, R., Arduino, P., Jonathan D. Bray., Olson, Scott, M., Hashash Youssef, M.A., Verdugo, R., Frost David, J., Robert, E., Kayen and Rollins, K. (2012). "Effects Ground Failure on Bridges, Roads and Railroads." Earthq. Spectra, 28(S1): S119-S143. https://10.1193/1.4000024.

118. Lee, C. J., Chen, H. T., Lien, H. C., Yu-Chen Wei, Y. C. and Hung, W. Y. (2014). "Centrifuge modeling of the seismic responses of sand deposits with an intra-silt layer." Soil Dynamics and Earthquake Engineering. http://dx.doi.org/10.1016/j.soildyn.2014.06.002.

119. Lee, F. H. and Schofield, A. N. (1988). "Centrifuge modelling of sand embankments and islands in earthquakes." Geotechnique 38, No. 1, 45-58.

120. Lee, K. Z-Z., Jensen, N., Gillette, D. R. and Wittwer, D. T. (2019). "Seismic Deformation Analysis of Embankment Dams Using Simplified Total-Stress Approach." Journal of

Geotechnical and Geoenvironmental Engineering, 145(10). https://doi.org/10.1061/(ASCE)GT.1943-5606.0002135.

121. Li, Y., Kitazume, M., Takahashi, A., Harada, K. and Ohbayashi, J. (2021). "Centrifuge study on the effect of the SCP improvement geometry on the mitigation of liquefaction-induced embankment settlement." Soil Dynamics and Earthquake Engineering, 148; 106852. https://doi.org/10.1016/j.soildyn.2021.106852.

122. Liao, S. S. C. and Whitman, R. V. (1986). "Catalouge of Liquefaction and Non-Liquefaction Occurrences during Earthquakes." Report, Department of Civil Engineering, MIT, Cambridge.

123. Lin, Y. l., Leng, Wm., Yang, Gl., Liang, L., Yang, J. S. (2015). "Seismic response of embankment slopes with different reinforcing measures in shaking table tests." Nat Hazards, 76:791–810. https://doi.org/10.1007/s11069-014-1517-5.

124. Liu, L. and Dobry, R. (1997). "Seismic response of shallow foundation on liquefiable sand." J. Geotech. Geoenviron. Eng. 123 (6), 557–567. https://doi.org/10.1061/(ASCE)1090-0241(1997)123:6(557).

125. Liyanapathirana, D. S. and Poulos, H. G. (2002). "Numerical simulation of soil liquefaction due to earthquake loading." Soil Dynamics and Earthquake Engineering, 22, 511–523.

126. Lizarraga, H. S. and Lai, C. G. (2014). "Effects of spatial variability of soil properties on the seismic response of an embankment dam." Soil Dynamics and Earthquake Engineering 64:113–128. http://dx.doi.org/10.1016/j.soildyn.2014.03.016.

127. Lombardi, D. and Bhattacharya, S. (2014). "Liquefaction of soil in the Emilia-Romagna region after the 2012 Northern Italy earthquake sequence." Nat. Hazards 73, 1749–1770. https://10.1007/s11069-014-1168-6.

128. Lopez-Caballero, F. (2021). "Probabilistic seismic analysis for liquefiable embankment through multi-fidelity codes approach." Soil Dynamics and Earthquake Engineering, 149:106849. https://doi.org/10.1016/j.soildyn.2021.106849.

129. Lopez-Caballero, F., Modaressi-Farahmand-Razavi, A. and Stamatopoulos, C. A. (2016). "Numerical Evaluation of Earthquake Settlements of Road Embankments and Mitigation by Preloading." International Journal of Geomechanics, 16(5). https://doi.org/10.1061/(ASCE)GM.1943-5622.0000593.

130. López-Querol, S. and Blázquez, R. (2006). "Identification of failure mechanisms of road embankments due to liquefaction: optimal corrective measures at seismic sites." Canadian

Geotechnical Journal; 43: 889–902. https://doi.org/10.1139/t06-051.

131. Maharjan, M. and Takahashi, A. (2014). "Liquefaction-induced deformation of earthen embankments on non-homogeneous soil deposits under sequential ground motions." Soil Dynamics and Earthquake Engineering; 66: 113–124. https://doi.org/10.1016/j.soildyn.2014.06.024.

132. Marcuson, W. F. (1996). "Seismic Rehabilitation of Earth Dams." Journal of Geotechnical Engineering, ASCE 122(1). https://doi.org/10.1061/(ASCE)0733-9410(1996)122:1(7).

133. Martin, G. R., Finn, W. D. L. and Seed, H. B. (1975). "Fundamentals of liquefaction under cyclic loading."J. Geotech. Engg. Div., ASCE, 101(5), 423-438.

134. Maruyama, Y., Yamazaki, F., Mizuno, K., Tsuchiya, Y. and Yogai, H. (2010). "Fragility curves for expressway embankments based on damage datasets after recent earthquakes in Japan." Soil Dynamics and Earthquake Engineering 30:1158–1167. https://doi.org/10.1016/j.soildyn.2010.04.024.

135. Matsuo, O. (1996). "Damage to river dikes." Soils Found. 235–40. Special. https://doi.org/10.3208/sandf.36.Special_235.

136. McCulloch, D. S. and Bonilla, M. G. (1967). "Railroad damage in the Alaska earthquake." J. Geotech. Eng. Div. 93(5), 89–100.

137. Meneses-Loja, J., Ishihara, K. and Towhata, I. (1998). "Effects of superimposing cyclic shear stress on the undrained behavior of saturated sand under monotonic loading." Soils Found; 38(4): 115–27. https://doi.org/10.3208/sandf.38.4_115.

138. Ming, H. Y. and Li, X. S. (2003). "Fully Coupled Analysis of Failure and Remediation of Lower San Fernando Dam." Journal of Geotechnical and Geoenvironmental Engineering, 129(4). https://doi.org/10.1061/(ASCE)1090-0241(2003)129:4(336).

139. Ming, H. Y., Li, X. S. and Zheng, T. Y. (2011). "Effects of soil density and earthquake intensity on flow deformation of the upper San Fernando dam." Geotechnique 61, No. 12, 1019–1034. http://dx.doi.org/10.1680/geot.9.P.004.3682.

140. Mohanty, S. and Patra, N. R. (2016). "Dynamic response analysis of Talcher pond ash embankment in India." Soil Dynamics and Earthquake Engineering, 84: 238–250. http://dx.doi.org/10.1016/j.soildyn.2016.01.021.

141. Mohanty, S. and Patra, N. R. (2016). "Liquefaction and Earthquake Response Analysis of Panipat Pond Ash Embankment in India." Journal of Earthquake and Tsunami, 10(2). DOI: 10.1142/S1793431116500093.

142. Namdar, A. and Pelko, A. K. (2011). "Embankment loading analysis in laboratory conditions." Ingenieria e Investigación 31(2):48-51. 10.15446/ing.investig.v31n2.23602.

143. Ng, C. W. W., Li, X. S., Van Laak, P. A. and Hou, D. Y. J. (2004). "Centrifuge modeling of loose fill embankment subjected to uni-axial and bi-axial earthquakes." Soil Dynamics and Earthquake Engineering, 24: 305–318. doi:10.1016/j.soildyn.2003.12.002.

144. Nonaka, T., Yamada, S. and Noda, T. (2017). "Verification of a macro-element method in the numerical simulation of the pore water pressure dissipation method – A case study on a liquefaction countermeasure with vertical drains under an embankment." Soils and Foundations, 57: 472–487. http://dx.doi.org/10.1016/j.sandf.2017.05.012.

145. NRC. (1985). "Liquefaction of soils during earthquakes." Report by the Committee on Earthquake Engineering Washington, DC: National Research Council, National Academy Press.

146. Obermeier, S. F. (1996). "Use of liquefaction-induced features for paleoseismic analysis: An overview of how seismic liquefaction features can be distinguished from other features and how their regional distribution and properties of source sediment can be used to infer the location and strength of Holocene paleo-earthquakes." Engineering Geology 44: 1-76. https://doi.org/10.1016/S0013-7952(96)00040-3.

147. Oblak, A., Kosič, M., Viana Da Fonseca, A. and Logar, J. (2020). "Fragility Assessment of Traffic Embankments Exposed to Earthquake-Induced Liquefaction." Applied Sciences. 10(19):6832. https://doi.org/10.3390/app10196832.

148. Oka, L. G., Dewoolkar, M. M. and Olson, S. (2012). "Liquefaction assessment of cohesionless soils in the vicinity of large embankments." Soil Dynamics and Earthquake Engineering, 43, 33-44.

149. Okamura, M, Ishihara, M, Tamura, K. (2006). "Liquefied soil pressures on vertical walls with adjacent embankments." Soil Dynamics and Earthquake Engineering, 26: 265–274. doi:10.1016/j.soildyn.2005.02.017.

150. Okamura, M. and Matsuo, O. (2002). "Effects of remedial measures for mitigating embankment settlement due to foundation liquefaction." International Journal of Physical Modelling in Geotechnics 2: 01-12. https://doi.org/10.1680/ijpmg.2002.020201.

151. Okamura, M. and Tamura, K. (2004). "Prediction Method for Liquefaction-induced settlement of Embankment with Remedial Measure by Deep Mixing Method." Soils and Foundation, 44(4): pp. 53-65.

152. Okamura, M., Abdoun, T. H., Dobry, R, Sharp, M. K. and Taboda, V. M. (2001). "Effects of sand permeability and weak aftershocks on earthquake-induced lateral spreading." Soils Found; 41(6):63–77. https://doi.org/10.3208/sandf.41.6_63.

153. Okamura, M., Tamamura, S. and Yamamoto, R. (2013). "Seismic stability of embankments subjected to pre-deformation due to foundation consolidation." Soils and Foundations, 53(1):11–22. http://dx.doi.org/10.1016/j.sandf.2012.07.015.

154. Olsen, R. S. (1997). "Cyclic liquefaction based on the cone penetrometer test." In Proceedings, NCEER Workshop on Evaluation of Liquefaction Resistance of Soils, National Center for Earthquake Engineering Research, State University of New York at Buffalo, Report No. NCEER-97-0022, pp. 225-76.

155. Olson, S. M. and Stark, T. D. (2003). "Yield Strength Ratio and Liquefaction Analysis of Slopes and Embankments." Journal of Geotechnical and Geoenvironmental Engineering, 129(8). https://doi.org/10.1061/(ASCE)1090-0241(2003)129:8(727).

156. Olson, S. M., Stark, T. D., Walton, W. H. and Castro, G. (2000). "1907 Static Liquefaction Flow Failure of the North Dike of Wachusett Dam." Journal of Geotechnical and Geoenvironmental Engineering, 126(12). https://doi.org/10.1061/(ASCE)1090-0241(2000)126:12(1184).

157. Ozutsumi, O., Sawada, S., Iai, S., Takeshima, Y., Sugiyama, W. and Shimazu T. (2002). "Effective stress analyses of liquefaction-induced deformation in river dikes." Soil Dynamics and Earthquake Engineering, 22:1075–1082.

158. Park, Y-H., Kim, S-R., Kim, S-H. and Kim, M-M. (2000). "Liquefaction of embankments on sandy soils and the optimum countermeasure against the liquefaction." J Korean Geotech Soc 2000;16:15–21.

159. Paull, N. A., Boulanger, R. W. and DeJong, J. T. (2020). "Accounting for Spatial Variability in Nonlinear Dynamic Analyses of Embankment Dams on Liquefiable Deposits." Journal of Geotechnical and Geoenvironmental Engineering, 146(11). https://doi.org/10.1061/(ASCE)GT.1943-5606.0002372.

160. Petalas, A. and Galavi, V. (2013). "Plaxis Liquefaction Model UBC3D-PLM." PLAXIS B.V.

161. Pillai, V.S. and Stewart, R. A. (2011). "Evaluation of liquefaction potential of foundation soils at Duncan Dam." Canadian Geotechnical Journal, 31(6): 951-966. https://doi.org/10.1139/t94-110.

162. Plaxis 2D, reference manual, version 21, 2021.

163. Popescu, R. and Prevost, H. (1993). “Centrifuge validation of a numerical model for dynamic soil liquefaction.” Soil Dynamics and Earthquake Engineering, 12, 73-90.

164. Pourakbar, M., Khosravi, M., Soroush, A., Hung, W-Y., K. K. and Nabizadeh, A. (2022). Dynamic Centrifuge Tests to Evaluate the Seismic Performance of an Embankment Resting on Liquefiable Ground Improved by Unreinforced and Reinforce Soil–Cement Columns. Journal of Geotechnical and Geoenvironmental Engineering, 148(12). https://doi.org/10.1061/(ASCE)GT.1943-5606.0002891.

165. Power, M. S., Rosidi, D., Kaneshiro, J., Gilstrap, S. D. and Chiou, S. J. (1998). “Summary and evaluation of procedures for the seismic design of tunnels.” Final Report for Task 112-D-5.3(c). FHWA Contract No. DTFH61-92-C-0012. Multidisciplinary Center for Earthquake Engineering Research: Buffalo, New York, U.S.

166. Pramaditya, A. and Fathani, T. F. (2021). “Physical Modelling of Earthquake-induced Liquefaction on Uniform Soil Deposit and Earth Structures Settlement.” Journal of the Civil Engineering Forum, 7(1): 85-96.

167. Priebe, H. J. (1989). “The prevention of liquefaction by vibro-replacement.” International conference on earthquake resistant construction and design; A.A. Balkema, Rotterdam . Berlin, Germany.

168. Puebla, H., Byrne, M. and Phillips, P. (1997). “Analysis of canlex liquefaction embankments prototype and centrifuge models.” Canadian Geotechnical Journal 34, pp. 641-657. https://doi.org/10.1139/t97-034.

169. Qin, C., Hazarika, H., Pasha, S. M. K., Furuichi, H., Kochi, Y., Matsumoto, D., Fujishiro, T., Ishibashi, S., Watanabe, N. and Yamamoto, S. (2021). Evaluation of Hybrid Pile Supported System for Protecting Road Embankment Under Seismic Loading. In: Hazarika, H., Madabhushi, G.S.P., Yasuhara, K., Bergado, D.T. (eds) Advances in Sustainable Construction and Resource Management. Lecture Notes in Civil Engineering, vol 144. Springer, Singapore. https://doi.org/10.1007/978-981-16-0077-7_62.

170. Rapti, I., Lopez-Caballero, F., Modaressi-Farahmand-Razavi, A. and Foucault, A., Voldoire, F. (2018). “Liquefaction analysis and damage evaluation of embankment-type structures.” Acta Geotech. 13, 1041–1059. https://doi.org/10.1007/s11440-018-0631-z.

171. Robertson, P. and Wride, C. (1998). “Evaluating cyclic liquefaction potential using the cone penetration test.” Canadian Geotechnical Journal, 35(3), pp.442--459.

172. Robertson, P. K., Woeller, D. J. and Finn, W. D. L. (1992).“Seismic conepenetration test for

evaluating liquefaction potential under cyclicloading."Can. Geotech. J., 29(4), 686–695.

173. Saade, C., Li, Z., Escoffier, S., Thorel, L. (2023). "Centrifuge and numerical modeling of the behavior of homogeneous embankment on liquefiable soil subjected to dynamic excitation." Soil Dynamics and Earthquake Engineering, 172:107999. https://doi.org/10.1016/j.soildyn.2023.107999.

174. Saha, P., Horikoshi, K. and Takahashi, A. (2020). "Performance of sheet pile to mitigate liquefaction-induced lateral spreading of loose soil layer under the embankment." Soil Dynamics and Earthquake Engineering, 139:106410. https://doi.org/10.1016/j.soildyn.2020.106410.

175. Sasaki, Y., Towhata, I., Miyamoto, K., Shirato, M., Narita, A., Sasaki, T. and Sako, S. (2012). "Reconnaissance report on damage in and around river levees caused by the 2011 off the Pacific coast of Tohoku earthquake." Soils Found; 52 (5): 1016–32. https://doi.org/10.1016/j.sandf.2012.11.018.

176. Seed, H. B. (1968). "Landslides during earthquakes due to soil liquefaction." J. Soil Mech. Found. Div., 94(5), 1055–1123. https://doi.org/10.1061/JSFEAQ.0001182.

177. Seed, H. B. (1968). "Landslides during earthquakes due to soil liquefaction." J. Geotech Eng, Div. 94(5), 1055-1123. https://doi.org/10.1061/JSFEAQ.0001182.

178. Seed, H. B. (1979). "Soil Liquefaction and Cyclic Mobility Evaluation for Level Ground During Earthquakes." J. Geotech. Engng. Div., ASCE, Vol. 105, No. GT2, Feb., pp. 201-255.

179. Seed, H. B. and Booker, J. R. (1977). "Stabilization of potentially liquefiable sand deposits using gravel drains." J. of Geotechnical Eng. Div., ASCE. Vol. 103, No. GT7, July, pp. 757-768. https://doi.org/10.1061/AJGEB6.0000453.

180. Seed, H. B. and Idriss, I. M. (1967). "Analysis of Soil Liquefaction: Niigata Earthquake." J. of the Soil Mechanics and Foundations Div., ASCE, 93(SM3), 83-108.

181. Seed, H. B. and Idriss, I. M. (1971). "Simplified Procedure for Evaluating Soil Liquefaction Potential."J. of soil Mechanics and Foundations Division, ASCE 92(6), 1249-1273.

182. Seed, H. B. and Idriss, I. M. (1981). "Evaluation of Liquefaction Potential of Sand Deposits Based on Observations of Performance in Previous Earthquakes." Preprint 81 544, Session on In Situ Testing to Evaluate Liquefaction Susceptibility, ASCE National Convention, St Louis, MO, October.

183. Seed, H. B. and Idriss, I. M. (1982). "Ground Motions and Soil Liquefaction during

Earthquakes." Earthquake Engineering Research Institute Monograph, Oakland.

184. Seed, H. B., Idriss, I. M. and Arango, I. (1983). "Evaluation of liquefaction potential using field performance data." Journal of Geotechnical Engineering Division, ASCE, 109(3), 458-482.

185. Seed, H. B., Lee, K. L. and Idriss, I. M. (1969). "Analysis of Sheffield Dam Failure." Journal of Soil Mechanics and Foundations Division, Proceeding of the American Society of Civil Engineers. https://doi.org/10.1061/JSFEAQ.0001352.

186. Seed, H. B., Lee, K. L., Idriss, I. M. and Makdisi, F. (1973). "Analysis of the Slides in the San Fernando Dams During the Earthquake of Feb. 9, 1971." EERC 73-2. Berkeley, California: Earthquake Engineering Research Center.

187. Seed, H. B., Martin, P. P. and Lysmer, J. (1976). "Pore-Water Pressure Changes during Soil Liquefaction", Journal of the Geotechnical Engineering Division, Proceedings of ASCE, Vol. 102, No. GT4, pp. 323–346.

188. Seed, H. B., Tokimatsu, K., Harder, L. F. and Chung, R. M. (1985). "Influence of SPT procedures in soil liquefaction resistance evaluations." Journal of the Geotechnical Engineering Division, ASCE, 111(12), 1425-1445.

189. Seed, H. B., Tokimatsu, K., Harder, L. F. Jr. and Chung, R. (1985). "Influence of SPT procedures in soil liquefaction resistance evaluations." Journal of Geotechnical Engineering, ASCE, 111(12), 1425-1445.

190. Sengara, I. W., Puspito, N., Kertapati, E., Hendarto. (2006). "Survey of Geotechnical Engineering Aspects of the December 2004 Great Sumatra Earthquake and Indian Ocean Tsunami and the March 2005 Nias–Simeulue Earthquake." Earthquake Spectra. 2006;22(3_suppl):495-509.

191. Shahbodagh, B., Sadeghi, H., Kimoto, S. and Oka, F. (2020). "Large deformation and failure analysis of river embankments subjected to seismic loading." Acta Geotech. 15, 1381–1408. https://doi.org/10.1007/s11440-019-00861-3.

192. Shahir, H. and Pak, A. (2010). "Estimating liquefaction-induced settlement of shallow foundations by numerical approach." Journal of Computers and Geotechnics, 37(3), 267–279.

193. Shan, Z., Ling, D. and Ding, H. (2012). "Exact solutions to one-dimensional transient response of incompressible fluid-saturated single-layer porous media." Applied Mathematics and Mechanics, 34(1), 75–84.

194. Sica, S. and Pagano, L. (2009). "Performance based design of earth dams: Procedures and application to a simple case." Soils and Foundations Vol. 49, No. 6, 921-939. https://doi.org/10.3208/sandf.49.921.

195. Silver, M. L. and Seed, H. B. (1971). "Deformation Characteristics of Sands under Cyclic Loading." J. of the Soil Mechanics and Foundations Div., ASCE, 97(SM8),1081-1098.

196. Singh, R., Roy, D. and Jain, S. K. (2005). "Analysis of earth dams affected by the 2001 Bhuj Earthquake." Engineering Geology, 80: 282– 291. doi:10.1016/j.enggeo.2005.06.002.

197. Sluys, L. J. (1992). "Wave propagation, localisation and dispersion in softening solids." Dissertation, Delft University of Technology, Delft.

198. Smith, I. M. and Griffiths, D. V. (1982). "Programming the Finite Element Method." John Wiley & Sons, Hoboken.

199. Sriskandakumar, S. (2004). "Cyclic loading response of Fraser river sand for validation of numerical models simulating centrifuge tests." M.S. thesis, The Faculty of Graduate Studies Dept. of Civil Engineering, The Univ. of British Columbia.

200. Stamatopoulos, C., Petridis, P., Bassanou, M., Allkja, S., Loukatos, N. and Small, A. (2013). "Improvement of dynamic soil properties induced by preloading verified by a field test." Engineering Geology, 163:101–112. http://dx.doi.org/10.1016/j.enggeo.2013.06.003.

201. Steedman, R. S. and Madabhushi, S. P. G. (1993). "Earthquake-induced Liquefaction of Confined Soil Zones: a Centrifuge Study." ANS&A Reprot Number : 26-04-R-05. Contract Number: DAJA45-93.C-0029.

202. Sykora, D.W. (1987). "Creation of a database of seismic shear wave velocities for correlation analysis." Geotech. Lab. Miscellaneous Paper GL-87-26, U.S. Army Engineer Waterways Experiment Station, Vicksburg, Miss.

203. Tabatabaei, S. A., Esmaeili, M. and Sadeghi, J. (2019). "Investigation of the Optimum Height of Railway Embankments during Earthquake Based on Their Stability in Liquefaction." Journal of Earthquake Engineering, 23:5, 882-908, DOI: 10.1080/13632469.2017.1342301.

204. Tabatabaei, S. A., Sadeghi, J. and Esmaeili, M. (2020). "Investigation of sand columns effect on stability of railway embankments overlaid on liquefiable foundations." Journal of Earthquake Engineering, 24:5, 845-868. DOI: 10.1080/13632469.2018.1453408.

205. Taiebat, M. and Dafalias, Y. F. (2008). "SANISAND: simple anisotropic sand plasticity model." Int J Numer Anal Methods GeoMech. 32(32):915–48. https://doi.org/10.1002/nag.651.

206. Taiebat, M., Shahir, H. and Pak, A. (2007). “Study of pore pressure variation during liquefaction using two constitutive models for sand.” Soil Dynamics Earthquake Engineering, 27, 60–72.
207. Takeuchi, M., Yanagihara, S. and Ishihara, K. (1991). “Shaking table tests on model dikes founded on sand deposits with compacted zone.” Proc., Geo-Coast’91, 509–514. Coastal Development Institute of Technology, Yokohama, Japan.
208. Tani, S. (1991). “Consideration of Earthquake Damage to Earth Dam for Irrigation in Japan.” Proceedings: Second International Conference on Recent Advances in Geotechnical Earthquake Engineering and Soil Dynamics. St. Louis, Missouri, Paper No. 7.42.
209. Tani, S. (1996). “Damage to earth dams.” Soils and Found, pp 263–272. https://doi.org/10.3208/sandf.36.Special_263.
210. Tasiopoulou, P. and Gerolymos, N. (2016). “Constitutive modeling of sand: formulation of a new plasticity approach.” Soil Dynam Earthq Eng. 82 , pp. 205-221. https://doi.org/10.1016/j.soildyn.2015.12.014.
211. Terzaghi, K. (1943). “Theoretical soil mechanics.” New York, Wiley.
212. Tiznado, J. C., Dashti, S., Ledezma, C., Brad, P. W. and Badanagki, M. (2020). “Performance of Embankments on Liquefiable Soils Improved with Dense Granular Columns: Observations from Case Histories and Centrifuge Experiments.”
213. Tokida, K. (2012). “Seismic potential improvement of road embankment.” Advances in Geotechnical Earthquake Engineering Soil Liquefaction and Seismic Safety of Dams and Monuments, Moustafa A (ed.). 269–296. ISBN: 978-953- 51-0025-6 InTech, DOI: 10.5772/28710.
214. Tokimatsu, K., Tamura, S., Suzuki, H. and Katsumata, K. (2012). “Geotechnical problems in the 2011 Tohoku Pacific earthquake.” Joint Conference Proceedings of 9th International Conference on Urban Earthquake Engineering and 4th Asia Conference on Earthquake Engineering, March 6-8, 1, 49-61.
215. Tsegaye, A. (2010). “Plaxis liqueafaction model.” report no. 1. PLAXIS knowledge base.
216. Tsukamoto, Y., Noda, S., Nakatsukasa, M. and Katayama, H. (2022). „Use of weight sounding for examining the liquefaction-induced river levee failures.” Proceedings of the Institution of Civil Engineers - Geotechnical Engineering 175(5): 483–494, https://doi.org/10.1680/jgeen.20.00062.
217. Tyagunov, S., Vorogushyn, S., Jimenez, C. M., Parolai, S. and Fleming, K. (2018). “Multi-

hazard fragility analysis for fluvial dikes in earthquake- and flood-prone areas." Nat. Hazards Earth Syst. Sci., 18, 2345–2354. https://doi.org/10.5194/nhess-18-2345-2018.

218. van Ballegooy, S., Malan, P., Lacrosse, V., Jacka, M. E., Cubrinovski, M., Bray, J. D., O'Rourke, T. D., Crawford, S. A. and Cowan, H. (2014). "Assessment of liquefaction-induced land damage for residential christchurch." Earthq Spectra 30(1):31–55.

219. Vargas, R. R., Ueda, K. and Uemura, K. (2020). "Influence of the relative density and K0 effects in the cyclic response of Ottawa F-65 sand - cyclic Torsional Hollow-Cylinder shear tests for LEAP-ASIA-2019." Soil Dynamics and Earthquake Engineering 133: 106111. https://doi.org/10.1016/j.soildyn.2020.106111.

220. Vermeer, P. A. and de Borst, R. (1984). Non-associated Plasticity for Soils, Concrete and Rock." HERON, Vol. 29, No. 3, Delft University of Technology.

221. Vijayasri, T., Patra, N. R. and Raychowdhury, P. (2016). "Cyclic Behavior and Liquefaction Potential of Renusagar Pond Ash Reinforced with Geotextiles." Journal of Materials in Civil Engineering, 28(11). https://doi.org/10.1061/(ASCE)MT.1943-5533.0001633.

222. Vijayasri, T., Raychowdhury, P. and Patra, N. R. (2016). "Seismic Response Analysis of Renusagar Pond Ash Embankment in Northern India." International Journal of Geomechanics, 17(6). https://doi.org/10.1061/(ASCE)GM.1943-5622.0000828.

223. Vijayasri, T., Raychowdhury, P. and Patra, N. R. (2020). "Dynamic Behavior of a Geotextile-Reinforced Pond Ash Embankment." Journal of Earthquake Engineering, 24:11, 1803-1828. DOI: 10.1080/13632469.2018.1483848.

224. Villavicencio, G., Espinace, R., Palma, J., Fourie, A. and Valenzuela, P. (2013). "Failures of sand tailings dams in a highly seismic country." Canadian Geotechnical Journal. 51(4): 449-464. https://doi.org/10.1139/cgj-2013-0142.

225. Wang, G. (2012). "Efficiency of scalar and vector intensity measures for seismic slope displacements." Front. Struct. Civ. Eng; 6 (1): 44–52. https://doi.org/10.1007/s11709-012-0138-x.

226. Wang, R., Cao, W., Xue, L. and Zhang, J. M. (2021). "An anisotropic plasticity model incorporating fabric evolution for monotonic and cyclic behavior of sand." Acta Geotechnica 16: 43-65. https://doi.org/10.1007/s11440-020-00984-y.

227. Wang, R., Zhang, J.M., Wang, G. (2014). "A unified plasticity model for large post-liquefaction shear deformation of sand." Computers and Geotechnics 59: 54-66. https://doi.org/10.1016/j.compgeo.2014.02.008.

228. Wang. L., Huang, Y. and Wen, Z. Q. (2018). "Centrifuge Modeling of a Constructed Reservoir Embankment: Antiliquefaction Performance Improvement Using Nanoparticles." Journal of Performance of Constructed Facilities, 32(6). https://doi.org/10.1061/(ASCE)CF.1943-5509.0001225.

229. Werner, S. D., Taylor, C. E., Cho, S., Lavoie, J.P., Huyck, C., Eitzel, C., Chung, H. and Eguchi, R. T. (2006). "REDARS 2: methodology and software for seismic risk analysis of highway systems." MCEER-06-SP08, University at Buffalo, State University of New York.

230. White, L. W. and Zaman, M. (1998). "A simple model for fluid accumulation and flow in a porous medium." Applied Mathematics and Computation, 90 (2-3): pp. 181-203. https://doi.org/10.1016/S0096-3003(97)00398-6.

231. Wijewickreme, D., Sriskandakumar, S, and Byrne, P. (2005). "Cyclic loading response of loose air-pluviated Fraser River sand for validation of numerical models simulating centrifuge tests." Canadian Geotechnical Journal. 42(2), 550-561. https://doi.org/10.1139/t04-119.

232. Wu, C. and Kiyota, T. (2019). "Effects of specimen density and initial cyclic loading history on correlation between shear wave velocity and liquefaction resistance of Toyoura sand." Soils and Foundations 59: 2324–2330. https://doi.org/10.1016/j.sandf.2019.03.018.

233. Wu, Q., Li, D-Q., Liu, Y. and Du, W. (2021). "Seismic performance of earth dams founded on liquefiable soil layer subjected to near-fault pulse-like ground motions." Soil Dynamics and Earthquake Engineering 143: 106623. https://doi.org/10.1016/j.soildyn.2021.106623.

234. Xia, Z-F., Ye, G-L., Wang, J-H., Ye, B. and Zhang, F. (2010). "Fully coupled numerical analysis of repeated shake-consolidation process of earth embankment on liquefiable foundation." Soil Dyn Earthq Eng; 30(11): 1309–18. https://doi.org/10.1016/j.soildyn.2010.06.003.

235. Yamada, G. (1966). "Damage to earth structures and foundations by the Niigata earthquake, June 16, 1964." Soils Found. 6(1), 1–13. https://doi.org/10.3208/sandf1960.6.14.

236. Yamaguchi, A., Mori, T., Kazama, M. and Yoshida, N. (2012). "Liquefaction in Tohoku district during the 2011 off the Pacific Coast of Tohoku Earthquake." Soils Found. 52: 811–829. https://doi.org/10.1016/j.sandf.2012.11.005.

237. Yang, C., Zhang, J., Wang, Z., Hou, J. and Si, C. (2018). "Model test of failure modes of high embankment and aseismic measures for buried strike-slip fault movement." Environmental Earth Sciences, 77:233. https://doi.org/10.1007/s12665-018-7324-7.

238. Yang, M., Taiebat, M. and Dafalias, Y. F. (2022). “SANISAND-MSf: a sand plasticity model with memory surface and semifluidised state.” Geotechnique 72, No. 3, 227–246. https://doi.org/10.1680/jgeot.19.P.363.

239. Yang, Z. H., Elgamal, A., Adalier, K. and Sharp, M. K. (2004). “Earth dam on liquefiable foundation and remediation: numerical simulation of centrifuge experiments.” Journal of Engineering Mechanics, ASCE, 130(10): 1168–1176

240. Yang, Z., Elgamal, A. and Parra, E. (2003) Computational model for cyclic mobility and associated shear deformation. J Geotech Geoenviron Eng. 129(12):1119–27. https://doi.org/10.1061/(ASCE)1090-0241(2003)129:12(1119).

241. Yang, Z., Elgamal, A. and Parra, E. (2003). “Computational model for cyclic mobility and associated shear deformation.” J Geotech Geoenviron Eng. 129(12):1119–27. https://doi.org/10.1061/(ASCE)1090-0241(2003)129:12(1119).

242. Ye, B., Ye, G. and Zhang, F. (2012). Numerical modeling of changes in anisotropy during liquefaction using a generalized constitutive model. Computers and Geotechnics 42: 62-72. https://doi.org/10.1016/j.compgeo.2011.12.009.

243. Ye, B., Ye, G., Zhang, F. and Yashima, A. (2007). “Experiment and numerical simulation of repeated liquefaction-consolidation of sand.” Soils Found; 47(3): 547–58. https://doi.org/10.3208/sandf.47.547.

244. Yegian, M. K. (1994). “Liquefaction and Embankment Failure Case Histories, 1988 Armenia Earthquake.” Journal of Geotechnical Engineering, ASCE 120(3). https://doi.org/10.1061/(ASCE)0733-9410(1994)120:3(581).

245. Yokomura, S. (1966). “The damage to river dykes and related structures caused by the Niigata Earthquake.” Soils Found., 6(1), 38–53. https://doi.org/10.3208/sandf1960.6.38.

246. Yoo, M. and Kwon, S. Y. (2023). “Evaluation of Reliquefaction Behavior of Coastal Embankment Due to Successive Earthquakes Based on Shaking Table Tests”. J. Mar. Sci. Eng. 11:1002. https://doi.org/10.3390/jmse11051002.

247. Youd, T. L. and Idriss, I. M. (2001). “Liquefaction resistance of soils: Summary report from the 1996 NCEER and 1998 NCEER/NSF workshops on evaluation of liquefaction resistance of soils.”J. Geotech. And Geoenvir. Engg. Div., ASCE, 127(10), 817-833.

248. Zaregarizi, S. and Khosravi, M. (2022). “Seismic Performance of an Embankment Underlain by a Liquefiable Layer and Supported by Spatially Variable Soil-Cement Wall.” Journal of Geotechnical and Geoenvironmental Engineering, 148(11).

https://doi.org/10.1061/(ASCE)GT.1943-5606.0002895.

249. Zhang, S., Wang, G. and Sa, W. (2013). "Damage evaluation of concrete gravity dams under mainshock–aftershock seismic sequences." Soil Dyn Earthq Eng; 50:16–27. https://doi.org/10.1016/j.soildyn.2013.02.021.

250. Zhang, Y. (2003). "Treatment of seismic input and boundary conditions in nonlinear seismic analysis of a bridge ground system." 16th ASCE Engineering Mechanics Conference, (July 16-18, Seattle), 1–11.

251. Zhang, Y., Chen, Y., Chen, S., Liu, H., Fu, Z. (2019). "Experimental study on deformation of a sandy field liquefied by blasting." Soil Dynamics and Earthquake Engineering, 116:60–68. https://doi.org/10.1016/j.soildyn.2018.09.042.

252. Zhou, H., Liu, X., Tan, J., Zhao, J. and Zheng, G. (2023). "Seismic fragility evaluation of embankments on liquefiable soils and remedial countermeasures." Soil Dynamics and Earthquake Engineering, 164: 107631. https://doi.org/10.1016/j.soildyn.2022.107631.

253. Zhou, S. (1980). "Evaluation of the liquefaction of sand by static cone penetration test." In Proceedings, 7th World Conference on Earthquake Engineering, Istanbul, Turkey, Vol. 3, 156-162.

254. Zhou, Z., Ren, C., Xu, G., Zhan, H. and Liu, T. (2019). "Dynamic Failure Mode and Dynamic Response of High Slope Using Shaking Table Test." Shock and Vibration, Hindawi. Article ID 4802740. https://doi.org/10.1155/2019/4802740.

255. Zienkiewicz, O. C. and Shiomi, T. (1984). "Dynamic behaviour of saturated porous media; the generalized Biot formulation and its numerical solution." International Journal for Numerical Methods in Engineering, 8, 71–96.

256. Zienkiewicz, O. C., Taylor, R. L. (1991). "The finite element method; Solid and Fluid mechanics, Dynamics and Non-Linearity, volume 2." Mc Graw-Hill, U.K., 4 edition.

LIST OF PUBLICATIONS

1. Chakraborty, A. and Sawant, V. A. (2022). "Numerical Simulation of Earthen Embankment Resting on Liquefiable Soil and Remediation Using Stone Columns." International Journal of Geomechanics, 22(11), 04022205:1-20 https://doi.org/10.1061/(ASCE)GM.1943-5622.0002559.
2. Chakraborty, A. and Sawant, V. A. (2022). "Earthquake response of embankment resting on liquefiable soil with different mitigation models." Natural Hazards, 116, 3093–3117 (2023). https://doi.org/10.1007/s11069-022-05799-6.
3. Chakraborty, A. and Sawant, V.A. (2023). "Fragility Assessment of Highway Embankment Resting on Liquefaction-Susceptible Soil." Computers and Geotechnics, 161-105568. https://doi.org/10.1016/j.compgeo.2023.105568.
4. Chakraborty, A., Sawant, V.A. "Response of Embankment on Liquefiable Soil to Sequential Ground Motions Considering Mitigation Measures." Soil Dynamics and Earthquake Engineering (Under Review - Revision Submitted).
5. Chakraborty, A. and Sawant, V. A. (2023). "Calibration of UBC3D-PLM constitutive model to simulate the dynamic response of earthen embankment resting on liquefiable soil." Proceedings of 17th Symposium on Earthquake Engineering (Vol. 3), Lecture Notes in Civil Engineering (LNCE, volume 331). Springer.
6. Chakraborty, A. and Sawant, V. A. (2023). "Numerical study on the behaviour of earthen embankment built on liquefiable soil." The 10th European Conference on Numerical Methods in Geotechnical Engineering (NUMGE 2023), Imperial College London, 26-28 June, 2023. ISSMGE.
7. Chakraborty, A. and Sawant, V. A. "Highway embankment fragility behaviour subjected to liquefaction-induced settlement." 8th international conference on earthquake geotechnical engineering (8ICEGE), Osaka, Japan, 07-10 May, 2024. ISSMGE (Full length paper submitted).
8. Chakraborty, A. and Sawant, V. A. "Effect of foundation liquefiable soil on the response of earthen embankment." Indian Geotechnical Conference, Civil Engg. Dept. IIT Roorkee, India, 14-16 December, 2023. (Full length paper submitted).